p-ISSN 1811-1165
e-ISSN 2413-2179
VOLUME 18, No. 3(37), 2021

EURASIAN PHYSICAL TECHNICAL JOURNAL

E.A. BUKETOV KARAGANDA UNIVERSITY

KARAGANDA, THE REPUBLIC OF KAZAKHSTAN

EURASIAN PHYSICAL TECHNICAL JOURNAL

p - ISSN 1811-1165
e - ISSN 2413-2179

Volume 18, No. 3(37), 2021

1st issue – March, 2004

Journal Founder:

E.A. BUKETOV KARAGANDA UNIVERSITY

Е.А.БӨКЕТОВ АТЫНДАҒЫ ҚАРАҒАНДЫ УНИВЕРСИТЕТІ

КАРАГАНДИНСКИЙ УНИВЕРСИТЕТ ИМ. Е.А.БУКЕТОВА

Contact information:

Editorial board of EPhTJ (Build. 2, room 216)
E.A. Buketov Karaganda University
Universitetskaya Str.28, Karaganda,
Kazakhstan, 100028
Subscription index: 75240

Tel: +7(7212)77-04-03
Fax: +7(7212)77-03-84
E-mail: ephtj@mail.ru

Signed to print on 24.09.2021.
Format 60x84 1/8. Offset paper.
Volume 14.13 p.sh. Circulation 200 copies.
Agreed price. Order No. 107.

Басуға 24.09.2021 ж. қол қойылды.
Пішімі 60×84 1/8. Офсеттік қағазы.
Көлемі 14.13 ес.-б.т. Таралымы 200 дана.
Бағасы келісім бойынша. Тапсырыс № 107.

Подписано к печати 24.09.2021.
Формат 60 × 84 1/8. Офсетная бумага.
Объем 14.13 печ.л. Тираж 200 экз.
Ценадоговорная. Заказ № 107.

Printed in the Publishing House
of the E.A.Buketov KarU

Е.А. Бөкетов атындағы ҚарУ баспасының
баспаханасында басылып шықты

Отпечатано в Издательстве
КарУ имени Е.А.Букетова

Registration Certificate No.4382-Zh, November 7, 2003.
Re-registration Certificate No.KZ50VPY00027647, October 6, 2020 issued by Information Committee of the Ministry of Information and Public Development of the Republic of Kazakhstan

Eurasian Physical Technical Journal, Vol. 18, No. 3(37), 2021

CONTENTS

Dear authors and readers!
Dear Colleagues!

It is already becoming a tradition to inform you with the latest news about the state of the "Eurasian Physical Technical Journal" as an international scientific publication with a non-zero impact factor, indexed in the Scopus database. According to update on 4th September 2021 Cite Score Tracker 2021 is 0.7.

The increase in indicators, as confirmation of international recognition, is due to the results of scientific research provided by the authors on the most pressing problems of modern physics and technology and thanks to the careful and high-quality work of the members of the editorial board and reviewers in preparing materials for publication. This issue presents the original scientific research results of our authors.

In the field of materials science, the possibilities of modern methods for studying phase transformations in ferroelectrics are shown; models of radiation inhibition of relaxation of nonequilibrium defects have been developed; the features of the surface layer of perfect single crystals in the range of nanosized carbon materials have been investigated; features of the forming a hydroxyapatite coating process on a titanium substrate during detonation sputtering; luminescent properties of ceramic samples from their position in the crucible under irradiation, etc.

Some works are devoted to the problems of modern energy, the theory of heat and mass transfer, various aspects of the use of renewable energy sources, the possibility of using organic solid domestic waste as a promising source of fuel, the use of flexible carbon heat-generating material for heating mobile living quarters, etc. A new contribution to the modeling of macro and micro phenomena is the tachyonization cosmological model within the framework of linear form-invariance of transformations.

An important practical application is the results of the variation of the under-reactor trap of the melt of a light-water nuclear reactor with a heat-resistant composite coating with a fluidized bed, the development of a method for the destruction of bottom oil deposits in oil storage tanks using the electro-hydraulic effect, the creation of a biogas plant for processing organic waste from agriculture and food production, etc.

In accordance with the requirements for international scientific publications, we continue to update the editorial board. In this issue we present a new member of the editorial board - Dean of the Faculty of Physics and Technology Zeynidenov Asylbek Kalkenovich (ih = 4). Zeynidenov A.K. - PhD doctor, associate professor, author of many articles, underwent an internship at a number of foreign scientific centers: Instituto Superior de Engenharia do Porto (Porto, Portugal), at the Solar Energy Center of the Southwestern University Neofit Rylsky (Bulgaria, Blagoevgrad), Center for Physicochemical Methods of Analysis, Tomsk Polytechnic University, Russia, etc.

Preparation for publication of each issue of the journal is associated with the responsible work of editors and reviewers, with various technical aspects and processing of materials for publication and many organizational issues. Like the leadership of our university, despite being busy at the main job, Professor A.K. Zeinidenov A.K. always provides great help in solving a number of issues.

We are confident that the work of professor A.K. Zeinidenov, as part of the editorial board of the Eurasian Physical Technical Journal help to further expand and strengthen international cooperation, improve the quality of publications, which will also provide a sufficient level of training for higher education specialists.

We hope that the proposed scientific works will interest our readers.
I'll be glad to see you among our authors of the next issues materials.
Best regards, ch. editor Eurasian phys. tech. j.
Sakipova S.E.
September, 2021

DOI 10.31489/2021No3/5-10

UDC 538.971

STUDY OF PHASE TRANSFORMATIONS IN FERROELECTRICS BASED ON CALCIUM TITANATE

Kozlovskiy A.L.[1,2*], Zdorovets M.V.[1,2,3]

[1]Institute of Nuclear Physics of the Kazakhstan Republic of, Almaty, Kazakhstan
[2]L.N. Gumilyov Eurasian National University, Nur-Sultan, Kazakhstan, kozlovskiy.a@inp.kz
[3]Ural Federal University, Yekaterinburg, Russia

The aim of this work is to study phase transformations kinetics in ferroelectrics based on calcium titanate. The relevance of this study is in the assessment of new methods for obtaining complex phase composition ferroelectrics, which have the potential for application in microelectronics, photocatalysis, and power engineering. The methods of scanning electron microscopy and X-ray diffraction were used as the main methods of analysis. Analysis of morphological features made it possible to establish the kinetics of changes not only in grain sizes, but also in their geometry. During the studies of phase transformations, the following dependence of the TiO_2 – anatase/$CaTi_2O_4$ → TiO_2– anatase /$CaTi_2O_4$/$CaTiO_3$ → $CaTiO_3$/TiO_2 – rutile type was established depending on the annealing temperature. At the same time, at a temperature of 1000°C, a stable structure of ceramic with a perovskite-like structure of the $CaTiO_3$ type and a high structural ordering degree (more than 92%) is formed.

Keywords: calcium titanate, phase transformations, perovskites, ferroelectrics, crystallinity degree.

Introduction

Today, one of the promising materials in microelectronics, photocatalysis and power engineering are ferroelectrics with a perovskite-like structure of the ABO_3 type, where A – Ba, Ca,Sr, B – Ti, Zr, Fe, at.al. [1-5]. Interest in them is due to their semiconductor and ferroelectric properties, which make it possible to use them as capacitors, semiconductor devices, microwave resonators, photocatalysts, as well as the basis for creation of high-frequency electronics devices [6, 7]. A distinctive feature of titanates of barium, calcium and strontium are high dielectric constant, which open up broad prospects for research, as well as their practical application [8-10].

One of the important features affecting the properties of materials, as well as their practical application, is the structural ordering degree and the phase composition of ceramics, which directly depends on the conditions and methods of production. The choice of synthesis methods of ferroelectrics plays an important role on the structural ordering degree and phase composition [11-15]. In most cases, methods of hydrothermal synthesis or plasma sputtering with subsequent heat treatment are used to obtain these types of ceramics [15-25]. However, despite all the positive aspects of these methods, there is a number of limitations imposed on the obtained samples, primarily related to control of structural parameters, as well as the possibility of their variation and obtaining complex composition structures [25-30]. In recent years, alternative methods for production of ferroelectric ceramics with given properties are solid-phase synthesis methods combined with thermal isochronous annealing, which allow controlling the phase composition and crystallinity degree with high accuracy.

Based on the above, the purpose of this work is to study the kinetics of phase transformations in ferroelectrics based on calcium titanate obtained using the solid-phase synthesis method depending on the annealing temperature in the range of 200-1000°C. The relevance of these works is due to the great potential for the applicability of these types of ceramics in microelectronics and photocatalysis.

1. Experimental part

As the initial salts, the following precursors were used: $CaCO_3$ and TiO_2 - anatase, manufactured by Sigma Aldrich (USA) with chemical purity of 99.95 %. The main method for producing ferroelectric ceramics was the method of solid-phase synthesis combined with thermal isochronous annealing at temperatures of 200-1000°C in a muffle furnace for 5 hours. The choice of the annealing time and

.

temperatures is determined by the estimated data from the literature sources of the kinetics of phase transformations in titanates. After annealing, the resulting mixtures were cooled for 24 hours together with a muffle furnace until they completely cooled down and reached room temperature.

The assessment of the morphological features and geometric dimensions of the obtained ferroelectrics was carried out using scanning electron microscopy via Jeol 7500F, Jeol, Japan scanning electron microscope. The study of phase transformations was carried out using the X-ray diffraction method, by analyzing the obtained X-ray diffraction patterns in the Bregg-Brentano geometry in the angular range of 2θ=20-85° with a step of 0.03° and a spectrum set time at a point of 1 sec. Phase and structural parameters were determined using the program code DiffracEVA v.4.2. The phases were refined by comparing the obtained diffraction patterns with the PDF-2(2016) database. Phase selection was carried out when the coincidence probability of the registered diffraction maxima with the positions of the database values was more than 90%. Determination of crystallinity degree was carried out by definement of the ratio of diffraction peak areas to background radiation area. This parameter allows assessing the structural ordering degree of the crystal structure depending on external factors, including thermal annealing.

2. Results and discussion

Figure 1 shows SEM images of synthesized ceramics depending on the annealing temperature, which reflect the kinetics of changes in the morphological features of the samples under study. As can be seen from the data presented, in the case of annealing temperatures of 200-400°C in the structure of ceramics, the presence of large cubic and diamond-shaped particles surrounded by small grains of a spherical or sphere-like shape is observed. The presence of such particles is due to the grinding and phase formation processes, which have arisen as a result of mechanochemical synthesis. An increase in the annealing temperature to 600°C and above leads to the complete melting of large diamond-shaped structures with the formation of small spherical particles covered with a porous shell. At an annealing temperature of 1000°C, particles grow larger with the formation of branched conglomerates, the size of which is several hundred nanometers. In this case, the formed conglomerates are also covered with a porous shell. This behavior of the morphological features and geometry of grains indicates a change in the phase composition as a result of thermal annealing, and the presence of several types of particles during low-temperature annealing indicates the presence of several phases in the structure of ceramics.

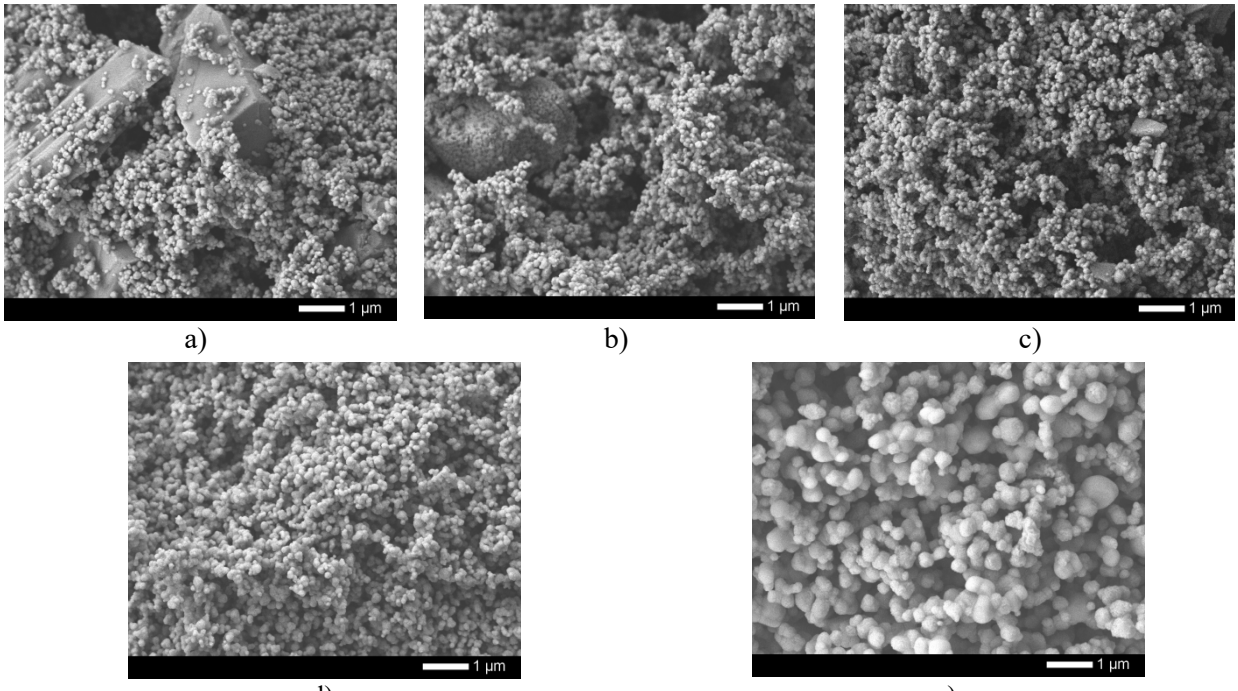

Fig.1. SEM – images: a) 200°C; b) 400°C; c) 600°C; d) 800°C; e) 1000°C

Figure 2 shows X-ray diffraction patterns of synthesized ceramics, reflecting phase transformations and the formation of a crystal structure depending on the annealing temperature. The general appearance of changes in diffraction patterns depending on the annealing temperature indicates the dynamics of change in phase composition of ceramics due to the formation of new phases at an annealing temperature above 600°C. In the case of the ceramics annealing temperature of 200°C, the phase composition, according to the applied full-profile analysis method for diffraction peaks evaluation, is characterized by the presence of two phases: the tetragonal phase of titanium dioxide (TiO_2) and the orthorhombic phase of $CaTi_2O_4$. At the same time, the shape of diffraction lines and their angular position indicate a large degree of structural distortions and deformations in the crystal lattice, the presence of which is due to mechano-chemical grinding processes.

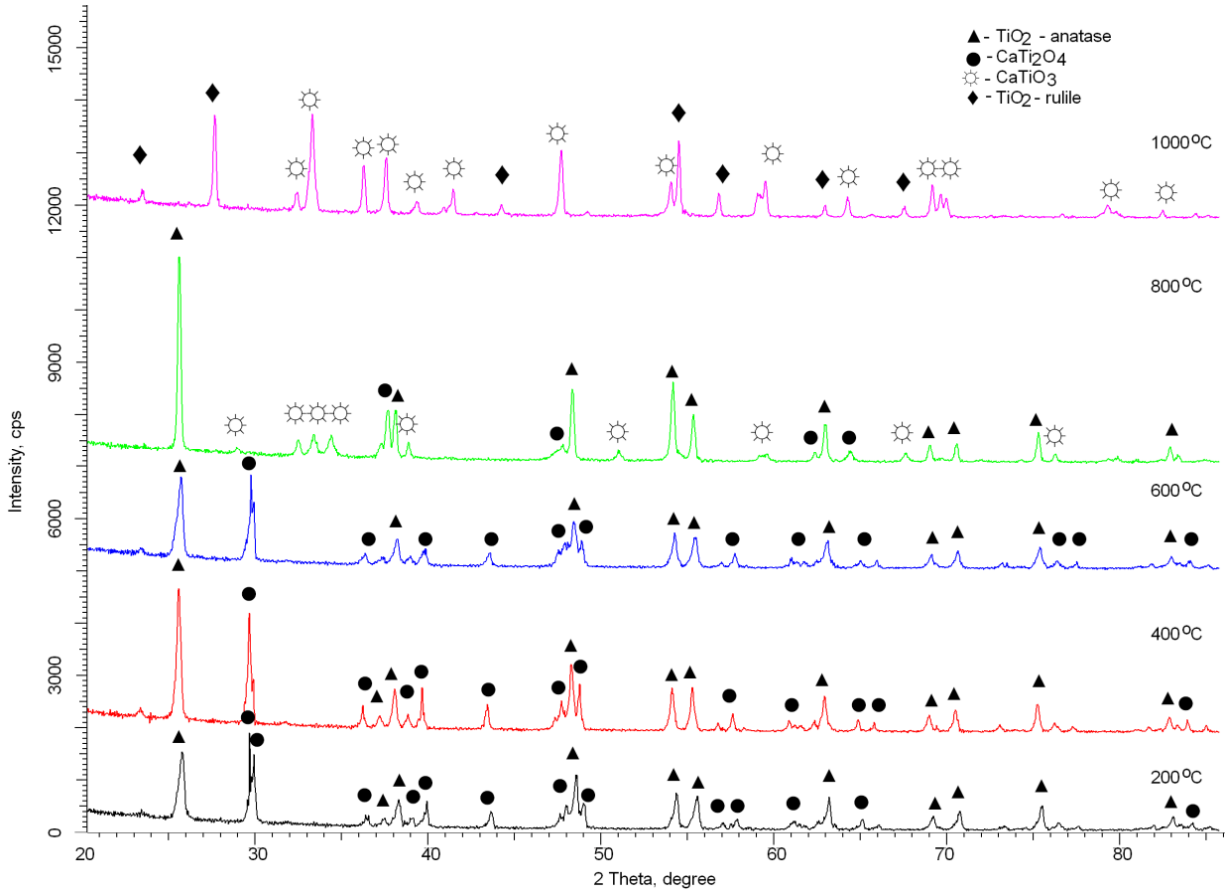

Fig.2. X-ray diffraction patterns of synthesized ceramics versus annealing temperature

At 400°C and 600°C, the appearance of new phases has not been established, but there is an increase in structural ordering, which is evidenced by a change in the shape of diffraction lines and a decrease in their asymmetry. Also, an increase in the structural ordering degree is evidenced by a change in the crystallinity degree, the results of which are shown in Figure 3a. An increase in the crystallinity degree with an increase in the annealing temperature is also associated with a change in the content of TiO_2 and $CaTi_2O_4$ phases in the ceramics structure, the results of which are shown in Figure 3b.

At annealing temperatures of 200 and 400 ° C, the dominant phase in the structure of ceramics was the anatase TiO_2 phase, the content of which was twice the content of the $CaTi_2O_4$ phase, which is known to be a metastable and transitional phase for the $CaTiO_3$ phase. An increase in the annealing temperature from 400 to 600°C leads to the dominance of the $CaTi_2O_4$ phase, which indicates its ordering in the structure. At an annealing temperature of 800°C, a phase transformation is observed with the formation of the orthorhombic $CaTiO_3$ phase from the $CaTi_2O_4$ phase, as well as a decrease in the anatase phase contribution. This phase transformation is also accompanied by a sharp increase in the structural ordering degree and compaction of ceramics. A further increase in the annealing temperature to 1000°C leads to complete displacement of the anatase phase from the structure and its transformation into the rutile phase, the content of which is less than 10 %, as well as the complete transformation of the $CaTi_2O_4 \rightarrow CaTiO_3$ type.

.

Thus, from the data presented, it can be concluded that at a temperature of 1000°C, a stable structure of ceramics with a perovskite-like structure of the $CaTiO_3$ type and a high structural ordering degree (more than 92%) is formed. Also, based on the data obtained, it is possible to chart a diagram of phase transformations of the TiO_2 – anatase/$CaTi_2O_4$ → TiO_2– anatase /$CaTi_2O_4$/$CaTiO_3$ → $CaTiO_3$/TiO_2 – rutile type.

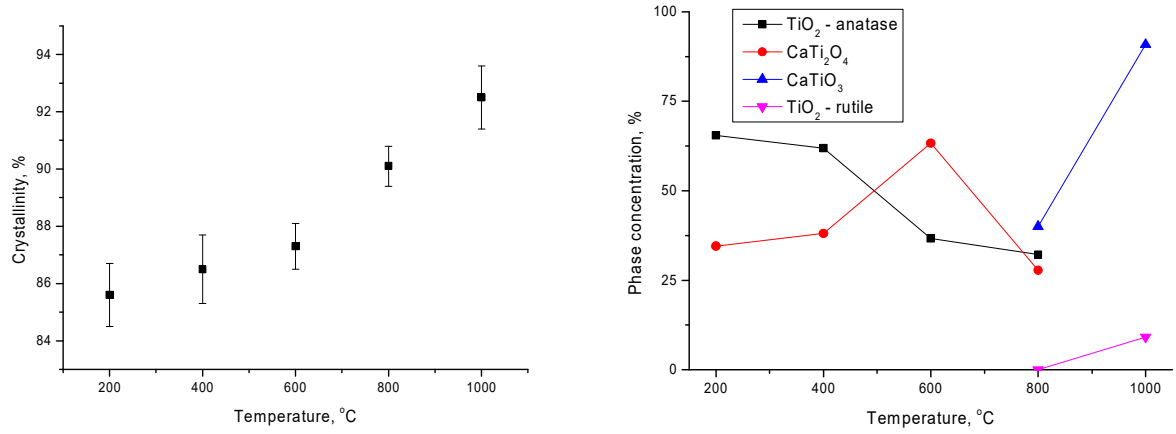

a) b)

Fig.3. a) Graph of the change in the crystallinity degree depending on the annealing temperature; b) Graph of changes in the phase composition of ceramics, obtained on the basis of a full-profile analysis of X-ray diffraction patterns.

Table 1 shows the results of determination of the crystal lattice parameters for each specific phase depending on the annealing temperature. As can be seen from the data presented, an increase in the annealing temperature, leading to an increase in the crystallinity degree, also leads to a decrease in the crystal lattice parameters and, consequently, to its compaction and to a decrease in the structure disorientation.

Table 1. Crystal lattice parameters data

Temperature, °C	Phase			
	TiO_2 – anatase	**$CaTi_2O_4$**	**$CaTiO_3$**	**TiO_2 – rutile**
200	a=3.74751 Å, c=9.45451 Å, V=132.78 Å^3	a=9.69323 Å, b=9.98148 Å, c=3.14554 Å, V=304.34 Å^3	-	-
400	a=3.73355 Å, c=9.51198 Å, V=132.59 Å^3	a=9.74455 Å, b=10.04606 Å, c=3.16836 Å, V=310.16 Å^3	-	-
600	a=3.72550 Å, c=9.49892 Å, V=131.84 Å^3	a=9.71589 Å, b=10.00469 Å, c=3.14910 Å, V=306.11 Å^3	-	-
800	a=3.72624 Å, c=9.47843 Å, V=131.61 Å^3	a=9.81305 Å, b=10.05373 Å, c=3.16824 Å, V=312.57 Å^3	a=5.35063 Å, b=5.42338 Å, c=7.64146 Å, V=221.74 Å^3	-
1000	-	-	a=5.32650 Å, b=5.41168 Å, c=7.62798 Å, V=219.88 Å^3	a=4.45210 Å, c=2.94830 Å, V=61.34 Å^3

Conclusion

In this work, the kinetics of phase transformations in calcium titanate ceramics of the TiO_2 – anatase/$CaTi_2O_4$ → TiO_2– anatase /$CaTi_2O_4$/$CaTiO_3$ → $CaTiO_3$/TiO_2 – rutile type was estimated using scanning electron microscopy and X-ray diffraction.

According to the data obtained, it was found that an increase in the annealing temperature leads not only to a change in the phase composition, but also in the structural ordering degree and volume of the crystal lattice, as well as to a decrease in the deformation of the structure. During the studies, it was found that at a temperature of 1000°C, a stable structure of ceramics with a perovskite-like structure of the $CaTiO_3$ type and a high structural ordering degree (more than 92%) is formed. The chosen synthesis method allows obtaining ferroelectric ceramics of various phase compositions depending on the annealing temperature.

Acknowledgments

This research was funded by the Science Committee of the Ministry of Education and Science of the Republic of Kazakhstan (No. AP09259182).

REFERENCES

1 Yan, Yuxiang, et al. Design of ternary CaTiO3/g-C3N4/AgBr Z-scheme heterostructured photocatalysts and their application for dye photodegradation. *Solid State Sciences,* 2020, Vol. 100, pp.106102-106110.

2 Wang, Dawei, et al. Cold sintered CaTiO3-K2MoO4 microwave dielectric ceramics for integrated microstrip patch antennas. *Applied Materials Today,* 2020, Vol. 18, pp. 100519.

3 Kadam, A. R., et al. Thermoluminescence study and evaluation of trapping parameters CaTiO3: RE (RE= Eu3+, Dy3+) phosphor for TLD applications. *Journal of Molecular Structure.* 2021, Vol. 1225, pp. 129129.

4 Soltani, Tayyebeh, et al. Effect of transition metal oxide cocatalyst on the photocatalytic activity of Ag loaded CaTiO3 for CO2 reduction with water and water splitting. *Applied Catalysis B: Environmental.* 2021, Vol. 286, pp. 119899.

5 Dai, Fangxu, et al. ZnIn2S4 modified CaTiO3 nanocubes with enhanced photocatalytic hydrogen performance. *International Journal of Hydrogen Energy.* 2020, Vol 45.53, pp. 28783-28791.

6 Lanfredi S., et al. K-and Cu-doped CaTiO3-based nanostructured hollow spheres as alternative catalysts to produce fatty acid ethyl esters as potential biodiesel. *Applied Catalysis B: Environmental.* 2020, Vol. 272, pp. 118986.

7 Zhang, Jiawei, et al. Enhanced energy storage performances of CaTiO3-based ceramic through A-site Sm3+ doping and A-site vacancy. *Journal of the European Ceramic Society.* 2021, Vol. 41.1, pp. 352-359.

8 Yatish, K. V., et al. Ochrocarpus longifolius assisted green synthesis of CaTiO3 nanoparticle for biodiesel production and its kinetic study. *Renewable Energy*. 2020, Vol. 147, pp. 310-321.

9 Chen, An-Nan, et al. Enhanced densification and dielectric properties of CaTiO3-0.3 NdAlO3 ceramics fabricated by direct coagulation casting. *Journal of the European Ceramic Society.* 2020, Vol. 40.4, pp. 1174-1180.

10 Liu, Hao, and Sufang Wu. In situ preparation of CaTiO3 and its effect on CO2 sorption performance of nano-CaO–CaTiO3 adsorbent. *Environmental Technology.* 2020, pp. 1-11.

11 Pei, Jingyuan, et al. Effects of Ca/Ti ratio on morphology control and photocatalytic activity of CaTiO3/Ca (OH) 2 composite photocatalyst. *Materials Letters.* 2020, Vol. 276, pp. 128229.

12 Rizwan, Muhammad, et al. Electronic and optical behaviour of lanthanum doped CaTiO3 perovskite. *Materials Research Express.* 2020, Vol.7.1, pp. 015920.

13 Zhang, Yanni, et al. Enhanced osteogenic differentiation of osteoblasts on CaTiO3 nanotube film. *Colloids and Surfaces B: Biointerfaces.* 2020, Vol.187, pp.110773.

14 Vasconcelos, S. J. T., et al. High thermal stability and colossal permittivity of novel solid solution LaFeO3/CaTiO3. *Materials Chemistry and Physics.* 2021, Vol.257, pp. 123239.

15 Yadi, Minoo, et al. CaTiO3/α-TCP coatings on CP-Ti prepared via electrospinning and pulsed laser treatment for in-vitro bone tissue engineering. *Surface and Coatings Technology.* 2020, Vol.401, pp. 126256.

16 Yin, Qian, et al. Enhancements of luminescent properties of CaTiO3: Dy3+, Pr3+ via doping M+=(Li+, Na+, K+). *Materials Letters*. 2020, Vol.266, pp. 127488.

17 Li, Shuiping, et al. Improvement of photovoltaic performance of perovskite solar cells by interface modification with CaTiO3. *Journal of Power Sources.* 2020, Vol.449, pp. 227504.

18 Zdorovets, M.V., Kozlovskiy A.L. The effect of lithium doping on the ferroelectric properties of LST ceramics. *Ceramics International*. 2020, Vol.46.10, pp. 14548-14557.

19 Dimza, Vilnis, et al. Effects of Mn doping on dielectric properties of ferroelectric relaxor PLZT ceramics. *Current Applied Physics.* 2017, Vol.17.2, pp. 169-173.

.

20 Zdorovets, M.V., Kozlovskiy A.L. Study of the effect of La3+ doping on the properties of ceramics based on BaTiOx. *Vacuum,* 2019 Vol.168, pp. 108838.

21 Kozlovskiy A.L., et al. Synthesis, phase composition and structural and conductive properties of ferroelectric microparticles based on ATiOx (A= Ba, Ca, Sr). *Ceramics International.* 2019, Vol. 45.14, pp. 17236-17242.

22 Popov, A.I., Balanzat E. Low temperature X-ray luminescence of KNbO3 crystals. *Nuclear Instruments and Methods in Physics Research Section B: Beam Interactions with Materials and Atoms.* 2000, Vol.166, pp. 305-308.

23 Jumpatam, Jutapol, et al. Influences of Sr2+ Doping on Microstructure, Giant Dielectric Behavior, and Non-Ohmic Properties of CaCu3Ti4O12/CaTiO3 Ceramic Composites. *Molecules.* 2021, Vol.26.7, pp. 1994.

24 Klotins, E., Popov, A.I., Pankratov, V., Shirmane, L., Engers, D. Numerical evidences of polarization switching in PMN type relaxor ferroelectrics. *Integrated Ferroelectrics*, 2011, Vol. 123(1), pp. 32–39.

25 Grigorjeva, L., et al. Luminescence properties of KNbO3 crystals. *Journal of luminescence.* 1997, Vol.72, pp. 672-674.

26 Li, Runrun, et al. Thickness-dependent and tunable mechanical properties of CaTiO3 dielectric thin films determined by nanoindentation technique. *Ceramics International.* 2020, Vol. 46.14, pp. 22643-22649.

27 Abdul Kareem, et al. Effect of annealing temperatures on the structural and crystalline properties of CaTiO3 powder synthesized via conventional solid-state method. *Materials Today: Proceedings.* 2021, Vol.42, pp. 2674-2679.

28 Savchyn V.P., et al. Cathodo-luminescence characterization of polystyrene-BaZrO3 hybrid composites. *Low Temperature Physics.* 2016, Vol.42.7, pp. 597-600.

29 Yang, Liu, et al. Intense and recoverable piezoluminescence in Pr3+-activated CaTiO3 with centrosymmetric structure. *Applied Physics Letters.* 2021, Vol.118.5, pp. 053901.

30 Sasidharan, Sajesh, G. Jyothi, and K. G. Gopchandran. Solution combustion synthesis and luminescence dynamics of CaTiO3: Eu3+, Y3+ nanophosphors. *Journal of Luminescence.* 2021, Vol. 235, pp. 118048.

Article accepted for publication 17.09.2021

DOI 10.31489/2021No3/11-14

UDC 616.874

EFFECT OF NORMALIZING HEATING OF FERRITE COMPACTS ON COMPACTION DURING RADIATION-THERMAL SINTERING

Stary O.[1], Surzhikov A.P.[2], Malyshev A.V.[2*], Lysenko E.N.[2], Sheveleva E.A.[2]

[1]Ceské vysokéucenítechnické v Prague, Prague, Czech Republic

[2]National Research Tomsk Polytechnic University, Tomsk, Russia,malyshev@tpu.ru

The study investigated linear shrinkage of lithium-titanium ferrite samples during radiation-thermal and thermal sintering. Prior to compaction, part of the powders were subjected to thermal heating for 2h at temperatures of 1273, 1373, and 1473 K. It is found that changes in the shrinkage kinetics of ferrites after powder annealing are consistent with the classical concepts of thermal deexcitation of powders due to annealing of defects. Such defects were formed in powder grains during grinding. The obtained data analysis allowed us to offer the most likely model for radiation-thermal activation of powder ferrite sintering. This is a model of radiation inhibition of non-equilibrium defects relaxation.

Keywords: ferrites, sintering, electron beams, pre-annealing of powders, linear shrinkage, shrinkage activation model.

Introduction

The effect of ionizing radiation fluxes during production and modification of materials has been employed in recent years [1–5]. Particularly interesting and fundamentally new results were obtained for objects exposed to a combined effect of powerful radiation fluxes and high temperature (the so-called radiation-thermal (RT) effect). The most important result obtained is the effect of multiple acceleration of synthesis [6–8] and sintering [9–15] of powder inorganic materials. Radiation-thermal sintering mode has been most comprehensively studied on lithium-titanium ferrites and similar structures [16–19]. These studies revealed the effect of multiple acceleration of sintering of ferrite compacts in this specific processing mode.

In [20, 21], a model for activation of RT sintering of ferrites based on radiation-induced diffusion (RID model) by the Deans mechanism was proposed. The authors performed a comparison with the experiment of the kinetic equation of shrinkage of ferrite compacts to confirm this model. The equations of shrinkage in turn were obtained by calculating the sintering kinetics of irradiated powder grains of arbitrary geometry.

In [22], the kinetics of compaction of lithium-titanium ferrites in thermal and radiation-thermal sintering modes was analyzed to elaborate an alternative model for RT sintering activation based on the theory of radiative deceleration of thermal heating of powder grain defects involved in mass transfer (RD model). Within the framework of this model, an active initial phase of sintering is identified with the mass transfer into the compact cavity with active involvement of intrinsic non-equilibrium defects of crystallites accumulated during synthesis and grinding of powders. Thermally-activated defect annihilation occurs simultaneously with sintering and decreases the sintering rate.

Radiation-induced point defects show a short lifetime at sintering temperature; however, they are capable of inhibiting the annealing of intrinsic defects due to distorted potential relief of crystallites. As a result, the duration of the active state of powders increases. The confirmation of both representations displays agnate deprivations change in the choice of contact geometry (RID model) and schematism of the phenomenological approach (RD model). At the identical age both representations are in arrangement with the fundamental concepts of sintering physics and radiation physics. In this regard, additional studies are required to prove the adequacy of the mechanisms of RT sintering activation.

This study presents experimental results that indicate the dominant role of the RD mechanism at early stages of isothermal sintering of ferrite compacts. The RT-sintering mechanism is confirmed based on different efficiency of the RID and RD models with the initial imperfection of powder grains. Indeed, the conditions for the RSD mechanism are most favorable in defect-free grains. On the over-the-counter give the RD device effectiveness is related tothe content of initial non-equilibrium defects.

.

Therefore, the effect of RT sintering activation should be estimated for powders with different contents of non-equilibrium defects to reveal the dominant mechanism of radiation activation of sintering.

1. Experimental part

1.1. Materials

The samples used were lithium-titanium ferrite powders synthesized from a mechanical mixture of oxides and carbonates containing (wt.%): Li_2CO_3 – 11.2; TiO_2 – 18.65; ZnO 7.6; $MnCO_3$ 2.74; the rest is Fe_2O_3. The samples were prepared using 10% solution of polyvinyl alcohol added to the synthesized mixture in an amount of 12 wt.% of the mixture. All compacts were produced in the form of pellets by cold single-action compaction.

1.2 Characterization techniques

The compaction mode used was as follows: P=130 MPa, pressure holding time of 1 min. Two modes of ferrite compact sintering were used: radiation-thermal (RT- sintering) and thermal (T- sintering).For RT-sintering, the samples were exposed to a pulsed electron beam with energy of (1.5–2.0) MeV using an ILU-6 accelerator. The beam current in the pulse was (0.5–0.9) A, the irradiation pulse duration was 500 μs, the pulse repetition rate was (5–50) Hz, and the heating rate of the samples was 1000 °C/min. The samples were irradiated in a lightweight chamotte box with a wall bottom thickness of 15 mm. On the exposed side, the box was covered with a radiation-transparent protector with a mass thickness of 0.1 $g \cdot cm^{-1}$. The temperature was measured using a control sample placed in close proximity to the sintered samples.

T-sintering was performed in a preheated electric chamber furnace to ensure a heating rate comparable to the radiation heating rate. The cell design and the temperature control technique are similar to those used for RT sintering. Sintering in both modes was performed in air.

The electrical resistivity of ferrites was measured at direct current based on a two-electrode scheme on pellet-shaped samples with a near-electrode layer of soft graphite. The measurements were performed during heating from room temperature to 1300 K. The air pressure in the measuring cell did not exceed 19 Pa, the heating rate of samples was 10 degrees per minute. The electric field applied to the sample was 10 V/cm.

Prior to compaction, powders were subjected to thermal heating to control pre-radiation non-equilibrium defect structure. Normalizing warming was performed for 2 h in a resistance furnace at 1273, 1373, and 1473 K. Upon culmination of heating, dusts were slowly cooled to room temperature, and after the addition of a binding additive, pellets 15.1 mm in diameter and 15.0 mm thick were compacted. The shrinkage of samples after sintering was determined by measuring the geometric dimensions L.

2. Results and discussion

Figure 1a presents the results that show the effect of normalizing heating of powders on the sintering kinetics in the electron beam radiation mode. Samples sintered in the T mode show similar dependences (Fig. 1b). Changes in the shrinkage kinetics of ferrites after annealing of compacts are in estimable conformity with the definitive concepts of thermal dismissal of dusts due care to annealing of grinding-induced shortcomings in powder grain [23]. The changes ascertained do not depend on the sintering mood. These points out a similar attribute of the mass transferee devices in both fashions. For quantitative judgement of the effect of compaction activation during RT-sintering at the initial positions of isothermal sintering, the value of the relative shrinkage of compacts for a fixed sintering time can be used (Fig. 1).

Comparison of $\Delta L/L_{PT}$ with a similar value $\Delta L/L_T$ obtained in T sintering can help reveal the effect of preheating of powders on the RT activation effect. Table 1 shows the comparison results for the sintering parameters: T = 1370 K, τ_c = 15 min.

Table 1. Effect of compact heating on the relative efficiency (Z) of isothermal RT-sintering

$T_{heating}$, K	Initial powder	1273	1373	1473
Z, %	90	19	11	0

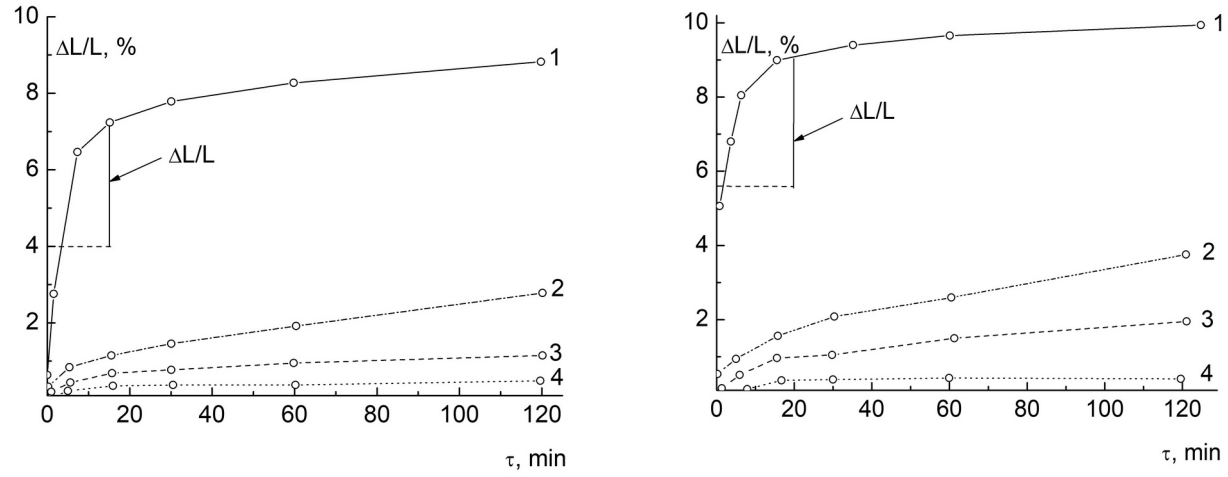

Fig.1. Kinetic patterns of linear shrinkage of ferrites: RT-sintering (a); T-sintering at 1373 K (b). The powder was heated before compaction for 1 h at 1273 K (2), 1373 K (3), 1473 K (4); non-heated powder (1).

The relative efficiency of isothermal RT-sintering (Z) was calculated according to (1) [24].

$$Z = \frac{\Delta L/L_{RT} - \Delta L/L_T}{\Delta L/L_T} \quad (1)$$

Data in Table 1 show that the RT-sintering rate almost twofold exceeds the T sintering grade (in original powders); nevertheless it sharply diminishes abaft preheating of dusts When the warming temperature surpasses the sintering temperature, the compaction effectiveness regularizes (Z=0). That is, the radiation core all vanishes in ferrite dusts deactivated at temperature like to the sintering temperature. This points out that the modeling for dispersal prohibition of non-equilibrium desert leisure is the near most likely device for activation of RT sintering of ferrite dusts.

Conclusion

The scientific value of the research is determined by the model of radiation prohibition of non-equilibrium desert leisure for activation of RT sintering of ferrite powders. Sintering of ferrite powders at yearly stages proceeds by the mechanism of threshold dislocation creep. In this case the activating role of radiation is due to the inhibition of dislocation defect annealing. At later sintering stages, dominate mechanisms of volumetric self-diffusion. Emphasize, the radiation effects manifested by the model of radiation-stimulated diffusion is supposed to occur at these stages only.

Acknowledgments

The research is funded by the Ministry of Education and Science of the Russian Federation as part of the ‘‘Science’’ Program (project No. FSWW-2020-0014).This research was supported by TPU development program.

REFERENCES

1 Groom D.E., Klein S.R. Review of Particle Physics. *European Physical Journal C*. 1998, Vol.3, pp. 144 – 151.

2 Sagynganova I.K., Markin V.B. The organizations of the tasks implementation in the distributed automatic control systems of heat supply stations. *News of the National Academy of Sciences of the Republic of Kazakhstan*. 2019, Vol. 1, No. 433, pp. 63 – 67.

3 Ershov B.G. Radiation technologies: their possibilities, state, and prospects of application. *Herald of the Russian Academy of Sciences*. 2013, Vol. 83, No. 5, pp. 437 – 447.

4 Obodovskiy I. Radiation: fundamentals, applications, risks, and safety. Elsevier Inc., 2019, 694p. https://doi.org/10.1016/C2014-0-00520-5

5 Yurov V.M., Baltabekov A.S., Laurinas V.C., Guchenko S.A. Dimensional effects and surface energy of ferroelectric crystals. *Eurasian phys. tech. j.* 2019, Vol. 16, No. 1(31), pp. 18 – 23. doi 10.31489/2019No1/18-23

.

6 Sharma P. Uniyal, Investigating thermal and kinetic parameters of lithium titanate formation by solid-state method, *J. Therm. Anal. Calorim*. 2017, Vol. 128, pp. 875 – 882.

7 Rakshit S.K., Parida S.C., Naik Y.P., Venugopal V. Thermodynamic studies on lithium ferrites*, J. Solid State Chem.* 2011, Vol. 184, pp. 1186 – 1194.

8 Boldyrev V.V., Voronin A.P., Gribkov O.S., Tkachenko E.V., Karagedov G.R., Yakobson B.I., Auslender V.L. Radiation-thermal synthesis. Current achievement and outlook, *J. Solid State Ion.* 1989, Vol. 36, pp. 1 – 6.

9 Lyakhov N.Z., Boldyrev V.V., Voronin A.P., Gribkov O.S., Bochkarev I.G., Rusakov S.V., Auslender V.L. Electron beam stimulated chemical reaction in solids. *J. Therm. Anal. Calorim*. 1995, Vol. 43, pp. 21 – 31. https://doi.org/10.1007/BF02635965.

10 Halamani Koushallya M., Mathad Shalini K., Kulkarni Akshay B., Mathad Shridhar N., et al. Variation of structural properties of al doped ni-cd ferrites with sintering time. *Eurasian Physical Technical Journal*.2020, Vol. 17, No.2 (34), pp. 11 – 18.

11 Kostishyn V.G., Komlev A.S., Korobeynikov M.V., Bryazgin A.A., Shvedunov V.I., Timofeev A.V., Mikhailenko M.A. Effect of a temperature mode of radiation-thermal sintering the structure and magnetic properties of Mn-Zn-ferrites. *Journal of Nano- and Electronic Physics*. 2015, Vol. 7, pp. 04044.

12 Stary O., Malyshev A.V., Lysenko E.N., Petrova A. Formation of magnetic properties of ferrites during radiation-thermal sintering. *Eurasian Physical Technical Journal*.2020, Vol. 17, No. 2(34). pp. 6 – 10. doi 10.31489/2020No2/6-10.

13 Nikolaev E.V., Astafyev A.L., Nikolaeva S.A., Lysenko E.N., Zeinidenov A.K. Investigation of electrical properties homogeneity of li-ti-zn ferrite ceramics. *Eurasian Physical Technical Journal*. 2020, Vol. 17, No.1(33), pp. 5 – 12.

14 Sharipov M.Z., Hayitov D.E., Rizoqulov M.N., Islomov U.N., Raupova I.B. Domain structure and magnetic properties of terbium ferrite-garnet in the vicinity of the magnetic compensation point. *Eurasian Physical Technical Journal*.2019, Vol. 16, No. 2(32). pp. 21 – 25.

15 Mehnert R. Review of industrial applications of electron accelerators. *Nuclear Instruments and Methods in Physics Research Section B: Beam Interactions with Materials and Atoms*. 1996, Vol. 113, pp. 81 – 87. https://doi.org/10.1016/0168-583X(95)01344-X.

16 Martins M.N., Silva T.F. Electron accelerators: History, applications, and perspectives. *Radiation Physics and Chemistry.* 2014, Vol. 95, pp. 78 – 85. https://doi.org/10.1016/j.radphyschem.2012.12.008.

17 Surzhikov A.P., Frangulyan T.S., Ghyngazov S.A. A thermoanalysis of phase transformations and linear shrinkage kinetics of ceramics made from ultrafine plasmochemical $ZrO_2(Y)$-Al_2O_3 powders. *Journal of Thermal Analysis and Calorimetry*.2014, Vol. 115, No. 2, pp. 1439 – 1445.

18 Surzhikov A.P., Pritulov A.M., Lysenko E.N., Sokolovskiy A.N., Vlasov V.A., Vasendina E.A. Calorimetric investigation of radiation-thermal synthesized lithium pentaferrite. *J. Therm. Anal. Calorim*. 2010, Vol. 101, No. 1, pp. 11 – 13.

19 Surzhikov A.P., Pritulov A.M., Lysenko E.N., et al. Influence of solid-phase ferritization method on phase composition of lithium-zinc ferrites with various concentration of zinc. *J. Therm. Anal. Calorim*. 2012, Vol. 109, No. 1, pp.63 – 67.

20 Surzhikov A.P., Lysenko E.N., Vlasov V.A., Malyshev A.V., Nikolaev E.V. Investigation of the process of ferrite formation in the Li_2CO_3-ZnO-Fe_2O_3 system under high-energy. *Russian Physics Journal.* 2013, Vol. 56, No. 6, pp. 681 – 685.

21 Grishaev V.V., Lebed' B.M. About mechanism of electron-thermal sintering of ferrites. *Electronic equipment. Ser. Materials.* 1985, No. 1, pp. 18 – 24. [in Russian]

22 Smith J., Wijn H.P.J. *Ferrites: Physical properties of ferromagnetic oxides in relation to their technical application*. Eindhoven, Phillips Technical Library, 1959, 233p.

23 Neronov V.A., Voronin A.P., Tatarintseva M.I., et al. Sintering under a high-power electron beam. *Journal of the Less Common Metals*. 1986, Vol. 117, pp. 391 – 394. https://doi.org/10.1016/0022-5088(86)90065-2

24 Geguzin J.E. *Physics of Sintering*.1984, Moscow, Nauka, 360 p.

Article accepted for publication 17.09.2021

DOI 10.31489/2021No3/15-24

UDC 539.013

ANISOTROPY OF THE SURFACE OF CARBON MATERIALS

Yurov V.M.[1], Goncharenko V.I.[2,3], Oleshko V.S.[2], Sha Minggong[4]

[1] E.A. Buketov Karaganda University, Karaganda, Kazakhstan, exciton@list.ru
[2] Moscow Aviation Institute (National Research University), Moscow, Russia, ovs_mai@mail.ru
[3] V.A. Trapeznikov Institute of Control Sciences of Russian Academy of Sciences, Moscow, Russia
[4] Northwestern Polytechnical University (NPU), School of Civil Aviation, Beilin District, Xi'an Shaanxi, P.R. China, Shamg2020@nwpu.edu.cn

In this work, a model of the surface layer of perfect single crystals is used and the role of surface energy in physical processes occurring in the region of nanosized carbon materials is clarified. Of these, diamond, graphite, carbyne and fullerenes have been investigated. The thickness of the surface layer of diamond with cubic symmetry is 8.2 nm and is a nanostructure. The average size of the synthesized nanodiamond is of the order of ~ 8 nm. The value of the surface energy σhkl calculated by us along the diamond planes (100), (110), and (111) is in good agreement with experiment and other calculations. The thickness of the surface layer of graphite along the a axis is equal to $R(I)_a$ = 8.0 nm and also represents a nanostructure. But along the c axis we have a layer thickness of about 1.5 nm and the number of monolayers is only 2. On this c axis, graphite can be created a monolayer by turning it into graphene. The σ_{hkl} value calculated by us along the a and c planes of graphite is 25957 and 5515 mJ/m^2, respectively. Carbines represent a polymeric polyyne or cumulene chain composed of sp-hybridized carbon atoms. If we imagine that the thickness of the surface layer of carbyne is stretched into a one-dimensional chain along the c axis, then the length of this chain is up to 200 nm for α-carbyne. The thickness of the surface layer of fullerenes significantly exceeds the thickness of the surface layer of pure metals. The surface energy of fullerenes σ_{hkl} increases with an increase in the number of carbon atoms $C_{36} \rightarrow C_{96}$. It also changes in the series (111) → (100) → (110).

***Keywords**: diamond, graphite, carbyne, fullerenes, nanostructures, surface layer thickness, surface energy, anisotropy.*

Introduction

This work is a continuation of works [1-3], where for the first time a model of the surface layer of perfect single crystals was constructed and the role of surface energy in physical processes occurring in the nanoscale region was clarified. Calculations of the surface energy will be carried out according to the formula derived under the assumption that there are no first-order phase transitions in these substances up to their melting point, which for crystals with a body-centered (bcc) and face-centered (fcc) cubic structure is given by the relations [4], where Z is the number of formula units of the unit cell, l_{hkl} is the thickness of the first coordination sphere in the [hkl] direction, and is the lattice constant:

$$\begin{aligned} &\text{Im3m, } Z=2;\ l_{100}=a;\ l_{110}=a\sqrt{2};\ l_{111}=a/\sqrt{3},\\ &\text{Fd3m, } Z=4;\ l_{100}=a;\ l_{110}-a/\sqrt{2};\ l_{111}=2a/\sqrt{3}. \end{aligned} \tag{1}$$

In works [5, 6] for the thickness of the surface layer R and surface energy σ, we obtained the following relations:

$$\begin{aligned} R(I) &= \left[\text{kg/mol}\cdot\text{m}^3/\text{kg}\cdot\text{m}^{-2}\right]\cdot 0{,}24\cdot 10^{-9}\cdot M/\rho,\ \text{nm}\\ R(I)_{x=a} &= \left[\text{m}^3\cdot\text{m}^{-2}\right]\cdot 0{,}54\cdot 10^{-11}\cdot x(a)^3,\ \text{nm}\\ R(I)_{y=b} &= \left[\text{m}^3\cdot\text{m}^{-2}\right]\cdot 0{,}54\cdot 10^{-11}\cdot y(b)^3,\ \text{nm}\\ R(I)_{z=c} &= \left[\text{m}^3\cdot\text{m}^{-2}\right]\cdot 0{,}54\cdot 10^{-11}\cdot z(c)^3,\ \text{nm}\\ \sigma_a &= \left[\text{mJ/m}^2\cdot\hat{E}/\hat{E}\right]\cdot 10^{-3}\cdot T_m\cdot R_a(I)/R(I),\ \text{mJ/m}^2\\ \sigma_b &= \left[\text{mJ/m}^2\cdot\hat{E}/\hat{E}\right]\cdot 10^{-3}\cdot T_m\cdot R_b(I)/R(I),\ \text{mJ/m}^2\\ \sigma_c &= \left[\text{mJ/m}^2\cdot\hat{E}/\hat{E}\right]\cdot 10^{-3}\cdot T_m\cdot R_c(I)/R(I),\ \text{mJ/m}^2 \end{aligned} \tag{2}$$

.

Here M is the molar mass of the crystal, ρ is its density, a, b, c are the unit cell parameters of the crystal, and Tm is its melting point. In this work, we investigate the thickness of the surface layer and the surface energy of carbon materials.

3. Diamond

In general, 11 varieties have been identified among crystals and polycrystalline formations of diamond [7]. We will consider only the single crystals shown in Figure 1.

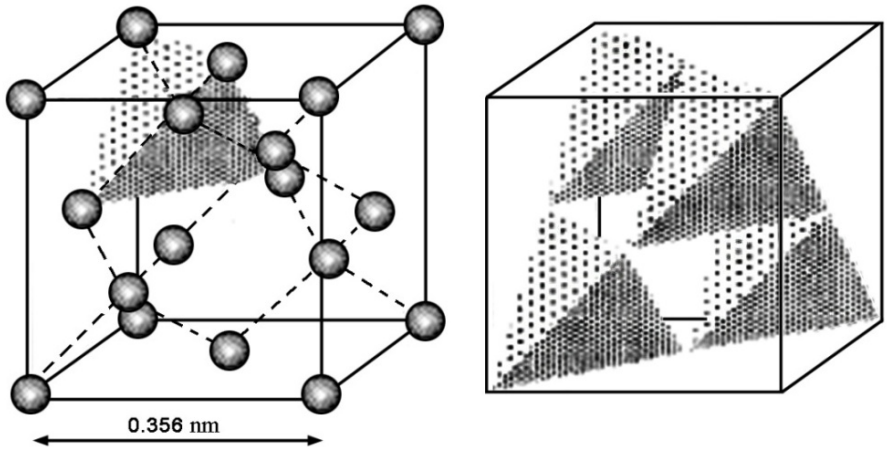

Fig.1. The structure of diamond (allotropic form of carbon C): "ball" model (left) and polyhedral model (right) [8].

Of all the proposed structural modifications of diamond, the structure (allotropic form of carbon C), which belongs to the holohedral class Oh, having the symmetry of the Fedorov space group Oh7-Fd3m, is most confirmed theoretically and experimentally. Lattice parameter at a temperature of 25 ºC and p = 1 atm. is equal to a = 3.57 Å [9], and the melting point T_m = 3973-4273 K, density ρ = 3.47-3.55 (g/cm^3), molar mass M = 12.01 (g/mol).

The structural cell of a diamond crystal is two cubes with a period of 0.356 nm, shifted relative to each other along the diagonal of the cube [9], then instead of (1) one should write:

$$\sigma \approx 2 \cdot 10^{-3} T_{m,}$$
$$\text{Fd3m, } Z = 4; l_{100} = \sigma; l_{110} - \sigma/\sqrt{2}; l_{111} = \sigma/\sqrt{3}. \quad (3)$$

Using (2) and (3), we calculate the surface energy anisotropy (table 1).

Table 1. Anisotropy of the surface energy of diamond

Diamond	(hkl)	Structure	T_m, K	R(I), nm	σ_{hkl} by (1), mJ/m^2	σ_{hkl} by [10], mJ/m^2	σ_{hkl} by [11], mJ/m^2
C	100	Fd3m	4273	8,2 (23)	8546	9100	-
	110				6104	6274	-
	111				5027	5270	4999±355

Let us now analyze Table 1. The thickness of the surface layer of diamond R(I) = 8.2 nm, that is, this layer is a nanostructure, which contains 23 monolayers of diamond. In this layer with atoms of pure metals and non-metals, there is a reconstruction and relaxation associated with the rearrangement of the surface [1-3]. The size effects in the R(I) layer are determined by the entire collective of atoms in the system (collective processes). Almost classic dimensional effects are observed only in nanoparticles and nanostructures [1-3]. Experimentally, they can be observed in very pure single crystals with grazing incidence of X-ray radiation, when the angle of incidence is equal to or less than the critical angle of total internal reflection.

The value of σ_{hkl} calculated by us for the planes (100), (110) and (111) is compared with the results of [10] and [11]. The calculations are based on the work of Harkins [10], published back in 1942. It is performed theoretically on the basis of Gibbs thermodynamics. Assuming the C-C bond energy in diamond equal to 90 kcal/mol, and the cohesion energy of diamond equal to twice the surface energy, he obtained the σ_{hkl} values presented in Table 1. The results of the experimental measurement of the surface energy of diamond by the Griffiths method were carried out in 2017 in [11] along the (111) plane and are also presented in Table 1. This experimental value of the surface energy of diamond is very close to the value of σ_{hkl} obtained by us (Table 1). Theoretical estimates of the surface energy of diamond for the (100) plane were carried out in many works (mJ/m^2): 9400 [12], 6513 [13], 6118 [14].

4. Graphite

Graphite is a unique native mineral, an allotropic modification of the element carbon, which is the most stable in the earth's crust. Graphite has that unique set of qualities that make it indispensable for problems in nuclear physics and power engineering [15]. The hexagonal lattice of graphite belongs to the space group C6/mmc-D^4_{6h} with four atoms per unit cell. The parameter a of the hexagonal cell is 2.46 Å, the parameter c = 6.74 Å, the theoretical density of such a crystal is 2.267 g/cm^3. In each plane, carbon atoms form a network of regular hexagons with an atom spacing of 1.42 Å. The bonds within the layers, which have a covalent nature, represent trigonal hybrids (2s, 2px, 2py) (Figure 2) [8]. Melting temperature range T_m = 4218-4163 K.

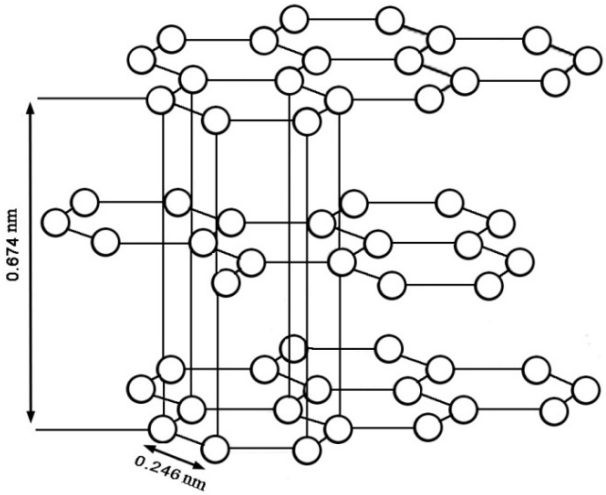

Fig. 2. Hexagonal graphite C [8].

Let us determine the thickness of the surface layer of hexagonal graphite and the anisotropy of its energy. The thickness of the surface layer of diamond R(I) = 8.2 nm, which almost coincides with $R(I)_a$ = 8.0 nm and also represents a nanostructure. But along the c axis we have a layer thickness of about 1.5 nm and the number of monolayers is only 2. On this *c* axis, graphite can be created a monolayer by turning it into graphene.

To determine the free surface energy of pyrographite by the Gilman method in a vacuum, a special installation was constructed. The experiments were carried out with pyrographite grade P2100V with the maximum sample thickness. The free surface energy of pyrographite of the indicated grade was found to be σ_c = 5000 mJ/m^2 [11], which is close to that obtained by us in Table 2.

Table 2. Thickness of the surface layer and anisotropy of the surface energy of graphite

Graphite	Structure	$R(I)_a$, nm	$R(I)_c$, nm	σ_a, mJ/m^2	σ_c, mJ/m^2
C	C6/mmc- D^4_{6h}	8,0 (33)	1,7 (2)	25957	5515

.

5. Carbyne

Carbines represent a polymeric polyyne $(–C\equiv C–)_m$ or cumulene $(=C=C=)_n$ chain, consisting of carbon atoms in sp-hybridization (Fig. 3a, b). Polymer chains in carbyne crystals are packed in the form of hexagons along the (001) face. The presence of bends in the chains causes displacement of the layers (Fig. 3c).

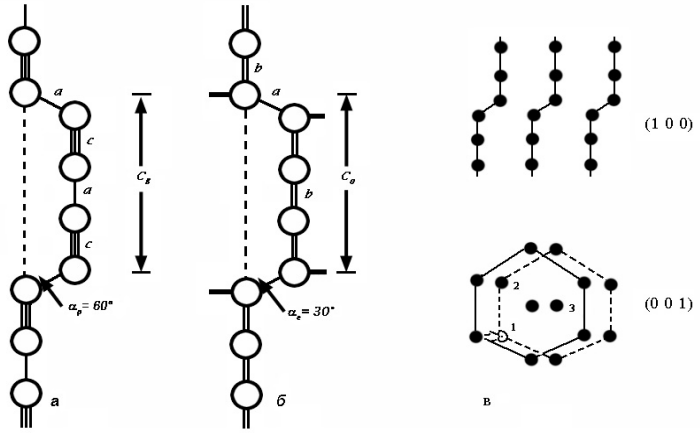

Fig. 3. Heimann's model of α-carbyne (a) and β-carbyne (b); c - two-layer model [16].

The hexagonal cell of the α-carbyne crystal has the following crystal lattice parameters: $a = b = 0.894$ nm and $c = 1.536$ nm; for β-carbyne - $a = b = 0.824$ nm and $c = 0.768$ nm [17]. The density of carbyne crystals is 1.9-2.0 g/cm^3. The melting point is about 3970 K. Using these data, we estimate the thickness of the surface layer and the anisotropy of the surface energy of the carbine (formula 2). Here R(I) = 36, since the molar mass of carbon in the unit cell is M = 12x6 = 72, where 6 is a six-atomic chain [18], and $\rho \approx 2.0$ g/cm^3.

Table 3. Surface layer thickness and surface energy anisotropy of carbyne

Carbin	Structure	$R(I)_a$, nm	$R(I)_c$, nm	σ_a, mJ/m^2	σ_c, mJ/m^2
C	α-carbin	38,6 (43)	196,7 (128)	4257	21692
C	β-carbin	30,2 (37)	40,0 (52)	3330	4411

The thickness of the surface layer of carbyne differs significantly from those for diamond and graphite, but closer to carbon materials like fullerenes, which we will discuss below. The anisotropy of the surface energy of carbines, which also have a hexagonal crystal cell, does not differ much from the surface energy of grphites.

6. Fullerene

Fullerene was discovered in 1985 by G. Kroto (Great Britain), R. Curl, R. Smelli (USA), for which they were awarded the Nobel Prize in 1996. A review of fullerenes for 15 years from 1991 to 2006 was carried out in [19]. The most recent monograph on the structure and stability of higher fullerenes is described in [20]. It discusses a completely new - molecular - form of carbon existence; these closed carbon clusters were able to capture and enclose within themselves individual atoms, several atoms, and even small molecules. All this is new and unusual from the point of view of theoretical chemistry and fundamental science in general.

Fullerenes are carbon clusters with an even, more than 20, number of carbon atoms forming three bonds with each other; atoms in fullerene molecules are located on the surface of a spheroid at the vertices of hexagons and pentagons. Examples of fullerenes are shown in Fig. 4 [21]. In [22], a relationship was found between the mass of the C_{cn} fullerene molecule and the properties of fcc fullerites, such as: the sublimation

energy, the distance between the centers of the nearest molecules, the Grüneisen parameter. compression modulus at zero pressure and temperature.

Based on the data of the correlation dependences, the parameters of the Mee-Lennard-Jones pair potential for the inter-fullerene interaction in fcc fullerites were reconstructed. On the basis of the obtained parameters of the potential, the properties of fullerites are calculated and good agreement with the data known from the literature is obtained. It is shown that at nc <15-20 crystals of fullerites C_{cn} are unstable. At the same time, fullerites where nc> 100 will have anomalously low surface energies, which should lead to fragmentation of nanoclusters from such large Cnc molecules. The parameters of the triple and critical points of fullerenes are estimated.

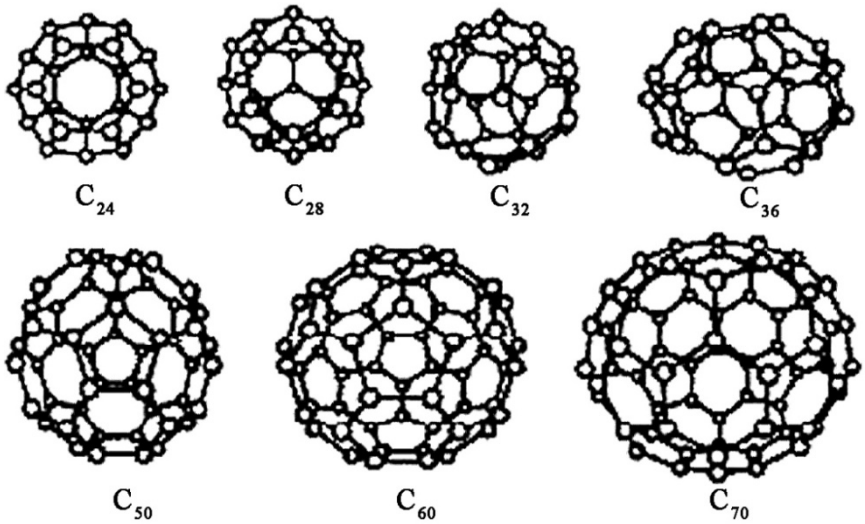

Fig. 4. Schemes of the structure of fullerenes [21]

The evolution of the parameters of the potential and the indicated properties with a change in the molecular weight of the fullerene has been studied. The parameters T_m, M, ρ for calculating R(I) and σ_{hkl} were taken by us from [22]. In addition, knowing the thickness of the surface layer R(I) and the crystal lattice parameter *a*, one can estimate the number of monolayers that form the R(I) layer (n = R(I)/*a*). Thus, for gold and silicon, we showed [23] that the R(I) layer contains 3 monolayers of gold and 4 monolayers of silicon. The same order of magnitude in the R(I) layer contains the number of monolayers of pure metals. Table 4 shows that the thickness of the surface layer of fullerenes R(I) significantly exceeds the thickness of the surface layer of metals.

It follows from Table 4 that the thickness of the surface layer of fullerenes R(I) in C_{84} and C_{96} exceeds 100 nm according to Glater [24], which is characteristic of nanostructures. At h ≈ 10 R(I), a phase transition occurs in the surface layer of fullerenes. For example, in fullerene C_{60}, the phase transition is due to the action of the forces of pair van der Waals interaction, which have a significant noncentral component due to the anisotropy of the electron density on the surface of molecules [25]. So at 2600 K the fcc lattice transforms into a simple cubic (PC) lattice. In the PS structure, there is the possibility of hindered rotations of molecules around ordered axes between two energetically nonequivalent orientational configurations: pentagons and hexagons. The surface energy of fullerenes σ_{hkl} increases with an increase in the number of carbon atoms $C_{36} \rightarrow C_{96}$. It also changes in the series (111) → (100) → (110) (table 4).

7. Carbon materials

Carbon materials can be viewed as spatially cross-linked polymeric substances. In these compounds, carbon is tetravalent and is in one of three ground states corresponding to sp^3 -, sp^2 - and sp-hybridization of electrons. In a number of substances, carbon atoms are in different, including intermediate (sp^m-), electronic states. To describe them, the most convenient classification (Figure 5) by the type of chemical bonds, based on the hybridization of electron orbitals of carbon atoms [26]. Let us now compare the results obtained by us, presented in tables 1-4. Table 1 shows that the thickness of the surface layer of diamond is 8.2 nm and is a nanostructure. That is, nanodiamonds are of interest. Detonation nanodiamonds were first synthesized in 1963 by the explosive decomposition of powerful mixtures of explosives with a negative oxygen balance in a

.

non-oxidizing environment. Such diamonds are characterized by nanoscale particles, chemical resistance of the diamond core, and activity of the peripheral shell [27]. Moreover, as a result of detonation of a charge weighing 140 kg in an aqueous shell, particles of an average size of ~ 8 nm were obtained (compare with Table 1)

Table 4. Thickness of the surface layer and anisotropy of the surface energy of fullerene

Fullerene	(hkl)	Structure	T_m, K	M, g/mol	ρ, g/sm^3	R(I), nm	σ_{hkl} mJ/m^2
C_{36}	100	Fd3m	1404	432.40	1.810	40.61 (36) *a*=11.725 Å	1404
	110						1003
	111						1652
C_{60}	100	Fd3m	2031	720.66	1.484	85.56 (60) *a*=14.17 Å	2031
	110						1451
	111						2321
C_{70}	100	Fd3m	2260	840.23	1.547	93.39 (64) *a*=14.96 Å	2260
	110						1614
	111						2659
C_{76}	100	Fd3m	2387	912.84	1.582	98.09	2367
	110						1705
	111						2808
C_{84}	100	Fd3m	2547	1008.92	1.589	107.93	2547
	110						1819
	111						2997
C_{96}	100	Fd3m	2763	1153.06	1.452	135.00	2763
	110						1974
	111						3251

Nanodiamonds are complex objects, usually with a three-layer structure, including:

- a diamond core with a size of 4-6 nm, which contains from 70 to 90% of carbon atoms;
- a transitional carbon shell (intermediate layer) around the core of X-ray amorphous carbon structures with a thickness of 0.4 - 1.0 nm, which can contain from 10 to 30% of carbon atoms;
- the surface layer, in which, in addition to carbon atoms, other heteroatoms (N, O, H) can be located, forming a number of functional groups (all this is at a level of ~ 8 nm (compare with Table 1).

Nanodiamonds began to be produced by industry on a large scale and their use is increasing all the time (Figure 6). From Table 2, the thickness of the surface layer of graphite along the *c* axis is about 1.5 nm and the number of monolayers is only 2. Along this axis, a monolayer can be created from graphite, turning it into graphene, which can be called "nanographite". The unique electrical properties of graphene (due to its two-dimensional nanostructure), confirmed by numerous studies, are extremely interesting (usually two-layer structures, as in Table 2), both in fundamental and applied terms [28, 29].

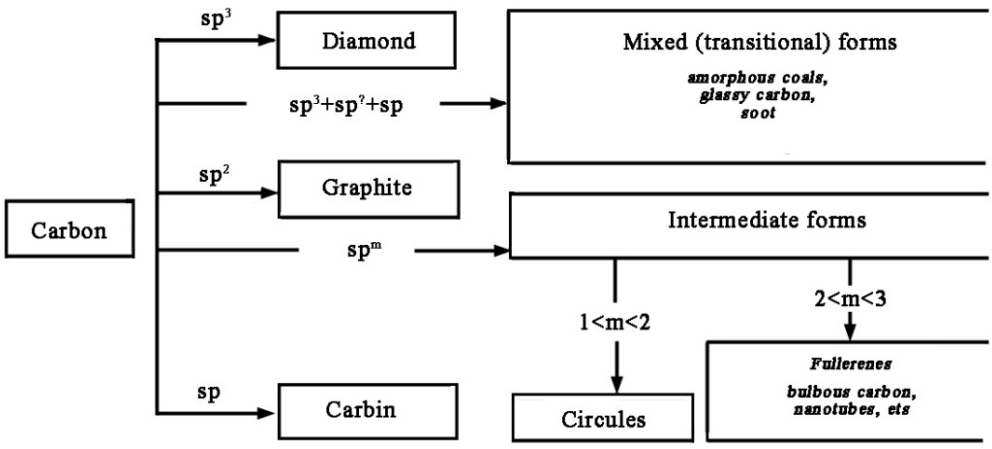

Fig. 5. Classification scheme of allotropic forms of carbon [26].

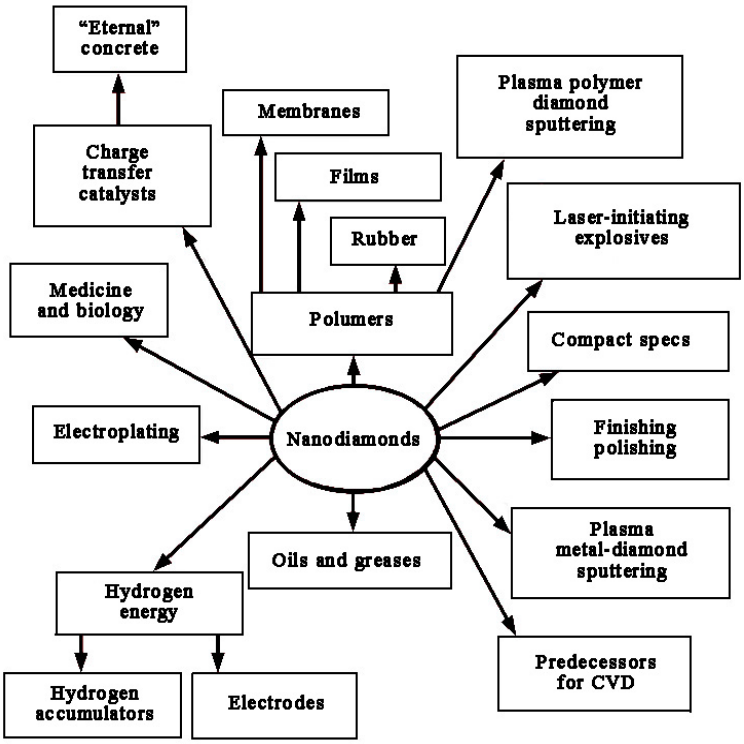

Fig.6. Spheres of application of nanodiamonds [27].

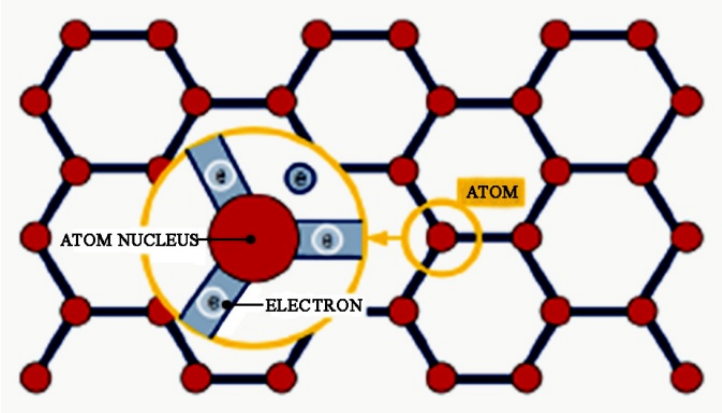

Fig.7. Schematic representation of grapheme.

The amazing properties of graphene are due to the unique nature of its charge carriers - they behave like relativistic particles (Figure 7) [28]. Graphene has a unique structure and exceptional physical and chemical properties, which lead to many possibilities for its application (Fig. 8).

As shown above, the structure of carbyne is formed by carbon atoms assembled into chains by double bonds (α-carbyne) or alternating single and triple bonds (β-carbyne). If we imagine that the thickness of the surface layer of carbyne is stretched into a one-dimensional chain along the *c* axis, then the length of this chain is up to 200 nm for α-carbyne (Table 3). This result was obtained in [30] and is shown in Figure 9.

It turned out that carbyne is the most durable of all known materials. The specific strength of carbine is $6.0\ 10^7$ - $7.5\ 10^7$ N m/kg, while the specific strength of diamond is $2.5\ 10^7$ - $6.5\ 10^7$ N m/kg, graphene is $4.7\ 10^7$ - $5.5\ 10^7$ N m/kg, carbon nanotubes - $4.3\ 10^7$ - $5.0\ 10^7$ N m / kg. Carbyne is the toughest material known. The specific stiffness of carbyne is about 10^9 N m/kg, which is two times higher than the specific stiffness of graphene - $0.45\ 10^9$ N m/kg. The use of carbine is shown in Figure 10. Fullerenes with a large thickness of the surface layer (Table 4), like rare minerals in nature, are quite rare. Their application in practice is also still limited (Figure 11).

.

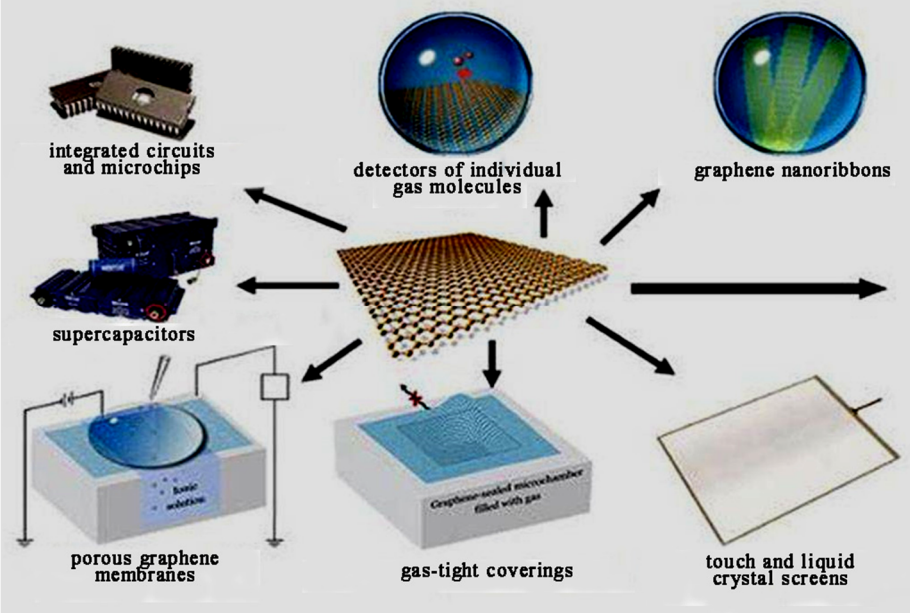

Fig.8. Application of 2D structures of graphite - graphene

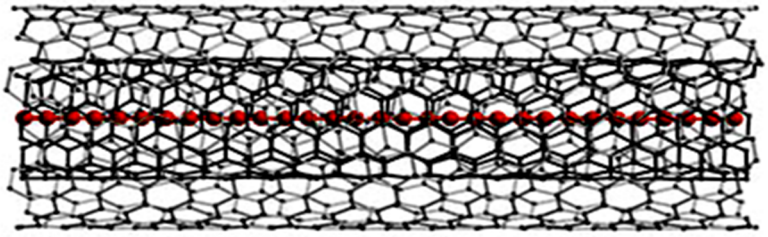

Fig.9. Linear 1D structure of a carbyne molecule (red atoms) inside double-walled carbon nanotubes [30].

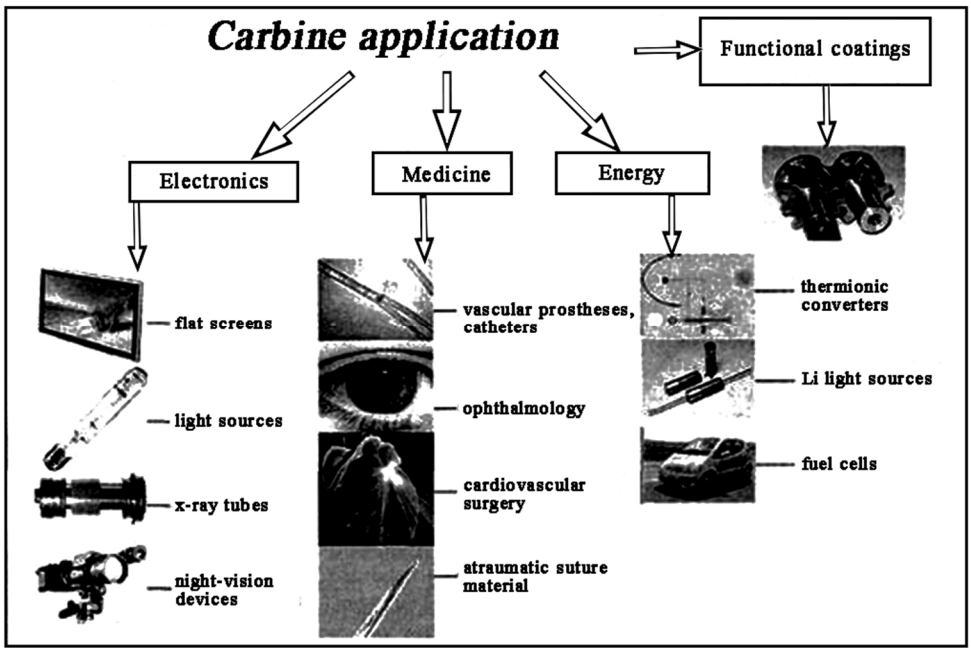

Fig.10. Application of Carbyne nanostructures

Fig.11. Application of fullerene nanostructures

Conclusion

Thus, our model of the surface layer showed that the surface of carbon materials is a nanostructure, the properties of which differ significantly from the bulk properties of the material. Currently, in various fields of science, industry and construction, materials are used that are united by dimensional features, namely, nanocrystals, nanoporous materials, nanostructures, and nanocomposites. The range of nanoobjects is extremely wide and continuously increasing, which makes it possible to obtain new catalytic systems in chemistry, engineering materials with unique material science characteristics, structures with nanometer geometry for recording information, converters of various types of energy, superconducting materials in physics, new drugs and their carriers in medicine.

Today, various kinds of materials, the structural elements of which are on the order of millionths of a millimeter, are beginning to be widely used all over the world to provide improved electrical, magnetic, optical and other consumer qualities. Analysis of the state and development trends of the nanoindustry at the present time allows us to conclude that the following types of carbon nanomaterials are the most promising: nanodiamonds, graphene, nanocarbines, fullerenes, which we have considered in detail, as well as soot, amorphous coals, glassy carbons and many other carbon nanomaterials, analysis and calculation of properties of which can be carried out according to the model we have outlined and tested.

Acknowledgments

The work was carried out under the program of the Ministry of Education and Science of the Republic of Kazakhstan Grant No. 0118RK000063.

REFERENCES

1 Yurov V.M., Oleshko V.S. The impact of the environment on the contact potential difference of metal machine parts. *Eurasian Physical Technical Journal*. 2019. Vol.16, No. 1(31), pp. 99 – 108.

2 Yurov V.M., Makeeva O.V., Oleshko V.S., Fedorov A.V. Development of a device for determining work electron output. *Eurasian Physical Technical Journal*. 2020, Vol.17, No. 1(33), pp. 127 – 131.

3 Yurov V.M., Goncharenko V.I., Oleshko V.S. Anisotropy of the surface of cubic body-centered crystal lattices. *Eurasian Physical Technical Journal*, 2021, Vol.18, No. 1(35), pp. 9-15.

4 Bochkarev V.P. *Development of physical and chemical principles for assessing the effect of surface energy on the properties of materials and processes for microelectronic technology*. Dissertation for degree of Doctor of Technical Sciences, Moscow, 2020, 299 p.

5 Yurov V.M., Goncharenko V.I., Oleshko V.S. Anisotropy of surface energy and thickness of the surface layer of magnetic nanostructures. *Nano- and microsystem technology*, 2021, V. 23, No.2, pp. 8-14.

6 Yurov V.M., Goncharenko V.I., Oleshko V.S. Anisotropy of the surface layer of d - elements. *Modern high technologies*. 2021, No. 2, pp. 88-93.

7 Orlov Yu.L. *Mineralogy of diamond*. Moscow: Nauka, 1984, 70 p.

8 Bullakh A.G., Zolotarev A. *Atlas of structures of minerals - simple substances, sulfides*. St-Petersburg, I997, 28 p.

9 Liopo V.A., Ovchinnikov E.V., Sabut A.V., Voznyakovsky A.A. Structural features of diamond nanocrystals. *Progressive technologies and systems of mechanical engineering*, 2017, No. 1 (56), pp. 73-84.

10 Harkins W. D. Energy Relations of surface of Solids. *Journal Chem. Phys*., 1942, V. 10, pp. 268–272.

11 Nozhkina A.V., Kostikov V.I. Surface energy of diamond and graphite. *Rock-cutting and metal-working tools - technique and technology of its manufacture and application*, 2017, No. 20, pp. 161-167.

.

12 Ormont B.F.*Introduction to physical chemistry and crystal chemistry of semiconductors*. Moscow, 1968, 487p.

13 Oshcherin B.N. On surface energies of A^NB^{8-N} semiconducting compounds. *Phys. Status Solidi*, 1976, A 34, No. 2, pp. K 181-K186.

14 Magomedov M.N. On the surface properties of nanodiamonds. *Physics of the Solid State*, 2010, Vol. 52, No. 6, pp. 1206 – 1214.

15 Zhmurikov E.I., Bubnenkov I.A., Pokrovsky A.S., Kharkov D.V., Dremov V.V., Samarin S.I. *Graphite in Science and Nuclear Engineering*. Novosibirsk, 2013, 198 p.

16 Kudryavtsev Yu.P., Evsyukov S., Guseva M., Babaev V., Khvostov V. Chemistry and Physics of Carbon: *A Series of Advances.* New York-Basel-Hong Kong: Marcel Dekker, Inc., 1997, Vol. 25, pp. 1 – 65.

17 Kasatochkin V.I., Savransky V.V., Smirnov B.N., Melnichenko V.M. Study of Carbyne Condensed from Carbon Vapors. *DAN SSSR*, 1974, Vol. 217, No. 4, pp. 796 – 799.

18 Korobova Yu.G., Bazhanov D.I., Khvostov V.V., et al. Effect of hydrogen impurity on the atomic and electronic structure of the crystalline modification of carbyne. *VMU. Series 3. Physics. Astronomy*. 2013, No. 1, pp. 37-44.

19 Zeynalov E.B. *Fullerenes: Information Collection (1991-2006).* Baku: "Nurlan", 2007, 521p.

20 Kovalenko V.I., Khamatgalimov A.R. *Structure and stability of higher fullerenes*. Moscow, RAS, 2019, 212 p.

21 Shpilevsky E. Fullerenes -new molecules for new materials. *Science and Innovation*, 2006, No.5(39), pp.32-38.

22 Magomedov M.N. About fullerene interaction and properties of fullerites. *Thermophysics of high temperatures*, 2005, V. 43, No. 3, pp. 385 – 395.

23 Yurov V.M., Guchenko S.A., Laurinas V.Ch. Surface layer thickness, surface energy, and atomic volume of an element. *Physicochemical aspects of studying clusters, nanostructures and nanomaterials*, 2018, Vol. 10, pp. 691-699.

24 Gleiter H. Nanostructured materials: basic concepts and microstructure. *Acta mater*. 2000. V.48, pp. 1 – 29.

25 Borisova P.A. *Phase transitions in amorphous fullerenes and their interaction with metals*. Dissertation for degree of the Candidate…, Moscow, 2016, 113 p.

26 Romanenko A.V., Simonov P. *Carbon materials and their physical and chemical properties*. Moscow, 2007, 128p.

27 Dolmatov V.Yu. Detonation nanodiamonds: synthesis, structure, properties and application. *Advances in Chemistry*, 2007, Vol. 76(4), pp. 375 – 397.

28 Novoselov K.S., Geim A.K., Morozov S.V., Jiang D., Zhang Y., Dubonos S.V., Grigorieva I.V., Firsov A.A. Electric field effect in atomically thin carbon films. *Science*, 2004, V. 306, pp. 666 – 669.

29 Neto A.C., Guinea F., Peres N.M.R., Novoselov K.S., Geim A.K. The electronic properties of grapheme. *Rev. Mod. Phys.,* 2009, Vol. 81. - pp. 109-161.

30 Shi L., Rohringer P., Suenaga K. et al. Confined linear carbon chains as a route to bulk carbyne. *Nature Mater.* 2016, Vol. 15, pp. 634–639.

Article accepted for publication 17.09.2021

DOI 10.31489/2021No3/25-29

UDC 547-302: 544.032.2:544.13:539.261

MODIFICATION OF POLYTETRAFLUOROETHYLENE ON THE BASE OF ULTRAFINE POWDER

Tlebaev K.B., Kurmanbaeva G.A.

Abai Kazakh National Pedagogical University, Almaty, Kazakhstan, tlebaev@mail.ru

This paper presents the results of a study of the influence of thermal and mechanical effects on the formation of a structure in an ultrafine powder heated to a temperature above the melting point of polytetrafluoroethylene (327°C). The ultrafine powder was obtained by mechanical grinding of an industrial sample of polytetrafluoroethylene in a rotary knife mill. Studies of the ultra powder with a transmission microscope showed that the powder particles are quasi-spherical particles of a size of 5 microns. The thermal (sintering, slow and fast quenching) and mechanical (creation of high pressure) effects on ultrafine powder particles were determined by the methods of an automated digital microscope Leica DM 6000, X-ray diffraction, and Vickers. It was found that the formation of a supramolecular structure depends on the applied force (pressure) and temperature. Measurement of the hardness of the modified sample showed that its hardness in relation to the hardness of the industrial sample increased by 4 units.

Keywords: *polytetrafluoroethylene, modification, ultrafine powder, supramolecular structure, thermal and mechanical effects*

Introduction

With the growing requirements for polymers, the problem arises from finding alternative ways to improve the properties of polytetrafluoroethylene (PTFE). Despite the comprehensive list of known positive qualities and properties, PTFE has several technological disadvantages that restrain the active use of this material. We can say that modern technologies of fluoropolymers have exhausted their innovative potential, and there is a search for new forms of fluoropolymers, technological methods that eliminate the noted limitations. Proceeding from this, to eliminate the noted limitations and more efficient and expanded application of PTFE, the problem arises of the need to modify it in various ways and to find new ways to improve its properties. Over the years, many approaches [1-11] have been developed for modifying PTFE to improve certain properties. The main ones include copolymerization. Such traditional approaches have made it possible to achieve serious results, but today it can be stated that they have not made it possible to make a qualitative leap in improving the properties of the resulting composites. In particular, with the help of all of the above, it is not possible to overcome the limit reached for the wear rate during friction without lubrication and is (0.5 - 1.0) × 10^{-7} μm/km. The same applies to creep, hardness and radiation resistance of PTFE-based composites. Currently, the most effective method for solving this problem is: - creation of ultrafine (nanosized) PTFE powders. It is known [12] that adhesion of nanoparticles is very high. This article studies the influence of the thermal and mechanical effects on the processes of contact interaction of ultra dispersed particles.

1. Material and research methods

The studied object was the ultrafine powder (UPTFE) with a particle size of up to 5 μm, obtained by mechanical grinding of an industrial PTFE sample in a rotary knife mill. Ultrafine powder heated to a temperature above the melting point of PTFE (327°C). The analysis of the shape of the UPTFE powder particles and the supramolecular structure of the modified PTFE for reflection and transmission was carried out on an automated digital microscope (ACM) Leica DM 6000 M (Nanotechnological laboratory of the engineering profile, KazNU named after al-Farabi). To obtain samples from PTFE nanopowder, we applied the following technology [4]. At the preliminary stage, cylindrical samples 10 mm in diameter and 4 mm in height were formed from the powder during cold pressing on a special mechanical press.

The press was a screw with an M15 thread, which, with the help of knobs, created a force of up to 7000 Newtons. Under the screw was a mold made of steel with a diameter of 40 mm and a height of 30 mm with a

.

plunger with a diameter of 10 mm and an area of 0.78 cm. The surfaces of the mold and the base were made with high precision and were fastened together with two 5 mm screws, which excluded powder leakage. A dosed amount of PTFE nanopowder was poured into a mold, in which a pressure of 35 MPa was created. To create a stationary pressure on the powder, the plunger of the mold was pressed by a spring with a force of 300 Newtons. At the second stage, the mold with the sample obtained by cold pressing was placed in a SNOL muffle furnace and kept in it up to the sintering temperature T = 393^{0}C. The temperature in the muffle furnace was set automatically and the sintering time was 20 minutes per mm of thickness. Shrinkage of the sample during heat treatment was compensated by the force of the spring placed on the plunger. After sintering, the sample was removed from the mold and cooled under running cold water. X-ray diffraction data for UPTFE powder were obtained on a MiniFlex-600 bench top X-ray diffractometer (RIGAKU, Japan). Shooting conditions: voltage across the tube 40 kV, current in the tube 15 mA, anode material - copper, range of scanning angles from - 3 ° to 145 ° (depending on scanning Θ-2Θ.). The scanning speed was from 0.01 to 100 ° / min (2Θ). The minimum step is 0.005 ° (2Θ.). X-ray structural data of the modified PTFE sample were obtained on a DRON-7 diffractometer at a sintering temperature T = 393^{0}C (Nanotechnological laboratory of the engineering profile, KazNU named after al-Farabi). Shooting conditions: interval: from 10.00 ° to 100.00°, survey method: 2theta - theta, exposure, sec. = 1, shooting step, deg. = 0.050 °. The hardness of the samples was measured with Vickers's tester.

2. Results and discussion

Figure 1a shows the ultrafine UPTFE powder. Figure 1b shows a microphotograph of UPTFE powder. The transmission microscope studies of the UPTFE powder have shown that the powder particles are quasi-spherical particles with a size of 5 μm.

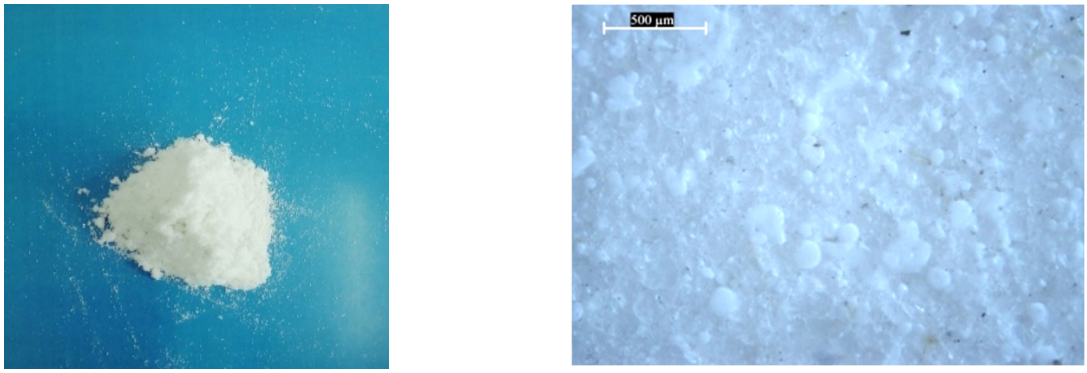

a) b)

Fig.1. a) Ultrafine PTFE powder, b) microphotograph of UPTFE powder.

Monoparticles of UPTFE powder consist of smaller blocks combined into conglomerates, which, in turn, form associates larger than 10 μm in size. In addition to quasi-spherical formations that make up most of the elements of the powder, the blocks and the polymer filling the space between them have a different structure. As a result of this technology, we received modified samples, which are presented in Figure 2 a, b.

a) b)

Fig.2. Modified PTFE samples obtained a) cold pressing, sintering at the temperature T = 393 ^{0}C and rapid quenching; b) after sintering at the temperature T = 393 ^{0}C, slow quenching and standing under the press for a day.

The first sample (Fig.2a) obtained from PTFE powder by cold pressing and sintering at the temperature of T = 393 ° C and rapid quenching. The second sample (Fig. 2b) obtained by sintering, slow quenching and standing for a day under the press,

Figure 3a shows an electron microphotograph of a sample obtained from PTFE powder by cold pressing and sintering at the temperature of T = 393 ° C. In the bulk of the sample (Fig. 3a) obtained by cold pressing and sintering of PTFE nanopowder, it was found that pressing, sintering, and rapid quenching lead to a change in the morphology of the UPTFE structure. The sample contains loosely packed, separated from each other globular, extended, not having a definite shape, supramolecular formations - crystallites. However, a microphotograph of the second sample (Fig. 3b), obtained by sintering, slow quenching and standing for a day under the press, a completely different picture is observed. Here we find that the supramolecular structure is tightly packed, monotonic and uniform throughout the matrix. We observe crystalline formations in the form of bundles - lamellas, having strictly defined shapes and sharply defined boundaries. Blocks in the form of packs are tightly knit together. Gaps between blocks are not observed. These blocks are arranged in an orderly manner. Such a supramolecular structure allows us to conclude that sintering, and then the subsequent slow quenching of the sample and prolonged holding of the sample under pressure for a day, change the structure of the crystal lattice and increase the degree of crystallinity of the sample.

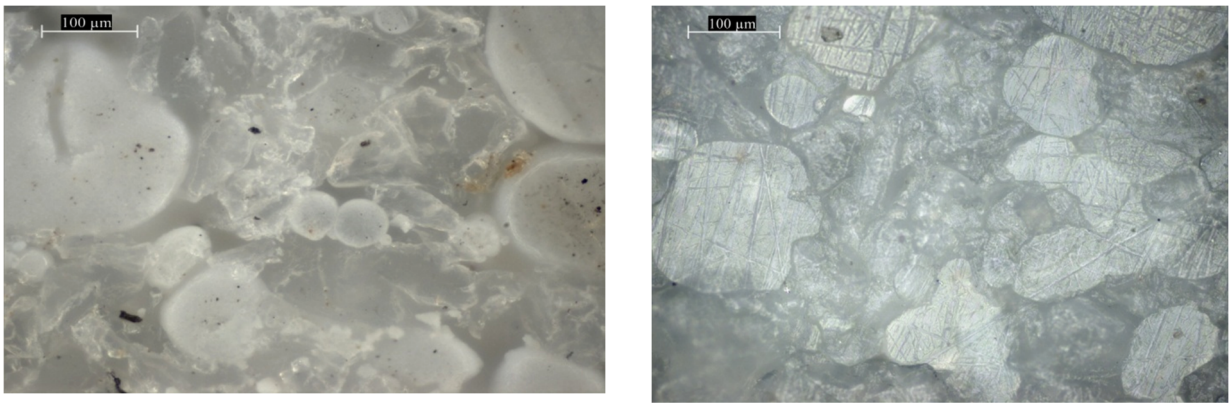

a) b)

Fig.3. Microphotographs of modified PTFE specimens obtained a) by cold pressing, by sintering at a temperature of T = 3930C, b) after sintering, which stood under the press for 24 hours.

This is confirmed by the data of X-ray diffraction analysis .The X-ray diffraction pattern (Fig. 4a) of the ultrafine PTFE powder shows an intense peak at an angle (2θ = 18.158 °) and an amorphous halo at an angle (2θ = 40.00).

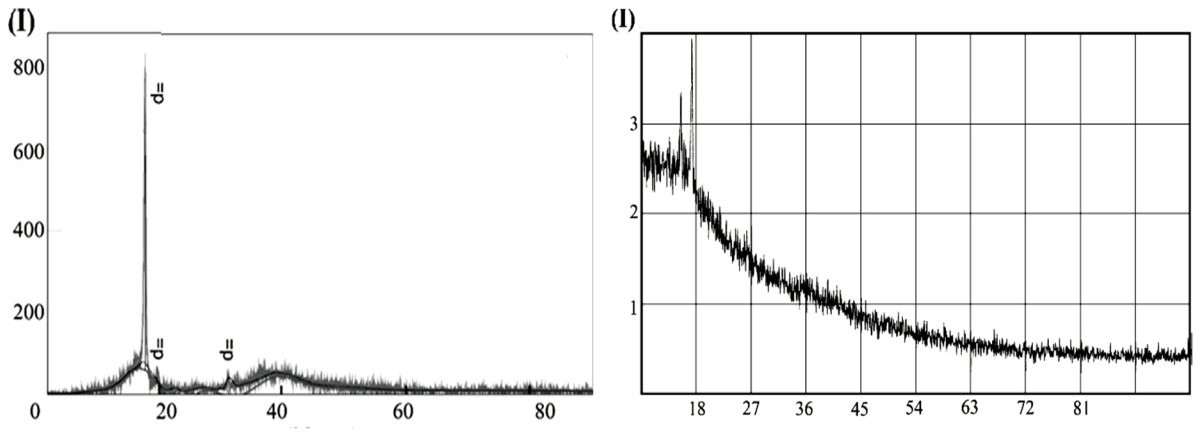

a) b)

Fig.4. X-ray profiles of ultrafine powder (a) and modified PTFE (b).

.

An intense peak at an angle (2θ = 18.158 °) is a first-order phase transition II → IV and is caused by the rearrangement of the crystal lattice from triclinic II to a three-dimensional hexagonal cell IV with parameters a = 5.653 Å, c = 19.512 Å at a temperature of 20^0 C, which is characteristic of crystalline PTFE, which is in good agreement with the literature data [12]. In the X-ray diffraction pattern (Fig. 4b) of the modified PTFE, in addition to the peak at an angle (2θ = 18.158 °), a second peak is observed at an angle (2θ = 16. 396^0), which are less intense. The appearance of only two reflections of the form (h, k, l) means that this set of reflections is described by a flat (two-dimensional) hexagonal lattice with the parameter a = 5.681 Å.

The lattice parameter is in good agreement with the unit cell parameters of PTFE at a temperature of 27^0 C. The presence of only basal-type reflections in the X-ray diffraction pattern is caused by the strong preferential orientation of particles on the surface [12, 13]. The hardness values of the industrial and modified PTFE samples are presented in Table 1.

Table1. Hardness values of industrial and modified PTFE samples

Vicker's hardness, **HV**	
Industrial sample	58
Modified	62

The measurement of the hardness of the modified PTFE sample showed that its hardness in relation to the hardness of the industrial sample increased by 4 units [14].

Conclusion

1. The technology of the modification of the structure and properties of the ultrafine PTFE powder was developed using a special mechanical press and heating powder to the melting temperature of PTFE.

2. It was found that the energy activation of the ultrafine PTFE molecules and the formation of a supramolecular structure depend on a high mechanical pressure, temperature.

In the ultrafine powder, PTFE molecules are clusters of three atoms. Atoms located at the ends of the molecule come into contact and a bond is formed between the atoms. These forces are directly proportional to the contact area of the atoms. The applied force (pressure) influences on these forces through the actual contact area. When the pressed powder is heated to the melting point of PTFE, the contact between the atoms of the pressed powder becomes plastic, and the actual contact area increases significantly.

3. The practical significance of obtained research results will allow them to be used in the development of new polymer materials characterized by an improved set of operational properties.

Acknowledgments

This work was supported by the Ministry of Education and Science of the Republic of Kazakhstan
Project (No 0220 PK 0069)

REFERENCES

1 Fuchs B., Scheler U. Branching and Cross-Linking in Radiation-Modified Polytetrafluoroethylene: A Solid-State NMR Investigation. *Macromolecules*, 2000, Vol. 33, No 1, pp. 120-124.

2 Oshima A., Ikeda S., Katoh E., Tabata Y. Modification of perfluorinated polymers by high-energy irradiation. *Radiation Physics and Chemistry,* 2001, Vol. 62, No. 1, pp. 39 – 45.

3 Lappan U., Geißler U., Haußler L., Jehnichen D., Pompe G., Lunkwitz K. Radiation-induced branching and crosslinking of polytetrafluoroethylene (PTFE). *Nuclear Instruments and Methods in Physics Research Section B: Beam Interactions with Materials and Atoms*, 2001, Vol. 185, No.14, pp. 178 – 183.

4 Lappan U., Fuchs B., Geiβler U., Scheler U., Lunkwitz K. Number-average molecular weight of radiation-degraded poly(tetrafluoroethylene). An end group analysis based on solid-state NMR and IR spectroscopy. *Polymer,* 2002, Vol. 43, No.13, pp. 4325– 4330.

5 Lappan U., Fuchs B., Geiβler U., Scheler U., Lunkwitz K. Identification of new chemical structures in poly(tetrafluoroethylene-co-perfluoropropyl vinyl ether) irradiated in vacuum at different temperatures. *Radiation Physics and Chemistry,* 2003, Vol. 67, No. 4, pp. 447– 451.

6 Lunkwitz K, Lappan U., Fuchs B., Scheler U. Modification of perfluorinated polymers by high-energy irradiation. *Journal of Fluorine Chemistry,* 2004, Vol. 125, No. 5, pp. 863– 873.

7 Khatipov S.A., Nurmukhametov R.N., Seliverstov D. I., Sergeev A. M. Spectrophotometric and luminescent analysis of polytetrafluoroethylene treated by γ-irradiation near the melting point. *High molecular weight compound.* A, 2006, Vol. 48, No. 2, pp. 263-270.

8 Tabata Y., Ikeda S., Tabata Y., Suzuki H., Miyoshi T., Katsumura. Formation of crosslinked PTFE by radiation-induced solid-state polymerization of tetrafluoroethylene at low temperatures. *Radiation Physics and Chemistry,* 2008, Vol. 77, № 9, pp. 401 - 408.

9 Khatipov S. A., Konova E. M., Artamonov N. A. Radiation-modified polytetrafluoroethylene: structure and properties. *Russian Chemical Journal*, 2008, Vol. LII, No.5, pp. 64-72.

10 Khatipov S. A., Kabanov S. P., Konova E. M. Ivanov S. A. Change in the porosity of polytetrafluoroethylene during radiation modification above the melting temperature. *Polymer Science Series A*, 2012, Vol.54, pp.644–650.

11 Vasilev A P., Okhlopkova A.A., Struchkova T.S., Alekseev A.G., Kolesova E. S., Grakovich P. N. Operational Characteristics of Polytetrafluoroethylene of Various Grades Modified with Carbon Fibers. *Bulletin North-East Federal University,* 2017, Vol. 60, No. 4, pp.34–46.

12 Lyakhov N.Z. Metal-polymer nanocomposites. *Siberian Branch of the Russian Academy of Sciences, Novosibirsk*, 2005, 400 p.

13 Kupchishin A.I., Tlebaev K.B. X-ray structural studies of polytetrafluoroethylene. *Eurasian Physical Technical Journa*l, 2018, Vol.15, No.1, pp. 29–33.

14 Voronova N.A., Kupchishin A.I., Niyazov M.N., Lisitsyn V.M., Tlebaev K.B., Gerasimenko N.N. Deformation of polytetrafluoroethylene at various static strain and electron irradiation. *Nuclear Instruments and Methods in Physics Research Section B: Beam Interactions with Materials and Atoms*, 2020, Vol. 465, pp.59 – 61.

Article accepted for publication 17.09.2021

.

DOI 10.31489/2021No3/30-36

UDC 621.793.71:538.911

OBTAINING OF HYDROXYAPATITE COATINGS ON A TITANIUM SUBSTRATE BY DETONATION-GAS SPRAYING

Rakhadilov B.K.[1,2], Sagdoldina Zh.B.[1], Baizhan D.R.[1],Zhurerova L.G.[1], Yeskermessov D.K.[2], Kalitova A. A.[3], Smaiylova M.[1]

[1]Sarsen Amanzholov East Kazakhstan University, Ust-Kamenogorsk, Kazakhstan, daryn.baizhan@mail.ru
[2]PlasmaScience LLP, Ust-Kamenogorsk, Kazakhstan
[3]Institute for Composite Materials, Ust-Kamenogorsk, Kazakhstan

The article considers research results of the formation process of a hydroxyapatite coating on a titanium substrate during detonation spraying. Powders for sputtering and obtained coatings of hydroxyapatite were studied by Raman spectroscopy and X-ray structural analysis. It was determined that the appearance of α-tricalcium phosphatephase is characteristic of a pure hydroxyapatite coating obtained by detonation spraying. Still, the hydroxyapatite phase is retained in the coating composition. Results obtained by Raman spectroscopy indicate that hydroxyapatite is the main phase in coatings. The morphology of the sprayed coatings was characterized using scanning electron microscopy, and the coatings elemental composition analysis was obtained using an energy-dispersive spectrometer detector. Energy-dispersive spectrometer analysis showed that the elemental composition of the obtained coatings is similar to the elemental composition of the initial powder, which is very important for preserving the coatings services life.

Keywords: hydroxyapatite, detonation spraying, structure, phase composition, microhardness.

Introduction

The requirements for the functional, strength and aesthetic parameters of orthopaedic structures have increased significantly with the development of new concepts in the technology, production and application of implants for the bioengineering of bone tissue [1]. First of all, this refers to creating biocoatings, which are most close to the structure of human bone tissue [2]. Natural bone is a composite consisting of a mineral fraction containing tiny crystals of apatite and non-stoichiometric calcium phosphate and an organic fraction, which together give the material mechanical strength.In recent years, to stimulate the structure of natural bone, the synthesis of hydroxyapatite (HA), $Ca_{10}(PO_4)_6(OH)_2$has attracted considerable attention [3-5]. Hydroxyapatite (HA) – $Ca_{10}(PO_4)_6(OH)_2$, which is the main mineral component of bone tissue, is traditionally used as a material for obtaining biocoatings on metal implants for dentistry and orthopaedics.

Despite the many different coating methods, it is difficult to obtain crystalline HA coatings with characteristic hydroxyl and phosphate groups. The mechanical tests show that the destruction of the bone-(coating)-implant joints are associated with the amorphous phase, which is the cause of the coatings mechanical and adhesive instability. These disadvantages are inherent in sol-gel technologies [6]. It should be noted that a set of techniques is used to achieve the required mechanical and adhesive strength. For example, it is possible to control the coatings composition and structure by varying the parameters of the magnetron sputtering process, which makes it promising for the coatings deposition on implants. The use of the self-propagating high-temperature synthesis method expands the capabilities of the magnetron sputtering method, providing high density, structure homogeneity and achieving the required mechanical properties. The detonation-gas spraying method has good prospects using the medicine, primarily due to the initial material's identity of the phase composition and the formed coating.

The authors of [7] found that the coatings obtained by detonation-gas spraying on the “Katun-M” installation consist of particles and conglomerates of particles that form a pronounced surface relief. The adhesion strength of detonation coatings based on calcium hydroxyapatite varies from 10 to 30 MPa. The coatings physical-mechanical characteristics are showed that the detonation spraying method can be used to obtain high-quality biocoatings on titanium implants. However, there are few works aimed at obtaining hydroxyapatite coatings by detonation gas spraying. In addition, in connection with the emergence of new detonation spraying devices, it is interesting to study hydroxyapatite coatings obtained by detonation-gas spraying. In this regard, this work aims to study the structural-phase state of hydroxyapatite coatings

obtained by detonation-gas spraying on an automated installation of a new generation CCDS2000 (Computer-Controlled Detonation Spraying) [8].

1. Materials and methods

The detonation complex CCDS2000 was used to obtain coatings, which has a system of electromagnetic gas valves that regulate the supply of fuel and oxygen and control the purging system (Fig. 1) [8-10]. An acetylene-oxygen mixture was used as combustible gas. It is the most demanded fuel for the detonation spraying of powder materials. The deposition was carried out at the ratio of the O_2/C_2H_2 = 1.856 acetylene-oxygen mixture. The barrel filling volume with an acetylene-oxygen mixture was 50%. Nitrogen was used as a carrier gas. The distance between the sample treated surface and the detonation barrel was 70 mm. Straight barrel diameter - 20 mm.

As a substrate, we used technically clean VT1-0 titanium (99.5%), which is widely used in medicine. Before spraying, VT1-0 plates with dimensions of 30×30×3 mm were sanded and polished, after which they were subjected to sandblasting.Sandblasting was carried out on the detonation unit itself using corundum powders with grain sizes of 0.5-1.3 mm in the following mode: the barrel filling volume with an acetylene-oxygen mixture - 30%, the ratio of acetylene-oxygen mixtures O_2/C_2H_2 = 1.856.

a)

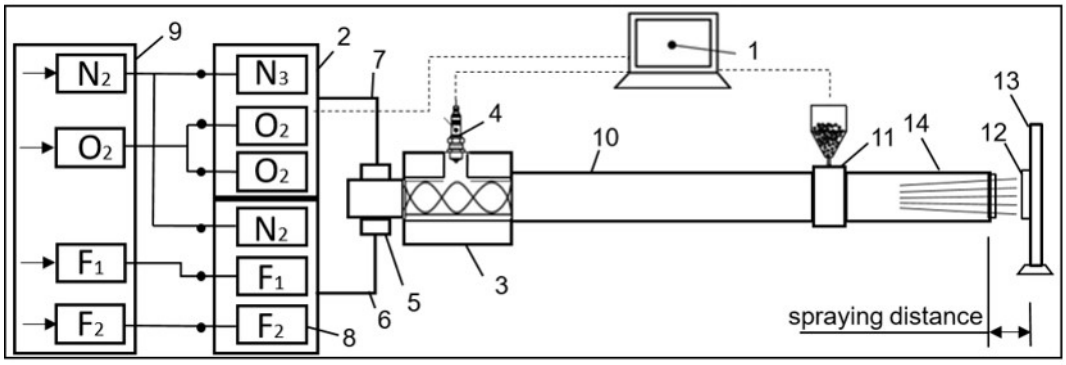

b)

Fig.1. Computerized detonation complex CCDS2000: general view (a) and schematic diagram of the installation (b): 1 - control computer, 2 - gas distributor, 3 - mixing-ignition chamber, 4 - spark plug, 5 - barrel valve, 6 - fuel line, 7 - oxygen line, 8 - gas valves, 9 - gas supply unit, 10 - breech, 11 - powder dispenser, 12 - workpiece; 13 - manipulator, 14 - muzzle of the barrel

.

The research of surface morphology was carried out by scanning electron microscopy (SEM) using backscattered electrons (BSE) on a JSM-6390LV scanning electron microscope. The structure of the obtained samples was studied using Raman spectroscopy on a spectrometer of AFM-Raman Solver Spectrum, NT-MDT. A blue laser with a wavelength of 473 nm and a maximum laser power of 35 mW with an objective lens of 100× and a spot size of $2 \cdot 10^{-6}$ m was used to excite vibrational modes. The obtained spectra were processed by the Savitzky-Golay method [11] by using a 2nd order polynomial. The error in register the spectra was 4 cm^{-1}. The samples phase composition was studied by X-ray structural analysis on X'PertPro diffractometer using CuK_α -radiation. The survey was carried out in the following mode: voltage across the tube U = 40 kV; tube current I = 30 mA; exposure time 1 s; shooting step 0.02º. The coating roughness surface was measured by the Ra parameter using a model 130 profilometer on a section with a length of 7 mm on the sample surface.The samples microhardness was measured by the Vickers method on a "Metolab-502" microhardness meter according to GOST 2999-75.

2. Research results

As noted in several works [12, 13], the phase composition of coatings has a significant effect on the growth of bone tissue during the osseointegration of implants.The implants compatibility is improved due to the approximation of the resulting coating phase-structural state and its properties to the bone tissue parameters.The phase state of the bone-implant biocoatings also determines the nature of their physicochemical and mechanical properties [14]. Therefore, in this work, the phase composition of the obtained calcium-phosphate coatings was studied by X-ray diffraction analysis. The X-ray powder diffraction pattern of the HA sample is shown in Figure 2a. The XRD pattern shows the characteristic peaks of hydroxyapatite, according to the International Center for Diffraction Data database, ICDD-PDF 9-0432.The hydroxyapatite structure was published nearly simultaneously by Náray-Szabó and Mehmel in 1930. it possesses a hexagonal structure with a $P6_3/m$ space group and cell dimensions a=b=9.42Å, and c=6.88Å, where $P6_3/m$ refers to a space group with a six-fold symmetry axis with a threefold helix and a mirror plane [15]. Figure 2b shows diffraction patterns of a calcium-phosphate coating obtained by detonation spraying. In the case of detonation spraying of pure HA, the appearance of phases of α-Tricalcium phosphate (ICDD-PDF 9-0348) is characteristic, but the HA(ICDD-PDF 9-0432) phase is retained in the coating composition. It is known [16]α-TCP crystallizes in the monoclinic crystal system and belongs to the space group $P2_1/a$. α-TCP phase is not very strong, and its mechanical strength is low compared to the cortical bone, limiting its use in areas subject to low mechanical stress. However, α-TCP is completely replaced by biological tissues when interacting with the body's environment, which ensures high bioactivity [17].

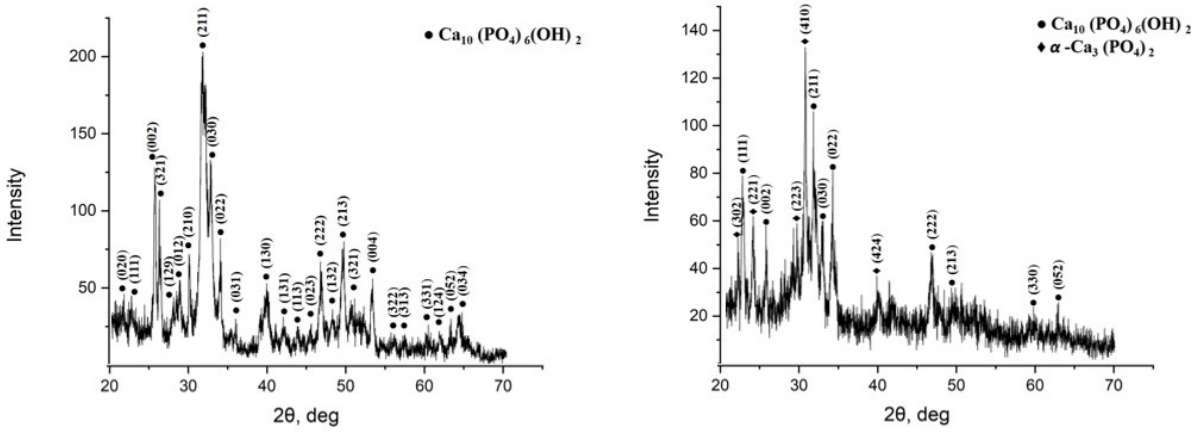

a) b)

Fig.2. Diffraction pattern of hydroxyapatite powder (a) and coating (b) obtained bythe detonation spraying method

Figure 3 presents the Raman spectrum of a hydroxyapatite coating obtained by detonation spraying. In the obtained Raman spectrum of the hydroxyapatite coating, the most intense band is the band with a frequency shift of 961 cm^{-1}, which indicates that HA is the main phase in the coatings. This band belongs to

the P-O symmetric extension mode (ν_1) of the PO_4 group is the most characteristic band of carbonized apatites. The sharpness of this band confirms the good crystallinity of the HA coating, which is also confirmed by other authors [18]. Similarly, the bands associated with the antisymmetric stretching mode (ν_3) of the PO_4 groups show a shift from 1045 cm^{-1} to the shoulder at 1033 cm^{-1}. In addition, it should be emphasized that this change in the carbonate content in the coatings is closely related to changes in the growth morphology and crystallite size, which are known to occur with a temperature change - higher atomic disorder corresponding to smaller crystal sizes (nanometer scale).

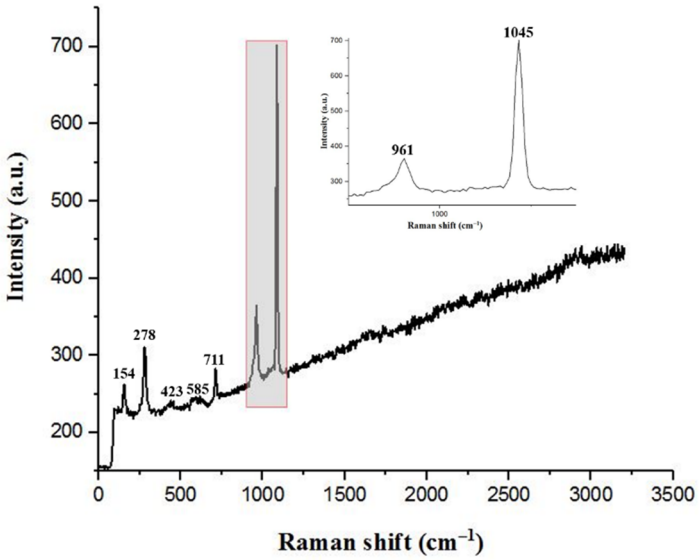

Fig.3. Raman spectrum of a hydroxyapatite coating obtained by the detonation spraying method

Table 1. Results of hydroxyapatite coating with different frequencies of the corresponding lines

Raman frequency shift, cm^{-1}	Fragment, wobble
154	(Ti-O) – (Anataz)
278	(Ti-O) – (Anataz)
423	$(PO_4)^3-(\nu_2)$ (P-O vibrational)
585	$(PO_4)^3-(\nu_4)$ (P-O deformation)
711	$(PO_4)^3-(\nu_4)$ (P-O deformation)
950–965	$(PO_4)^{3-}(\nu_3)$ (P-Oasymmetric valence)
1030–1045	$(PO_4)^{3-}(\nu_3)$ (P-Oasymmetric valence)

The morphology of the hydroxyapatite coating showed the formation of a layered porous structure, which, in turn, facilitates the effective growth of bone tissue into the implant's pores.Pores are observed in the obtained coatings, which are formed when the coating particles melt. As previously observed, detonation coatings have a porous structure and a pronounced relief.According to the analysis results of the coatings elemental composition, other elements besides the basic composition of the substrate and powder weren't identified. It can be argued based on elemental analysis results that detonation spraying did not cause a change in the chemical composition of the coating, which is critical for the biocompatibility and preservation of the coating service life. There is a uniform coating structure consisting of a molten powder sprayed with single particles.

Figure 4 presents the energy-dispersive X-ray spectra of the coating. The elemental composition analysis did not reveal other elements, except for the basic composition of the substrate and powder. According to the obtained results of the coating elemental analysis, it can be argued that detonation spraying does not cause changes in the chemical composition of the coating, and this factor is of decisive importance for biocompatibility and preservation of the coating service life. The Ca/P ratio in the coatings is one of the main parameters that determine bioactivity. The elemental analysis allows comparing the concentrations of the elements that make up the coatings and calculate the Ca/P ratio. The research results of the chemical composition showed that the ratio of calcium and phosphorus in the sprayed coating is Ca/P - 2.2, which is

.

significantly higher than for the initial powder - Ca/P - 1.67. This fact may indicate the presence of impurity phases in the coating.

In figure 4 presents an SEM image and elemental analysis of detonation coating based on HA.Cross-sectional micrographs of detonation coating on the bases of HA showed a high coating density at the substrate interface. The result showed (Fig.5) the formation of a layered-porous structure of coatings with a thickness of 100-120 μm, and there are no pores and cracks at the interface.

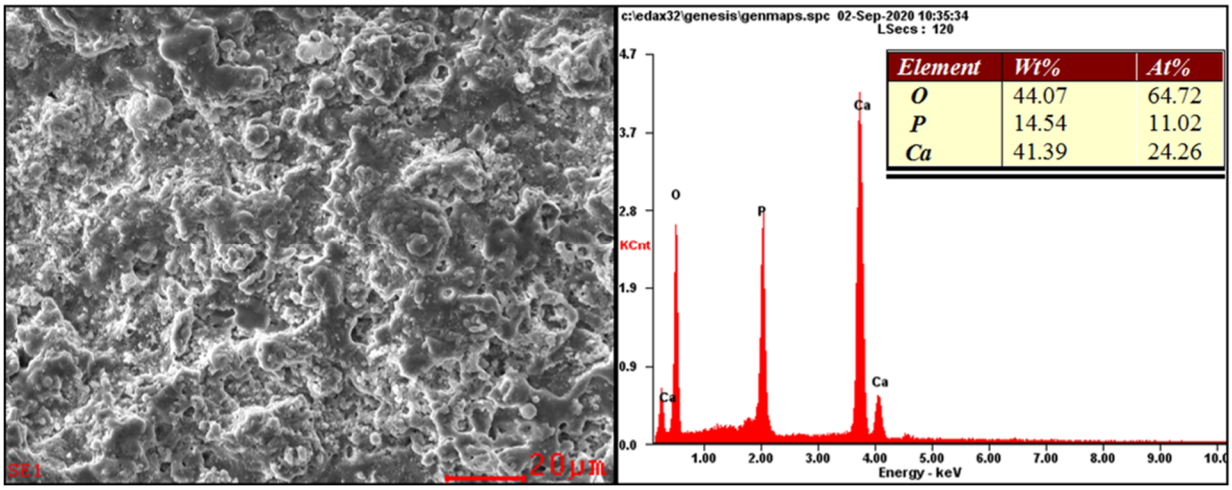

a) b)

Fig.4. SEM (a) imageand (b) elemental analysis of hydroxyapatite coating

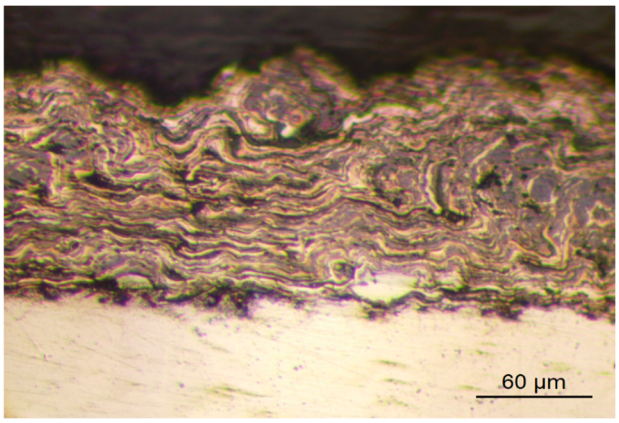

Fig. 5. Micrograph of a cross-section of a hydroxyapatite coating obtained by the detonation spraying method

Figure 6 shows micrographs of the surface and the roughness measuring results of the hydroxyapatite coating obtained by the detonation spraying method. The coating surface has a heterogeneous structure with pores, a typical layered, wavy arrangement of structural components. The coating roughness surface was measured by the Ra parameter using a 130 profilometer model on a section with a length of 7 mm on the sample surface. The coating roughness is 7.82 from the obtained data.The hydroxyapatite coating obtained by the detonation spraying method has a developed surface, which will serve as their improved fusion with bone tissue.

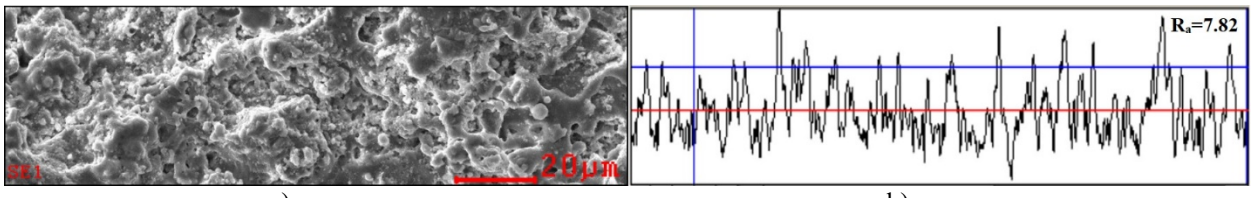

a) b)

Fig.6. Micrograph and roughness of hydroxyapatite coating obtained by the detonation spraying method

The cross-section microhardness of the hydroxyapatite coating obtained by the detonation spraying method was carried out at an angle of 45° along with the coatings. The average microhardness of HA coatings obtained by the detonation spraying method is 380 $HV_{0.1}$. Figure 7 shows a hardness distribution graph over the depth of coating.

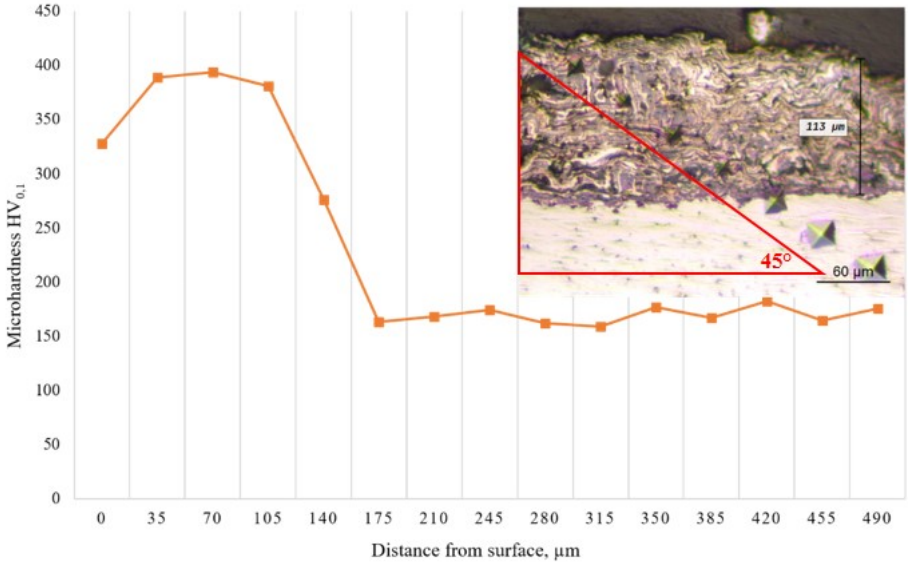

Fig.7. Hardness distributiongraph over the depth of coatings

Conclusion

The structural-phase states and microhardness of the calcium-phosphate coating obtained by detonation spraying were studied. The study of hydroxyapatite coating morphology showed that the coating has a pronounced relief and a layered porous structure. The results of X-ray diffraction analysis showed that the obtained coating consists of HA and α-TCP phases (α-$Ca_3(PO_4)_2$ - tricalcium phosphates). The Raman spectroscopy study method results showed that HA is the main phase in the coating and the coating has high crystallinity. Despite the presence of α-TCP phases, the coating has a high hardness, and the average microhardness of the obtained calcium-phosphate coating was 380 $HV_{0,1}$. Thus, the high hardness, porous structure and the formation of α-TCP phases can provide high service characteristics of the detonation calcium-phosphate coating used in medical implants.

Acknowledgments

This research has been funded by the Science Committee of the Ministry of Education and Science of the Republic of Kazakhstan (Grant No. AP09563455).

REFERENCES

1 AlexanderB., Maurice Y.M. In vivo biofunctionalization of titanium patient-specific implants with nano hydroxyapatite and other nano calcium phosphate coatings: A systematic review. *Journal of Cranio-Maxillofacial Surgery,*2016, Vol. 44, pp. 400–412.

2 Rodionov I.V. Nauchnyye podkhody k sozdaniyu biosovmestimykh implantatsionnykh materialov. *Saratov: Izd-vo Sarat. gos. tekhn. Zhurnal,* 2004, pp. 9-14. [in Russian]

3 Shtansky D.V., Gloushankova N.A., Sheveiko A.N., et al. Design characterization and testing of Ti-based multicomponent coatings for load-bearing medical applications. *Biomaterials,* 2005, Vol. 16, No. 26, pp. 09–24.

4 Rakhadilov B.K., Baizhan D.R., Sagdoldina, Z.B., Buitkenov, D.B., Maulet M. Phase composition and structure of composite Ti/HA coatings synthesized by detonation spraying. *AIP Conference Proceedings* 2297, *020022* 2020. doi:10.1063/5.0029754.

5 Cattini A., Bellucci D., Sola A., Pawłowski L., Cannillo V. Functional bioactive glass topcoats on hydroxyapatite coatings: analysis of microstructure and in-vitro bioactivity. *Surf. Coating. Technol.,* 2014,Vol.240, pp. 110–117. https://doi.org/10.1016/ j.surfcoat.2013.12.023.

6 Liu D., Yang Q., Troczynski T. Sol–gel hydroxyapatite coatings on stainless steel substrates. *Acta Biomaterialia*, 2007, Vol.3, pp. 403–410.

.

7 Sharkeyev Yu. P. Biopokrytiye na osnove gidroksiapatita napylennoye detonatsionno-gazovym metodom na titanovuyu podlozhku. *Tezisy dokladov Mezhdunarodnoy shkoly seminara "Mnogourovnevyye podkhody v fizicheskoy mezomekhanike. Fundamentalnyye osnovy i inzhenernyye primeneniya",* 2008, pp. 265-266. [in Russian].

8 Ulianitsky V.Yu., et al. Computer-Controlled Detonation Spraying: Flexible Control of the Coating. *Chemistry and Microstructure*.2014, Vol.3, pp. 33–42.

9 Dastan, B., Bauyrzhan, R., Dosym, E., Zhuldyz, S. Influence of heat treatment on the phase composition and microhardness of coatings based on Ti3SiC2/TiC. *Key Engineering Materials*, 2020, Vol. 839, pp. 137-143.

10 Rakhadilov B., Maulet M., Abilev M., Sagdoldina Z., Kozhanova R. Structure and tribological properties of Ni-Cr-Al-based gradient coating prepared by detonation spraying. *Coatings*, 2021, Vol. 11, No. 2, pp. 1–14.

11 Savitzky A. Smoothing and differentiation of data by simplified least squares procedure. *Analytical Chemistry*, 1964, Vol. 36, pp.1627–1639.

12 Fidancevska E. Fabrication and characterization of porous bioceramic composites based on hydroxyapatite and titania. *Materials Chemistry and Physics,* 2007, Vol. 103, pp. 95-100.

13 Yanovska A., Kuznetsov V., Stanislavov A., Danilchenko S., Sukhodub L. Synthesis and characterization of hydroxyapatite-based coatings for medical implants obtained on chemically modi fi ed Ti6Al4V substrates. *Surf. Coating. Technol.* 2011, Vol. 205,pp. 5324–5329. https://doi.org/10.1016/j.surfcoat.2011.05.040.

14 Vahabzadeh S., Roy M., Bandyopadhyay A., Bose S. Phase stability and biological property evaluation of plasma sprayed hydroxyapatite coatings for orthopedic and dental applications. *Acta Biomater.,* 2015. https://doi.org/10.1016/j. actbio.2015.01.022.

15 Yacoubi A. E., Massit A., Moutaoikel S. E, Rezzouk A., Idrissi B. C. E., Rietveld Refinement of the Crystal Structure of Hydroxyapatite Using X-ray Powder Diffraction. *American Journal of Materials Science and Engineering*, 2017, Vol. 5, No. 1, pp 1-5. doi:10.12691/ajmse-5-1-1.

16 Carrodeguas R.G., Aza S. D α-Tricalcium phosphate: Synthesis, properties and biomedical applications. *Acta Biomater*, Vol. 7, No. 10, pp. 3536–3546.

17 Singh A., Singh G., Chawla V. Materials Today: proceedings In-vitro performance of reinforced hydroxyapatite coatings deposited using vacuum plasma spray technique on Ti-6Al-4V. *Mater. Today Proc.,* 2020, https://doi.org/10.1016/j. matpr.2019.12.363, 0–5.

18 Timchenko E.V., Timchenko P.E., Taskina L.A., Volova L.T., Miljakova M.N., Maksimenko N.A. Using Raman spectroscopy to estimate the demineralization of bone transplants during preparation. *J. Opt. Technol*, 2015,Vol. 82, No. 3, pp. 153–157.

Article accepted for publication 17.09.2021

DOI 10.31489/2021No3/37-42

UDC 535.37

LUMINESCENCE OF CERIUM DOPED YTTRIUM ALUMINUM GARNET CERAMICS SYNTHESIZED IN THE FIELD OF RADIATION FLUX

Alpyssova G.K.[1,2], Lisitsyn V.M.[3], Karipbayev Zh.T.[2], Golkovski M.G.[4]

[1,2]Academician E.A.Buketov Karaganda University, Karaganda, Kazakhstan, gulnur-0909@mail.ru
[2] L.N. Gumilyov Eurasian National University, Nur-Sultan, Kazakhstan
[3] National Research Tomsk Polytechnic University, Tomsk, Russia
[4] Budker Institute of Nuclear Physics of the Siberian Branch of the RAS, Novosibirsk, Russia

The paper presents the results of ceramic samples' dependence of luminescent properties on their position in the crucible during irradiation. For the synthesis, a blend of powders of aluminum oxide, yttrium oxide and cerium oxide was prepared. The ratio of oxides in the charge corresponded to stoichiometric. The particles of the oxide powders had a size of about 1 micron and less. Synthesis was carried out on gas pedal electron accelerator at Institute of Nuclear Physics SB RAS (Novosibirsk). Luminescent properties were measured on spectrofluorimeter SM 2203 "SOLAR" under excitation by monochromatic radiation at 450 nm. Two types of samples differing in the value of bulk density and the prehistory of yttrium oxide were investigated.

Keywords: white LEDs, yttrium-aluminum garnet, phosphor, ceramics, synthesis in the radiation field.

Introduction

Synthesis on the basis of yttrium-aluminum garnet (YAG) materials of different morphologies (single crystals, powders, ceramics, films) is carried out using different technologies [1-8]. Exposure to powerful radiation streams can solve an important problem: increasing the reactivity of reagents to produce new materials and the efficiency of the synthesis of refractory materials [9-12]. High temperatures are used, preliminary preparation of mixtures of different compositions, addition of additional materials to facilitate the synthesis processes, etc. Obviously, this affects the reproducibility of the synthesis results. In addition, the complexity of the synthesis makes it difficult to optimize the technology in order to achieve the maximum values of luminescence characteristics.

In this work, the radiation synthesis of ceramics was carried out by scanning a powerful beam of electrons over the surface of the charge in the crucible. The scanning was carried out in such a way that the absorbed energy at each point of the surface was the same. The number, shape, and position of the samples in the crucible after synthesis in each experiment with the same initial charge doesn't depend on the direction of the beam movement. However, there is a tendency for differences in the shape and size of the samples obtained at the beginning and end of synthesis. The beam scans in the transverse direction of the crucible and shifts with each step from the initial position in the crucible to the final position. At a scanning speed of 1 cm/s, the movement of the beam in the transverse direction of the crucible takes 4 s. In total the whole irradiation cycle from the beginning to the end of the crucible takes 36s [13]. At the beginning of the experiment the crucible has an ambient room temperature, which in the room is 20 - 25°C. During the irradiation process, at a scanning speed of 1 cm/s, energy equal to (at a power density of20 kW/cm^2) 20 kJ/cm2 is transferred to the charge. Immediately upon interaction, 99% of the energy is spent on transferring electrons from valence to conduction zones [14-16].

It takes energy equal to 2-3 Eg to create one electron-hole pair in YAG. Bandgap width in YAG is 6.5 eV, in metal oxides used for synthesis - YAG (Y_2O_3, Al_2O_3) - about 8 eV. Relaxation of electrons and holes from states in zones, in which they appeared under influence of electron flux, to corresponding bottom of conduction zone for electrons and ceiling of valence zone for holes takes time less than 10-15s. During relaxation of each pair energy equal to 1-2 Eg is released. Therefore, about 0.5-0.7 energy of absorbed radiation is spent on heating of charge and forming ceramics. With an exposure dose of 20kJ/cm^2 and a run depth in the charge equal to 0.6 cm, 15 to 20 kJ/cm^3 is spent on heating. This is a lot of energy, which leads to heating of the charge and, consequently, the crucible. As the electron beam moves during scanning, the temperature of crucible and charge in the place of irradiation increases, the conditions of ceramic formation change. In works [17-22] the possibility of radiation synthesis of luminescent ceramics based on YAG was

.

shown. For the synthesis, a charge of Al, Y oxides of stoichiometric composition with different contents of Ce, Gd was prepared. Under the action of a powerful flux of electrons from the charge, ceramics with properties characteristic of YAG luminophores was formed.

1. Experimental technique

The object of the study is ceramics obtained by radiation synthesis. Ceramics were synthesized using the gas pedal ELV-6 at the INP of the Siberian Branch of the Russian Academy of Sciences (Novosibirsk). The electron gas pedal allows to generate electron fluxes with energies of 1.4 MeV and power up to 100 kW (beam current 100 mA) in steady-state mode. Beam power could be varied by varying the emitter current. Luminescence properties of ceramic samples were investigated depending on their position in the crucible during irradiation.

2. Results and discussions

The experiments were performed as follows. After synthesis, the crucible with the samples was cooled. The state of the synthesis result was photographed: the location of the samples in the crucible (Figure 1). Each sample was assigned a number. The numbering was carried out according to the location of the samples in the crucible from left to right, from top to bottom along the movement of the beam. Photographs of the ceramic samples synthesized using a power density of 20 kW/cm2 and their appearance after crushing in packages are shown in Figure 1. The samples of 56 and 59 series were chosen for the research. The initial charge compositions for the synthesis of these samples were the same, but differed in the background of the yttrium oxide used. The synthesis was performed under the same irradiation conditions. The luminescence spectra of the powders were measured with a spectrofluorimeter SM 2203 made by SOLAR under excitation by monochromatic radiation at 450 nm.

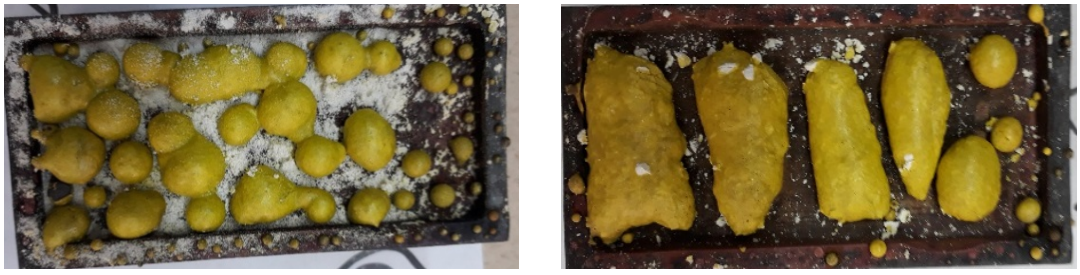

a) b)

Fig.1. Photos of 56 (a) and 59 (b) series samples in the crucible.

For luminescence measurements, samples were mechanically crushed and poured into plastic bags transparent in the spectral region of 350 to 800 nm. To obtain reliable information about the characteristics of the spectra, the measurements were performed as follows. The luminescence spectra of each sample were measured 10 times. Before each measurement, the bag with the powder was shaken in order to mix the particles in the bag. Figure 2 shows, for example, the non-normalized luminescence spectra of samples 56-1and 56-13 in order to clearly show their similarity. In all measurements, the luminescence intensities were different.

This is due to the fact that we do not know the distribution of the powder in the excitation field and the emission in the excitation field. But this could only affect the intensity, but not the spectral characteristics of the luminescence, which is the subject of the research. The average values of the positions and half-widths of the bands and the values of measurement errors are presented in Table 1. When processing the measurement results, the outliers due to unknown causes were highlighted. Accordingly, the outliers were not taken into account when calculating the error.

A total of 13 samples were formed in crucible 56. Each sample was measured 10 times. Figure 3 (a,b) also shows diagrams of the dependence of the fringe position (a) and the half-width of the fringes (b) on the arrangement in the crucible. The red horizontal lines show the limiting measured values of the fringe position and the half-width of the fringes. The crucible average of the maximum band position is 555.8. The variation of the fringe position across the crucible is within 2-4 nm. The variation of band half-widths is 0.01-0.02 eV.

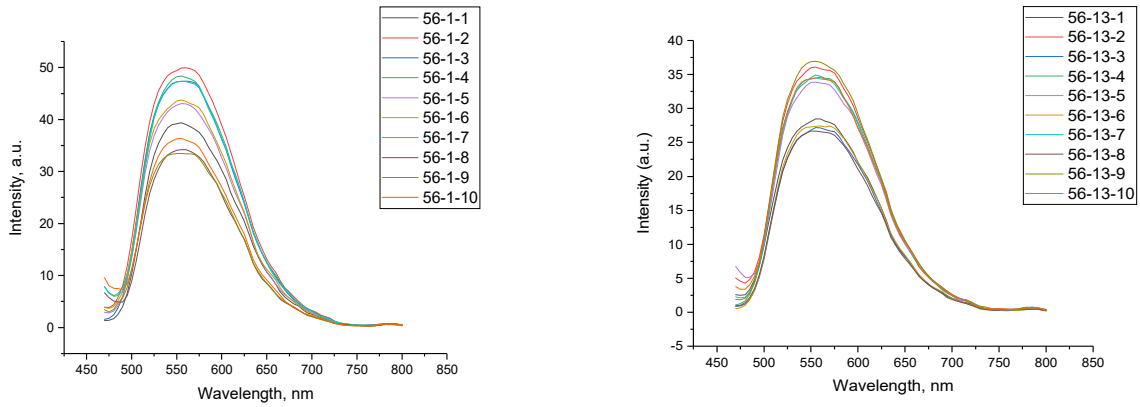

a) b)

Fig. 2. Luminescence spectra of samples from series: a) 56-1; b) 56-13

Table 1. Mean values of fringe positions and half-widths and values of measurement errors

Sample name	$\lambda_м$, nm	ΔE, eV
56-1	556.7±0.8	0.455±0.01
56-2	556.6±0.9	0.455±0.008
56-3	557.1±0.8	0.459±0.006
56-4	554±0.6	0.44±0.01
56-5	554.3±0.9	0.459±0.007
56-6	558.1±0.6	0.451±0.01
56-7	553±0.9	0.445±0.008
56-8	556.1±0.5	0.456±0.01
56-9	557.7±0.5	0.463±0..,01
56-10	555.2±1.,2	0.46±0.008
56-11	557.6±0.5	0.469±0.002
56-12	555.5±1.1	0.458±0.006
56-13	555±0.8	0.469±0.004
56	**555.8**±2.0	0.457±0.01

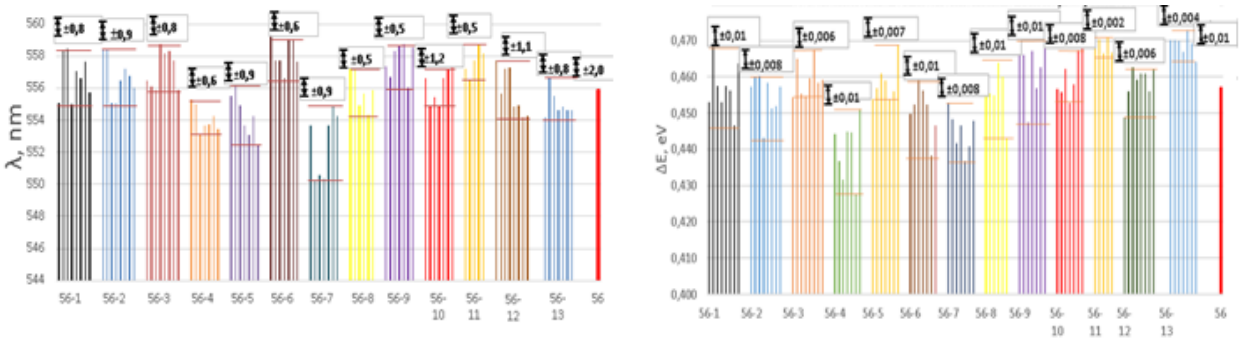

a) b)

Fig. 3. Dependence of band position (a) and band half-width (b) on the position in the crucible No.56

The same measurements were carried out for samples of series No.59. Photographs of the ceramic samples synthesized using a power density of 20 kW/cm2 and their appearance after crushing in packages are shown in Figure 4. From the comparison of the photographs in Figures 1 a and b, it can be seen that the appearance of the synthesized samples 56 and 59 is quite different. The synthesis was carried out under the

.

same irradiation conditions. The only difference was the difference in the yttrium oxide used for the synthesis while the stoichiometric composition of the initial charge was unchanged.

This difference also manifested itself in the bulk density value. The bulk density of the charge for sample 56 was 1.15 g/cm^3, while for sample 59 it was 1.05 g/cm^3. It should be emphasized that we cannot claim that the difference in bulk density in the mentioned intervals is determined by the bulk density value. As the experience of radiation synthesis of YAG:Ce ceramics has shown, there has never been a complete repetition of the samples during synthesis. The reason for this effect remains unknown.

The procedure for measuring the luminescence spectra of samples of series No. 59. When excited by radiation at 450 nm was completely similar to that described above. The results of the measurements are similar: the intensities are slightly different, the nature of the spectra is not. The results of the analysis are presented in Fig. 4, 5 and Table 2.A total of 7 samples were formed in crucible No.59. The measurements were carried out 10 times. Table 2 shows the average values of fringe position and half-width of the fringes with the indication of their error.

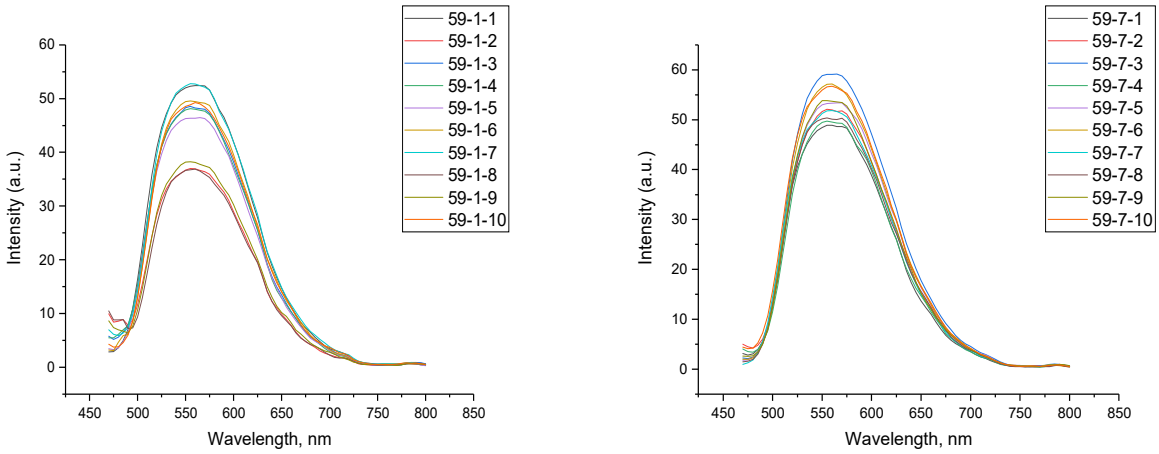

a) b)

Fig.4. Luminescence spectra of sample series: a) 59-1; b) 59-7.

Table 2. Mean values of the positions and half-widths of the bands and the values of measurement errors

Sample name	λ м, nm	ΔE, eV
59-1	558.2±1.0	0.456±0.01
59-2	560±1.6	0.465±0.005
59-3	558.9±1.5	0.459±0.006
59-4	561.9±0.9	0.469±0.008
59-5	560.3±1.7	0.456±0.009
59-6	560.3±1.3	0.459±0.007
59-7	558.2±2.2	0.453±0.01
59	**559.6±1.8**	**0.459±0.008**

Figure 5 (a,b) also shows diagrams of the dependence of the fringe position (a) and fringe half-width (b) on the arrangement in the crucible. The crucible average of the band maximum is 559.6. The scatter of the band positions in the crucible is within 2-3 nm. The band half-width spread is 0.01-0.02 eV. Sample 59-7 has the largest scatter in the position of the bands than the other samples.

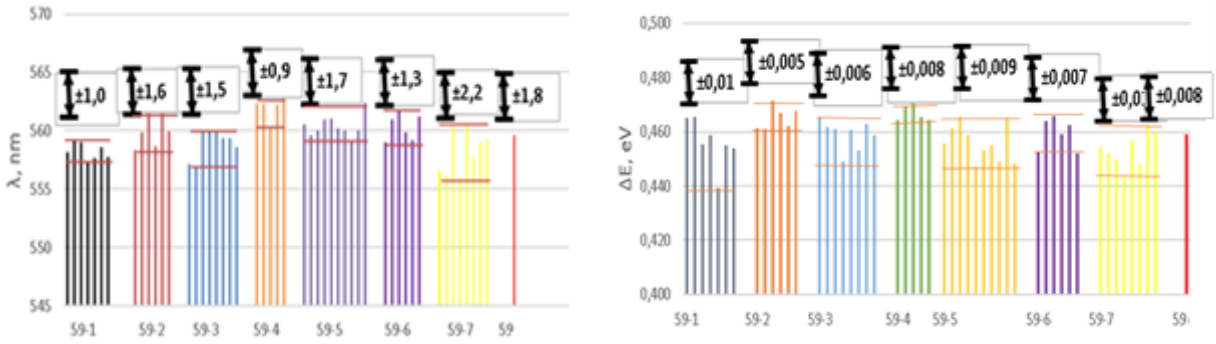

a) b)

Fig. 5. Dependence of band position (a) and band half-width (b) on the position in the crucible No. 59

Conclusion

Thus, in the field of a powerful flux of high-energy electrons, it is possible to synthesize ceramics based on YAG: Ce from a mixture of yttrium, aluminum, and cerium oxides with a predominant YAG structure. The type of ceramics obtained depends on the history of the reagents used. The spectral characteristics of the luminescence of YAG: Ce-based ceramic samples synthesized in the field of powerful radiation fluxes were measured, depending on the synthesis conditions. Were investigated samples of ceramics obtained at different times, with different compositions, different prehistories of the initial powders of oxides and the bulk density of the charge. In general, it can be seen that the scatter of the measured values of the characteristics of the bands in different samples of series 56 and 59 is approximately the same. The relative spread of the values of the positions of the bands and their half-widths in each individual sample can be greater than the average for all samples of the series. Thus, the change in the temperature regime during the formation of ceramics during scanning does not affect the scatter of the values of the characteristics of the bands in the samples.

The most probable reason for the scatter in the values of the spectral characteristics of luminescence may be that, at a high synthesis rate, a strained spatial structure is formed in crystallites due to the introduction of high concentrations of lattice defects. Distortion of the structure surrounded by luminescence centers, cerium ions, leads to deformation of the energy structure of the centers and, accordingly, their radiative properties.

Acknowledgments

The work was carried out within the framework of the grant AP08052050 of the Ministry of Education and Science of the Republic of Kazakhstan. This research was supported by Tomsk Polytechnic University CE Program.

REFERENCES

1 Michalik D., Sopicka-Lizer M., Plewa J., Pawlik T. Application of mechanochemical processing to synthesis of YAG:Ce garnet powder. *Archives of metallurgy and materials*. 2011, Vol. 56, pp.1258 – 1263.

2 Zehua Liu, Shuxing Li, et al. The effect of porosity on the Al_2O_3-YAG:Ce phosphor ceramic: Microstructure, luminescent efficiency, and luminous stability in laser driven lighting. *Journal of Alloys and Compounds.*2019, Vol. 785, pp.125-130.

3 Jian Xu, Baofu Hu, Chao Xu, et al. Carbon-free synthesis and luminescence saturation in a thick YAG:Ce film for laser-driven white lighting. *Journal of the European Ceramic Society.* 2019, Vol. 39, pp. 631–634.

4 Vaqueiro P., Lopez-Quintella M.A. Synthesis of yttrium-aluminium garnet by the citrate gel process. *J.Mater. Chem.*1998,Vol.8, No. 1, pp.161-163.

5 Davydova O.V., et al. Features of the synthesis of ultrafine powders of yttrium-aluminum garnet activated by cerium ions using the combustion method. *Vestnik GSTU after P.O. Sukhoi.* 2016, No. 2, pp.45-52.[in Russian].

6 Yadav P., Vijay K. Kumar Gupta, et al. One step combustion synthesis of YAG:Ce phosphor for solid state lighting. *AIP Conference Proceedings*. 2011, Vol.1391, pp. 200-202.

7 Ya-Wei Lee, Su-Hsen Wu. Fabrication and performance assessment of coprecipitation- based YAG:Cenanopowders for white LEDs.*MicroelectronicEngineering.*2018, Vol. 199, pp. 24-30.

8 Nien Y.T., Lu T.H., Bandi V.R., Chen I.G. Microstructure and photoluminescence characterizations of $Y_3Al_5O_{12}$:Ce phosphor ceramics sintered with silica. *J. Am. Ceram. Soc.*2012, Vol.95, pp.1378–1382.

9 Gyngazov S.A., Vasiliev I.P., Surzhikov A.P., et al. Ion treatment of zirconium ceramics with powerful pulsed beams. *Journal of technical physics*. 2015, Vol. 85, pp. 132 – 137.[in Russian].

10 Alekseev A.A., Mironovich A.Yu., Salogub D.V. Features of the Magnetic Structure of $Y_3Fe_5O_{12}$ Polycrystals Synthesized by Radiation Thermal Sintering. *Physics of the Solid State.* 2020, Vol. 62, pp. 1156–1164.

.

11 Kostishin V.G., Shakirzyanov R.I., Nalogin A.G., et al. Electrophysical and dielectric properties of polycrystals of yttrium iron garnet ferrite obtained by radiation-thermal sintering technology. *Solid State Physics*. 2021, Vol. 63, pp. 356 – 362. [in Russian].

12 Alekseev A.A., Mironovich A.Yu., Salogub D. V. Features of the Magnetic Structure of $Y_3Fe_5O_{12}$ Polycrystals Synthesized by Radiation Thermal Sintering. *Physics of the Solid State*. 2020, Vol. 62, pp. 1156–1164.

13 Karipbaeyev Z., Polisadova E., Alpyssova G., et al. Dependence of the Efficiency Electron Beam Assisted Synthesis of YAG:Ce Ceramics on the Power Density of the Electron Flow. *Proceedings of the 7th International Congress on Energy Fluxes and Radiation Effects, EFRE 2020.* 2020, pp. 892–895.

14 Lushchik Ch., Vitol IK, Elango MA Decay of electronic excitations into radiation defects in ionic crystals. *Uspekhi fizicheskikh nauk.* 1977, Vol. 122, no. 2, pp. 223–251.[in Russian].

15 Klinger I., Pushchin Ch.V., Mashovsts T.V., et al. Creation of defects in solids during decay of electronic excitations. *Uspekhi fizicheskikh nauk.* 1985, Vol.147, pp.523-558.[in Russian].

16 Elango, M.A. *Elementary inelastic radiation processes*.Nauka. 1988, 148 p.

17 Karipbayev Zh.T., Lisitsyn V.M., Mussakhanov D.A., Alpyssova G.K., et al. Time-resolved luminescence of YAG:Ce and YAGG:Ce ceramics prepared by electron beam assisted synthesis. *Nuclear Instruments and Methods in Physics Research Section B: Beam Interactions with Materials and Atoms.* 2020, Vol.479, pp. 222-228.

18 Lisitsyn V.M., Lisitsyna L.A., Golkovsky M.G., et al. Formation of luminescent high-temperature ceramics in a powerful flow of high-energy electrons. *Izvestiya VUZov.* 2020,No. 9, pp.102-107 [in Russian].

19 Alpyssova G., Mussakhanov D., Karipbayev Zh., et al. Luminescence spectra of YAG:Ce phosphors synthesized in a field of radiation. *IOP Conf. Series: Materials Science and Engineering*. 2020, No.754, pp. 012014.

20 Mussakhanov D.A., Tulegenova A.T., Lisitsyn V.M., et al. Structural and luminescent characteristics of YAG phosphors synthesized in the radiation field. *IOP Conference Series: Materials Science and Engineering*. 2019, Vol. 510, Issue 1, pp. 012031.

21 Karipbaev Zh., Musakhanov D., Lisitsyn V., Alpyssova G., et al. Synthesis, the study of the structure of YAG and YAGG phosphors in the radiation field. *Bulletin of Karaganda University. Physics series*. 2019, No. 4(96), pp. 24 – 29.

22 Karipbayev Zh., Alpyssova G., Mussakhanov D., Lisitsyn V., Kukenova A., Tulegenova A. Time-resolved luminescence excited with N_2 laser of YAG:Ce Ceramics formed by electron beam assisted synthesis. *Eurasian Physical Technical Journal.* 2020, Vol.17, No.1(33), pp.73 – 76.

Article accepted for publication 17.09.2021

DOI 10.31489/2021No3/43-47

UDC 536.24: 532.526

LOCAL APPROACH FOR EVALUATING HEAT TRANSFER OF PRISMATIC ELEMENTS ON A FLAT SURFACE

Suprun T.T.

Institute of Engineering Thermophysics, National Academy of Sciences of Ukraine, Kyiv, suprun@secbiomass.com

Heat-exchange prismatic elements located on a flat surface are typical for many technical applications. The purpose of the work is to develop local approach for evaluating heat transfer of working surfaces based on local control of thermophysical parameters in characteristic zones of the working environment, using the methods of heat and mass analogy and hot-wire anemometry. The local approach allows more accurately diagnosing the types of flow in the boundary layer of a streamlined element and thereby, the temperature state of individual prismatic elements and the entire arrangement as a whole is determined more accurately. For calculating the local heat transfer of each face of the prism separately and the average surface heat transfer depending on the geometric and operating parameters equations of similarity are proposed.

Keywords: prismatic heat exchange surface, local thermophysical parameters

Introduction

To improve the efficiency and reliability of the equipment it is necessary to constantly develop the methods of control and management of work processes. This is achieved on the basis of penetration into the complex mechanism of boundary layers development and targeted impact on their internal structure, which is typical for the general approach of the Institute of Engineering Thermophysics of the National Academy of Sciences of Ukraine to the management of transfer processes in the flow path of thermal power equipment for various purposes [1]. One of the most promising methods for studying transport processes occurring under complicated conditions is physical modeling [2, 3].

The object of this research is heat-exchange prismatic surfaces, which are typical for many technical applications. Increasing the intensity of transfer processes in heat exchange, chemical and technological equipment is often achieved using specially designed prismatic intensifiers located on flat surfaces. In some devices the presence of prisms on flat surfaces is due to the peculiarities of the technological process. In particular, prisms are typical elements of electronic equipment boards. Application of the method of local control of thermophysical parameters under conditions of action of turbulizing effects of various nature allows to optimize typical arrangement, to develop methods for calculating heat exchange of elements and units of electronic equipment, in turn, leads to a decrease in costs for product development, selection of the required power for a cooling system, improvement of equipment design, its reliability and resource. The experimental results presented below contribute to the solution of this urgent problem.

Until recently the most common approach for calculating the heat transfer of electronic equipment elements was another approach, which we called the channel one [4]. This approach is fundamentally different from the proposed local approach. With the channel approach the average heat transfer of prismatic elements is calculated using the similarity equation for a stabilized flow in channels using correction factors for inlet conditions, channel geometry and element arrangement. In this case the Reynolds number for all elements is determined by the average flow rate, thus it is assumed to be the same for any of the elements in a given channel, and diagnostics of the type of flow in the boundary layer that occurs on the element surface is made only on the basis of this Reynolds number, without dividing it into laminar, turbulent, pseudolaminar, quasi-turbulent, transient and separated flow regimes [5].

The limitations of this approach are obvious, since the information about the velocity and temperature fields is ignored, the type of flow is roughly diagnosed, and the influence of the configuration and size of elements and their location on the hydrodynamic structure of the flow is insufficiently taken into account.

.

1. Experimental technique

To study the influence of turbulizing effects of various nature on the flow around prismatic elements located on a flat surface a special aerodynamic stand ADS-1 was created. The investigated flat surface with prismatic elements was installed in the working section of the ADS-1.The thermal efficiency of individual prismatic elements was tested for the arrangement shown in Fig. 1, which included four rows of prismatic elements. Turbulence in the first row was created by the input conditions and in the second, third and fourth rows - by the traces of the previous rows; flow separation occurred when flowing around the input edges of the elements. In Fig. 1 each prism is designated by a number, the first digit of which corresponds to the number of the row along the direction of the air flow, and the second to its ordinal number in the row. In this work we compared the average heat transfer between prism No. 23 located in position 1 (flow conditions 1) and prism No. 43 in position 2 (flow conditions 2). These conditions from the point of view of flow hydrodynamics were fundamentally different from each other, which will be described in detail below.

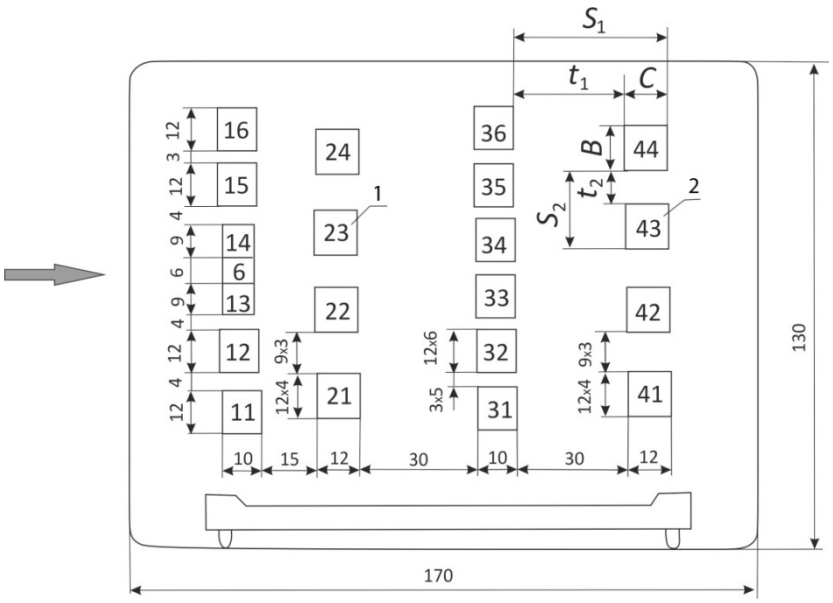

Fig.1. Flat surface with prismatic elements

For local control of thermophysical parameters in the channel of the ADS-1 working section, a hot-wire digital flow meter of the RPS-1 type developed by IET NAS of Ukraine was used, as well as hot-wire anemometer equipment DISA-55M. The aerodynamic features of the flow around the prismatic elements were determined based on the visualization of the flow using a soot-oil suspension applied to the prisms and aluminum powder, which was introduced into the air flow and whose particles adhered to the surface of the prism. Visualization was carried out both over individual prisms (for example, No. 23 for flow condition 1 and No. 43 for flow condition 2), and over the entire flat surface with installed prisms.

To study the heat transfer of prismatic elements, the method of heat and mass analogy was used, in particular, the method of sublimation of a substance in air. In this work, naphthalene was used as such a substance. The production of prismatic elements models was carried out using isobaric pressing technology. To determine the average mass loss from the surface of the model under study, an analytical balance of the VLR-200 type was used. The sample was weighed before and after the experiment. Local mass loss was determined by taking profilograms of the investigated surfaces of the models before and after the experiment on a special device.

2. Results and discussion

To determine the hydrodynamic structure of the flow in this study an assessment of the deviations of the local velocities over various prismatic elements U_{ii} relative to their average flow rates in the working channel of the stand $\overline{U}$ was made (Table 1). As you can see from the table 1, the relative local velocities vary

over a fairly wide range: from 0.47 to 1.20. Therefore, the use of the average flow rate when carrying out the corresponding calculations in the general case can lead to significant differences between the calculated and actual values of the heat transfer coefficients of the prisms.

Table 1. Relative local flow velocities over different prismatic elements

prism No.	11	14	16	23	24	31	34	36	41	43	44
$U_{ii}/\overline{U}$	0.86	1.20	1.07	0.75	0.88	0.47	0.63	0.47	0.63	0.62	0.55

As evidenced by the results of visualization, the separation zones located on the prisms and due to the features of their flow have different lengths: the maximum - in the final (fourth) row and the minimum - in the first. An increase in the length of the separation zones on the upper faces of the prisms along the length of the channel (flow conditions 1 and 2) indicates a general tendency for a decrease in the part of the kinetic energy of turbulence, which is perceived by the boundary layers developing on these faces, that is, it directly affects the process of their flow around. All these characteristic aerodynamic features of the flow around elements (flow conditions 1 and 2) have a significant effect both on the average heat transfer of these elements and on the local heat transfer coefficients. The determination of the average heat transfer was carried out for 11 prisms located in each of the four rows of this arrangement. The analysis of the results showed that the intensity of the average heat transfer for the prisms located in positions 1 (prism No. 23) and 2 (prism No. 43) is different, which is associated with the aerodynamic features of their flow.

The average heat transfer coefficient for prism No. 23 practically coincides with the values of the average heat transfer coefficients for the prisms located in the first three rows of the arrangement, and with an error of ± 7% are generalized by the dependence:

$$\overline{Nu} = C\,\mathrm{Re}^{0.6}, \tag{1}$$

where $C = 0.536$.

An exponent of 0.6 at the Reynolds number indicates the existence of a pseudolaminar boundary layer (PLBL) on the surfaces of most prisms [6]. A specific feature of the PLBL is the intensification of heat transfer, which can be estimated by the ratio of the average heat transfer coefficients in it to their values in the laminar boundary layer, determined from the known dependence:

$$\overline{Nu} = 0.59\,\mathrm{Re}^{0.5} \tag{2}$$

The intensification of heat transfer in the PLBL progresses with an increase in the Reynolds number. For 1-3 rows the intensification of the average heat transfer at Reynolds numbers of 10^3 is ~ 1.7-1.9, and at 10^4 - 2.1-2.4. Particular attention should be paid to the analysis of heat transfer for the prisms of the final (fourth) row (Fig. 2).

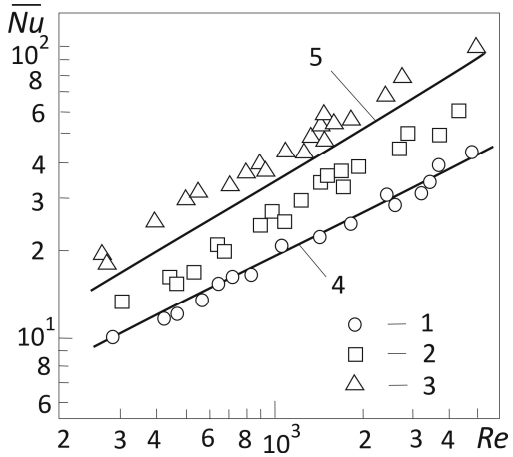

Fig.2. The average heat transfer of the last row of prisms located on a flat surface:
1 - prism No.41; 2 - prismNo.43; 3 - prismNo.44, 4 - eq. (2), 5 – eq. (1)

.

As can be seen from Fig. 2, the elements of the fourth row are characterized by both laminar (prism No. 41) and pseudo-laminar flow regimes (prisms No. 43, 44) of various intensities, which are also generalized by dependence (1), where C = 0.34 for prism No. 43 and C = 0.56 for prism No. 44. The average heat transfer of the last row of prisms is less intense than the heat transfer of the first three rows. So, for prism No. 43 the intensification of the average heat transfer at $\mathrm{Re} \approx 3 \cdot 10^2$ is ~ 1.4, and at $\mathrm{Re} \approx 3 \cdot 10^3$ - ~ 1.65.

A comparative analysis of the heat transfer of an element under flow conditions 1 and 2 shows that during the constructive development of a flat surface with prismatic elements the most heat-stressed of them must be located under conditions of maximum heat removal. In this case such conditions turned out to be flow conditions 1.This is a very important practical conclusion.

According to the local approach in equation (1) to calculate the average heat transfer it is necessary to use the local velocity over the prism. Taking into account the dependence $(U_{ii} / \overline{U_n})^n$ connecting the local velocity over the prism U_{ii} with the average flow rate in the channel $\overline{U_n}$, the similarity equation (1) takes the form:

$$\overline{Nu} = \overline{Nu}_{cp} \left(U_{ii} / \overline{U_n} \right)^n , \tag{3}$$

where $\overline{Nu} = C\,\mathrm{Re}^n$, $\overline{Nu}_{cp} = C\,\mathrm{Re}_{cp}^n$, Re and Re_{cp} - Reynolds numbers, determined by local (U_{ii}) and average ($\overline{U_n}$) flow rates, respectively.

The determination of the local heat transfer coefficients was carried out on the basis of the distributions of local mass carryover on the faces of the prism model. The distributions of local heat transfer coefficients along the central axis of each face (at U = 5 m / s, Re = 4200) for prism No. 23 are shown in Fig. 3.

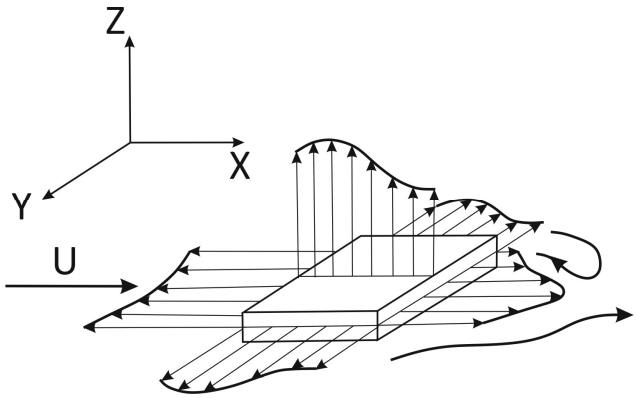

Fig.3. Distribution of local heat transfer coefficients along the central axes of the faces of prism No. 23

At the top and side faces a separated flow first occurs, which leads to the appearance in the distributions $\alpha = f(x)$ maxima located at distances x_r from the leading edge of the element and corresponding to the point of reattachment of the flow. Behind this point, at $x > 1.25\,x_r$, the development of the PLBL begins.

The main results of the experimental study are presented in Table.2. They can be used for calculations of a single prismatic element mounted on a flat surface without a gap when flowing around a highly turbulized air flow. For the data presented in Table 2 in the investigated range of Reynolds numbers the heat balance for the entire element is observed with a maximum error of + 4.3% (at Re = 500).When carrying out these calculations, the average heat transfer coefficient of the entire element was calculated on the basis of the average heat transfer coefficients of each face determined from the table, taking into account its surface.

This approach allows us to single out the role of each face in the total heat transfer. So, for example, for a given element the contribution of the upper face is prevailing and amounts to ~ 50% in the total heat removal (provided that the temperature difference is constant).At the same time, the highest are the heat transfer coefficients on the frontal face, which exceed by 1.6-2 times their value on the upper face, thereby compensating for the lower intensity of heat transfer on the back and side faces.

Table 2. Recommendations for calculating the average heat transfer of a prismatic element and its faces in 1-3 rows gap-free installed on a flat surface in a stream

General view of the similarity equation		$\overline{Nu} = C\,\mathrm{Re}^{n}$		
Average heat transfer	Defining size	Heat exchange surface	C	n
The element as a whole	C	$\sum F$	0.536	0.6
The upper face	C	$C \times B$	0.536	0.6
The side face	C	$C \times h$	0.487	0.6
The frontal face	h	$B \times h$	0.75-0.89	0.5
The back face	h	$B \times h$	0.116	0.667

This leads to the fact that the total heat transfer coefficient practically coincides with the average heat transfer coefficient on the upper face. In this case, the contribution of the front face to the total heat transfer is only 19-22% (at $\mathrm{Re} = 4000$ and 500, respectively).

Conclusions

Complex experimental studies of heat and momentum transfer processes in difficult conditions of interaction of external (increased turbulence) and internal (separation) turbulizing effects typical for thermal power equipment have been carried out. A bank of new experimental data on the intensity of the processes occurring for a flat surface with prismatic elements has been obtained.

During the research a local approach was used, the advantage of which is the ability to fix the thermophysical parameters of the process in any characteristic zone of the working space. The meaning of the local approach is to determine the average surface heat transfer coefficient from the local velocity measured over each prismatic element. This makes it possible to assess the spatial temperature heterogeneity of the arrangement and, if necessary, by maneuvering the location of the elements, take measures to change the temperature in the desired direction.

Equations of similarity are proposed for calculating the local heat transfer of each face of the prism separately and the average surface heat transfer. Based on the recommendations received, the thermal state of a specific arrangement was assessed and measures were developed to improve it by purposefully rearranging the elements.

REFERENCES

1 Suprun T.T. Methods for managing transient processes on streamlined surfaces of power equipment. *Thermophysics and Thermal Power Engineering*, 2017, Vol.39, No.7, pp. 125. [in Ukrainian]

2 Suprun T. Physical modeling the unsteady flow with wakes. *Eurasian phys. tech. j.* 2017, Vol.14, No. 2(28), pp.113 - 119.

3 Suprun T.T. Simulation of turbulized flows typical for thermal power equipment. *Thermophysics and Thermal Power Engineering*, 2019, Vol. 41, No. 5, pp. 112. [in Ukrainian]

4 Gidalevich V.B., Mironenko Yu.P., Spokoyny Yu.E., Trofimov VE, Isaychenko V.V. Determination of local heat transfer coefficients of microcircuits with forced air cooling. *Radio electronics issues*.1983, Series TRTO, No.3, pp.3-9. [in Russian]

5 Dick E., Kubacki S. Transition Models for Turbo machinery Boundary Layer Flows: A Review. *Int. J. Turbomach. Propuls. Power*, 2017. Vol.2, No.2, pp.1-45. https://doi.org/10.3390/ijtpp2020004

6 Epik E.Ya., Suprun T.T. Impulse and heat transport processes at by pass transition. *Eurasian phys. tech. j.* 2007, Vol.4, No. 1(7), pp. 52 - 57.

Article accepted for publication 17.09.2021

.

DOI 10.31489/2021No3/48-52

UDC 533.6

STUDY OF AERODYNAMIC CHARACTERISTICS OF A CYLINDRICAL BLADE WITH DEFLECTOR

Tanasheva N.K.[1], Sakipova S.E. [1], Minkov L.L.[2], Bakhtybekova A.R.[1*], Shuyushbaeva N.N.[3], Burkov M.A[1]

[1]E.A. Buketov Karaganda University, Karaganda, Kazakhstan, asem.alibekova@inbox.ru
[2]National Research Tomsk State University, Tomsk, Russia
[3]Sh.Ualikhanov Kokshetau University, Kokshetau, Kazakhstan

The article discusses some aspects of the renewable energy sources use, in particular, the problem of small wind power. A brief analysis of the development rates of wind energy in the world and in Kazakhstan is presented. The study is devoted to finding ways to optimize the blade of a wind power plant based on the Magnus effect, designed to generate electrical energy at low wind speeds. A cylindrical blade with a turbo-deflector has been developed to ensure independent starting of the blade rotation without the use of additional trigger mechanism. Laboratory tests of a cylindrical blade with a turbo deflector were carried out on a T-I-M wind tunnel at various flow regimes. The obtained dependences of aerodynamic forces on the air flow velocity at different angles of attack are shown.

Keywords: cylindrical blade with deflector, wind turbines, aerodynamic coefficients, drag force, lift force, angle of attack, Reynolds number

Introduction

Renewable energy sources (RES) are sources of green, inexhaustible and increasingly competitive energy [1-4]. They differ from fossil fuels mainly in their diversity, abundance and potential for use anywhere in the world, but above all in that they do not produce greenhouse gases and atmospheric pollutants that cause climate change. The growth of clean energy sources is unstoppable, as reflected in statistics published annually by the International Energy Agency (IEA). Almost half of all new generating capacity installed in 2014, after coal, was obtained using RES [1]. According to the IEA, by 2040 the global demand for electricity will grow by 70% - its share in final energy consumption will grow from 18 to 24% [1]. As part of the development of a "green" economy and in order to reduce CO^2 emissions, Kazakhstan continues to actively work on the development of RES [3]. Last year, projects with a total capacity of 45 MW were implemented in Kazakhstan. Currently, there are 89 renewable energy facilities in Kazakhstan with an installed capacity of 1022.1 MW, Table 1. Our country possesses significant RES, which include hydropower, wind and solar energy. It should be noted that all projects in the field of renewable energy in Kazakhstan are carried out at the expense of investors' own and borrowed funds and are not financed from the republican budget.

Table 1. Generation volume energy due to renewable energy sources in Kazakhstan in 2020 [4]

Type of the renewable energy facilities	Number	Installed capacity, MW
Wind power plants	26	404.4
Solar power plants	42	891.6
Hydroelectric power plants	37	224.6
Bioelectric power plants	5	7.82
Total	89	1022.1

Wind energy is one of the fastest growing energy industries using RES. The world installed capacity of electric energy obtained by wind turbines (WPP) during period 2010 to 2020 increased from 177.193 MW to 698.909 MW, Fig.1. According to the last IRENA data [2], energy production from wind conversion doubled between 2009 and 2013.

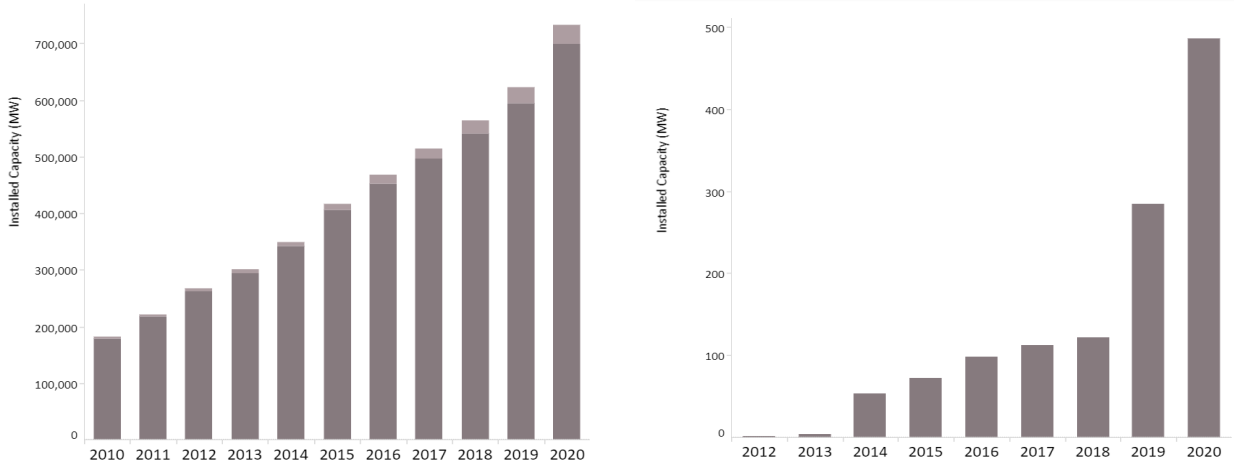

a) b)

Fig.1. Wind Energy data, installed capacity trends: a) by all countries in the World; b) in Kazakhstan [2].

Currently, the wind turbine market is diverse and large [2]. However, many existing installations with relatively low power ratings generate electrical power at free stream air velocities of 8-10 m / s. In areas with low-speed wind resources, most wind turbines do not work efficiently. The solution to this problem can be achieved by creating wind turbines that convert the energy of low-speed wind. It is known that wind turbines based on the Magnus effect are designed for low wind speeds [5-11]. A distinctive feature of these installations is the start-up and power generation at a free air speed of 2 - 3 m / s. The highest efficiency of wind turbines based on the Magnus effect is observed at speeds below 8 m / s [7]. In this interval of wind speeds, the maximum power values were obtained, compared with bladed ones in wind turbines. The advantages of wind turbines based on the Magnus effect include the fact that their speed is 2-3 times less than that of bladed ones. This ensures the operational safety of wind turbines based on the Magnus effect.

Optimization of the performance and characteristics of the wind turbine based on the Magnus effect can be achieved by modifying the shapes and designs of the blades [9]. In this regard, a wind turbine is known, containing a wind wheel with a horizontal axis of rotation and radially mounted Magnus rotors in the form of cylinders, with an electric generator to drive the cylinders. Each rotor is made with a non-rotating root and rotating end parts and with a washer at the end of the blade [10]. In [11], a description of a wind turbine is given, in which a wind wheel with a horizontal shaft has radial blades in the form of cylindrical rotors with drives for their rotation. The disadvantages of these wind turbines are the complexity of the design of the blades, which increase the level of turbulence near the wind wheel, as well as the presence of drive motors with an additional source of energy. To increase the efficiency of wind power plants, it is necessary to optimize the power elements-blades. The aim of this work is to create a cylindrical blade with a deflector and study it's aerodynamics.

1. Experimental part

1.1 The device of the turbo deflector

The deflector is a mechanism that optimizes the air flow in order to increase the thrust [12, 13]. A deflector is literally a guiding device, which is what defines its purpose. The dynamic deflector consists of a fixed base and a rotating turbine part, Fig. 2. The direction of the air flow occurs due to the creation of a low pressure area in the lower part of the installation. When the air flow around the deflector, a "vortex" is formed in the lower lobes and an auxiliary thrust appears. The greater the air flow, the draft from the inside of the apparatus is stronger. In other words, the deflector directs the wind parallel to the flow, thereby increasing thrust due to the pressure decreasing. The deflector reduces the likelihood of reverse thrust. The spherical part rotates in the same direction regardless of the direction of the wind vector. The elements of the

.

spherical cap are made of light, thin metal, which allows the deflector with blades to turn on in operation with a slight wind - from 0.5 m / s.

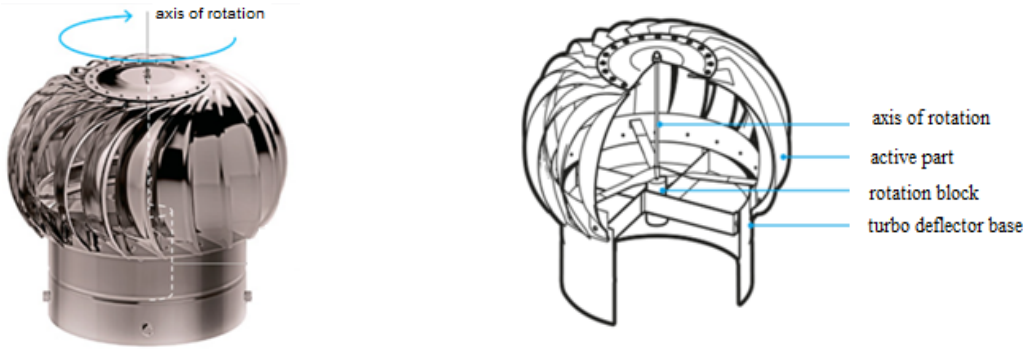

a) b)

Fig.2. Spherical turbo deflector: general view; device scheme [13].

In practice, a turbo deflector is used as an element of a ventilation system to effectively extract exhaust air from of rooms. TsAGI deflectors are widely known, which work without electricity consumption, using wind as the only source of energy [12]. In our study we used an active spherical deflector as an element of a cylindrical blade of a wind turbine based on the Magnus effect.

1.2 Experimental technique

Laboratory measurements of an experimental sample of a cylindrical blade with a turbo deflector were carried out at the Aerodynamics Laboratory of the Karaganda University named after E.A. Buketov. The regularities of aerodynamic characteristics, such as drag and lift forces, were studied in the open test section of the T-I-M wind tunnel, the scheme and parameters of the T-1-M installation were shown in detail in [7, 8]. The values of aerodynamic forces were measured using a three-component aerodynamic balance. To measure the air flow rate, a Skywatch Atmos cup anemometer was used, the error of which does not exceed ± 3%. The experiments were carried out with the air flow velocity varied in the range from 3 to 15 m / s.

The experimental sample of the blade consists of a cylindrical element with a deflector rigidly fixed at the end (Fig.3). The active element of the blade is a turbo deflector, the petals of which open when exposed to an air flow, designed to provide an independent start of the rotation of a cylindrical blade. The angle of attack α was measured by comparison with rigid control (reference) instruments.

a) b)

Fig.3. Experimental model of a cylindrical blade with deflector in the working section of the wind tunnel: a) top view; b) side view. Angle of attack α = 0 °

Geometrical parameters of a cylindrical blade with a deflector:
- the length of the cylindrical element - L = 0.205 m;
- cylinder radius R_1 = 0.025 m;
- deflector radius R_2 = 0.05m;

The drag coefficient C_x and lift coefficient C_y had been calculated using standard formulas:

$$C_x = \frac{\Delta F_x}{\rho \cdot \frac{u^2}{2} \cdot S}, \quad (1)$$

$$C_y = \frac{\Delta F_y}{\rho \cdot \frac{u^2}{2} \cdot S}, \quad (2)$$

where ΔF_x is the force of frontal resistance, [N]; ΔF_y - is the lifting force, [N]; ρ is the air density, ρ = 1.21 [kg / m^3]; u is the speed of the incoming air flow, [m / s]; S is the area of the midsection, [m^2].

The experimental sample of the blade is a complexly connected element consisting of a cylinder with a spherical deflector. Therefore, the equivalent blade diameter *D* had been calculated by formula:

$$D = \left(\frac{L}{\sum_{i=1}^{n} \frac{l}{D_i^{5-m}}} \right)^{\frac{1}{5-m}}, \quad (3)$$

where D_i is the diameter of each series-connected part of the blade, [m]; l_i - section length, [m]; L - total length, [m]; *m* is a dimensionless coefficient, which is 0.25 under turbulent mode for smooth surfaces blades.

Substituting the numerical value of D, it is possible to determine the value of the blade midsection area S = 0.0181 m^2.

The Reynolds number was calculated by the formula:

$$Re = \frac{u \cdot D}{\nu},$$

where ν is the coefficient of kinematic viscosity of air.

2. Discussion of results

As a result of the experiments carried out the aerodynamic coefficients of drag force and lift force of the experimental sample of a cylindrical blade were determined for different modes of air flow around the incoming air streams with a speed of (3-15) m / s. In fig.4, 5 show the values of the aerodynamic coefficients from the Reynolds number when the angles of attack α change from 0 ° (the direction of the air flow is perpendicular to the axis of the cylindrical blade) to 60 °. As a result of the study, it was found that the optimal angle of attack is α = 0 ° for the transverse direction of the air flow.

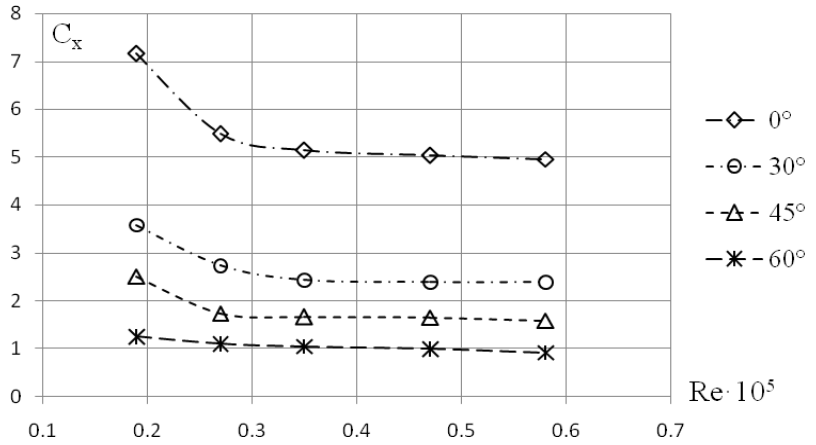

Fig.4. Dependence of the aerodynamic drag coefficient of a cylindrical blade with a deflector on the Reynolds number at different angles of attack α

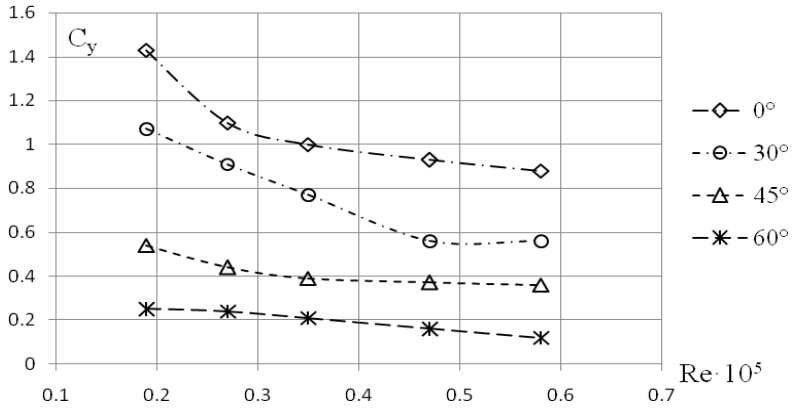

Fig.5. Dependence of the aerodynamic the lift coefficients of a cylindrical blade with a deflector on the Reynolds number at different angles of attack α

The optimal values of the drag coefficient $C_x = 7.16$ and lift coefficient $C_y = 1.43$ at $Re = 0.19 \cdot 10^5$ and the angle of attack $\alpha = 0$ ° have been established. It can be seen from the graphs that with an increase in the value of the angle of attack, the values of the aerodynamic coefficients decrease by approximately 1.5 times.

Conclusions

Within the framework of study a combined blade, consisting of a cylindrical element with a spherical turbo deflector, was developed and created. The description of the main parameters of the deflector, which creates additional thrust due to the turbulence of the flow, is given. At the initial stage, laboratory tests in a wind tunnel with an open working part of a cylindrical blade were carried out. The dependences of aerodynamic forces were obtained at different angles of attack and different air flow velocities. Experiments carried out many times show that the use of a deflector does not significantly affect the regularities of changes in aerodynamic forces and, accordingly, on the dynamics of aerodynamic coefficients. The use of a spherical turbo deflector at the end of a cylindrical blade can provide self-starting and starting rotation at low air flow velocities.

REFERENCES

1 Renewables 2020 Analysis and forecast to 2025. Fuel report — November 2020. Available at: www.iea.org/

2 International Renewable Energy Agency. *Future of wind. Deployment, investment, technology, grid integration and socio-economic aspects.* 2020, 88p. Available at: www.irena.org/wind

3 Lim N. Renewable Energy Sources Market in Kazakhstan: potential, challenges and prospects" as of the end of 2020. Available at: www.pwc.com/kz/en/assets/pdf/esg-dashboard-final-5.pdf

4 In 2021 Kazakhstan will build "green" power plants. Eenergy. media. Available at: www.astanasolar/en/news/

5 Bychkov N.M., Dovgal A.V., Kozlov V.V. Magnus wind turbines as an alternative to the blade ones. *Journal of Physics: Conference Series*. 2007, Vol. 75, pp. 012004.

6 Bychkov N.M. Wind turbine with the Magnus effect. 3. Design characteristics of the wind wheel. *Teplofizika i aeromekhanika*, 2008, Vol.15, No. 2, pp. 341-352.

7 Kusaiynov K., et al. Experimental research of aerodynamics of the system of the revolved cylinders in a turbulent stream. *Proceedings of the 7th Intern. Symp. on Turbulense, Heat and Mass Transfer*. 2012, pp. 577 – 580.

8 Sakipova S.E., Tanasheva N.R., Kivrin V.I., et al. Study of wind turbine model aerodynamic characteristics with a rotating cylinder. *Eurasian phys. tech. j.* 2016, Vol.13, No.2 (26), pp.112-117.

9 Sakipova S.E., Tanasheva N.K. Modeling aerodynamics of the wind turbine with rotating cylinders. *Eurasian phys. tech. j.* 2019, Vol.16, No. 1(31), pp. 88 – 93.

10 Bychkov N., Sorokin A., Nobukhiro M. *Wind turbine*, Russian Patent RF238138. Bull. 4, Publ.10.02.2010, 6 p.

11 Komarova N.M. *Power plant with an active method of wind processing based on the Magnus effect*. Russian Patent RF 2327898. Publ. 27.06.2008, 11p.

12 Delyudin A. *Ventilation deflector: device, types, installation rules*. Available at: www.sovet-ingenera.com/vent /oborud/ventilyacionnyj-deflektor.html (Aug. 2019)

13 Aprelev E. *Deflector ventilation TsAGI: features of calculation and manufacturing.* Available at: www.ventil ationpro.ru/vytyazhnaya-ventilyatsiya/deflektor-ventilyacionnyjj-cagi-osobennosti-rascheta/ (14.05.2018)

Article accepted for publication 17.09.2021

DOI 10.31489/2021No3/53-59
UDC 620.92; 620.97

POWER-GENERATING FUEL BASED ON THE PROCESSING OF MUNICIPAL SOLID WASTE ORGANIC COMPONENTS

Temirbekova M.N.[1], Wójcik W.[2]

[1]Almaty University of Power Engineering and Telecommunications named after Gumarbek Daukeev, Almaty, Kazakhstan, m.temirbekova@aues.kz
[2] Lublin University of Technology, Lublin, Poland

The article considers effective technologies for processing the organic fraction of solid waste, involving the use of various approaches with the concept of preserving the ecology of the environment. Biomass cannot be simply collected and burned, the authors suggest using an effective method of its processing, which will allow fuel from it. To obtain energy, biomass can be used to produce biogas or liquid biofuels using various technological processes, for example, by fermentation. They, in turn, can be converted into electricity and heat, through combustion or the creation of fuel cells or used as fuel for motor vehicles. The purpose of this article is to use alternative methods, such as pretreatment of the organic fraction of municipal solid waste, ethanol fermentation with alcohol yeast, and anaerobic digestion are attracting increased attention. Using these methods, a liquid with alcohol-containing substances has been obtained from 1.5 kg of the organic fraction of municipal solid waste, in which the percentage of ethyl alcohol was 97.5%. Therefore, organic municipal solid waste can be a promising source of fuel in modern energy.

Keywords: organic fraction of municipal solid waste, bioethanol, fermentation, ethanol fermentation with alcohol yeast, renewable energy sources.

Introduction

Nowadays, the production of ethanol from abundant and cheap waste, for example, agricultural waste [1-3], solid municipal and food waste [4-5] are of great interest. Among these inexpensive substrates organic solid municipal waste is an abundant raw material with zero cost and due to the excessive urban concentration and the emergence of large megapolises, the waste situation is deteriorating. Today, about 70% of municipal solid waste still come to landfills or uncontrolled disposal sites, which often pollute surface water, underground water or soil and emit greenhouse gases. Among the methods of municipal solid waste disposal in the world practice, the waste landfilling has gained the most practical widespread, but judging by the experience of waste management of the world's major economies, this type of disposal at the present time is becoming unpromising and makes no economic sense [6].

It should be noted that the composition and morphology of organic municipal solid waste are influenced by various factors, including culture, location, environmental conditions and climate, as well as the level of economy and development of this society [7]. Every year, municipal solid waste generated in emerging countries contains 40-88% of food waste [8-10]. The organic fraction of waste consists of starch, lignocellulose and lipids. Starch and lignocelluloses have great potential to be converted to ethanol, while other lipids cannot be converted to ethanol without pretreatment, but these biodegradable components can be converted to biogas by anaerobic digestion. Pretreatment involves increasing the bioavailability of lignocellulose, using the cellulase enzyme. Hydrothermal pretreatment reduces the formation of fermentation inhibitors that result from the breakdown and degradation of sugar. Pretreatment is an environmentally friendly process, since no chemicals are used, this treatment reduces the formation of hemicellulose and improves the availability of the enzyme for cellulose [11-12].

1. Materials and methods

For this qualitative experiment, fractional models of organic components of municipal solid waste have been used, which were formed in accordance with a similar chemical composition of waste, as well as a sample with real organic components from the solid municipal waste landfill of Tartyp Joint Stock Company

.

in Almaty, that is, the very same organic which is formed every day. A total of 6 fractions were collected with different chemical compositions and weights.

- natural sample from the municipal solid waste landfill in Almaty (1500 g);
- model fraction with lipids (509 g);
- model fraction with cellulose (850 g);
- model fraction with carbohydrates (900g);
- model fraction with fructose (1164 g)
- combined fraction (cellulose – 850 g, carbohydrates – 900 g, lipids – 509 g, fructose – 1164 g).

A qualitative experiment includes the following main stages: preliminary hydrothermal treatment, enzymatic hydrolysis (by such enzymes as: amylase, glucavamarine, amilosubtiline, cellulose), ethanol fermentation (using alcohol yeast) of the liquid fraction of waste. Each sample is formed in accordance with the composition, the selection of samples is based on what elements are usually present in the waste, humidity and pH are determined, after which hydrothermal treatment is carried out at 120°C for 4 hours. After the end of hydration, qualitative reactions are carried out for the presence of starch using iodine and glucose, then the samples are separated into liquid and solid fractions and the fermentation process is started. It is necessary to add 1.5 g of amylosubtilin in the liquid part of each sample for 1.5 hours at 65°C, the next stage is the addition of 2 g of glucavamarine for 1.5 hours at 50°C. Then 2 g of cellulase is added to the solid part of fractional models for 1.5 hours at 50°C and also 1.5 g of amylase at 650°C for 1.5 hours. After the fermentation process is completed, ethanol fermentation is carried out, during which the alcohol yeast (15 g) is added to the liquid part in order to produce ethanol [13].

2. Research results

As a result of a qualitative experiment, liquids with different volumes have been obtained from each model sample after preliminary hydrothermal treatment, fermentation, and ethanol fermentation, which have been then analyzed for the presence of alcohol-containing substances. Different masses of samples were taken and, accordingly, different volumes of substances were obtained, since it was important for our experiment to identify the presence of ethanol and its concentration in the samples.

Table1. Results of ethanol fermentation with alcohol yeast

	Sample name and weight (g)	Amount of liquid after ethanol fermentation with alcohol yeast (ml)
1.	Natural sample from the solid waste landfill in Almaty (1500 g)	135 ml
2.	Fractional model with lipids (509 g)	80 ml
3.	Fractional model with cellulose (850 g)	117 ml
4.	Fractional model with carbohydrates (900g)	95 ml
5.	Fractional model with fructose (1164 g)	87 ml
6.	Combined fraction (cellulose – 850 g, carbohydrates -900 g, lipids - 500 g, fructose 1164 g)	182 ml

After pretreatment, fermentation and ethanol fermentation, the samples have been analyzed by gas chromatography-mass spectrometry (Agilen 7890A\5975C) to determine the chemical composition and identify alcohol-containing substances. Passing through the chromatograph, the fractions are separated into components, and the mass spectrometer is responsible for their identification. This type of detection has a high accuracy (95%), its essence reduces to recording the readings not for the entire volume of the incoming ion current, but for the maximum ions for the supposed molecules, and a graph of the signal (intensity) against time (minutes) is plotted. The measurement error on the gas chromatograph is ±5 %. A chromatogram is a graphical representation of the detector signal used to measure the concentration of substances in the eluate, versus the time of the mobile phase. Chromatograms are diagrammed as sequences of Gaussian peaks on a baseline.

In the experiment, 6 samples with different compositions were used. There is also a sample with a combined composition and a natural sample from the landfill. The experiment shows that ethanol can be obtained from any organic fraction, but a comparative analysis of all samples can reveal that the percentage of ethanol in some samples is higher and separation into several separate components is not a prerequisite. The Table 2 shows data on retention times (minutes), peak areas (S) and components, intensity and

concentration of these substances. These data are the main ones for this method of analysis. The areas of chromatographic peaks (S) are proportional to the volume percentages of the substance in the liquid sample, provided that the catarometer is used to analyze liquid mixtures of substances similar in their chemical structure. Usually, the area of the chromatographic peak is proportional to the concentration (C) of the corresponding component. The area of the chromatographic peak in this case is proportional to the amount of substance that entered the detector at the outlet of the column.

The peak area of the chromatogram is the basis for quantitative calculations of component concentrations. The sum of the peak areas is taken as 100 % and the content of an individual component is calculated by the ratio of the peak areas of the component to the total peak area, thus the percentage (C1, %) of each component in the sample is obtained.

Table2. Combined Sample Components

Peaks#	Time(min)	Area(S)	Component	C, %	C1, %
1	1.681	4237936015	Ethanol	94	96
2	3.978	151571481	1-butanol 3-methyl-	62	2.8
3	6.389	3217162	Propanoic acid, 2-methyl	73	0.1
4	9.499	28243644	Oxim-, methoxy-phenyl-_	77	1
5	17.185	2258941	L-α-Terpineol	71	0.1

In accordance with Table 2, a gas chromatography graph with mass spectral detection is presented (Fig.1), which shows the result of recording the dependence of the column outlet intensity on time. The concentration of each peak (%) is calculated from the peak area. Each peak corresponds to the component and the time at which it was registered, as shown in the table and on the chromatogram, also the peak areas allow you to identify the percentage of each chemical element, this analysis on the chromatograph shows that the experiment really allows you to obtain ethanol and other alcohol-containing substances. The chromatograms of the first five samples were combined into one and only the ethanol concentration was shown. The Table 3 shows the results of gas chromatography analysis of a sample with lipids; this sample contains: ethanol (93.85%), the retention time required to elute the substance corresponds to the time of the peak maximum in the chromatogram, the peak areas, the intensity or signal of the detector, as well as the data on the percentage of substances in the sample. The percentage of ethanol in the sample with lipids is significantly lower than in the model combined sample, and the content of alcohol-containing substances in this sample is significantly higher than in the previous one.

The main stages of the experiment are thermal treatment, enzymatic hydrolysis and ethanol fermentation, judging by the results, these stages have a favorable effect on the samples and in all samples the predominant substance with a high concentration is ethanol. According to Table 3, a chromatogram is presented (Fig.1), which clearly shows the component intensity and the retention time dependence. The time required for the substance elution corresponds to the time of the peak maximum in the chromatogram. Each peak with a corresponding number reflects a component.

According to the component composition, the lipid sample contains specific aromatic heterocyclic organic compounds, such as pyrazine, monobasic short-chain saturated fatty acids (butyric acid), monohydric phenylethyl alcohol, which is contained in essential oils, which indicates the method reliability and the identification of such components in the sample with lipids.

The results of the analysis of mass spectrometric detection of the sample with cellulose (Table 4). This sample showed the lowest percentage of ethyl alcohol, in contrast to the others, since cellulose contains ligninocelluloses in its composition, which have a dense structure. Lignin is a molecule that consists of phenylpropane units linked in a three-dimensional structure, which is especially difficult to biodegrade, the higher the proportion of lignin, the higher the resistance to chemical and enzymatic degradation.

Figure 1(c) shows a dependence graph of the detector signal (substance intensity) versus time (peak) in a sample with cellulose. Ethanol corresponds to a time and a peak that records the detector response. The sample with carbohydrates (Table 5) after analysis on a gas chromatograph revealed the content of ethanol (96.27%). The percentage of ethanol in the sample with carbohydrates is close in value to the ethanol in the combined sample, and this sample also has the lowest content of other alcohol-containing components. Thus, it can be assumed that it is carbohydrates that give the greatest yield of ethanol in the combined sample.

.

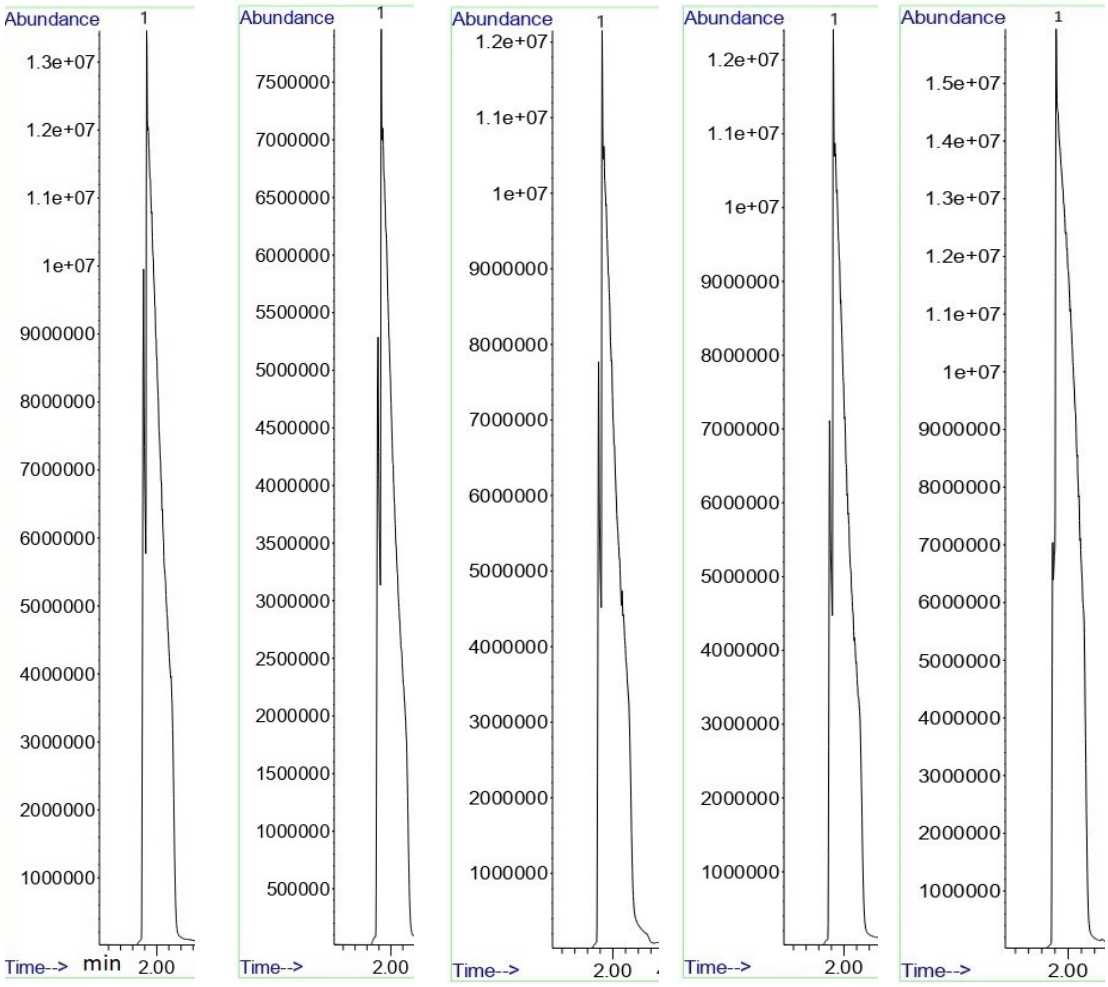

a b c d e

Fig.1. Dependence chromatogram of the components concentration of the combined sample versus time (a- combined sample, b-graph of sample components to lipids ratio, c-dependence chromatogram of the substances concentration and the cellulose sample time, d-graph of concentration of carbohydrate sample components versus time, e-dependence chromatogram of the substances concentration and the sample time the with fructose)

Table 3. Concentration of sample components with lipids

Peaks #	Time (min)	Area (S)	Component	C, %	C1, %
1	1.733	2084267735	Ethanol	93	93.85
2	3.974	66427254	1-butanol 3-methyl-	81	2.99
3	6.623	3468608	Propanoic acid, 2-methyl	83	0.16
4	7.407	4610257	Butanoic acid	77	0.21
5	8.522	10123063	Butyric acid, 3-methyl	63	0.46
6	9.576	31078988	Oxime-, methoxy-phenyl-	85	1.40
7	15.176	9813476	Pyrazine, tetramethyl-	80	0.44
8	16.477	9109129	Phenylethyl alcohol	74	0.41
9	27.674	1155125	Triethyl citrate	75	0.05
10	33.817	909606	Phthalic acid, butyl hex-3-yl ether	77	0.04

Table 4. Concentration of sample components with cellulose

Peak	Time (min)	Area (S)	Component	C, %	C1, %
1	1.718	2571350344	Ethanol	92	90.84
2	3.986	201445006	1-butanol 3-methyl	81	7.12
3	9.513	37545433	Oxime, methoxyphenyl	79	1.33
4	33.818	20161521	Dibutyl phthalate	96	0.71

Table 5. Concentration of sample components with carbohydrates

Peak	Time (min)	Area (S)	Component	C, %	C1, %
1	1.715	3312233598	Ethanol	93	96.28
2	4.215	88291610	1-butanol 3-methyl	69	2.57
3	9.497	39044278	Oxime methoxyphenyl	79	1.15

The chromatogram of the carbohydrate model sample is shown in Figure 1 (d), component corresponds to a peak number and retention time. Each peak of the chromatogram was indicated by a number, using the table. The model fraction with fructose (Table 6) after analysis on a gas chromatograph revealed the content of such chemicals as: ethanol (94.2%) and others. The sample with fructose has a few percent lower concentration of ethanol than the sample with lipids and carbohydrates, but higher than the cellulose sample.

Table 6. Concentration of sample components with fructose

Peak	Time (min)	Area (S)	Component	C, %	C1, %
1	1.651	6352024114	Ethanol	92	94.2
2	3.661	27886911	Vinegar acid	68	0.4
3	3.986	329117680	1-butanol 3-methyl	85	4.9
4	9.334	20281542	Oxime methoxyphenyl	79	0.3
5	33.819	15463353	Dibutyl phthalate	93	0.2

In accordance with Table 6, a gas chromatography graph (Fig.1) with mass spectral detection is presented, which shows the result of recording the dependence of the column outlet intensity on time. A natural sample from the Almaty landfill after a qualitative experiment with fermentation showed the highest ethanol content - 97.5% in contrast to the rest of the samples, the Table 7 shows the peak recording time, the area and intensity of each component, as well as the concentration of these substances. The chromatogram of the substances intensity, the peak area and the retention time of the sample with the organic fraction of the municipal solid waste of the landfill in Almaty is shown in Figure 2. The expanded chromatogram is shown in this figure.

Table 7. Concentration of natural sample components from the landfill of Tartyp JSC, Almaty:

Peak	Time (min)	Area (S)	Component	C, %	C1, %
1	1.731	2339904556	Ethanol	91	97.5
2	9.559	44417720	Oxim, methoxyphenyl	80	0.2
3	14.317	5705926	Ethyl 2- (5-methyl-5-vinyltetrahydrofuran-2-yl), propan-2-yl carbonate	86	0.2
4	15.18	7123396	Pyrazine, tetramethyl	81	0.3
5	16.779	2328081	2H-pyran-3-ol, 6-ethenyltetrahydro-2,2,6-trimethyl	63	0.1
6	17.185	1557327	α-Terpineol	67	0.1

A high concentration of ethanol was detected in a natural sample from a solid waste landfill. Thus, it can be assumed that even without separation and fractionation of elements that are usually present in the organic fraction of solid household waste during sample processing and performing enzymatic hydrolysis

.

and ethanol fermentation, ethanol and other alcohol-containing substances can be obtained and used as an alternative energy source in the future. This experiment showed that some elements, such as cellulose, inhibit the formation of ethanol, due to the presence of lignin in the composition. The lipid test revealed a large number of aromatic substances and proved its lipid component. The sample with carbohydrates also has a higher concentration, which indicates that carbohydrates give a greater effect of alcohol formation in comparison with other samples.

The effectiveness of this method lies in the fact that all the samples that were analyzed have a very high potential for producing ethanol. Solving the problem of the organic fraction of solid household waste, a large range of environmental, economic and energy problems is solved. The ecological situation near the municipal solid waste landfill in Almaty is well known and requires measures to prevent the formation of methane and carbon monoxide, which poisons the soil and water in the nearest settlements. The country's energy reserves require the search for an alternative, so ethanol or in other words, technical alcohol obtained from waste can serve as fuel for cars that collect waste throughout the city.

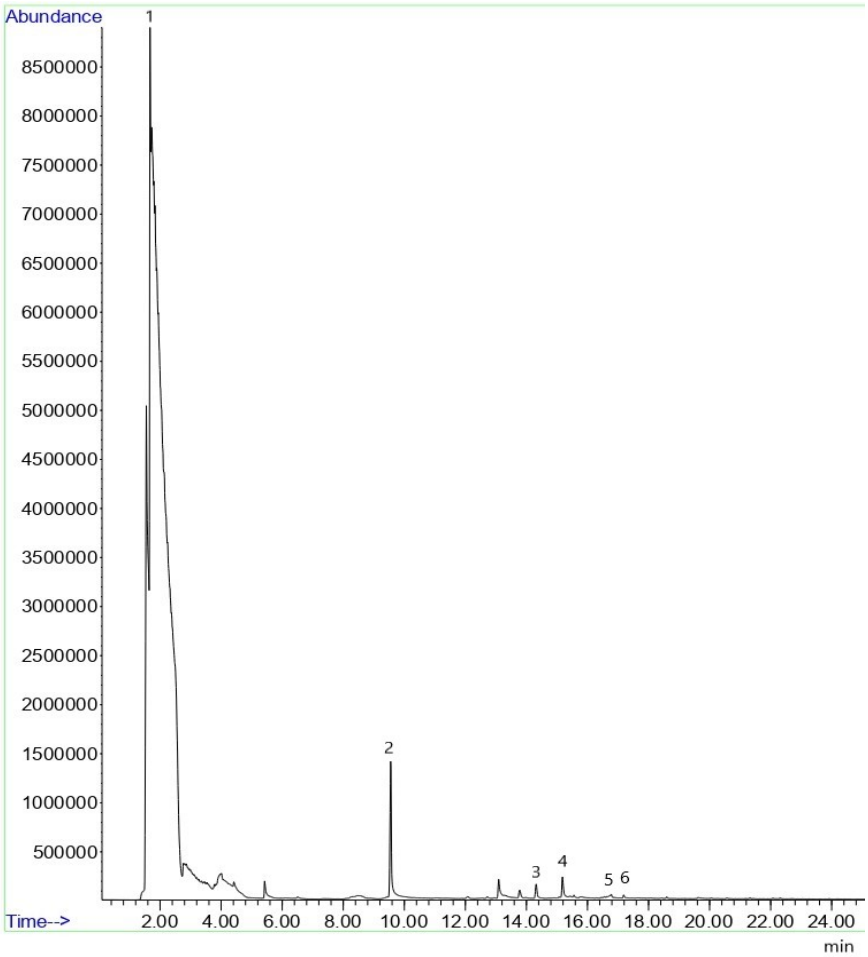

Fig.2. Graph of concentration of natural sample components from the landfill of Tartyp JSC in Almaty

Preliminary heat treatment was used in this experiment to resolve complex molecules and prepare raw materials for the formation of ethanol. Also, when working with waste, heat treatment is a very necessary stage, since the raw materials are decontaminated, which contributes to an environmentally friendly approach. Processing takes place at a temperature of 120 ° C. Enzymatic hydrolysis of samples is carried out for deep destruction with the formation of soluble sugars under the action of poly-enzyme systems. Amylosubtilin, glucavamorin, and cellulose were used as such systems. This stage prepares samples for ethanol fermentation.

Conclusions

Thus, ethyl alcohol is present in the highest concentration in all analyzed samples, which indicates that pretreatment, fermentation, and ethanol fermentation with alcoholic yeast had a positive effect. The ethanol concentration in a natural sample from the Almaty landfill has the highest rate of 97.5%, in contrast to the others, which indicates that this sample has the maximum potential for its production. Fractional samples with different homogeneous and heterogeneous composition and natural sample from the landfill have been selected to assess the difference in the fermentation degree and alcohol concentration.

According to the results, it can be inferred that the combination of components and a heterogeneous composition, as in a natural sample of municipal solid waste, can contribute to an increase in the concentration of alcohol and other alcohol-containing substances. Consequently, the mixed raw material contains more components and enzyme induction improves their bioavailability and prepares them for ethanol fermentation with alcoholic yeast, and pre-treatment promotes the decomposition of lignin and lignincellulose, which are present in the composition of various components of municipal solid waste.

Results from the presented experimental work indicated that waste collected in mixed form have a remarkable potential of use without the need of separation according to carbohydrate fractions to produce ethanol. Biofuel energy in our country is at the very beginning of its development, so the scientific novelty is that this technique is not used to solve environmental and energy problems, namely in relation to waste, when both the situation and the problem with them are significant.

Currently, renewable energy sources represent only about 2.3% percent in the energy balance of Kazakhstan. In fact, about 9/10 of all electricity is generated by burning hydrocarbons. The results obtained reflect the prospect of using ethanol from waste as renewable energy sources. The advantage of this method is environmental friendliness. Supporting global efforts to reduce greenhouse gas emissions and improve the climate, it is necessary to develop alternative energy by producing ethanol from the organic fraction of municipal solid waste.

REFERENCES

1 Kim S., Dale B.E. Global potential bioethanol production from wasted crops andcrop residues. *Biomass Bioenergy*. 2004, Vol. 26 (4), pp. 361–375.

2 Reijnders L. *Ethanol production from crop residues and soil organic carbon.* 2008, 658 p.

3 Sarkar, N., Ghosh, S.K., Bannerjee, S., Aikat, K. Bioethanol production from agricultural wastes: an overview. *Renewable Energy/ 2021, No.* 37 (1), pp. 19–27.

4 Ma, Y., Cai, W., Liu, Y., 2017a. An integrated engineering system for maximizing bioenergy production from food waste. *Appl. Energy*. 2017, 206 (C), pp. 83–89.

5 Yan, S., Li, J., Chen, X., Wu, J., Wang, P., Ye, J., Yao, J. Enzymatical hydrolysis of food waste and ethanol production from the hydrolysate. *Renewable Energy*. 2001, No. 36 (4), pp. 1259 – 1265.

6 Nozhevnikova A.N. *Biotechnology and microbiology of anaerobic digestion of organic household waste*. 2016, 320 p.

7 Alavi Moghadam M.R., Mokhtarani N., Mokhtarani B. Municipal solid waste management in Rasht City. *Iran. Waste Manage.* 29 (1), 2009, 485–489 p.

8 Sharholy M., Ahmad K., Vaishya R., Gupta R. Municipal solid waste characteristics and management in Allahabad, India. *Waste Manage.* 2007, No. 27 (4), pp. 490–496.

9 Talyan V., Dahiy R., Sreekrishnan T. State of municipal solid waste management in Delhi, the capital of India. *Waste Manage.* 2008, No. 28 (7), pp. 1276 – 1287.

10 Yousuf T.B., Rahman M., Monitoring quantity and characteristics of municipal solid waste in Dhaka City. *Environ. Monit. Assess*. 2007, No. 135 (1), pp. 3–11.

11 Taherzadeh M.J., Karimi K., Pretreatment of lignocellulosic wastes to improve ethanol and biogas production: a review. *Int. J. Mol. Sci.* 9, 2008, pp. 1621 - 1651.

12 Komilov O.S., Sharipov M.Z., Tilloev L.I., Majidov J.A., *Autonomous biogas installation with solar heating system. Eurasian Physical Technical Journal,* Vol.15, No. 1(29), 2018, 82-85 p.

13 Mahmoodia P., Karimi K., Taherzadeh M.J. Hydrothermal processing as pretreatment for efficient production of ethanol and biogas from municipal solid waste. *Bioresource Technology*. 2018, Vol. 261, pp. 166-175.

Article accepted for publication 17.09.2021

.

DOI 10.31489/2021No3/60-64
UDC 697.1

MOBILE PREMISES HEATING SYSTEM

Bedych T.V.[1], Shayakhmetov A.B.[1*], Omarov M.S.[1], Isintaev T.I.[2]

[1] Kostanay Engineering and Economic University named after M. Dulatov, Kostanay, Kazakhstan, shayahmetov0501@mail.ru
[2] Kostanay Regional University named after A. Baitursynov, Kostanay, Kazakhstan

In production and in everyday life, various heating systems are used. Alternative heating methods have also been used in recent years. One of the sources for the heating system is the Sun. The use of solar energy is of great importance for objects cut off from centralized heat and power supply systems: small villages and auls, farm formations, distant pasture breeding, mobile houses. Heating from the sun, created on the basis of solar panels, is carried out by installing an electric heater. Currently, more and more attention of consumers is drawn to the electrically conductive carbon-based fuel material (carbon). The aim of the study was to study the use of an alternative energy source in the form of solar radiation and carbon thermal flexible material as a heater for heating mobile living quarters of farmers. To carry out the research, a solar station and a heater with a carbon fiber heat-emitting flexible material were installed on the farmer's mobile house. Studies have shown that the proposed system is efficient and in comparison with other systems, such as solar collectors, the system has a number of advantages.

Keywords: heating, heat supply, sun, fuel, energy, solar panel, carbon, carbon-based fuel material, premises.

Introduction

Analysis of energy savings in traditional residential architecture points to the inadequacy of the use of solar energy resources in different climatic conditions. This refers to the orientation of buildings relative to the cardinal points, as well as relative to the prevailing wind direction. Real urban planning has traditionally tended to locate buildings arbitrarily or according to the relief of the terrain (along highways, riverbanks, extended folds of terrain, etc.) [1, 2]. Another problem related to the energy saving of buildings is the minimization of heat loss through the construction of buildings. The decisive role in this case belongs to the standards for the thermal resistance of enclosing structures. A research was conducted on the modernization of the villa, using a combination of passive and active measures to improve thermal comfort. The walls and ceilings were insulated, three solar air collectors were turned on, and two pellet stoves were installed. The results of the thermal comfort showed a 66% savings on heating [3].

In particular, when designing houses, it is recommended to be guided by the following:

- consider the energy savings of the whole building (due to thermal insulation);
- there must be a guarantee of economic efficiency of the system and its environmental friendliness in operating modes;
- ensure the use of advanced engineering solutions in the design that will ensure the efficient operation of inexpensive systems.

1. Object of study and experimental technique

Various heating systems are applied in production and in household use. Also in recent years, alternative methods of heating have been used. One of the most powerful and inexhaustible sources is the Sun, which daily supplies a huge amount of kilowatts of free energy. Solar energy is always available, although it depends on the weather conditions or time of the day. Solar heating provides a lot of opportunities and advantages [4]. The use of solar energy is most feasible for facilities that are disconnected from centralized heat and power supply systems: villages, farms, distant pastures, mobile homes. The basis of the project is the practical application of the results of the house energy balance calculation [5].

Considering the various schemes for solar heat supply, and their elements, it is revealed that:

- it's application in the north-east of Kazakhstan, direct solar water heating must be used as a supplementary to the traditional "spring-summer-autumn" mode;

- flat collectors are not recommended for use in cold regions of Kazakhstan;
- for the north-east of Kazakhstan it is possible to use systems with direct solar heating

Systems for creating indoor comfort using solar energy can be divided into different schemes. The intermediaries between the solar rays and the energy generating mechanism are solar panels or collectors, which differ both in purpose and design [6]. Batteries accumulate energy from the sun; and they represent panels with photovoltaic cells on one side and a locking mechanism on the other. Photovoltaic batteries assembled from monocrystalline cells are considered the most suitable option for the installation of autonomous heating systems in northern regions. The sun rays that reach the Earth's surface are divided into two types: direct and scattered [7].

The sun reaches a lower angle in winter than in summer, so the solar modules must be positioned at a higher angle in winter than in summer. This allows them to work more efficiently and allows the solar modules to absorb reflected sunlight from the snow. By positioning the solar modules at a higher angle, you also partially solve the problem of accumulated snow on the panels. In many cases, it will simply not linger on the solar module. The opposite situation with the angle of inclination occurs in the summer. The smaller the angle, the better, of course the optimum angles depend on the geographical location. If there is no possibility of changing the angle twice a year (summer/winter), it is better to fix the modules at the optimum angle, the value of which is an average value between the optimum summer and winter angle. Each latitude has its own optimum angle of inclination for the solar modules. Each latitude has its own optimal tilt angle for solar modules. For spring and autumn, the best slope angle is equal to the latitude value of the terrain. In winter, 10-15 degrees are added to this value, and in summer they are taken away. That is why we usually recommend adjusting the inclination angle twice a year, summer/winter. Small deviations of up to 5 degrees from the optimum values do not significantly affect generation efficiency. The most common way to mount solar panels on the roof of a house is at a 45 degree angle.

If you have a summer/winter tilt system installed, you get an increase in generated electricity of around 10-12%, which is quite high. This is especially important in winter. Solar heating, based on solar panels, is achieved by installing an electric heater. The photovoltaic cells only provide power to the heating elements installed in the electric heater, not directly related to the heating circuit [4].

The disadvantages of heating elements include high metal consumption and cost due to the use of expensive materials (nichrome, stainless steel), not very long service life, the inability to repair when the spiral burns out [8]. To obtain composite materials suitable for use in solar water heaters without tanks, expanded graphite with different mass fractions is used [9]. Currently, more and more attention of consumers is drawn to the electrically conductive carbon-based fuel material (carbon). Carbon includes all composite materials in which the carrier base is carbon fibers. Carbon fiber reinforced plastic (carbon) has unique performance properties, which are provided by a combination of various materials - carbon cloth and epoxies. Heating elements made of such material work on the principle of "infrared heating": infrared radiation, which bypasses the air gap relatively unobstructed, first heats up interior objects, walls, floors, people, animals, etc. in the room; these heated objects then give off the heat to the surrounding atmosphere. Carbon material is one of the innovative options for maintaining a comfortable temperature in heated rooms and has unique performance characteristics [10, 11].

Therefore, an innovative carbon fiber flexible material is proposed for use as a heating device, and is a thermo-film (heating mesh) made of interlaced longitudinal and transverse carbon fibers, which are covered with an electrically insulating material for safety purposes. The heat source in the mesh is a heating carbon filament with a conductive layer without the use of metal. The heating elements are laminated on both sides in special electro technical polyester that provides full water resistance and high protection against electrical breakdown. The film can therefore be used for both supplementary and primary space heating by installing in wall panels, ceilings and floors. At the same time, the heater is not designed for outdoor use without proper protection. The product is manufactured using a polymer film (polyester) with high dielectric values; it conducts infrared heat easily and is heat resistant. The carbon paste is applied to the polymer film with a technological precision of less than 1 micron. And the process of applying the carbon and other materials and the final lamination itself takes place at 140 °C (see figures 1 and 2).

.

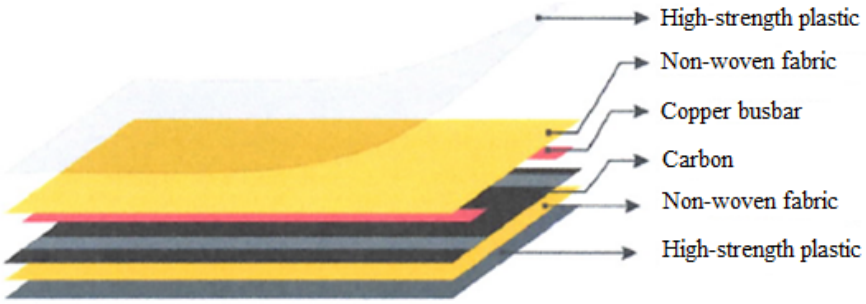

Fig.1. Infrared heating system film design

The aim of the current study was to investigate the use of an alternative energy source in the form of solar radiation and carbon-based fuel flexible material as a heater for heating mobile living quarters of farmers. The scientific novelty of the research is the possibility of using carbon-based fuel flexible material and solar energy in mobile living quarters.

2. Results and discussion

In order to conduct research on the application of a mobile residential heating system using solar panels and carbon-based flexible fuel material, a solar station and a heater with carbon-based flexible fuel material were installed on the farmer's mobile house (see Figures 2). Previously, a solar panel was installed on the house, the energy from which is used for lighting (in Figure 2a near the window). Solar plant includes two monocrystalline solar modules ZDNY-250C60 sized 1650x992x45 mm with capacity 250 W, PWM controller, sinusoidal inverter IS-24-1500U, two storage batteries with capacity 100 A/h. The angle of inclination of the solar panels is 55°.

a) b)

Fig.2. Solar plant: a) solar panels; b) batteries, controller, inverter

The structure of the ZDNY-250C60 monocrystalline solar module consists of many silicon cells that convert sunlight into electricity (see figure 3) [12]. The advantages of these panels are the compactness, low weight and higher efficiency. The monocrystalline panels are placed in a robust and sturdy fiberglass enclosure that protects the photovoltaic cell from moisture and dust penetration. The technical characteristics of the ZDNY-250C60 monocrystalline solar module are shown in Table 1 [12].

Farmer's house: room height 2.5 m, width 2.4 m, length 4.2 m. During the research period, the temperature outside the room ranged from-16^{0}C to -22^{0}C; inside the room from -11^{0}C to -16^{0}C; wind speed - from 3 m/s to 6 m/s; the walls of the house are made of sandwich panels on a basalt base with a thickness of 50 mm; the floor was insulated with linoleum on a felt base.

Table 1. Technical characteristics of the ZDNY-250C60 monocrystalline solar module

Indicator name	***Value***
Maximum power, Pmax	250 W
Voltage at Pmax, Vm	31.17 V
Current at Pmax, Im	8.03A
Open circuit voltage, Voc	37.85V
Short circuit type, Isc	8.40A
Cell efficiency	17.4%
Panel efficiency	15.3%
Cell type	Monocrystal, 156x156 mm
Power deviation (Pmax)	+0..3%
Number of cells	60
Panel size, mm	1650x992x45
Weight, kg	22.5
Operating temperature	-40°… 85°C
Nominal operating cell temperature	47°C

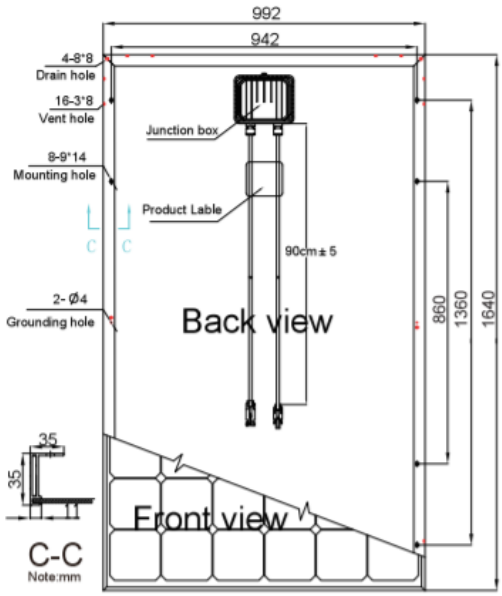

Fig.3. Monocrystalline solar module ZDNY-250C60

The heating system works as follows. The electric current from the two batteries is supplied to the inverter, which converts the direct current into alternating current and changes the voltage from 24 V to 220 V. The current from the inverter is then supplied to the heater with the carbon-based fuel material. To regulate the temperature of the carbon heater, a thermostat is installed between the inverter and the heater, which regulates the temperature of the carbon-based fuel material installed in the heater. During operation, the batteries are charged from the two solar panels via the controller.

In the course of the research, natural light was measured on different days and hours using the luxmeter "TKA-Lux", the current flow to the heater using the M266 current clamp, outdoor temperature, indoor temperature, battery condition using the discharge tester, and the temperature produced by the carbon heater using the Testo 875 thermal imager. The research was carried out in an unheated room.

In the course of research, the following results were obtained:

1. The power consumption of the carbon heater was between 480 W and 540 W at a constant voltage of 220 V and the electrical current was between 2.18 A and 2.45 A.

2. The maximum heating temperature of the carbon heater was +65 ^{0}C from the start after 3 hours, which was observed in particularly sunny weather with an illuminance of 91 klx. At the same time, the room temperature increased from -11 ^{0}C to 12-16 ^{0}C.

.

3. The state of charge of the two 100 A/h batteries varied from 14 V to 9 V for 3 hours under load. Also, the loss of battery charge occurred due to the low temperature inside the room. As a result, it was found that the capacity of the batteries and their number must be increased to ensure the normal operation of carbon heaters.

Conclusions

The research has shown that in order for the batteries to work properly, the indoor temperature must be maintained in accordance with the operating requirements. At low temperatures there is a rapid decrease of discharge and capacity. Cold temperatures affect different types of lead acid batteries in different ways, but are equally damaging for battery operation and performance. The electrolyte freezes and crystallises, which can damage the battery banks and the spongy plate material.

In our region, the daylight hours are considerably shorter in winter and there are more overcast days and the panels can no longer produce the same amount of energy. Therefore, there is a need to increase the number of solar panels and batteries in order to run the heater for a longer period of time. Compared to other systems, such as solar collectors, the heating system we offer has a number of advantages:

- less energy is expended to heat the the carbon-based fuel material than in the solar collector of liquid and air;
- a simpler design of the heating system;
- not significant heat losses, since the carbon heater is located inside the room;
- not complicated installation and transportation;
- the ability to use in mobile rooms;
- many studies have found that it is recommended to use solar photovoltaic panels rather than solar air and water heaters. Better to install more PV panels and use an efficient electric heater [13].

Acknowledgments

The research is funded by the Science Committee of the Ministry of Education and Science of the Republic of Kazakhstan (Grant № AP08956558).

REFERENCES

1 Murgul V.A. Capabilities of Using The Solar Energy for Energy Supply of the Dwelling Buildings of the Historical Area of Saint-Petersburg and for City Environment Quality Improvement. *Architecture and Modern Information Technologies*, 2013, No.1(22), pp. 22/13-07.

2 Izzet Yüksek, Tülay Tikansak Karadayi. Energy-Efficient Building Design in the Context of Building Life Cycle, Energy Efficient Buildings. *Eng Hwa Yap, Intech Open*, (January 18th 2017). DOI: 10.5772/66670.

3 Ghoreishi K., Fernández-Gutiérrez A., Fernández-Hernández F., et al. Retrofit planning and execution of a mediterranean villa using on-site measurements and simulations. *Journal of Building Engineering*. 2021, Vol. 35, Article 102218.

4 Solar heating of a detached house - what you need to know? 2021. Available at: https://energo.house/sol/solnechnoe-otoplenie.html (25.02.2021).

5. Selivanov N.P, Melua A.I., Zokolei S.V. *Energoactive buildings*. Moscow, Stroyizdat, 1988, 376 p.

6 Borutsky V. *Heating of a detached house with solar panels: schematics and system*. 2019. Available at: https://sovet-ingenera.com/eco-energy/sun/otoplenie-na-solnechnyx-batareyax.html (19.01.2021)

7 Solar module positioning, 2020. Available at: https://s-ways.ru/blog/faq/7315.html (04.03.2021)

8 Heating elements: Structure, selection, exploitation, installation of heating elements.2019. Available at: http://electricalschool.info/main/ekspluat/238-trubchatye-jelektricheskie-nagrevateli.html (26.02.2021)

9 Li C., Zhang B., Xie B., et al. Stearic acid/expanded graphite as a composite phase change thermal energy storage material for tankless solar water heater. *Sustainable Cities and Society*. 2019, Vol. 44, pp. 458 – 464.

10 Kogay I.V., Pak V.A., Chan L.S. *Method of manufacturing electrically conductive filament for electric heating fabric and apparatus for its implementation*. Patent No.17940 RK. Publ. 16.10.2006, Bull. 10, 1 p.

11 Kogay I. V. *Method of manufacturing electrically conductive filament for electric heating fabric and apparatus for its implementation*. International depository «INTEROCO». Berlin: European Union, 2015, No EU-000678, 3 p.

12 *Passport of monocrystalline solar module* ZDNY-250C60, China, 2020, 1 p.

13 Ryan McCarthy. *Why We No Longer Sell Solar Air Heaters.* 2019. Available at: https://reductionrevolution.com.au/blogs/news-reviews/why-we-no-longer-sell-solar-air-heaters (26.07.2021).

Article accepted for publication 17.09.2021

DOI 10.31489/2021No3/65-70

UDC 621.039

HEAT-RESISTANT COMPOSITE COATING WITH A FLUIDIZED BED OF THE UNDER-REACTOR MELT TRAP OF A LIGHT-WATER NUCLEAR REACTOR

Bekmuldin M.K.[1,3], Skakov M.K.[1], Baklanov V.V.[1], Gradoboyev A.V.[2], Akaev A.S.[1]

[1]Institute of Atomic Energy, Kurchatov, Kazakhstan, Bekmuldin@nnc.kz
[2]National Research Tomsk Polytechnic University, Tomsk, Russia
[3]Shakarim State University, Semey, Kazakhstan

The paper is devoted to the analysis of existing options of under-reactor melt traps, designs and disadvantages of these traps. A variation of its own under-reactor melt trap with a heat-resistant composite coating with a fluidized bed is proposed. The description of facility for experimental studies of the heat-resistant composite coating with the fluidized bed is presented. The results of a thermal calculation of the variation of the under-reactor trap with fluidized bed melt are presented. Thermal calculations showed that an increase in the average temperature of the melt is less intense in the model of an under-reactor trap with a fluidized bed, due to heat removal from the corium to the metal to complete the phase transition.

Keywords: severe accident, under-reactor melt trap, corium, heat-resistant composite coating, LAVA-B facility

Introduction

As it is known, currently, thirty-one countries in the world receive energy from nuclear power plants. Kazakhstan is also considering the possibility of building the III + reactor. In this regard, improving the NPP safety is one of the urgent and priority tasks. After several major accidents, the entire world community is solving this problem. The experience of NPP operation has shown that there is a possibility of a severe accident developing even with a sufficiently low probability. There are many scenarios for a severe accident development, one of which is the interaction between reactor core melt (corium - molten core material, which forms, according to their chemical composition and oxidation conditions, a system of two immiscible liquids - oxide and metal [1]) and the vessel, with its further penetration and leakage into under-reactor melt trap. The under-reactor melt trap provides receiving, placement and cooling of the corium. Increased safety is achieved by eliminating the release of liquid and solid radioactive materials outside the under-reactor melt trap, which ensures the elimination of damage to the hermetic enclosure system for the accident localization area [2].

1. Analysis of the existing variations of under-reactor melt traps

At the first stages of the nuclear power development, it was proposed to have a pool at the bottom of the reactor shaft, filled with water, in case of destruction of the nuclear reactor vessel, falling into which the melt would be cooled due to the evaporation of the stored water. The vulnerability of this method of heat removal from corium is hydrogen generation, where there is a probability of a steam explosion [3], parameters of the shock wave of which exceed the safety margin of the containment.

It was proposed[4]to install channels lined with heat-resistant ceramics and equipped with cooling fins on the outside under the NPP foundation. The disadvantage was the complication and weakening of the NPP foundation and the length of such channels: with the required total surface of more than 350 - 400 m^2 and maximum possible diameter of 300 mm, required length would be more than 350 - 400 meters. There is an option of the device within the containment with an increased heat removal surface due to a system of longitudinal slots, inside which the fuel melt enters, and a system of cooling pipes is placed in the walls of the slots, where water will be supplied in case of a severe accident. The disadvantage is formation of a large amount of hydrogen, loss of tightness of the slotted cavities for the corium with their filling with water, which will create a risk of steam explosions [4].

.

The main thread in localizing the consequences of a severe accident with core melting of a light-water nuclear reactor is the option with a crucible-type trap(for example, in[5 – 21], as one of the promising and effective methods of confining and cooling the corium. There are many variations of the dry crucible trap. The main purpose of this type of trap is to localize residual energy release in the corium and prevent it from falling outside the trap. This concept is based on filling the under-reactor space with blocks of cassettes filled with sacrificial material [22], placed in a steel heat exchanger-crucible [23, 24], which in turn is also melted sacrificial material and is surrounded by heat-insulating layers cooled by an annular sectioned pool with boiling water. The main difference between all crucible-type traps lies in the design and composition of the sacrificial material. In [11], the trap is mounted on supports under the reactor vessel and is made in the form of a container with a spherical bottom, which includes a heat-insulating protective layer of zirconium dioxide and an outer layer of stainless steel. The heat-insulating protective layer contains an additional bulk layer made of a mixture of fragments of porous high-temperature ceramics and neutron-absorbing materials.

In work [12], the under-reactor melt trap includes a cooled double-walled casing, the bottom of which is deepened towards the center with a slope, filled with sacrificial material. The material consists of several upper and lower cassettes. The upper and lower cassettes contain ceramic plates made with microchannels, separated by horizontal and vertical slotted channels, and mounted on top of each other.

In [14], the trap consists of a cooled double-walled vessel filled with sacrificial material, a guiding element for organizing the melt movement, and a passive system for supplying water to the melt surface. In this case, the sacrificial material is folded into blocks, each of which is divided into segments by attachment points mounted radially relative to the vertical axis of the device. The segments are filled with sacrificial material with formation of free areas communicating with the central through hole for the passage of the melt, while cooling the vessel is made in the form of a passive system that can function with natural circulation of cooling water for an unlimited time, using water from the volume of the containment and sump tanks. In [19], the under-reactor melt trap is equipped with a cooled shell in the form of a multilayer vessel to protect the outer heat exchange wall from dynamic, thermal and chemical influences, and a sacrificial material for diluting the melt. In this case, a multilayer vessel has metal outer and inner walls and a filler placed between them made of a material that is low-heat-conductive in relation to the walls' materials. In [20], a trap with sacrificial and protective materials was installed in the concrete shaft of the reactor. A room adjoins the concrete shaft with layers of sacrificial, steel and protective materials located on the floor successively from top to bottom. The sacrificial material is made using concrete technology with a minimum water content. The entire room together with the trap is a melt containment system. In addition to the design, there are various options in the composition of trap material, for example, in [21], the melt trap material includes Al_2O_3, SiO_2, additionally contains Fe_2O_3 and/or Fe_3O_4 and a target additive in the form of Gd_2O_3, orEu_2O_3, or Sm_2O_3.

Thus, the issue of choosing the design and materials of the under-reactor melt trap for efficient localization of residual energy release in corium has limited experience and is still relevant.

2. Heat-resistant composite coatings with a fluidized bed

The issue of choosing a trap material is to ensure deep subcriticality of the core melt of a nuclear reactor, its nuclear safety and high efficiency of localization. Fast and reliable localization of the melt requires efficient removal of heat released in the volume of the corium melt. The best coolant for heat removal is water, however, the need to prevent steam explosions and generate large amounts of hydrogen requires additional technical solutions. In this regard, methods of heat removal from the melt, which exclude the direct supply of water to the surface, are becoming relevant. In this connection, an idea arose to install a certain amount of metal at the bottom of the trap, together with the sacrificial material. When corium enters the under-reactor melt trap, heating and further phase transition of the metal will occur, which accordingly requires a significant amount of energy. The advantage of molten metal is the absence of hydrogen formation reactions, as well as a low risk of steam explosion compared to water.

The requirements for the material shall satisfy not only the physical and chemical properties, but also the economic feasibility of using a heat-resistant material:

- efficient heat removal from the corium (comparable to water);
- dilution of corium, and, accordingly, a decrease in the density of energy release from fission products and ensuring the state of nuclear subcriticality of the system;

– protection of the trap wall from mechanical and/or thermal shock when corium entry;
– reducing the corium density to prevent the effect of focusing heat fluxes on the water-cooled surface of the vessel of the under-reactor melt trap [25];
– use of the material should not significantly lead to an increase in the cost of building future traps.

The work will be devoted to the preparation and implementation of experimental studies of the interaction between corium with heat-resistant composite coatings and a fluidized bed, as well as further development of recommendations on possible use of a heat-resistant fluidized bed coating for a protective lining of the under-reactor melt trap. Experimental studies will allow to carry out a substantiated analysis of efficiency of a heat-resistant fluidized bed coating for a designed under-reactor melt trap intended to increase the safety of a nuclear power plant in the event of a severe accident with reactor core melting. The use of a fluidized bed enables limiting the refractory temperature by the boiling point of the layer facing the corium, and also provides effective heat removal from the corium due to the energy spent on the phase transition of the fluidized bed material into vapor state.

To analyze the heat removal efficiency of residual energy release of the corium by the heat-resistant composite coating, we carried out a thermal calculation in the ANSYS program of the heat-resistant composite coating with and without a fluidized bed, using the finite volume method for solving the problems of fluid flow and heat transfer. The finite volume method is based on dividing the area of interest into a finite set of control volumes. In this case, the equations of conservation of mass, momentum, energy by combining all compound equations into a system of algebraic equations. Due to the symmetry of the traps with respect to the central axis, a two-dimensional axisymmetric computational domain was chosen to simulate heat transfer in melt traps.

Figure 1 shows models of an under-reactor melt trap with a heat-resistant coating with a fluidized bed and without a fluidized bed. In one of the models there is a metal layer. To compare the original model, the melt traps with the trap with a lead layer in each of the calculations are equivalent:

a) initial conditions (corium temperature 2000 °C);
b) the mass of the heated corium;
c) thermophysical properties of materials;
d) power released in the melt as a result of the presence of residual energy release [26];
e) estimated heating time.

The calculation models take into account the heat transfer by radiation between the surface of the corium, the concrete trap, as well as convective heat transfer between the external surfaces of the model and the environment.

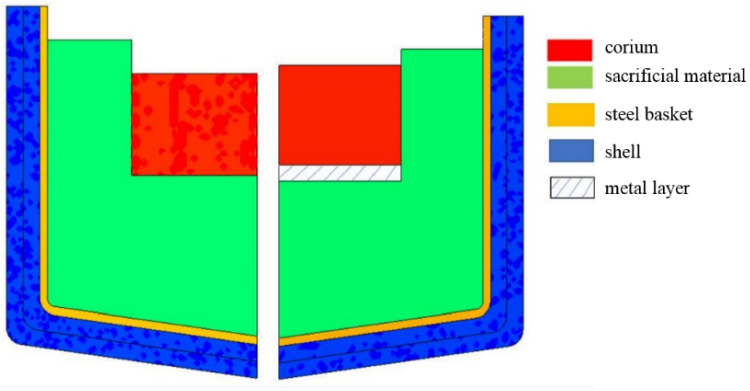

Fig.1. Model of an under-reactor trap without and with a fluidized bed.

As a result of computer modeling of the developed thermophysical model of the interaction of the corium with the elements of the concrete trap, its temperature field was obtained. Figure 2 shows calculated temperature field after interaction between corium and sacrificial materials of the under-reactor melt trap in 150 minutes. It can be seen that temperature field of the under-reactor melt trap with a fluidized bed is lower and more uniformly distributed than temperature field of the under-reactor trap without a fluidized bed.

Changes in average temperature of the melt in under-reactor traps with a composite refractory material without a fluidized bed (model 1) and with a fluidized bed (model 2) are shown in Figure 3.The increase in the average temperature of the melt is caused by residual energy release from the corium.

.

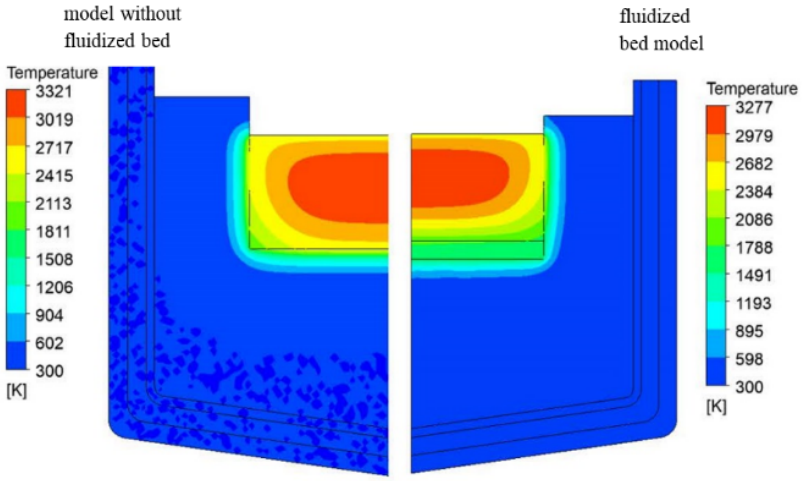

Fig.2. Calculated temperature field of the under-reactor melt trap in 150 minutes after interaction with corium.

As can be seen from Fig. 3, an increase in the average melt temperature is less intense in the model of the under-reactor trap with a fluidized bed, due to heat removal from the corium to the metal for the phase transition.

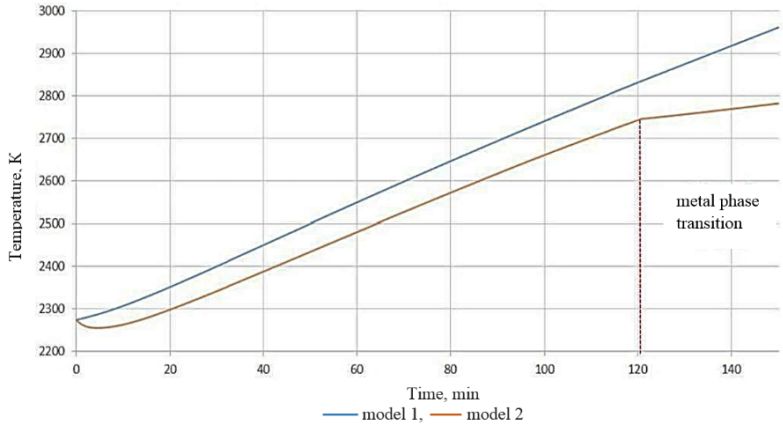

Fig.3. Change in the average temperature of the melt in different models.

Research on this work will be carried out on the LAVA-B experimental facility, created at the IAE NNC RK. This facility is used to study the processes accompanying a severe accident in a light water power reactor [26]. The facility allows melting up to 60 kg of a prototype mixture of LWR core materials by induction melting in a “hot crucible” followed by pouring the melt into the experimental section. To date, as part of the work at the LAVA-B facility, several research programs have been carried out:

– Experimental study of the interaction between fuel and coolant (FCI series) [27];

– Experimental study of the interaction between fuel and residual water inside reactor vessel (LHI series)[27];

– Studies of the interaction between core melt and concrete (MCCI)[27];

– Experimental study of non-stationary processes during retention of the corium in the reactor vessel while simulating residual heat release (INVECOR Project) [27];

– Experimental study of the interaction between corium and refractory materials (CORMIT Project) [28];

– Experimental studies to produce a model solidified corium, similar to the corium formed as a result of the accident at the Fukushima-1 Nuclear Power Plant (Fukushima Debris Project) [29].

– The experimental facility (Figure 4) includes two main functional blocks: an electric melting furnace (EMF) for preparing the prototype corium melt and a melt receiver (MR), which houses an experimental section for modeling the studied processes.

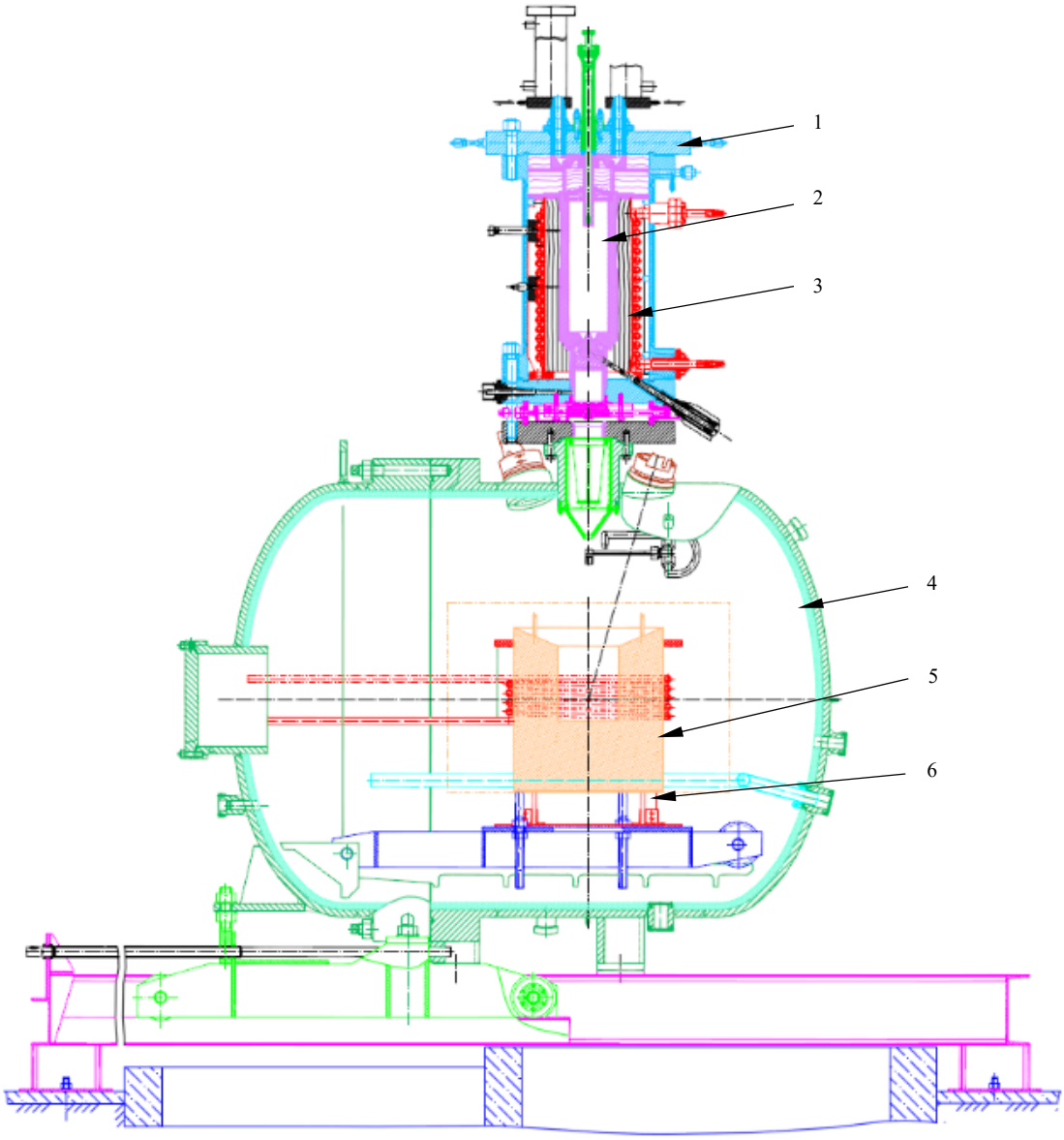

Fig.4. LAVA-B facility: 1 – EMF (electric melting furnace), 2 – graphite crucible, 3 – EMF inductor, 4 – MR (melt receiver), 5 – MR inductor, 6 – concrete trap.

Conclusion

In the process of analyzing the results obtained in the course of modeling, conclusions were made about the influence of the presence of a lead layer on the process of interaction of the corium with the elements of the trap. This analysis allows us to conclude about the effectiveness of the presence of this layer, since it makes it possible to increase the heat removal from the corium for its heating and subsequent phase transition. Thus, in our opinion, one of the simplest alternative options for heat removal from the melt is use of a fluidized metal bed at the bottom of the trap during a period of time when supply of water to the melt is undesirable due to generation of hydrogen and a risk of steam explosion. It is necessary to experimentally determine and theoretically substantiate composition, thermal and physical properties of metal layer, which can create significant heat removal (more than 170-200 kJ/mol) from the corium during its boiling. The results of experimental studies will make it possible to conduct a substantiated analysis of the efficiency of a heat-resistant fluidized bed coating for an under-reactor melt trap designed to improve the safety of a nuclear power plant in the event of a severe accident with reactor core melting.

.

Acknowledgement

The work is carried out within the framework of the event «Development of nuclear energy in the Republic of Kazakhstan» for 2021-2023, in the budget program «Physics and technology of nuclear power», the topic «Investigation of the erosion properties of a composite material when interacting with corium».

REFERENCES

1 Gusarov V.V., et al. Physicochemical modeling and analysis of interaction between the core melt of a nuclear reactor and sacrificial material. *Physics and chemistry of glass*. 2005, Vol.31, No.1, pp.71–90.

2 Sidorov I.A. Melt localization device for NPP with WWER-1200. *Proceeding of the 7th ISTC "Ensuring the safety of NPP with WWER"*, Podolsk, May 17-20, 2011, 13 p.

3 Sehgal B.R., et al. *Melt-Structure-Water Interactions During Severe Accident in LWRs. NPSD*, Royal Institute of Technology, Annual Report, Sweden, Nov. 2000, 147 p.

4 Stolyarevsky A. Does the trap save? *Atomic strategy XXI*, 2014, No.89, pp.16–18.

5 Sidorov A.S., Rogov M.F., Novak V.P., et al. *Proceeding of the Conf. "Safety Issues of NPP with WWER"*, St. Petersburg, 2000, Vol.1, pp. 37 – 66.

6 Kukhtevich I.V., Bezlepkin V.V., Khabensky V.B., et al. *Proceeding of the conf. "Safety Issues of NPP with WWER"*, St. Petersburg, 2000, Vol.1, pp. 23 – 36.

7 Gusarov V.V., Khabensky V.B., Beshta S.V., et al. *Proceeding of the conf. "Safety Issues of NPP with WWER"*, St. Petersburg, 2000, Vol.1, pp. 105 – 140.

8 Gusarov V.V., Almyashev V.I., Beshta S.V., et al. Sacrificial materials for the safety system of nuclear power plants - a new class of functional materials. *Heat Power Engineering*, 2001, No.9, pp.22–24.

9 Gusarov V.V., AlmjashevV.I., Bechta S.V., et al. *Proceeding of the 6th Int. Workshop High-temperature. Super conductors and novelinorg. mater. engineering*. Moscow, MSU, 2001, pp. 11 – 32.

10 Almjashev V.I., Gusarov V.V., Bechta S.V., et al. *Proceeding of the 6th Int. Conf. on Intermolec. Interact. In Matter*, Gdansk-Jelitkowo, 2001, 1 p.

11 Akopov F.A., et al. *Nuclear reactor core melt trap*. RF Patent RU 2169953 C2, 1999, 6 p.

12 Sidorov A.S., et al. *Melt localization device*. RF patent RU 2696612 C1, 2018, 10 p.

13 Gusarov V.V., et al. *Oxide material of a nuclear reactor core melt trap*. RF Patent RU 2192053, 2002, 6 p.

14 Bezlepkin V.V., et al. *Melt localization device.* RF Patent RU 100327 U1, 2010, 6 p.

15 Gusarov V.V., et al. *Method for producing ceramic materials for melting trap in the active zone of a nuclear reactor containing iron, aluminum and silicon dioxide*. RF Patent RU 2206930 C1, 2003, 7 p.

16 Gusarov V.V., Khabensky V.B., Bechta S.V., et al. *Oxide material for a molten core catcher of a nuclear reactor*. PCT patent WO 02/080188, Nov. 21, 2002, 10 p.

17 Gusarov V.V., Khabensky V.B., Bechta S.V., et al. *Oxide material for a molten-core catcher of a nuclear reactor*. PCT patent WO 03/032325, Apr. 17, 2003, 10 p.

18 Mozhzherin V.A., SakulinV.Ya., Migal V.P., et al. *Charge and oxide sacrificial material for a device for localizing a melt in the core of a nuclear reactor*. RF Patent RU 2559294 C1, 2014, 9 p.

19 Nedorezov A.B., Sidorov A.S. *Localization and cooling system of the core melt of a water nuclear reactor*. RF patent RU 2576516 C1, 2014, 13 p.

20 Granovsky V.S., Khabensky V.B., Vasilenko V.A., et al. *Device for localizing the corium of a pressurized water-cooled nuclear reactor*. RF Patent No. 0002696012, 2019, 9 p.

21 Gusarov V.V., Beshta S.V., Khabensky V.B., et al. *Oxide material of melt trap in the core of a nuclear reactor*. RF patent RU 2191436 C1, 2001, 5 p.

22 Gusarov V.V., Almyashev V.I., Beshta S.V., et al. Sacrificial materials of the safety system of nuclear power plants - a new class of functional materials. *Thermal Engineering*. 2001, No.9, pp.22–24.

23 Kukhtevich I.V., et al. The concept of localization of corium melt at the out-of-vessel stage of a beyond design basis accident at NPP with WWER-1000. *Thermal Engineering*. 2001, No.9, pp.2–7.

24 SidorovA.S., Rogov M.F., Novak V.P., et al. Device for localization of the melt of the Tianwan NPP with WWER1000.*Thermal Engineering*. 2001, No.9, pp.8–13.

25 Sehgal B.R., et al. Assessment of reactor vessel integrity (ARVI). *Nucl. Eng. and Des.*, 2003, pp. 23 – 53.

26 Broughton J. M., et al. A scenario of the TMI-2 accident. *Nuclear Technology*, 1989, Vol.87, pp. 34-53.

27 Nazarbayev N.A., et al. Study of the processes of severe accidents in reactor facilities. *Scientific, Technical and Engineering Work to Ensure the Safety of the Former Semipalatinsk Test Site,* 2016, Vol. III, pp. 320 – 356.

28 Tomohisa Kurita, Isao Sakaki, Fumiyo Sakaki, et al. Test and evaluation plan for passive debris cooling system, *ICNRP – 2013. Proc. of the 9th Intern. Conf."Nuclear and radiation physics"*, 2013, Almaty, pp. 19 – 29.

29 Shohei Kawano, et al. Characterization of fuel debris by large-scale simulated debris examination for Fukushima Daiichi nuclear power station, *Proceedings of the ICAPP 2017* – Fukui and Kyoto (Japan), pp. 1105 - 1110.

Article accepted for publication 17.09.2021

DOI 10.31489/2021No3/71-75

UDC 531.226; 621.38

THE INFLUENCE OF A HIGH-VOLTAGE DISCHARGE ON THE OIL BOTTOM SEDIMENTS FORMED AT THE OIL STORAGE FACILITIES OF THE ATASU-ALASHANKOU STATION

Satybaldin A.Zh.[1], Zhakipbaeyev B.Y.[2], Tusipkhan A.[1],Baykenov M.I.[1*], Khalikova Z.S.[1], Alpyssova G.K.[1]

[1]E.A. Buketov Karaganda University, Karaganda, Kazakhstan, murzabek_b@mail.ru
[2]Orda University, Chimkent, Kazakhstan

From three to ten per cent of the total oil produced can ultimately not be used for further processing. When the oil is transported by oil pipelines and oil tankers and stored in reservoirs, oil bottom sediments are deposited on the bottom comprising particles of mineral (non-oil origin) and the heaviest hydrocarbons, mainly paraffin series, whose specific gravity is higher than the density of oil and water. For reliable operation of the tanks, it must be periodically cleaned from the accumulated sediment. The study novelty is the use of the electrohydraulic effect for the processing of oil bottom sediments and creation of a waste-free technology for the disposal of oil bottom sediments in field conditions. The optimal mode for electrohydraulic impact, ensuring the destruction of bottom deposits of oil in the oil storage tanks of the Atasu-Alashankou station, is determined.

Keywords: electrohydraulic phenomenon, catalyst, oil bottom sediment.

Introduction

When oil is transported by an oil pipeline and oil-loading transports and stored in tanks, an oil bottom sediment consisting of particles of mineral and the heaviest hydrocarbons, mainly of the paraffin series, whose specific gravity is higher than the density of oil and water, is deposited at the bottom.The methods used for cleaning and disposing of oil bottom sediments (OBS) accumulated in reservoirs are not effective, so the problem is not solved today. At the same time, there are many technical difficulties with high cost processes, there is no economic interest. A scientific approach to the processes of processing oil-containing waste is of paramount importance. The most appropriate is an integrated waste management, i.e. processing of oil bottom sediments with maximum consideration of properties and the use of all components, as a result of which oil sedimentsbecome raw materials, reagents or fillers in the production process or participate in the processing of other waste [1, 2].

Methods of disposal and cleaning of the tanks and the containers are divided into three types: manual, mechanical and mechanized cleaning method using detergents. In the manual cleaning method, the container is steamed after removing solid residues, washed with hot water (30 – 50) C° from the fire barrel at a pressure of (0.2–0.3) MPa. Washing water with the remaining oil sludge is pumped out by a pump.The mechanized method of tank cleaning on tankers is widely used in our country and abroad. With a mechanized cleaning method, surface contamination is washed with hot or cold water supplied under pressure through special washing machines as hydro monitors. The mechanized cleaning method significantly reduces the cleaning time, reduces the downtime of the tank, reduces the volume of heavy operations, which are harmful to human health, and reduces the cost of the tank cleaning process.

The disadvantages of the mechanized method of tank cleaning include a large consumption of thermal energy for heating cold water, the need to pump contaminated water to treatment facilities, and, relatively, large losses of light fractions from oil aggregates. The chemical-mechanized method of cleaning tanks using detergent solutions improves the quality of cleaning, the intensity of the cleaning process, and is characterized by a low degree of manual labour. The main disadvantages of the method that limit the possibilities of its practical application are the need to use a special reagent and further cleaning of detergent solutions from oil sludge [3-5].

.

In recent years, interest in low-energy effects on substances in order to change their properties has remained consistently high. In order to change the molecular structures of the fraction and create more desirable products, special oil refining processes are used. Taking into account the individual characteristics of the substance and with the right choice of the type of impact, it is possible to rearrangeits structure in the right direction without noticeable external energy costs. We used the electrohydraulic effect as such effects that control the structure of the substance. The essence of the effect is as follows: electrodes are injected into the liquid (most often into water), to which a high pulse voltage is applied. At the same time, complex processes occur, covering a wide range of different physical effects [6-8].The development of new technological solutions aimed at efficient utilization of oil bottom sediments of oil storage facilities and reservoirs is significant on a national scale and has great practical significance for the Republic of Kazakhstan. The got light-boiling fractions using the cavitation phenomenon under the electrohydraulic effect and the process of hydrogenation of the oil bottom sediment will be used not only in oil refining but also in coal chemistry and petro-chemistry.To conduct systematic laboratory studies on the effect of electrohydroimpulse action on the physico-chemical structure of hydrocarbon compounds and for the release of light and medium fractions from the oil bottom sediment, an experimental stand, designed for processing oil and petroleum products with short-pulse discharges, was assembled.Two measuring electrodes are installed inside the cell, one of them is fixed, and the second was fixed on a micrometer screw to adjust the distance between the electrodes. Figure 1 shows a general view of the processing cell by electrohydroimpulsive action of oil and petroleum products.

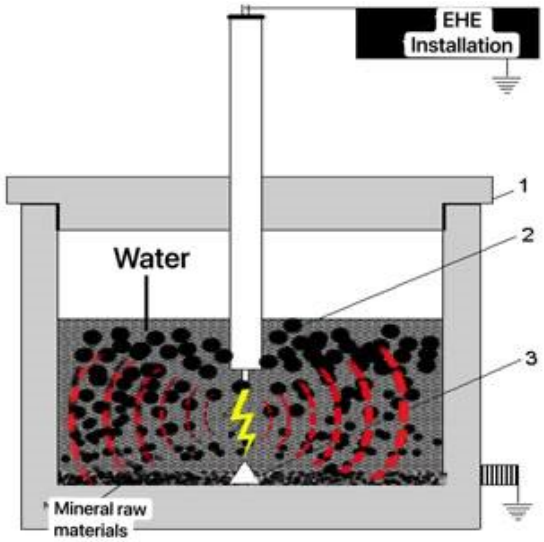

Fig.1. Working area for processing oil bottom sediment by electrohydroimpulse discharges:
1-cover; 2-positive electrode; 3-negative electrode

In the course of experimental studies, it was found that when a liquid(OBS) breaks through, a high-pressure zone appears around the discharge channel, the diameter of which is proportional to the pulse power. High hydraulic pressures drop rapidly as they move away from the discharge, approximately proportional to the square of the distance from it.The liquid (OBS), having received acceleration from the discharge channel expanding at a higher speed, moves from it to all sides, forming a significant cavity in the place where the discharge was, called a cavitation cavity, and causing the first (main) hydraulic shock. Then the cavity closes at a high speed, creating a second cavitation hydraulic shock. At this point, the single cycle of the electrohydraulic effect ends, and it can be repeated an unlimited number of times, according to the specified frequency of repetition of discharges.When performing a sequential series of pulsed discharges in a liquid, each subsequent electrohydraulic shock can occur only after the cavitation cavity from the previous discharge has time to close, which determines the possible maximum frequency of discharges of the electrohydraulic installation [9-10].

The purpose of the research carried out in this work was to establish the possibility of increasing the efficiency of the thermocatalytic transformation of the oil bottom sediment due to the influence of the electrohydraulic effect.

3. Experimental technique

Oil bottom sediments, which formed at the oil storage tanks of the Atasu-Alashankou station, were used as raw materials.Fly ash ferrospheres of TPP-3 (thermal power plant in Karaganda) were used as a catalyst. Microspheres were initially isolated from coal ashes, from which ferrospheres were then separated by magnetic separation. The chemical composition of ferrospheres is as follows, mass %: Fe_2O_3 - 83.4; CaO - 7.6; SiO_2 - 5.7; Al_2O_3- 3.2; the rest is MgO, Na_2O, K_2O, TiO_2, SO_3.After processing the oil bottom sediment of the Atasu-Alashankou oil storage tanks, the resulting product was divided into fractions: IBP–200 ^{0}C and 200-300^{0}C. The individual chemical composition of the light and middle fractions was determined using gas chromatography-mass spectrometry on an HP 5890/5972 MSD device from Agilent (USA).

4. Results and discussion

In the study of the effects of electrophysical characteristics (L is the inter-electrode distance, t is the processing time, C mF the capacitance of the capacitor bank, U kV is the discharge voltage) of an electrohydraulic installation on the output of light and medium fractions fromOBS of the Atasu-Alashankou station. From the data obtained (Figure 1), it can be seen that the electrohydroimpulse effect affects the yield of light and medium fractions. With an increase in the processing time of the OBP of the Atasu-Alashankou station reservoirs from 2 to 8 minutes, an increase in the yield of light and medium fractions is observed from 18 to 74% (the interelectrode space of the processing cell is L= 5-8 mm). The data presented (Figures 2, 3) showed that with an increase in the discharge voltage from 12 kV to 18 kV and the capacity of the capacitor bank from 0.25 mF to 1 mF, an increase in the yield of light and medium fractions from 18 to 74% is observed during the processing of the organic mass of the OBSformed at the Atasu-Alashankou oil storage facilities.

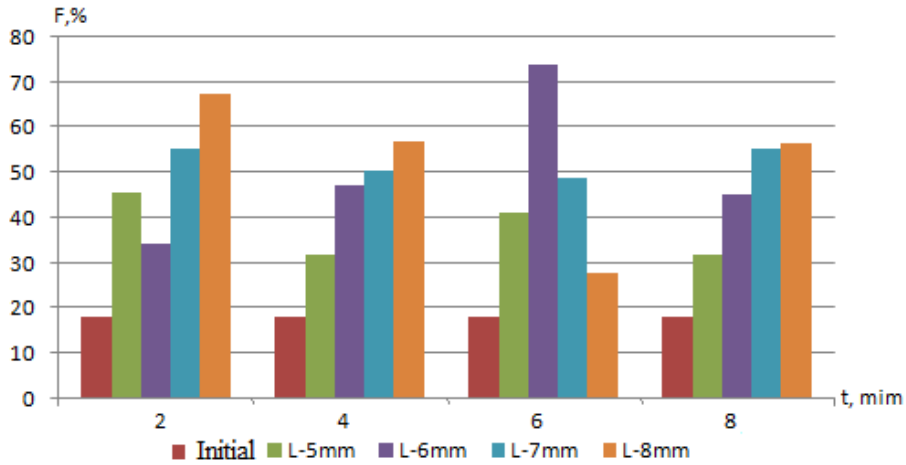

Fig.1. The effect of the time duration of electrohydroimpulse processing on the increase in the yield of light and medium fractions at the different interelectrode space

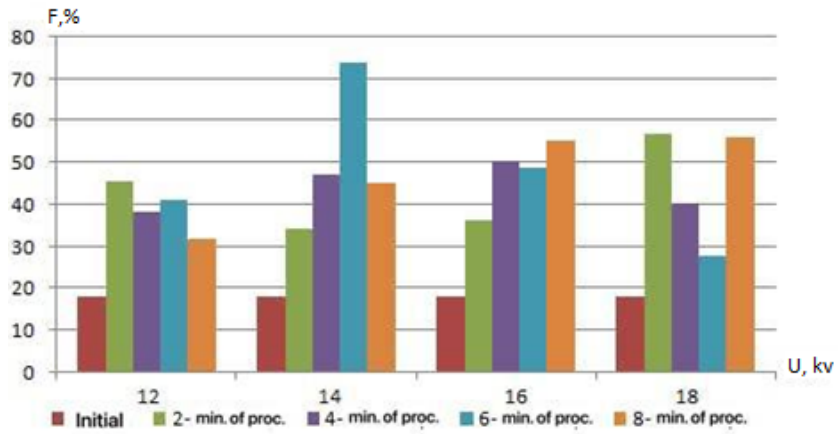

Fig.2. The effect of the discharge voltage on the increase in the yield of light and medium fractions from the OBS of the reservoirs of the Atasu-Alashankou station

.

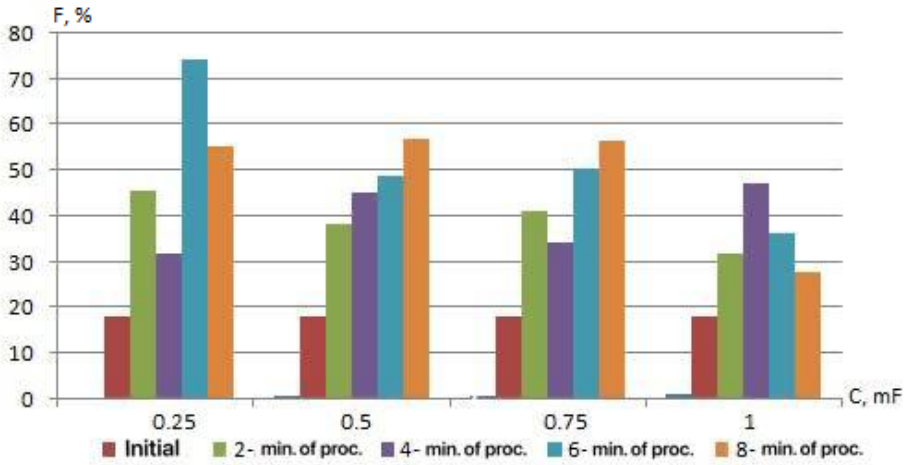

Fig.3. Influence of the capacity of the switching device on the increase in the yield of light and medium fractions from the OBS of the reservoirs of the Atasu-Alashankou station at the different interelectrode space

Fig.4 shows the effect of the amount of microsphere catalyst on the output of gasoline and diesel fuel. The amount of added catalyst (microspheres) ranged from 0.5 to 2.0 % per feedstock. The given indicator of the influence of the amount of added catalyst to the deposits of the Atasu-Alashankou station showed that the amount of added catalyst above 1.0 % leads to a decrease in the yield of target products from 74 to 47%.It is important to note that an increase in the added catalyst by 1% increases the yield of solid residue (oilcoke) on the reactor surface and gas. These changes in the output of gas and oilcoke, gasoline and diesel fuel are associated with a change in the individual composition of the obtained fractions, possibly with the content of aromatic compounds of a mixed structure in the fractions.

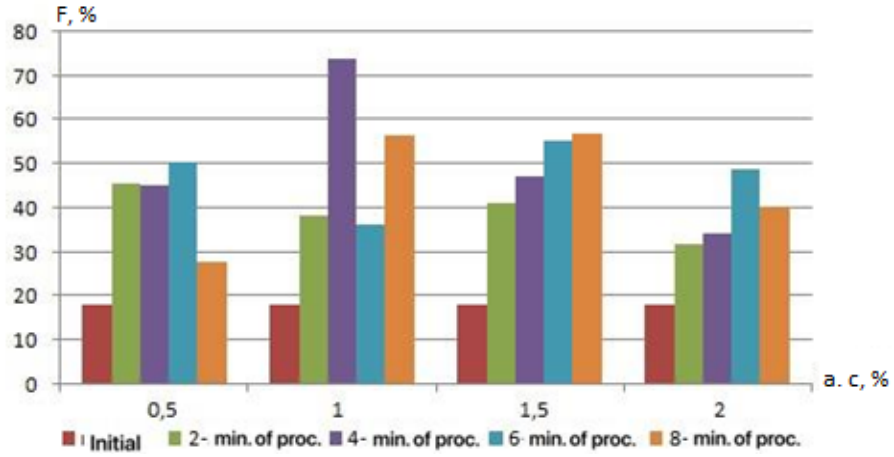

Fig.4. Influence of the amount of added catalyst on the yield of light and medium fractions from OBS of Atasu-Alashankou

All factors (L is the inter-electrode distance, t is the processing time, C mkF the capacitance of the capacitor bank, U kV is the discharge voltage) of an electrohydraulic installationaffecting the yield of the target products presented in Figures 1-4 indicate the predominance of electrohydraulic processes based on the reaction of polymerization addition and the formation of free radicals during the action. This is evidenced by an increase in the output of gasoline and diesel fractions, gas and oilcoke. A comparative analysis of the influence of various factors shows that an increase in the total yield of gasoline and diesel fractions is associated with an increase in the interelectrode space from 2 to 6 mm.

Conclusion

Thus, test experiments have shown that it is possible in principle to increase the efficiency of the process of catalytic cracking of petroleum raw materials under the action of an electrohydraulic effect. The achieved effect is associated with a change in the fractional and individual hydrocarbon composition of

OBSof the Atasu-Alashankou station during its activation and consists in increasing the yield of gasoline, diesel fuel and reducing the yield of coke during cracking. As a result of the study, the following optimal conditions for the destruction of oil bottom sediment using electrohydraulic processing were determined: the duration of processing of the OBS of the Atasu-Alashankou station is 6 minutes, the interelectrode distance is 6 mm, the amount of added catalyst in the OBS is 1%, the capacitor capacity is 0.25 mF, the applied voltage is 14 kV. The results during the processing of oil bottom sediments with a high content of mechanical impurities by electro hydro impulse discharges make it possible to get up to 60% of liquid hydrocarbons, which can be used (after refinement) as motor fuel.

Acknowledgments

The work was carried out within the framework of the grantAP09563282of the Ministry of Education and Science of the Republic of Kazakhstan.

REFERENCES

1 Kuvykin N. A., Bubnov A. G., Grinevich V. I. *Hazardous industrial waste.Hazardous industrial waste*. Study guide. 2004, 148 p. [in Russian].

2 Grosheva M.A. *Innovation and investment support of oil-containing waste processing*. Synopsis of the dissertation by PhD of Economical Sciences. 2006, 28 p. [in Russian].

3 Mansur A. Recovery and characterization of oil from waste crude oil tank bottom sludge from Azzawiya oil refinery in Libya. *J. Adv. Chem. Eng*., 2015, Vol.5, pp.1-11.

4 Shtin I.V. Technology of erosion of bottom sediments in reservoirs type of RVS. *Pipeline transportation of oil. Appendix*, 2001, No. 12, pp. 22 – 28. [in Russian].

5 Gimaletdinov G.M., Sattarova D.M. The methods for cleaning and preventing the accumulation of bottom sediments in reservoirs. *Oil and gas business*. 2006, pp. 1-12. [in Russian]

6 Satybaldin A.Zh., Sadenova K.K., Ospanova D.A. Quantum-chemical calculation of destruction of oil asphalten structure in the process of electrohydropulse influence. *Eurasian Physical Technical Journal*. 2011, Vol. 8, No. 2(16), pp. 25-28.

7 Satybaldin A.Zh. *Electro hydro-impulse technology of processing of oil sludge and oil-containing technogenic raw materials.* Report on research work (final). 2017, No. 0115PK00430, 75 p. [in Russian].

8 Satybaldin A.Zh., Baikenov M.I., Aitpayeva Z.K., Karimova A.B., Rakhimzhanova N.Zh. Investigation of the influence of electrohydroimpulse technology on physical-chemical characteristics of oil sludges. *Bulletin of the Karaganda University. Chemistry.* 2017, No. 3, pp. 131-136. [in Russian].

9 Kussaiynov K.K., Satybaldin A.Zh., Sadenova K.K., Sagimbekova M.N. Electrohydropulse technology processing of oil slimes and oil-containing technogenic raw materials. *Eurasian Physical Technical Journal*. 2015, Vol.11, No.1 (23), pp. 65–69.

10 Baikenov M.I.,Satybaldin A.Zh., Aitpayeva Z.K., Karimova A.B. Determination of optimal electro-physical parameters of the process of degradation of Zhanaozen oil sludge with the help of electrohydraulic effect. *Proceeding of the VIth Intern. Scien. Conf." Theoretical and experimental chemistry"*, Karaganda, 2017, p. 112-113. [in Russian].

Article accepted for publication 17.09.2021

.

DOI 10.31489/2021No3/76-82

UDC 62-932.2, 62-1/-9

DEVELOPMENT OF THE BIOGAS INDUSTRY AND PROSPECTS FOR THE IMPLEMENTATION OF BIOGAS PLANTS IN KAZAKHSTAN

Abilmazhinov E.T., Akimzhanov A.Zh., Shaiakhmetov E.Y.*, Anibaev S.N., Nurgaliyev N.N., Shakerkhan K.O., Sailauov D.M.

Shakarim University of Semey, East Kazakhstan region, Semey, Kazakhstan, shaiakhmeterzh@mail.ru

The article provides an overview of biogas technologies abroad and in Kazakhstan, the experience of foreign countries in the biogas industry, the development and prospects for the introduction of biogas plants in the Republic of Kazakhstan for the environmentally friendly and profitable processing of organic agricultural waste, food production, processing enterprises. Recommendations are given on the specifics of the design of biogas plants in the difficult climatic conditions of Kazakhstan (especially in the north, east and central Kazakhstan). The current design of a biogas plant (filling volume 3.7 m^3) is shown, in the design of which units of our own design were used, this is a peristaltic pump and a raw material grinder. The efficiency of a number of units, in particular a new design peristaltic pump, was shown in the course of the experiments.

Keywords: renewable energy sources, biomass, biogas, biogas plant, biofertilizer.

Introduction

Environmental pollution in the world has become rampant, therefore many countries, under pressure from the public, environmental organizations, are fighting harmful emissions, environmentally dirty industries. At the end of 2019, renewable energy sources showed good growth, wind energy reached (5.44%), solar energy (2.71%), biomass and waste (2.24%) and "other renewable energy sources" (0.4 %) of the total electricity generation in the world [1]. In 2020, the 27 countries of the European Union received more electricity from renewable sources than from fossil fuels for the first time. The share of coal, gas and oil decreased to 37%, while wind, sun, hydropower and biomass provided 38% of the total generation in the EU, increasing production by 10% [2-6].

It is most correct to evaluate and compare the cost of electricity obtained by different methods using the EROI (energy returned on energy invested) indicator - the ratio of energy received from a source to the amount of energy spent on its receipt. For example, EROI 20: 1 for a certain type of fuel means that from each consumed kWh it is possible to generate 20 kWh [7]. The hydroelectric power plant has the highest EROI, close to 100: 1. For coal and gas fired power plants, EROI ranges from 30: 1 to 75: 1. For renewable energy sources (except for hydro resources), the indicators are as follows: for wind power plants EROI reaches a maximum of 16: 1, for solar power plants a maximum of 3.8: 1 [7].

One of the types of renewable energy sources is biogas (purified biomethane), obtained by anaerobic methane fermentation of biomass, i.e. organic waste from agriculture and processing plants, etc. The advantage of using biomass energy by methane fermentation (as opposed to solar and wind energy) is independence from meteorological conditions, i.e. continuity and stability in energy use, a high EROI from 30: 1 to 75: 1 (depending on raw materials, technology perfection, climatic conditions, the degree of biogas purification and the volume of the bioreactor), additional income from the obtained biofertilizers and solving the ecological problem of waste and pollution environment. Biogas production prevents methane emissions into the atmosphere [3]. According to forecasts, the contribution of biomass as an additional source of energy by 2020 will reach 23.5% of the total energy consumption in the world [8].

The aim of the work is to create a relatively inexpensive, efficient and adapted to the conditions of work in the region (in our case, East Kazakhstan) industrial biogas plant, which is quite relevant. The practical significance and novelty of the developed design of the biogas plant is the use of auxiliary units of our own design, since the use of foreign analogues leads to a significant increase in the cost of the installation, this is the design of the peristaltic pump and the design of the raw material grinder being developed. The efficiency

of a number of units, in particular a peristaltic pump of a new design, was shown on the created bioreactor unit (Figure 1), with a total volume of the bioreactor V = 4.62 m^3.

The next stage of our work (it is planned to show at the end of the work in a separate article), the creation of an industrial underground biogas plant (based on climatic conditions) for peasant farms with the further use of the obtained gas for generating electricity and use in everyday life, which would solve the problem of distant farms in providing own electricity and heat.

1. Contents and methods. The use of biogas technologies abroad

The leaders in biogas production are the countries of the European Union (EU). In European countries, 75% of biogas is obtained from agricultural waste, 17% - from organic waste from private households and enterprises, another 8% - from wastewater (installations in sewage treatment plants). Denmark is the leader in the use of biogas: this type of fuel provides almost 20% of the country's energy consumption. [8-12].

Asian countries (China, India, Nepal, etc.) are the leaders in the world in terms of the number of functioning BGS, including mini-installations. In Africa and Asia, the bulk of biogas is produced from food waste, as well as from human waste (sewage). There are about 2 million biogas plants operating in African countries, which provide gas to more than 10 million people [10].

In Latin America, Brazil and Argentina are among the leading countries in the world in terms of the number of vehicles fueled by biogas. In 2010, a social project Biobolsa was launched in Mexico, which provided local farmers with inexpensive biogas plants; this project is actively developing in 9 countries of Latin America and Africa [13, 14]. The biogas market in the USA is much smaller than in Europe. Despite the presence of a large number of farms, there are only about 200 biogas plants operating on the waste of agricultural complexes on the territory of the country. At landfills, the United States is actively introducing technology for producing landfill gas, collecting and disposing of landfill gas [8-10]. In the CIS countries, biogas plants are being actively introduced in Ukraine, Belarus, Kyrgyzstan, and the Russian Federation. In Uzbekistan, at present, biogas plants (BGU) have been introduced in 45 farms with a total annual capacity of 1.1 million cubic meters of biogas [15]. Large BGS are designed mainly according to individual projects, depending on the type of raw materials (vegetable, industrial waste or animal husbandry waste), its quantity and the purpose of gas production (energy production, heating).

In the USA, Europe, the CIS countries (Ukraine, Belarus), they mainly use the designs of European manufacturers, these are large vertical aboveground reactors (due to climatic conditions), insulated, heating the reactor using a heat exchanger, heat is generated on the produced gas, the operating mode is thermophilic (for example, Swiss firm Zorg Biogas BMGH). In the countries of Asia, Africa, Latin America, along with large biogas plants, there are many small and medium biogas plants designed for small farms. The designs of small (gas production from 2 m3), often artisanal biogas plants differ in variety (vertical, horizontal, without mixing, etc.) and are made of improvised material (brick, plastic, rubber, metal), the temperature regime is psychophilic or mesophilic. However, there are a number of common features, these are mainly above-ground (or buried), non-insulated structures, with a vertical or horizontal reservoir (in a number of small biogas plants, the reservoir is a rubber or plastic bag, for example, according to the Biobolsa program in Latin America). Basically, China occupies the niche of selling small biogas plants [10, 13, 14].

2. Development and prospects for the introduction of BGP in Kazakhstan

The process of introducing BSU in the Republic of Kazakhstan is at the initial stage of its development. One of the successful BSU projects for generating electricity from the waste of a pig-breeding complex was implemented in the Zhambyl region. The daily productivity of biogas is 5300 cubic meters per day [16]. In the village of Vostok, Kostanay region, biogas and electricity were obtained on an industrial scale (the date of the launch of the biogas plant is 12/31/2009). All equipment for biogas and electricity production was designed and supplied by Zorg Biogas Ukraine. The biogas station, consisting of 2 reactors of 2400 m3 each, has been brought to full capacity; it is planned to receive 3 million kWh of electricity from biogas annually. The raw material for the station is manure from large and small livestock, as well as grain waste. The cost of the biogas plant is 400 million tenge [16].

In the East Kazakhstan region, in the village of Privolnoye, a biogas plant operates on the basis of the Bagration farm, which allows to process 10 tons of manure per day and produce 400 cubic meters of biogas [16]. In November 2017, in Shymkent, the first biogas plant with a capacity of 0.5 MW was launched in Central Asia. In the complex of this biogas plant, new technologies of the Czech company HEDVIGA

.

GROUP are used - the production of heat and electricity by treating wastewater from the city's treatment facilities and extracting biogas from it (300 m3 / day). The total cost of the project is 2 billion 200 million tenge [17].

In 2018, in the village of Kurminskoye, Abay district, Karaganda region, the poultry farm launched a biogas station for processing poultry manure. The cost is 573 million tenge, modern European equipment has been installed. Capacity - 8,800,000 kWh of electricity, over 18 thousand tons of biofertilizers per year, up to 23 thousand cubic meters are produced daily. m of biogas. The enterprise processes about 150 tons of poultry waste per day and produces about 14 thousand kWh of electricity from biogas [18].

In the North Kazakhstan region, a biogas plant is under construction for processing up to 40 tons of poultry farm waste per day with obtaining up to 9500 m3 / day of biogas, 1 MW electricity and biofertilizer. The equipment was supplied by the Russian company "AgroBioGas", the cost of the construction of the biogas plant is US $ 3 million [19]. They want to implement a similar project on the basis of the Ust-Kamenogorsk poultry farm in East Kazakhstan region [20].

Of the operating small biogas plants in the Republic of Kazakhstan, it is necessary to mention the installations of Samat Abenov (director of FE "Abenov"). The inventor made 4 experimental industrial prototypes. The biogas production process at one of the plants with a daily volume of 5 m3 is fully automated. Biogas is used by an entrepreneur for his own needs, and biofertilizers are sold at a bargain price to peasant farms (Enbekshi settlement, Talgar region, near Almaty) [21].

Anaerobic processing of manure four times - in comparison with unfermented manure - increases the content of ammonium nitrogen (20 ÷ 40% of nitrogen goes into the ammonium form). The assimilable phosphorus content doubles to 50% of the total phosphorus. In addition, during fermentation, weed seeds, which are always contained in manure, are completely killed, microbial associations, helminth eggs are destroyed, an unpleasant odor is neutralized, i.e. the required ecological effect is achieved [23]. When comparing biofertilizers with other types of fertilizers, we have the following quality indicators [24] (table 1). Comparison of biofertilizers and other fertilizers by value [24] (table 2).

Table 1. Comparison of quality indicators of biofertilizers with other types of fertilizers

Indicators	Biofertilizers	Mineral fertilizers	Organic fertilizers (manure, droppings)
Assimilation by plants, %	100	35 ÷ 40	80
Nitrogen loss, %	5 ÷ 8	50	30
Nitrate content in products	-	+	-
Leaching from the soil, %	15	50	80

Table 2. Cost indicators of biofertilizers and other fertilizers (in tenge)

Fertilizers	Application rate, kg / ha	Cost, tenge / kg	Total cost, tenge / ha
Mineral fertilizers	300	64	19200
Manure	6000	1,2	7200
Biofertilizers	3000	0,8	2400

Thus, biofertilizers are 8 times cheaper than mineral fertilizers, and 3 times cheaper than manure when applied per hectare, not to mention the quality indicators indicated above. As we see in Kazakhstan, all large biogas plants are mainly designed by European and Russian companies, however, the segment of medium (filling 15 - 55 m^3) biogas plants for peasant farms is practically not involved. China is present in this segment, but Chinese biogas plants are not always suitable for the harsh continental climate of Kazakhstan, and the development of a domestic heated biogas plant with an underground location of the reservoir is necessary. Thus, the object of research is a domestic biogas plant, raw material cattle manure. Anaerobic processing of biomass was carried out at a biomass plant with a reversible peristaltic pump and grinder. The biogas yield was determined according to generally accepted methods.

3. Discussion of results

Researchers of the scientific department "Natural Science and Engineering" of the University of Shakarim in Semey designed and then manufactured at the plant LLP "Metallist" (Semey, East Kazakhstan region) and successfully tested an industrial complex biogas plant with a wind turbine.

The installation (Figure 1) is automated, with a total volume of the bioreactor V = 4.62 m3 (filling volume Vfill = 0.8, V = 3.7 m3), can process 158.6 kg of fresh cow manure (or other organic waste) daily after the biogas plant enters the mode (mesaphilic, 16 days after the first loading) with the production of about 8 m3 and more biogas per day, after purification in columns and filters (biogas purification system) about 5 m3 of biomethane (more than 90% CH4). This BGP is protected by the RK patent No. 32805. The difference between this unit is the use of a peristaltic pump with a grinder (protected by RK patents No. 31872 and No. 33061), instead of a recirculation pump with a hydrocyclone to provide a lighter mode of mixing the biomass. The developed pump design has shown its energy efficiency in the course of experiments in comparison with foreign analogues (table3) [25-27].

Table 3. Comparative characteristics of peristaltic pumps

No.	Description	Foreign analogues		Proposed design
		НСТ-25-110	ПН-15-1,5/,5,5	
1	Hose diameter	25	15	50
2	Electric motor power, kW	1,5	0,75	0,75
3	Pump rotor speed, rpm	60	35,5	0-80 (adjustable)
4	Productivity, m3 / hour (liter / hour)	1,32 (1320)	1,2 (1200)	2,2 (2160)
5	Maximum pressure, kg / cm2	12	4	-
6	Specific electricity consumption	0,88	0,625	0,341
7	Cost, thousand tenge	700,000		299,700

Currently, biogas plants are not mass-produced in Kazakhstan, but large industrial installations on the market are mainly of foreign production and rather expensive, meanwhile the number of livestock and poultry in the country is increasing annually [28], and agricultural waste is a stable source of biomass. The annual output of livestock and poultry waste by dry weight is 22.1 million tons, or 8.6 billion m3 of gas (gas consumption - 13 million tons, sheep - 6.2 million tons, horses - 1 million tons), plant residues - 17.7 million tons (wheat - 12 million tons, barley - 6 million tons, or 8.9 billion m3), which is equivalent to 14 ÷ 15 million tons of standard fuel, or 12 , 4 million tons of fuel oil, or more than half of the volume of oil produced [29]. Currently, the following features and prerequisites for the development of the biogas industry in Kazakhstan have developed:

- Kazakhstan occupies the second place in the CIS in terms of area and the ninth in the world, while the total population is 18.833 million people (data as of November 1, 2020), therefore, there are no problems with land areas to increase the size of biogas plant in width and length for farms.

- The climate in Kazakhstan is sharply continental, average temperatures in January are from minus 18 ° C in the north to minus 3 ° C in the south, the average July temperature is from + 19 ° C in the north to + 29 ° C in the south. The lowest temperatures: up to minus 45 ° C in the north, east and central part, up to minus 30 ° C in the south. Daily drops can reach 20 ° C [22]. From the point of view of energy efficiency, it is more profitable to introduce bioreactor units in the south (as in the whole world), and in the north, east and central part of the Republic of Kazakhstan, special attention should be paid to thorough and thorough thermal insulation of bioreactors (methane tanks), to locate bioreactors indoors or underground.

- In the south of Kazakhstan, due to the rapid development of greenhouses, there are no problems with the sale of biofertilizers at a favorable price. In addition, in the south, it is beneficial to combine biogas with greenhouses for farms, and use biogas for their own needs, since it is problematic to sell it at a low price of natural gas (methane), with the exception of non-gasified areas.

- Agricultural lands of Kazakhstan occupy 222.998 million hectares [30]. The presented data show not only the huge potential of biomass, but also the potential for the use of biofertilizers, taking into account in this regard the program for the development of saline soils in Uzbekistan.

.

- RK is a manufacturer (and from its own resources) of metal products, building materials (including cement, gravel, crushed stone, bitumen, etc.) required for the manufacture of biogas plants and biogas equipment.

- In the Republic of Kazakhstan (in particular in the East Kazakhstan region), deposits of zeolite ores are being developed, including the production of zeolite, a valuable natural material for cleaning and drying biogas.

Fig.1. Industrial complex biogas plant of our own design.

It should be noted that most suppliers of bioreactor plants abroad (including the Russian Federation) [29] and individual entrepreneurs in the Republic of Kazakhstan widely advertise and sell bioreactor plants (moreover, it is expensive, about USD 1300 per 1 m^3 of bioreactor), not including an important and necessary for the normal implementation of the technological process, equipment as a raw material grinder. The fact is that there is a noticeable amount of fibrous part in the manure, which clogs pipelines and pumps with poor-quality grinding, contributes to the formation of a crust in the bioreactor, prevents the normal release of biogas, and increases the time of methane fermentation. The designs of grinders developed by the staff of the scientific department of the University of Shakarim are effective, practical and inexpensive in comparison with foreign counterparts (for example, a similar German grinder costs about 13,000 euros). Also not included in the kit in most cases, the biogas purification system and other equipment.

Conclusion

1. Kazakhstan has the potential and rich raw material base for the development of the biogas industry;

2. From the point of view of manufacturing, energy efficiency, reliability, ease of operation, maintenance, repair and low price (relative to the one offered on the market) in the Republic of Kazakhstan, it is more promising to introduce biogas plant of its own domestic developments from domestic (local) materials. These are installations of our own design with horizontal underground concrete or steel bioreactors

with thermal insulation, a heating system installed in the lower part of the concrete housing (for concrete) or in the form of a thermal jacket (for steel), with mobile submersible mixers made of corrosion-resistant materials with a sealed drive design, with a complete set of domestic technological equipment (a raw material grinder, a receiving tank with a mixer, pumps, instrumentation and automation, electrical equipment, pipeline fittings, connecting pipes and hoses, a water seal with a water indicator, a biogas purification system, a compressor for biogas injection, a gas holder).

3. These installations are obtained in the price range from 280 US dollars per 1 m3 of bioreactor volume of bioreactor, for installations with a volume of 250 m3 and more; for a bioreactor bioreactor volume of 50 m3 and more, the price is up to 480 US dollars per 1 m3 (for smaller volumes of bioreactor bioreactor it is more expensive), which makes them competitive in the market and enables a quick payback (no more than 2 years).

4. It is necessary to introduce in the biogas industry of the Republic of Kazakhstan biostimulants of our own domestic developments based on natural Kazakhstani raw materials to increase the yield of biomethane and reduce the time of methane fermentation.

5. Biofertilizers obtained as a result of methane fermentation should be used to improve and increase soil fertility of agricultural lands, expand greenhouse farms, to create a Kazakhstani market for biofertilizers, which is necessary for a short payback period for the introduced biofertilizers, as well as for the production of feed supplements.

Acknowledgments

This research has been is funded by the Science Committee of the Ministry of Education and Science of the Republic of Kazakhstan (Grant No. AP09259846)

REFERENCES

1 Ember UK think tank report. The share of renewable energy sources exceeded 8% in the share of the world energy. Available at: https://eenergy.media/2020/03/11/dolya-vie-prevysila-8-v-dole/ (March11, 2020).

2 Presentation by European think tanks Ember and Agora Energiewende, Renewable energy became the main source of electricity in the EU in 2020, the share of gas increased. Available at:https://www.dw.com/ru/vije-teper-glavnyj-istochnik-jelektrichestva-v-es/a-56339064 (January 25, 2021).

3 Alekseenko S., Non-traditional energy. *The Great Russian Encyclopedia*. 2006, Vol.35, pp. 166 – 169.

4 Mibach E., Elkina A. Germany is breaking records in "green energy": what is behind it. 2019. Available at: https://www.dw.com/ru

5 Enerdata logo World Energy Statistical Yearbook 2020. Share of renewable energy sources in electricity generation. Available at: https://yearbook.enerdata.ru/renewables/renewable-in-electricity-production-share.html (December11, 2020).

6 UN Secretary General's report (26.08.2019), The growth of renewable energy sources cannot be stopped Available at: https://news.un.org/ru/story/2019/08/1361871.

7 Toshiba Blog. Why does green energy have a difficult future? Available at: https://habr.com/ru/company/toshibarus/blog/481764/ (May15, 2019).

8 Gromova U. Biogas - an alternative fuel of the future Available at: http://www.solidwaste.ru/publ/view/581.html (August13, 2012).

9 Matthew R. Allen, et al. Trace Organic Compounds in Landfill Gas at Seven U.K. Waste Disposal Sites**.** *Hills Environmental Science & Technology* 1997, Vol.31, No.4, March 1997 DOI: 10.1021/es9605634

10 Kurnakova N.Yu., Katolichenko D.S., Sukharev O., Volkhonsky A.A. *Analysis of the development of bioenergy fuel production*. *Fundamental research*. 2016, 268 p.

11 Scarlat N., et al. Biogas: Developments and perspectives in Europe*. Renewable Energy.* 2018, Vol.129, Part A, pp. 457 – 472.

12 Cucchiella F., et al. An economic analysis of biogas-biomethane chain from animal residues in Italy. *Journal of Cleaner Production.* 2019, Vol. 230, 888 p.

13 Zalevski M. Biogas plants that provided energy for more than 3000 families in Latin America. Available at: https://medium.com/@rodovidme (February8, 2020).

14 Vinicius J., et al. Potential impacts of vinasse biogas replacing fossil oil for power generation, natural gas, and increasing sugarcane energy in Brazil*. Renewable and Sustainable Energy Reviews***.** 2021, Vol. 135, pp. 110 – 118.

15 Report of the United Nations Economic Commission for Europe, PT Prospects for the development of biogas technologies in Uzbekistan Available at: https://www.unece.org (May 8, 2011).

16 Information agency inbusiness.kz, Where else in Kazakhstan do biogas plants work. Available at: https://inbusiness.kz/ru/post/gde-eshe-v-kazahstane-rabotayut-biogazovye-ustanovki (October21, 2020)

.

17 Communication research agency Neftegaz.RU, Kazakhstan launched the first biogas plant in Central Asia with a capacity of 0.5 MW. Available at: https://neftegaz.ru (December14, 2017)

18 News agency baigenews.kz, In the Karaganda region, light is obtained from chicken droppings. Available at: https://baigenews.kz/special/pyat_initsiativ_prezidenta/v_karagandinskoi_oblasti_iz_kurinogo (October15, 2018)

19 News agency baigenews.kz, Biogas plant operating on waste from a poultry farm is being built in North Kazakhstan region. Available at: https: //baigenews.kz/news/v_sko_stroyat_biogazovuu_ustanovku _rabotaushchuu na_othodah_ptitsefabriki/ (September25, 2017)

20 Mikheeva N., East Kazakhstan: Biogas from poultry manure is not worse than from manure. Available at: https://kazakh-zerno.net/134722-vostochnyj-kazakhstan-biogaz-iz-ptichego-pometa-ne (October 11, 2017)

21 Kalimova A., Farmer from the Almaty region has developed a unique biogas plant. Available at: https://kazpravda.kz/ (March11, 2019)

22 Lasunjv N. Prospects for the use of a mobile biogas plant on a railway track in the climatic conditions of Kazakhstan. Available at: http://tekhnosfera.com/perspektivy-ispolzovaniya-mobilnoy-biogazovoy ustanovki-na zhele znodorozhnom-hodu-v-klimaticheskih-usloviyah-kazahstana (September15, 2015)

23 Rodina E., et al. Use of methane emissions from waste for biogas production. *Bulletin of the KRSU*. 2003, Vol.1, No. 6, pp. 65 – 72.

24 Skbvatra service company website. The concept of biofertilizers. Available at:https://skbvatra.com.ua/ informatsiya/ispolzovanie-digestata-v-kachestve-udobrenij/ (September 23, 2017)

25 Anibaev S., et al. *Biogas plant*. Patent RK No. 32805, 2018, 7 p.

26 Anibaev S., et al. *Peristaltic dosing pump*, Patent for invention No. 31872, 2017, 6 p.

27 Serikkaliuly A**.,** et al. *Working tube of the peristaltic pump*, Patent RK No. 33061, 2018, 8 p.

28 Ministry of Agriculture of the Republic of Kazakhstan. Available at: https://moa.gov.kz/ru/documents/2 (March 23, 2020)

29 Biogas plants for gas production. Available at: https://greda.kz/p59616395-biogazovye-ustanovki-dlya.html (September 11, 2020)

30 Mustafaev Zh.S. Reclamation of agricultural land in Kazakhstan: development, analysis and assessment. *Environmental management*. 2017, No. 1, p. 87.

Article accepted for publication 17.09.2021

DOI 10.31489/2021No3/83-87
UDC 691.32

EFFECT OF THE SHAPE AND STRUCTURE OF MATURITY SENSOR'S PLASTIC HOUSING ON ITS PHYSICO-MECHANICAL PROPERTIES

Utepov Ye.B.[1,2], Akhazhanov S.B.[3], Aniskin A.[4], Zharassov Sh.Zh.[1,*]

[1]L.N. Gumilyov Eurasian National University, Nur-Sultan, Kazakhstan, zhshzh95@gmail.com
[2]CSI Research&Lab, LLP, Nur-Sultan, Kazakhstan
[3]Buketov Karaganda University, Karaganda, Kazakhstan
[4]University North, Varaždin, Croatia

This paper presents how the shape and physical structure of the connections affect the performance of the housing of maturity sensor. A two parts rectangular and a keg-shaped cylindrical configurations of plastic housings were sequentially tested for water, shock and load resistance. The tests revealed the weak ingress and shock resistance of the rectangular housing, in comparison with cylindrical one, where no serious defects were identified. Both types of housings performed well during the compression tests on all three sides, showing the bearing capacities from 0.6 to 2.11 kPa, which are equivalent to 65.3 and 165.3 kg of human mass. Based on the results, the study demonstrates an easy-to-handle workflow for generic testing and evaluation of maturity sensors housing. The proposed workflow may be applicable for other types of small-scaled electronic devices.

Keywords: non-destructive testing method, concrete sensor, housing, durability, maturity sensor.

Introduction

The indoor electronic devices used in daily routine are not subjected to adverse conditions, unlike those used outdoor. The latter should comply with higher requirements, having a protected housing. The housing of such devices must stand for various aggressive environment [1, 2]. Depending on the type of device, their housing may be built of different materials as metal, aluminum, timber, plastic, etc. [3]. First three take much efforts to treatment and finishing, especially when it comes to small devices. Moreover, their large-scale production requires significant human and financial resources. Therefore, plastic housings have found broad application in small-sized instrumentation [3]. Despite this, the requirements for them are not a little less. This means the plastic housings should have certain physical and mechanical properties. And again, depending on the type of device they are used for, the list of such properties may vary a lot [4]. The maturity sensors [5–8], which will be discussed in this study, represent small electronic devices with the protected housing. Due to they are embedded into the concrete body, they are subjected to moist, alkaline, and pressurized environment [9].

Since a minor water penetration inside the housing through cracks or slots in the connectors may destroy their inner electronic components. Moreover, while being strapped to a rebar, they are subjected to a shock impact from the pouring concrete mixture [10].In addition, before the installation, the maturity sensors may be accidentally stepped by workers. Therefore, to confront potential external impact, the housing of maturity sensors must have specific physical and mechanical properties complying with the requirements of [11, 12]. Some important aspects influencing the characteristics of the plastic housing are its shape and structure [13]. If referring to the existing analogs of maturity sensors [1, 2], their housings mostly have rectangular shape. They classically consist of two components joining together with screws and nuts with rubber gasket in between. Few have monolithic housing [1], which makes them indestructible.

Despite the variety in shape and structure of the housings of existing maturity sensors, the majority of them have not strayed far from conventional solutions. Since no previous works were found studying the performance of the maturity sensors housing depending on its shape and structure. This suggests that the mature sensor manufacturers relied only on logical assumptions when designing the housings. Perhaps, this is due to insignificance of the production scale of maturity sensors in contrast with major industries of the national economy, where every single detail counts. For example, the automotive and aviation industry pays a lot of attention to the shape of the vehicles, structures of connections, and so on [14, 15]. Nevertheless, the application of maturity sensors is becoming more and more popular in construction sites worldwide [16].

.

And therefore, more and more issues related to the shape and their housing structure arises, which indicates to the relevance of this topic.

In view of the foregoing, this article studies the impact of the shape and structure on the physical and mechanical properties of the maturity sensors housing made of plastic. The following physical and mechanical properties are of interest: water resistance, shock resistance, and compressive strength. These properties were chosen due to the maturity sensors are subjected most to water ingress, drop of concrete while pouring, and squeeze while concrete hardening.

1. Materials and methods

To discover the effect of the shape and structure on the performance of plastic housing of the maturity sensor, two configurations of the housings were designed: 1) Two parts rectangular;2) Keg-shaped cylindrical. Two-component liquid plastic from the company Kimpur – Kimteks Kimya Teksti lÜrünlerive Ticaret A.Ş. formed the basis of the housings. This type of plastic is characterized by its hardness, resistance to mechanical influences, and short setting time. The components of this plastic were mixed in a 1:1 ratio by weight [17]. Both types of housings went through the major stages of design, prototyping, and replication. The wall thickness of housings was fall within the range between1.5 and 5 mm, depending on the part of the housing body. The prototyping was made with 3D printer. Then the prototypes were polished and used to mold the master formworks for replication. The master formworks were made of the two-component silicone HY-520 produced by the Shenzhen Hong Ye Jie Technology Co., mixed with a hardener in the ration of 1:40 by weight [18]. A distinctive feature of the cylindrical housing was the inner structure of its cap, which helped excluding any usage of the gaskets for hydro insulation (Figure 1), like in the plastic bottle caps.

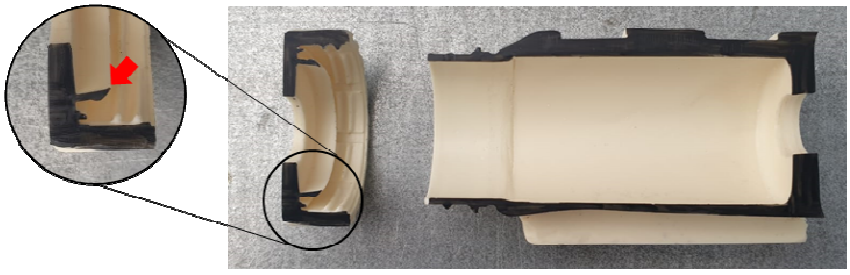

Fig.1. Design of the cylindrical housing

To test for water resistance, both types of housings were sealed with tissue paper inside and prepared for complete submerging in a tank of water [11], where they supposed to remain for 1 month. The tissue paper was planned to be used as an indicator of water proofness of the housings. To prevent them from floating to the surface, they were loaded with weights. The samples were checked on a daily basis till the water penetration is detected. The shock resistance of the housings is tested by a procedure of free-fall from the different heights (1, 1.5 and 2 m) according to [19]. Three samples of each type of housings were used for testing. Due to the complexity of the technical evaluation after dropping, a visual inspection of the samples condition was performed according to the [20] principle (identification of scratches, cracks, and destructions). The compression strength tests were carried out on three sides of the housings as shown in the Figure 2, according to [12].

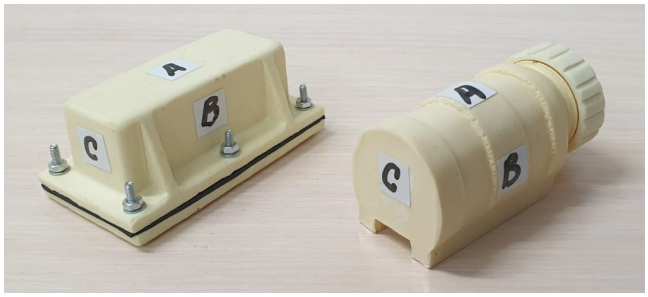

Fig.2. Compression load sides: left – rectangular housing; right –cylindrical housing

The compression load was subjected by an electromechanical press-machine UNIFRAME 70-T1182 with a load range up to 50 kN and displacement speed ranging from 0.05 to 51 mm/min. The measurements of the load resistance were taken each 2 seconds. The rectangular and cylindrical housing samples three each were destroyed during the compression tests. The load was transmitted with a constant speed of 5 mm per minute before cracking. This moment is characterized with the rapid drop of the resistance value. While calculating the strength, different nozzle area of the press piston was taken into account.

2. Results and discussion

The water-resistance test revealed the weakness of rectangular housing that failed the test at 3 days of submerging, which was confirmed by the blotting of the paper inside. Meanwhile, the cylindrical housing remained in the tank of water for 1 month, turned out to be completely waterproof, since the paper inside after the inspection still remained dry (Figure 3).

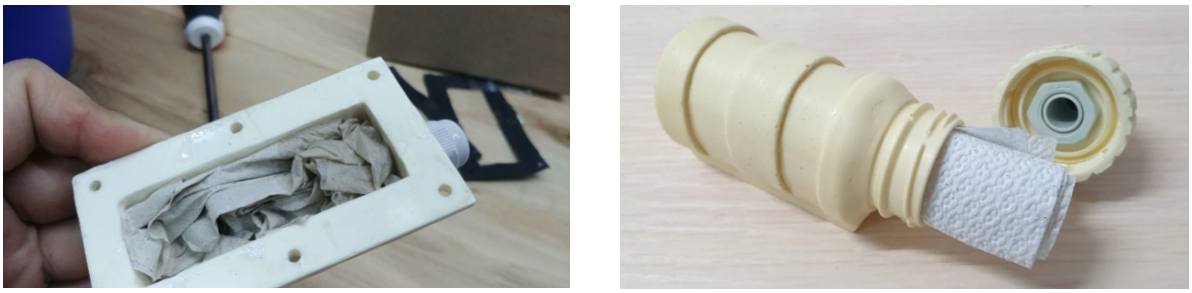

a) b)

Fig.3. Water-resistance test results: a) wet paper in the rectangular housing; b) dry paper in the cylindrical housing.

From the picture above is seen that the water mainly penetrated through the gaps in-between the rubber gasket and the two parts of the rectangular housing tightened with screws and nuts. Perhaps, when tightening, the plastic curved a bit and the gaps occurred. However, still this indicates unreliability of such structure of the rectangular housing, especially its joints. The cylindrical housing in contrast has a smaller number of joints. And therefore, has less chance to let the water run inside. Moreover, the clamping mechanism of the cap worked well. The shock resistance test results are shown in the Figure 4 below.

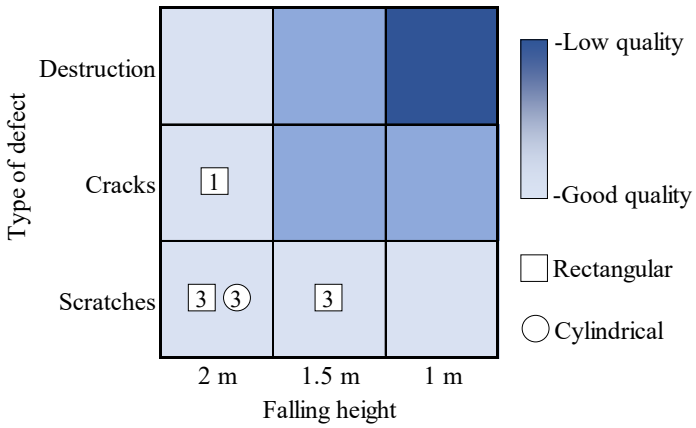

Fig.4. Results of shock resistance test of the housings as quality matrix

As is seen from the figure above, the tests did not cause notable damage on all the samples of both types of housings; no destructions were identified. After the tests the quality of the housings stood rather good. There were minor scratches on the surface of the samples, as well as a single crack in one of the samples of rectangular housing that fall from a height of 2 m. The rectangular housing was cracked at the screw connection part, which may be reasoned by the fact that the screw holes were located close to the edge of the housing. The results of compression test of the housings are demonstrated below (Figure 5).

.

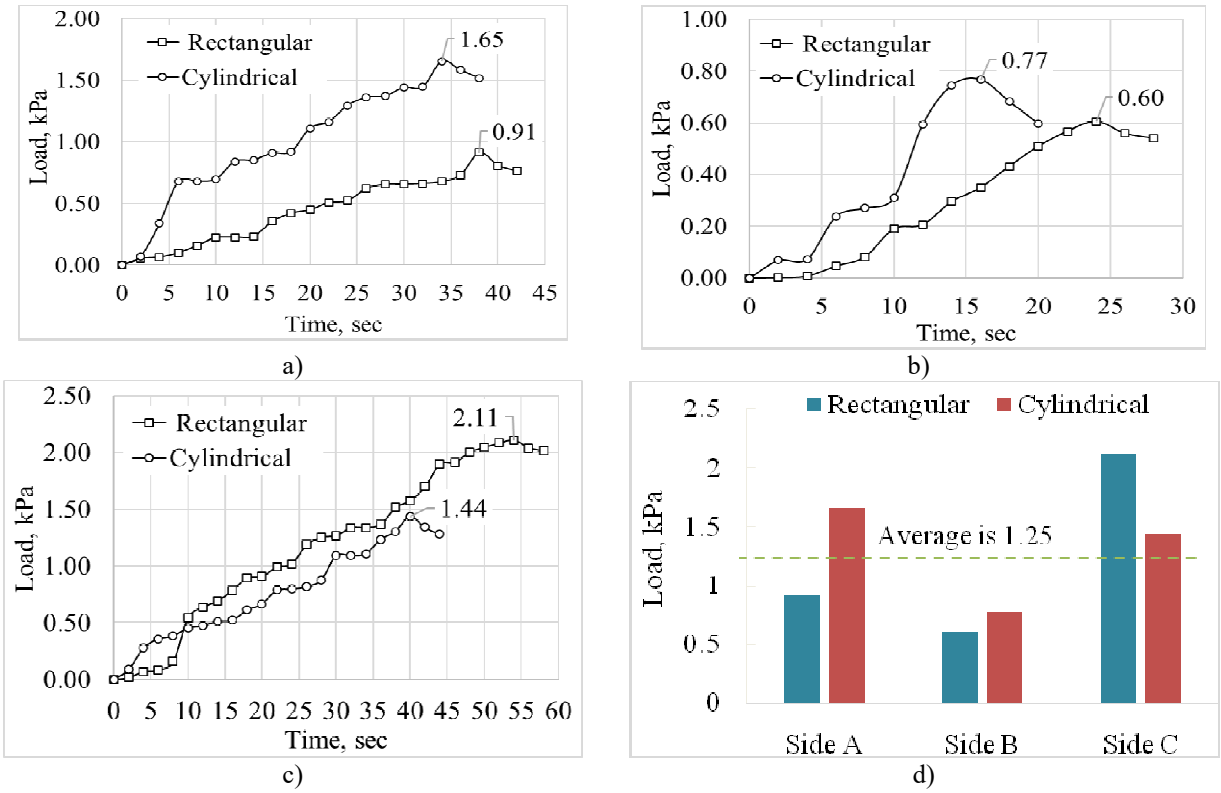

Fig.5. Compression test results of the housings: a) A-sides; b) B-side; c) C-side; d) Comparison

The diagrams above show that the cylindrical housing generically may bear more loads than those of rectangular one. It was ahead on the sides A and B of the housings, but lower in side C. The latter was predictable due to the thinness of wall thickness in the threaded part. The maximum loads that the rectangular and cylindrical housings could bear for sides A, B, and Care arranged in the following order: 0.91, 0.6, 2.11kPa and 1.65, 0.77, 1.44 kPa respectively. While the average load amounted 1.25 kP, only side A and C of the cylindrical, and side C of rectangular housing could exceed this level. Thus, the sides of the housings when ranked by bearing load may be given the following comparison: B < A < C for the rectangular shape, B < C < A for the cylindrical shape.

To sum up, both housings demonstrated fairly acceptable performance. However, the cylindrical housing turned out to be more reliable. Moreover, the keg-shaped cylindrical housing turned out to be 100% waterproof according to the test results, less cost and labor-intensive due to the exclusion of screw connections and rubber for waterproofing. It seen from the results of the study that the small changes of the structure and shape of the housings may significantly affect their physical and mechanical properties. For example, as it turned out, when using plastic materials to develop the housing, the hydro insulation with rubber and the screw tightening may be omitted. This eases the structural schema of the housing and saves the resources. In this regard, the proposed keg-shaped cylindrical housing with the screw cap may have some advantages with those of the housing of its existing analogues [1, 2]. The workflow formed for versatile testing and used to custom designs of the maturity sensors housings may be applicable for some other small-scaled electronic devices that are exposed to submergence and various loads, including homemade and (or) professional ones. Further work will be focused on testing the developed housings for melt in acid and alkaline environment, as well as for the various temperature conditions, including flame ignition.

Conclusion

To reveal the effect of the shape and structure of the housing of maturity sensors on its physical and mechanical properties, two configuration of housings were manufactured: the two-part rectangular and keg-shaped cylindrical. Both types of housing were tested for water, shock, and compression load from three sides. Of course, besides the mentioned properties, the housings may be additionally tested for, such parameters as transparency, quality to the touch, tearing, floatability, flammability, flame color, smell when burning, and solubility in liquids and scratching. However, these parameters were not important the concrete

maturity sensors housing. But may be important for the housings of other types of devices. Based on the results of the tests performed the following statements may be concluded:

- the shape and structure of the housing may significantly influence on its physical characteristics, such as its mass, free space inside, resources used for joints.
- small modifications of the structure of the joints may remarkably improve the water resistance of the housing;
- the monolithic design of the container part and the small number of parts in general in the assembly provides more structural robustness to the housing;
- the keg-shaped cylindrical housing appeared to be more reliable than those of rectangular one in several aspects, and could preserve its physical and mechanical properties in an acceptable level.

The workflow provided in the study and aimed on prompt verification of physical and mechanical properties of the housings, may be applied for various small and multi-scale electronic products.

Acknowledgments

This research was funded by the Science Committee of the Ministry of Education and Science of the Republic of Kazakhstan (Grant № AP08956209).

REFERENCES

1 Giatec. *Wireless SmartRockTM Concrete Sensors Keep Construction Workers Safe During Pandemic*. Available at: https://www.prnewswire.com/news-releases/wireless-smartrock-concrete-sensor (13.09.2021).

2 Olson C. i*Button Link Sensors Complete Space Mission* 2021. Available at: https://cdn.shopify.com/s/files/1/0164/3524/files/iButtonLink-Rhodium-NASA_NG-14_FINAL (13.09.2021).

3 Weichel C. Enclosed: a component-centric interface for designing prototype enclosures. *Proceedings of the 7th Intern. Conf. on Tangible, Embedded and Embodied Interaction - TEI '132013*. pp. 215–218.

4 Roger B. Requirements for physical testing of rubbers and plastics. *Polymer Testing*. 1984, Vol. 4, No. 24, pp. 91–100. doi: 10.1016/0142-9418(84)90003-5

5 Utepov Ye.B., Tulebekova A.S., Zharassov Sh.Zh., Bazarbayev D. Development of a case for a wireless sensor for monitoring of reinforced concrete structures. *Bulletin of Kazakh Leading Academy of Architecture and Construction*. 2021, Vol. 80, No. 2, pp. 264–274. doi: https://doi.org/10.51488/1680-080X/2021.2-06

6 Utepov Ye.B., et al. Development of an IT architecture for a wireless sensor for monitoring the strength of reinforced concrete structures. *Herald of the Kazakh - British technical university*. 2021, Vol. 18, No. 1, pp. 168–175.

7 Utepov Ye.B., Khudaibergenov O.A., Kabdush Ye.B., Kazkeev A.B. Prototyping an embedded wireless sensor for monitoring reinforced concrete structures. *Computers and Concrete*. 2019, Vol. 24, No. 2, pp. 95–102.

8 Utepov Ye.B., Aniskin A., Ibrashov A.P., Tulebekova A.S. Maturity sensors placement based on the temperature transitional boundaries. *Magazine of Civil Engineering*. Vol. 90, No. 6, pp. 93–103.

9 Colozza N., Tazzioli S., Sassolini A., Agosta L., Monte M.G., Hermansson K., Arduini F. Multiparametric analysis by paper-assisted potentiometric sensors for diagnostic and monitoring of reinforced concrete structures. *Sensors and Actuators B: Chemical*. 2021, Vol. 345, pp. 130352. DOI: 10.1016/j.snb.2021.130352

10 Zhang H. Building Materials in Civil Engineering: Woodhead Publishing, 2010, 441 p.

11 *GOST 14254-96 Degrees of protection provided by enclosures (IP Code)*, 1996, 32 p.

12 *GOST 16962.2-90 Electrical articles. Test methods as to environment mechanical factors stability*, 1990, 48 p.

13 BUD. *Enclosure Design Tips Handbook: Bud Industries*, Inc., 2005, 28 p.

14 Bouchard C., Aoussat A. Modellisation of the car design process. *International Journal of Vehicle Design*. 2003, Vol. 31, No. 1, pp. 1. doi: 10.1504/IJVD.2003.002043

15 Ivchenko A.V., Sharonov N., Ziatdinov R. New conceptual design of the adaptive compliant aircraft wing frame. *Engineering Science and Technology, an International Journal*. 2019, Vol. 22, No. 5, pp. 1149–1154.

16 Utepov Ye.B., Tulebekova A.S., Zharassov Sh.Zh., Abdulina S.A. Best practice in concrete strength measurement systems. *Bulletin of D. Serikbayev East Kazakhstan technical university*. 2021, Vol. 91, No.1, pp. 91–97.

17 *Kimteks-KimyaTekstilÜrünleri Tic.A.Ş. A*vailable at: https://www.kimteks.com.tr/en/ (13.09.2021).

18 Ye H. (2021) *Silicone Rubber for Rapid Prototyping* Available at: http://www.szrl.net /a/Products/Molding_Silicone_Rubber/Silicone_for_Prototyping/2021/0419/1742.html (accessed date: 13.09.2021).

19 *GOST 15150-69 Machines, instruments and other industrial products. Modifications for different climatic regions. Categories, operating, storage and transportation conditions as to environment climatic aspects influence*, 2010, 58 p.

20 Martínez S.S., Vázquez C.O., García J.G., Ortega J.G. Quality inspection of machined metal parts using an image fusion technique. *Measurements*. 2017, Vol. 111, pp. 374–383. DOI: 10.1016/j.measurement.2017.08.002

Article accepted for publication 17.09.2021

.

DOI 10.31489/2021No3/88-92

UDC 536.2

MODEL OF VOLUMETRIC HEAT SOURCES IN ANODE OF MICROFOCUS X-RAY TUBE

Kozlov E.A., Trubitsyn A.A.*, Fefelov A.A., Grachev E.Yu.

Ryazan State Radio Engineering University named after V.F. Utkin, Ryazan, Russia, assur@bk.ru

The work is developed a numerical-analytical approach to modeling thermal processes in a composite anode of microfocus X-ray tubes. At the first stage of modeling, with the help of well-known analytical approximations, the distribution function of volumetric heat sources is built. At the second stage, this function is used when solving a stationary boundary value problem with the Poisson equation by the Finite Elements Method. Using the proposed technique, an adequate assessment of the maximum power of the tube with the transmission type W-Be anode was developed.

Keywords: microfocus X-ray tube, composite anode, volumetric heat sources, Poisson equation.

Introduction

The use of microfocus tubes vs macrofocus ones in X-ray installations provides a number of indisputable advantages: equipment compactness, decreasing by the radiation load on the personnel and on the adjacent areas of the object under study, the possibility of local research, ability to obtain magnified images, higher image quality with the same radiation doses.

The improvement of microfocus X-ray tubes is under two main directions: 1) an increase in the power of X-ray radiation; 2) reducing the diameter of the focal spot. Both directions are associated with the solution of the dissipation problem by the anode of the microfocus tube of the heat output. The power of the X-ray tube and the diameter of the focus stain are mainly limited by the limit thermal power allocated on the anode. An increase in the specified limit will allow to expand the diagnostic capabilities of X-ray equipment.

Despite the fact that in recent years, X-ray sources have appeared with the anodes of original structures that can dispel significant thermal capacities [1 - 3], most of the commercial and scientific samples of the tubes use inexpensive classic solid composite anodes. Many questions relating to the optimal parameters of such anodes are still open. To obtain an adequate estimate of the capacity of the power allocated in a flat composite anode, it is necessary to clarify the existing models of heat propagation in the respective solid structures.

1. Analytical approximation of the heat generation area

Let us to consider the problem of determining the thermal mode of operation of the anode of the microfocus tube of the transmission type. The classic anode of the tube is a film structure in which the target material is applied to the substrate. Electrons, bombarding target, penetrate deep into the material, generating X-ray radiation due to the loss of kinetic energy during their braking. The scattering of electron energy occurs in the interaction area, the dimensions and the shape of which are determined by the accelerating voltage on the anode U, the diameter of the focal spot d_b and the atomic number z of the target material [4].

From the point of view of the heat propagation problem, the domain of interaction of the electron beam with the target is an internal heat source, the volumetric power of which is determined by the spatial distribution of energy losses by electrons when they are moved in a solid [5]. In the case of the internal heat sources, the stationary temperature field $T(x, y, z)$ is the solution of the Poisson equation:

$$\frac{\partial^2 T}{\partial x^2}+\frac{\partial^2 T}{\partial y^2}+\frac{\partial^2 T}{\partial z^2}=-\frac{q_\upsilon(x,y,z)}{\lambda(T)}, \tag{1}$$

where $q_\upsilon(x,y,z)$ is the spatial distribution of the volumetric power of the internal heat source, $\lambda(T)$ is the thermal conductivity coefficient depending on temperature.

One of the main factors affecting the maximum temperature in the target is the size and shape of the heat release region, which is determined by the dependence $q_v(x,y,z)$. For practical purposes, the interaction region is approximated by the hemisphere model [4] or, as suggested in this work, by the truncated sphere model shown in Fig. 1.

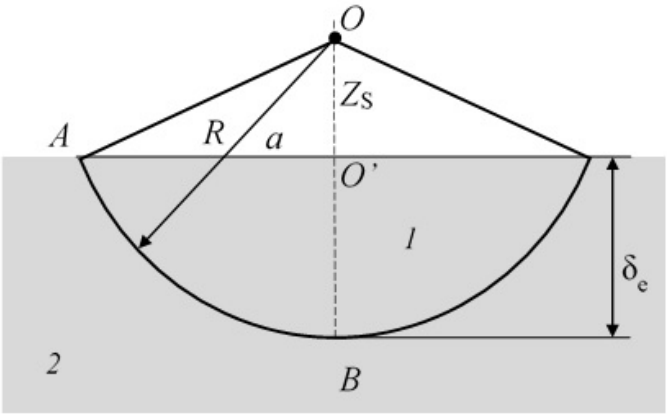

Fig. 1.Approximation of the region of interaction of electrons with the target material by a truncated sphere: 1 - region of interaction;2 – target.

The radius R and the value of the displacement of the center of the sphere Z_S are found from the triangle ΔOO'A by the simplest algebraic calculations

$$Z_S = \frac{\delta_e}{2}\left(\left(\frac{a}{\delta_e}\right)^2 - 1\right), \tag{2}$$

$$R = \frac{\delta_e}{2}\left(1 + \left(\frac{a}{\delta_e}\right)^2\right), \tag{3}$$

whereδ_e is the extrapolated depth of path of electrons in a solid, a is the radius of the region of electrons propagation in the near-surface layer of the target, equal to $a = \delta_e + 0.5d_b$.

The well-known semiempirical relations [6] can be used to determine the parameter δ_e. The most commonly used in applied research is the formula for determining δ_e in the Cosslett-Thomas model

$$\delta_e = \frac{0.074U^{1.55}}{\rho}[\mu m], \tag{4}$$

where U [kV] is the accelerating voltage at the anode, and ρ [g/cm^3] is the density of the target material.

The distribution of volumetric heat sources $q_v(x,y,z)$ will be determined by the normalized distribution function of electrons energy losses in the interaction region. Approximations of this function are known in one-dimensional and axisymmetric formulations of the problem. In the axisymmetric formulation of the problem, a normalized function of energy losses with a Gaussian distribution is traditionally used to determine volumetric heat sources, which has the form [7]:

$$q_v(r,z) = A\left(\exp\left(-\left[\frac{r^2}{a_1^2} + \frac{(z - z_{ms})^2}{z_{ms}^2}\right]\right) + B\exp\left(-\left[\frac{r^2}{a_2^2} + \frac{(z - z_{ss})^2}{z_{ss}^2}\right]\right)\right), \tag{5}$$

.

where $A=\dfrac{0.2(1-\eta)P}{a_1^{\,2}z_{\rm ms}\left(1-\eta+\eta\dfrac{z_{\rm ss}}{z_{\rm ms}}\right)}$, $B=\dfrac{\eta a_1^{\,2}}{(1-\eta)a_2^{\,2}}$, η is the reflection coefficient of primary electrons, parameters $a_1^{\,2}=z_{\rm ms}^{\,2}+0.72d_{\rm b}^{\,2}$ и $a_2^{\,2}=0.25z_{\rm ss}^{\,2}+0.72d_{\rm b}^{\,2}$, $z_{\rm ms}$ and $z_{\rm ss}$ are the depths of maximum electron energy losses for the primary beam and reflected electrons, numerically equal to 1/3 and 1/6 of the extrapolated path depth δ_e.

2. Estimation of the approximation accuracy

Let us estimate the accuracy of approximation (5) and the possibility of using it in our problem. Full power P supplied to the target is dissipated in the volume of the interaction region V_{IR} (Fig. 1) [8].In this case, the heat release volumetric power can be found as

$$q_{\upsilon}=\frac{P}{V_{\rm IR}}=\frac{6P}{\pi\delta_{\rm e}\left[3\left(\delta_{\rm e}+0.5d_{\rm b}\right)^2+\delta_{\rm e}^{\,2}\right]}. \tag{6}$$

Obviously, the average value of the volumetric power for distribution (5) must coincide with q_υ from (6).The average value of the volumetric power for the distribution $q_\upsilon(r, z)$ can be found as

$$\overline{q}_v=\int_{r_1}^{r_2}\int_{z_1}^{z_2}\frac{q_{\upsilon}(r,z)\partial z\partial r}{(r_2-r_1)(z_2-z_1)}. \tag{7}$$

For a tungsten W target and the parameters of an electron beam U = 200 kV, P = 20 W, d_b= 20 μm, the value of the volumetric power q_υ is 1.4 mW / μm^3, and the value of the average volumetric power is equal to $\overline{q}_v=1.9$ mW / μm^3, which indicates the correctness of formula (5)and applicability it for our task.In confirmation of the above, Fig.2 shows the spatial distribution of $q_\upsilon(r, z)$ in the interaction region for the purpose of comparison it with the value q_υ = 1.4 mW / μm^3.

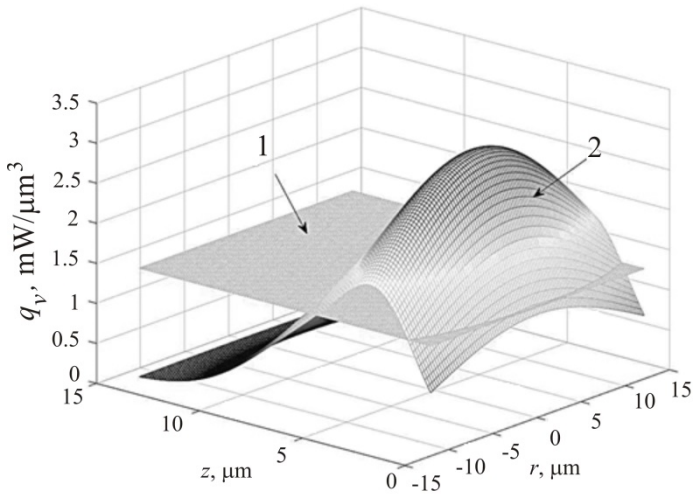

Fig.2. Spatial distribution of volumetric heat sources in the interaction region:
1 - q_υ = 1.4 mW / μm^3, 2 - $q_\upsilon(r, z)$.

From the analysis of the data in Fig.2, it can be concluded that the value q_υ = 1.4 mW / μm^3 really adequately reflects the average value of the distribution $q_\upsilon(r, z)$.Thus, we conclude that relation (5) is

applicable to the solution of stationary thermal problems for transmission type anodes of the of microfocus X-ray tubes.

3. Numerical modeling of the heat transfer process in a flat composite anode with an analytically determined heat release region

Let us consider the problem of determining the thermal mode of operation of the transmission type W-Be anode of a microfocus X-ray tube, taking into account the approximation of the interaction region by a truncated sphere. In view of the complexity of the analytical solution of the heat problem with equation (1), we will use numerical methods. The COMSOL Multiphysics numerical simulation environment allows you to simulate complex thermal problems taking into account all the processes of heat transfer from the solid surface (convection, radiation). The modeling process includes several stages: creation of the geometry of the considered area; selection of materials; setting up the physical interface of heat transfer, namely, setting the initial and boundary conditions, setting the heat source; building a mesh of finite elements; post-processing of the obtained results.

Fig. 3 shows the computational model of the object to the COMSOL environment.

In modeling, we assume that the layer thickness W equaled to δ_e, is calculated by the Cosslett-Thomas formula (4), and the thickness of the Be layer is 100 μm. The composite anode diameter is 10 mm. On the outer boundary, we set the condition of natural convection, which is characterized by the heat transfer coefficient α. Changing the voltage U at a constant power P, we can obtain the dependence T_{max} (U) for W and Be at different values of the diameter d_b. In this case, the beam current $I$is not taken into account in the simulation.

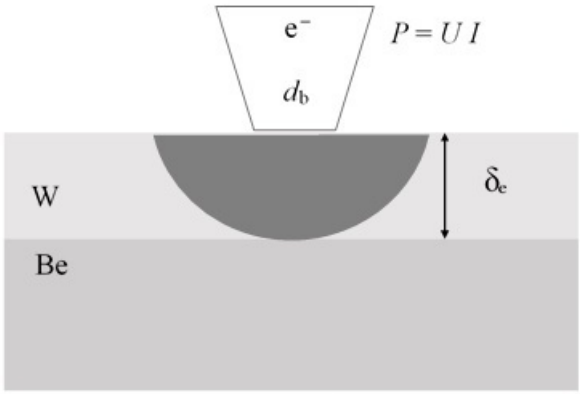

Fig.3. Computational model of heat propagation in ananode of the transmission type.

The purpose of the simulation is to determine the maximum power P_{max} supplied to the target, since the value of P_{max} is limited by the temperature value at which the destruction of the anode materials occurs. The simulation results are shown in Fig.4.

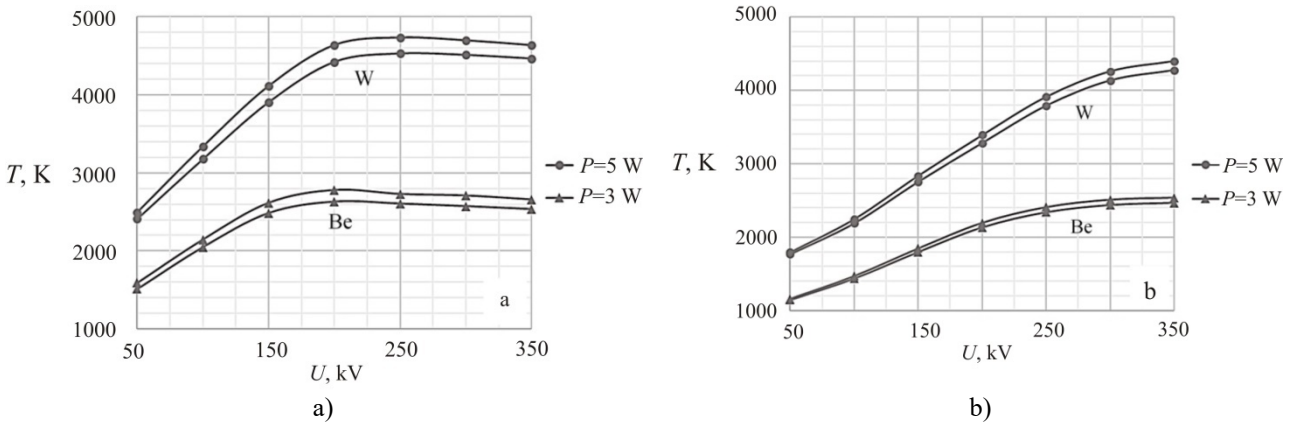

Fig.4. Dependence of the maximum temperature of the materials of the W-Be transmission anode on the voltage U at a fixed power P: a - the size of the focal spot d_b = 10 μm;b - focal spot size d_b = 20 μm

.

Based on the simulation results, it can be concluded that the value of P_{max} is about 3 W, both for d_b= 10 μm and d_b = 20 μm. In this case, the value of the maximum input power is mainly limited by the temperature of the beryllium substrate; moreover, insignificant changes in P lead to a strong increase in temperature. Noteworthy is the presence of a maximum in the curves, which arises as a result of the fact that with increasing U, the temperature difference ΔT increases due to an increase in the effective thickness W of the target. The factor of increasing the volume of the interaction region begins to slightly prevail at voltages of the order of 350 kV, i.e. at low voltages, it can be ignored.

Conclusion

Thus, based on the results of the work, a conclusion can be made that taking into account the influence of the distribution $q_v(r, z)$ makes it possible to carry out a comprehensive numerical study of the thermal mode of operation of the transmission type anode of microfocus tubes in order to establish the relationship between the main parameters of the anode (accelerating voltage U, current I, focal spot diameter d_b and atomic number Z) with the power P. The established relationships are the theoretical basis for achieving the limiting powers dissipated by solid anodes of microfocus X-ray tubes.

Acknowledgments

The research was funded by Russian Foundation for Basic Research (RFBR), project number 19-38-90231.

REFERENCES

1 Hemberg O., Otendal M., Hertz H. M. Liquid-metal-jet anode electron-impact X-ray source. *Applied Physics Letters*. 2003, Vol. 83, No. 7, pp. 1483-1485.

2 Trubitsyn A.A., Grachev E.Yu., Kozlov E.A. High-power x-ray tube for micro computer tomography. *Journal of Physics: Conf. Series.* 2019, Vol. 1164, pp. 012022-1 – 012022.

3 Trubitsyn A.A., GrachevE.Yu., Kozlov E.A., Shugayeva T.Zh. Development of High Power Microfocus Tube. *Eurasian Physical Technical Journal*. 2021, Vol.18, No. 1(35), pp. 43-50.

4 Pozdeeva T.Yu., Smetkin A.A.Monte Carlo simulation of the interaction of an electron beam with matter.Mashinostroyeniye.2017, No. 2, pp. 7-21. [in Russian]

5 Aamir Ihsan, Sung Hwan Heo, Sung Oh Cho. Optimization of X-ray target parameters for a high-brightness microfocus X-ray tube. *Nucl.Instr. and Meth.in Phys. Res. B.* 2007, Vol. 264, pp. 371 – 377.

6 Lukyanov F.A., Rau E.I., Sennov R.A. Depth of path of primary electrons, spreading of an electron beam and spatial resolution in electron probe studies. *Izvestia RAN. Physical series.* 2009, Vol. 73, No. 4, pp. 463 – 472. [in Russian]

7 Amrastanov A.N., Ginzgeimer S.A., Stepovich M.A., Filippov M.N. On one possibility of mathematical modeling of the thermal effect of a sharply focused electron beam on a homogeneous semiconductor. *Izvestia RAN. Physical series.* 2016, Vol. 80, No. 10, pp.1448-1452. [in Russian]

8 Kozlov E., Trubitsyn A., Fefelov A., Kirushin D. "Computer Simulation of Influence the Interaction Region Electrons at the Maximum Temperature in the Target". *Proc. of the 9th Mediterranean Conference on Embedded Computing (MECO 2020), Budva, Montenegro,* June 2020. Article number 9134114.

Article accepted for publication 17.09.2021

DOI 10.31489/2021No3/93-100

UDC 524.832

TACHYONIZATION COSMOLOGICAL MODEL IN THE FRAMEWORK OF LINEAR FORM-INVARIANCE TRANSFORMATIONS

Razina O.V.[1,*], Tsyba P.Yu.[1], Suikimbayeva N.[1, 2]

[1]L.N. Gumilyov Eurasian National University, Nur-Sultan, Kazakhstan, olvikraz@mail.ru

[2]M.Kh.DulatyTaraz Regional University, Taraz, Kazakhstan

This work dedicated to the investigation cosmological models based on tachyon field. It was showed that Einstein's field equations for spatially flat, homogeneous and isotropic Friedman-Robertson-Walker space-time have form-invariance of symmetry, obtained by form-invariance of transformations. The form-invariance of transformations is specified in the general case by the linear function $\bar{\rho} = n^2\rho$, and in particular, we investigate for $n = -1$. The tachyonization of the cosmological model was made for the entire range of values of the barotropic index γ. For the power-law function of the scale factor, a method for obtaining the potential and the function of the tachyon field was shown. The resulting potential is equivalent to the potential used in string theory.

Keywords: tachyon field, form-invariance transformations, equation of state, barotropic index, state finder parameters, deceleration parameter.

Introduction

Our universe is currently undergoing an accelerated expansion phase. This is confirmed by various observational data [1-4]. Theorists speculate that there is a component of matter that currently dominates the energy density of the universe, which is why gravity is repulsive even under standard general relativity. Due to the lack of a complete understanding of the nature of this component, it is called dark energy. Many models of dark energy have been proposed in the literature [5-16]. In this article, we will consider a dark energy model based on a tachyon field using methods of form-invariance transformations.

Form-invariance transformations (FIT) preserves the form of the equations of motion, since it has form-invariance symmetry (FIS) [17]. It was shown in [18] that transformations affect the Hubble expansion rate, energy density, and pressure of the cosmic fluid. Such transformations belong to the Lie group. FIS defines a set of identical cosmological models, since each representation of the Lie group is associated with a certain cosmology, through certain fluids. From the quantum field theory the T-duality comes, which connects a theory compactified on a circle of radius R with another compactified theory on a circle of radius $1/R$ [19-20]. In cosmology, the duality of the scale factor is used [21], which reflects the invariance property of the equations of motion. For the spatially flat FRW metric, the radius R is replaced by the scale factor a, and the dual transformation $a \to a^{-1}$ connects the contracting cosmology with the expanding one [18]. In [22], a method for obtaining phantom k-essence cosmologies using FIS is shown, in which phantom symmetry affects the potential, which leads to an expanded super-accelerated tachyon field.

Due to the emergence of a large number of different theoretical models and the improvement in the reliability of observational data, there is a need for reliable statistics that could distinguish cosmological models of dark energy from each other and from the ΛCDM model. One of these statistics is the pair of the statefinder parameters$\{r, s\}$ [23]. In this paper, we will derive formulas for these parameters after applying FIT and find their values for the power scale factor. Then compare the results with the fixed point ΛCDM model.

1. Model

In the model we are investigating, we choose the action in the form

$$S = \frac{1}{16\pi G}\int \mathrm{d}^4x\sqrt{-g}\{\frac{1}{2}R + \mathcal{L}_m\}, \qquad (1)$$

where R–is Ricci scalar, $\mathcal{L}_m$- density of matter Lagrangian.

.

Friedman-Robertson-Walker metric(FRW) describes by the following expression

$$ds^2 = -dt^2 + a(t)^2(dx^2 + \mathrm{d}y^2 + dz^2), \tag{2}$$

where $a(t)$scalar factor of the universe.

Our aim is investigating internal symmetry Einstein equations jointly spatially flat, homogeneous, and isotropic universe FRW(2). Einstein equations conjointly FRW universe tend to Friedman equations

$$3H^2 = \rho, \tag{3}$$
$$3H^2 + 2\dot{H} = -p, \tag{4}$$

where$H = \frac{\dot{a}}{a}$is a Hubble parameter and “dot” denotes derivatives with respect to the cosmic time.

A consequence of the Friedman equations (3)-(4) is anenergy conservation equation

$$\dot{\rho} + 3H(\rho + p) = 0. \tag{5}$$

For another cosmological model filled with an ideal fluid with energy density $\bar{\rho}$ and pressure $\bar{p}$, one can obtain similar expressions [24-25]

$$3\bar{H}^2 = \bar{\rho}, \tag{6}$$
$$3\bar{H}^2 + 2\dot{\bar{H}} = -\bar{p}, \tag{7}$$
$$\dot{\bar{\rho}} + 3\bar{H}(\bar{\rho} + \bar{p}) = 0. \tag{8}$$

The investigated cosmological models are invariant with respect to each other and it is possible to introduce a relationship between the energy densities

$$\bar{\rho} = \bar{\rho}(\rho). \tag{9}$$

The Friedman equations have three unknown variables (H, p, ρ), and using connection Eq.(9) can find relation for that variables

$$\frac{\bar{\rho}}{\rho} = \frac{3\bar{H}^2}{3H^2}, \Rightarrow \quad \bar{H} = H\left(\frac{\bar{\rho}}{\rho}\right)^{\frac{1}{2}}, \tag{10}$$
$$\bar{\rho} + \bar{p} = \frac{\dot{\bar{\rho}}}{\dot{\rho}}\left(\frac{\rho}{\bar{\rho}}\right)^{\frac{1}{2}}(\rho + p) = \frac{d\bar{\rho}}{d\rho}\left(\frac{\rho}{\bar{\rho}}\right)^{\frac{1}{2}}(\rho + p), \tag{11}$$
$$\bar{p} = -\bar{\rho} + \frac{d\bar{\rho}}{d\rho}\left(\frac{\rho}{\bar{\rho}}\right)^{\frac{1}{2}}(\rho + p). \tag{12}$$

Each of investigating cosmological models is filled with perfect fluid with a barotropic equation of states accordingly$p = (\gamma - 1)\rho$ и $\bar{p} = (\bar{\gamma} - 1)\bar{\rho}$. Barotropic indices γ and $\bar{\gamma}$ have the next connection

$$\bar{\gamma} = \frac{\bar{\rho}+\bar{p}}{\bar{\rho}} = \frac{d\bar{\rho}}{d\rho}\left(\frac{\rho}{\bar{\rho}}\right)^{\frac{3}{2}}\gamma. \tag{13}$$

Form invariance transformation (10)-(12) generates Lie group [18]. The form-invariance of the symmetry is confirmed by the form-invariance of the transformations and shows the equivalence of the investigating models.

2. Linear FIT

FIT can be introduced by following linear function[18]

$$\bar{\rho} = n^2\rho, \tag{14}$$

where n is arbitrary constant. In that case equations (10)-(12)take the form

$$\bar{H} = nH, \tag{15}$$
$$\bar{\rho} + \bar{p} = n(\rho + p), \tag{16}$$
$$\bar{p} = n[p + (1 - n)\rho]. \tag{17}$$

Linear FIT induces linear expresses of variables(H, p, ρ). We obtain power law connection for scale factors by integrating Eq.(15)

$$\bar{a} = a^n \tag{18}$$

and from Eq.(13) transformation for barotropic index

$$\bar{\gamma} = \frac{\gamma}{n}. \tag{19}$$

We can relate the scale factor a of the original cosmological model to the scale factor $\bar{a} = a^n$ of another model due to the existence of the structure of the Lie group [18], [24].

3. Tachyon model

Let us investigate the behavior of the tachyon field and will show its transformation in accordance with the FIT (14)-(17). Density of matter Lagrangian tachyon field in a FRW metric becomes

$$\mathcal{L}_\phi = -V(\phi)\sqrt{1 - \dot{\phi}^2}, \tag{20}$$

here $V(\phi)$ is potential of tachyon field. We substitute Lagrangian (20) in action (1) using the Euler-Lagrange equation and obtain a dynamical system for the tachyon field as follows

$$3H^2 = \rho, \tag{21}$$
$$3H^2 + 2\dot{H} = -p, \tag{22}$$

where energy densityρ and pressure p are defined by expressions

$$\rho = \frac{V}{\sqrt{1-\dot{\phi}^2}}, \tag{23}$$
$$p = -V\sqrt{1 - \dot{\phi}^2} \tag{24}$$

and Klein-Gordon equation

$$\frac{\ddot{\phi}}{1-\dot{\phi}^2} + 3H\dot{\phi} + \frac{V_\phi}{V} = 0. \tag{25}$$

We obtain an expression connecting the square of the derivative of the tachyon field $\dot{\phi}^2$ and the barotropic exponent γ , substituting into the equation of state $p = (\gamma - 1)\rho$ the value of the energy density ρEq.(23) and pressure pEq.(24) to analyze the stability of solutions. In this case it follows that

$$\gamma = \dot{\phi}^2, \tag{26}$$

where $0 < \gamma < 1$. Speed of sound $c_s^2 = 1 - \gamma > 0$or take into account(26)

$$c_s^2 = 1 - \dot{\phi}^2. \tag{27}$$

.

The converted energy density and pressure of the tachyon field are equal

$$\bar{\rho} = \frac{\bar{V}}{\sqrt{1-\dot{\bar{\phi}}^2}} = \frac{n^2 V}{\sqrt{1-\dot{\phi}^2}}, \tag{28}$$

$$\bar{p} = -\bar{V}\sqrt{1-\dot{\bar{\phi}}^2} = -\left(1-\frac{\dot{\phi}^2}{n}\right)\frac{n^2 V}{\sqrt{1-\dot{\phi}^2}}, \tag{29}$$

where we used FIT (14) and pressure (17). From Eq.(19) and Eq.(26)

$$\dot{\bar{\phi}}^2 = \frac{\dot{\phi}^2}{n}. \tag{30}$$

We obtain the transformation expression for the tachyon field $\bar{\phi} = \frac{\phi}{\sqrt{n}}$, integrating the last expression. The transformation conditions for the potential of the tachyon field and the speed of sound are

$$\bar{V} = \bar{\rho}\sqrt{1-\dot{\bar{\phi}}^2} = n^2 V\sqrt{\frac{1-\frac{\dot{\phi}^2}{n}}{1-\dot{\phi}^2}}, \tag{31}$$

$$\bar{c}_s^2 = 1-\dot{\bar{\phi}}^2 = 1-\frac{\dot{\phi}^2}{n}. \tag{32}$$

The usual tachyon field corresponds to$0 < \gamma < 1$. Tachyonization of the model at $1 < \gamma$will be achieved by the complementarytachyon fieldϕ_c, and at $\gamma < 0$ - thephantom tachyon fieldϕ_{ph}. These two kinds of tachyon field can be introduced from the tachyon field analyzed above by applying the transformations [22, 26-27].

The complementary tachyon field $\phi_c$characterized by$1 < \gamma$or$1 < \dot{\phi}_c^2$and expressions for it can be obtained from the standard tachyon field by an internal transformation $1-\gamma \to -(1-\gamma)$, $1-\dot{\phi}^2 \to -(1-\dot{\phi}_c^2)$and $\sqrt{1-\dot{\phi}^2} \to \sqrt{-1}\sqrt{1-\dot{\phi}_c^2} = i\sqrt{1-\dot{\phi}_c^2}$. Having carried out a simultaneous replacement, we get

$$\bar{\rho}_c = \frac{|\bar{V}|}{\sqrt{\dot{\bar{\phi}}_c^2-1}}, \tag{33}$$

$$\bar{p}_c = |\bar{V}|\sqrt{\dot{\bar{\phi}}_c^2-1}. \tag{34}$$

The phantom tachyon fieldϕ_{ph}characterized by$\gamma < 0$, $\dot{\phi}_{ph}^2 = -\gamma$and expressions for it can also be obtained from the standard tachyon field by an internal transformation. In that case $\sqrt{\gamma} \to -i\sqrt{-\gamma}$, $\phi \to i\phi_{ph}$and$\dot{\phi}^2 \to i^2\dot{\phi}_{ph}^2 = -\dot{\phi}_{ph}^2$. Having carried out a simultaneous replacement, we get

$$\bar{\rho}_{ph} = \frac{\bar{V}}{\sqrt{1-\dot{\bar{\phi}}^2}} = \frac{n^2 V}{\sqrt{1-\dot{\phi}^2}}, \tag{35}$$

$$\bar{p} = -\bar{V}\sqrt{1-\dot{\bar{\phi}}^2} = -\left(1-\frac{\dot{\phi}^2}{n}\right)\frac{n^2 V}{\sqrt{1-\dot{\phi}^2}}. \tag{36}$$

Expressions for two new types of tachyon fields were found using simple internal symmetries. All of them are needed to describe the time evolution of the scale factor (18) for all values of γ and to carry out complete tachyonization of the flat FRW universe filled with an ideal fluid with barotropic equations of state $p = (\gamma-1)\rho$.

4. State finder parameters

The various properties of dark energy are highly dependent on the chosen model. Previously, specific evaluation criteria were invented in order to distinguish between different and competing cosmological models involving dark energy. In [23], [28], two parameters, called statefinders, were introduced, which make it possible to distinguish several models of dark energy. These parameters contain the scale factor $a(t)$ and its third derivative with respect to cosmic time t

$$r = \frac{\dddot{a}}{aH^3} = \frac{\ddot{H}}{H^3} - 3q - 2, \tag{37}$$

$$s = \frac{r-1}{3(q-1/2)}, \tag{38}$$

where q is deceleration parameter $q = -a\ddot{a}/\dot{a}^2 = -\ddot{a}/aH^2$. Using Eq.(15)andEq.(18)we get transformation condition for statefinder parameters and deceleration parameter

$$\bar{r} = \frac{\dddot{\bar{a}}}{\bar{a}\bar{H}^3} = \frac{a^2\ddot{a}}{n^2\dot{a}^3} + 3\frac{(n-1)a\ddot{a}}{n^2\dot{a}^2} + \frac{(n-1)(n-2)}{n^2}, \tag{39}$$

$$\bar{s} = \frac{\bar{r}-1}{3(\bar{q}-1/2)} = \frac{2}{3n}\left(1 - \frac{a^2\ddot{a}+(3n-1)a\dot{a}\ddot{a}}{2a\dot{a}\ddot{a}+(3n-2)\dot{a}^3}\right), \tag{40}$$

$$\bar{q} = -\frac{\bar{a}\ddot{\bar{a}}}{\dot{\bar{a}}^2} = -\frac{a\ddot{a}}{n\dot{a}^2} + \frac{1-n}{n}, \tag{41}$$

where to derive the transformation conditions, we used the derivatives

$$\dot{\bar{a}} = na^{n-1}\dot{a}, \tag{42}$$

$$\ddot{\bar{a}} = n(n-1)a^{n-2}\dot{a}^2 + na^{n-1}\ddot{a}, \tag{43}$$

$$\dddot{\bar{a}} = n(n-1)(n-2)a^{n-3}\dot{a}^3 + 3n(n-1)a^{n-2}\dot{a}\ddot{a} + na^{n-1}\dddot{a}. \tag{44}$$

5. Solution

Let consider case when in transformation (14) $n^2 = 1$. When our solution divided into two subcases$n = 1$ и $n = -1$

$$\bar{H} = H, \quad \bar{\rho} + \bar{p} = \rho + p, \quad \bar{a} = a, \tag{45}$$

$$\bar{H} = -H, \quad \bar{\rho} + \bar{p} = -(\rho + p), \quad \bar{a} = \frac{1}{a}. \tag{46}$$

The first subcase corresponds to the identical transformation, and the second case corresponds to the dual transformation, for which the energy density $\dot{\rho} = -3H(\rho + \mathrm{p}) \geq 0$ is an increasing function of time [18].

For $n = 1$, the equations for the statefinderparameters and the deceleration parameter (39) - (41) take the standard form (37) - (38), and for $n = -1$ we get

$$\bar{r} = \frac{a^2\dddot{a}}{\dot{a}^3} - \frac{6a\ddot{a}}{\dot{a}^2} + 6, \tag{47}$$

$$\bar{s} = -\frac{2}{3}\left(1 - \frac{a^2\dddot{a}-4a\dot{a}\ddot{a}}{2a\dot{a}\ddot{a}-5\dot{a}^3}\right), \tag{48}$$

$$\bar{q} = \frac{a\ddot{a}}{\dot{a}^2} - 2. \tag{49}$$

From the conservation equation (5)

$$\frac{\dot{\rho}}{\rho} = -3H(1+\omega), \tag{50}$$

where ω equation of state parameter depends on cosmic time accordingly $\omega = p/\rho$. We substitute equation (50) in Friedman equations(3)take the form

.

$$1+\omega=-\frac{2\dot{H}}{3H^2}, \tag{51}$$

where we used the next relation $\frac{\dot{\rho}}{\rho}=\frac{2\dot{H}}{H}$. For tachyon field $\frac{p}{\rho}=\omega=\dot{\phi}^2-1$. When we can get expression $\dot{\phi}=\left(-\frac{2\dot{H}}{3H^2}\right)^{\frac{1}{2}}$, by integrating which we get

$$\phi(t)=\int\left(-\frac{2\dot{H}}{3H^2}\right)^{\frac{1}{2}}dt. \tag{52}$$

We multiply equations (23) and (24) and use the Friedman equation (3)

$$\rho p=-V^2,\qquad V=(-\rho p)^{\frac{1}{2}}=(-\omega)^{\frac{1}{2}}\rho=3H^2\left(1+\frac{2\dot{H}}{3H^2}\right)^{\frac{1}{2}}. \tag{53}$$

For any scale factor $a(t)$ find the time dependence of the potential $V(t)$ and the tachyon field $\phi(t)$, using equations (52) and (53) and hence the potential $V(\phi)$. Also from equation (52) we can conclude that for these models always $\dot{H}<0$. The tachyon potential, by analogy with the potential of a scalar field, can be used to control the expansion of the universe.

Consider the case when the expansion of the universe obeys the power law

$$a=a_0t^{\alpha}, \tag{54}$$

where a_0 and α some positive constants, and for the accelerated expansion of the universe it is necessary$\alpha>1$. In this case, equations (52) and (53) have the following solutions

$$\phi(t)=\left(\frac{2}{3\alpha}\right)^{\frac{1}{2}}t+\phi_0,\quad V(t)=3\alpha^2\left(1-\frac{2}{3\alpha}\right)^{\frac{1}{2}}\frac{1}{t^2}, \tag{55}$$

where ϕ_0 integration constant. We find the potential $V(\phi)$ by replacing $t$from Eq.(55)

$$V=\frac{V_0}{(\phi-\phi_0)^2}, \tag{56}$$

where $V_0=2\alpha\left(1-\frac{2}{3\alpha}\right)^{\frac{1}{2}}$. This potential diverges at $\phi=\phi_0$ and corresponds to the typical potential of bosonic string theory. The converted scale factor is $\bar{a}=\bar{a}_0t^{\bar{\alpha}}$ с $\bar{a}_0=a_0^n$ и $\bar{\alpha}=n\alpha$. Expressions (55) correspond to the usual tachyon at $0<\gamma<1$. For the complementarytachyon field ϕ_c at $1<\gamma$, which is a stiff matter with a cosmology of deceleration, using FIT we obtain

$$\bar{\phi}_c=\left(\frac{2}{3\bar{\alpha}}\right)^{\frac{1}{2}}t+\phi_{c0},\quad \bar{\alpha}=\frac{1}{3}\left(1\pm\sqrt{1-\frac{9V_0^2}{4}}\right). \tag{57}$$

For phantom tachyon field ϕ_{ph} with $\gamma<0$

$$\bar{\phi}_{ph}=\left(-\frac{2}{3|\bar{\alpha}|}\right)^{\frac{1}{2}}t+\phi_{ph0},\quad \bar{\alpha}=\frac{1}{3}\left(1-\sqrt{1+\frac{9V_0^2}{4}}\right). \tag{58}$$

For the scale factor (54), the statefinderparameters (37) - (38) and the deceleration parameter take the form

$$r=1-\frac{3}{\alpha}+\frac{2}{\alpha^2},\quad s=\frac{2}{3\alpha},\quad q=-1+\frac{1}{\alpha} \tag{59}$$

and after FIT at $n = -1$ parameters(47)-(49)

$$\bar{r} = 1 + \frac{3}{\alpha} + \frac{2}{\alpha^2}, \quad \bar{s} = -\frac{2}{3\alpha}, \quad \bar{q} = -1 - \frac{1}{\alpha}. \tag{60}$$

We exclude the parameter α from equations (59) and (60)

$$r(s) = \frac{9}{2}s^2 - \frac{9}{2}s + 1, \quad r(q) = 2q^2 + q, \tag{61}$$

$$\bar{r}(\bar{s}) = \frac{9}{2}\bar{s}^2 - \frac{9}{2}\bar{s} + 1, \quad \bar{r}(\bar{q}) = 2\bar{q}^2 + \bar{q}. \tag{62}$$

Point $\{r, s\} = \{1,0\}$ is fixed point for ΛCDM-model [23]. It can be seen from equations (61) - (62) that the graphs of the functions $r(s)$ and $\bar{r}(\bar{s})$ pass through this point and are located to the right of it. Dependency graphs $\{r, q\}$ and $\{\bar{r}, \bar{q}\}$ pass in the past through the point $\{1, 0.5\}$ corresponding to the universe with a predominance of matter (SCDM) and the point in the future $\{1, -1\}$ corresponding to stable state (SS) - de Sitter extensions.

Conclusion

By researching our model, we have shown that form invariance transformations can be used to obtain new solutions to the Einstein equation. Moreover, FIT allows you to move from annon-stable cosmology to a stable one and vice-versa. A static universe containing an ideal fluid is always stable at the speed of sound $c_s^2 > 1/5$. If the initially investigated model has a barotropic index γ corresponding to an unstable solution, then after using the transformation rule (32) we can obtain a stable cosmological model.

As in [26], we proved the possibility of the existence of two types of extended tachyons. The complementary $(1 < \gamma)$ and the phantom $(\gamma < 0)$ tachyon fields were obtained from the standard tachyon field ($0 < \gamma < 1$). These fields were used to complete tachyonization of the FRW universe filled with an ideal fluid with barotropic equations of state $p = (\gamma - 1)\rho$ for all values γ and scale factor (54).

A method was shown for finding the time dependence of the potential $V(t)$ and the tachyon field $\phi(t)$ for any scale factor $a(t)$. We were convinced that the tachyon potential, by analogy with the potential of a scalar field, can be used to control the expansion of the universe.

Derived formulas of the statefinder and the deceleration parameter after applying FIT. From the performed study of our tachyon model using statefinder, it can be seen that the results obtained $\{r, s\} = \{1,0\}$ agree with the theory proposed in [23].

Acknowledgments

This study was funded by the Science Committee of the Ministry of Education and Science of the Republic of Kazakhstan AP08955524.

REFERENCES

1 Perlmutter S. et al. Measurements of Ω and Λ from 42 high redshift supernovae. *The Astrophysical Journal*, 1999, Vol. 517, pp. 565–586.

2 Riess Adam G. et al. Observational evidence from supernovae for an accelerating universe and a cosmological constant. *The Astronomical Journal*, 1998, Vol. 116, pp. 1009–1038.

3 Riess Adam G. et al. Type Ia supernova discoveries at z > 1 from the Hubble Space Telescope: Evidence for past deceleration and constraints on dark energy evolution. *The Astrophysical Journal.* 2004, Vol. 607, pp. 665–687.

4 Spergel D. N. et al. First year Wilkinson Microwave Anisotropy Probe (WMAP) observations: Determination of cosmological parameters. *The Astrophysical Journal Supplement Series*, 2003, Vol. 148, pp 175–194.

5 Nojiri S., Odintsov S. D.Future evolution and finite-time singularities in F(R) gravity unifying inflation and cosmic acceleration. *Physical Review D*. 2008, Vol. 78, pp. 046006.

6 Nojiri S. and OdintsovS. D. Introduction to Modified Gravity and Gravitational Alternative for Dark Energy. *International Journal of Geometric Methods in Modern Physics*. 2007, Vol.04, N01, pp. 115-145.

7 BambaK., Nojiri S. and Odintsov S. D. The future of the universe in modified gravitational theories: approaching a finite-time future singularity. *Journal of Cosmology and Astroparticle Physics*, 2008, Vol. 10, pp. 045.

.

8 BambaK., Odintsov S. D., Sebastiani L., Zerbini S. Finite-time future singularities in modified Gauss-Bonnet and F(R,G) gravity and singularity avoidance. *European Physical Journal C*, 2010, Vol. 67, pp. 295-310.

9 Kulnazarov I., Yerzhanov K., Razina O., et al. G-essence with Yukawa Interactions. *The European Physical Journal C*. 2011. Vol.71, No.7, pp. 1698.

10 Razina O., Myrzakulov Y., Serikbayev N., et al. G-essence cosmologies with scalar-fermion interactions. *European Physical Journal Plus*, 2011, Vol.126, No. 9, pp. 85

11 Cai Y.F., Wang J. Dark Energy Model with Spinor Matter and Its Quintom Scenario. *Classical and Quantum Gravity*, 2008, Vol. 25, No.16, pp. 5014.

12 Razina O, Tsyba P, Meirbekov B, Myrzakulov R Cosmological Einstein-Maxwell model with g-essence. *International Journal of Modern Physics D*, 2019, Vol. 28, No.10, pp. 1950126.

13 Razina O., Tsyba P., Sagidullayeva Z. Power solution of the f(R)-gravity with Maxwell term and g-essence. *Bulletin of the Karaganda University. Physics*. 2019, Vol. 1, No.93, pp. 94-102.

14 Bamba K., Razina O., Yerzhanov K., Myrzakulov R. Cosmological Evolution of Equation of State for Dark Energy in g-essence Models. *International Journal of Modern Physics D*, 2013, Vol. 22, No.6, P. 1350023.

15 Myrzakulov R., Saez-Gomez D., Tsyba P. Cosmological solutions in F(T) gravity with the presence of spinor fields. *International Journal of Geometric Methods in Modern Physics*, 2015, Vol.12, No.2, P. 1550023.

16 Yerzhanov K., Yesmakhanova K., Tsyba P., Myrzakulov N., Nugmanova G., Myrzakulov R. g-Essence as the cosmic speed-up.*Astrophysics and Space Science,* Vol. 341, No.2, pp. 681-688.

17 Gieres F. Symmetries in Physics. *Proc. of the 5th Seminaire Rhodanien de Physique*. Dolomieu, 1997, pp.42

18 Chimento Luis P., Richarte Martin G., Sanchez G Ivan E. Form invariance symmetry generates a large set of FRW cosmologies. *Modern Physics Letters A*,2013, Vol. 28, No. 4, pp. 1250236.

19 Green M. B., Schwarz J. H., Witten E. *Superstring theory*. Cambridge University Press, 1987, 469 p.

20 Polchinski J. *String Theory I- II,* Cambridge University Press, 1998, 531 p.

21 Veneziano G. Scale factor duality for classical and quantum strings. *Physics Letters B*, 1991, Vol. 265, pp.287-294.

22 Aguirregabiria J.M., et al. Phantom k-essence cosmologies. *Physical Review D*, 2004, Vol.70, pp.023509.

23 Alam U, Sahni V, Saini D. T, Starobinsky A.A. Exploring the Expanding Universe and Dark Energy using the Statefinder Diagnostic. *Monthly Notices of the Royal Astronomical Society*, 2003, Vol. 344, No. 4, pp. 1057–1074.

24 Sanchez G., Ivan E. Extended tachyon field using form invariance symmetry. *Physical Review D*. 2014, Vol.90, pp. 027308.

25 Forte M. Linking phantom quintessences and tachyons. *Physical Review D*. 2014, Vol. 90, pp. 027302.

26 Chimento L.P., Forte M., Kremer G.M., Ribas M.O. Tachyonization of the ΛCDM cosmological model. *General Relativity and Gravitation*, 2010, Vol. 42, pp.1523-1535.

27 Chimento L. P. Extended tachyon field. Chaplygin gas, and solvable k-essence cosmologies. *Physical Review D,* 2004, Vol. 69, pp. 123517.

28 Sahni V, Saini T.D., Starobinsky A. A., Alam U. Statefinder – A new geometrical diagnostic of dark energy. *Journal of Experimental and Theoretical Physics Letters*, 2003, Vol. 77, pp. 201-206.

Article accepted for publication 17.09.2021

SUMMARIES	ТҮСІНІКТЕМЕЛЕР	АННОТАЦИИ

Козловский А.Л., Здоровец М.В.

Кальций титанаты негізіндегі ферроэлектриктердегі фазалық түрленулерді зерттеу.

Бұл жұмыстың мақсаты – кальций титанаты негізіндегі ферроэлектриктердегі фазалық түрленулердің кинетикасын зерттеу. Бұл зерттеудің өзектілігі микроэлектроникада, фотокатализде және энергетикада қолдану мүмкіндігі бар күрделі фазалық құрамды ферроэлектриктерді алудың жаңа әдістерін бағалауда жатыр. Талдаудың негізгі әдістері ретінде расторлық электрондық микроскопия мен рентгендік дифракция әдістері қолданылды. Морфологиялық ерекшеліктерді талдау түйіршіктердің өлшемдерінің өзгерістерін ғана емес, олардың геометриясындағы өзгерістердің кинетикасын орнатуға мүмкіндік берді. Фазалық түрленулерді зерттеу барысында, босаңдату температурасына байланысты тәуелділіктің келесі түрі анықталды: TiO_2 – anatase/$CaTi_2O_4$ → TiO_2– anatase /$CaTi_2O_4$/$CaTiO_3$ → $CaTiO_3$/TiO_2 – rutile. Сонымен бірге, 1000 °C температурада $CaTiO_3$ типті перовскит тәрізді құрылымы және жоғары дәрежелі құрылымдық реттілігі бар (92%-дан астам) керамиканың тұрақты құрылымы түзіледі.

Козловский А.Л., Здоровец М.В.

Исследование фазовых превращений в сегнетоэлектриках на основе титаната кальция.

Целью данной работы является исследование кинетики фазовых превращений в сегнетоэлектриках на основе титаната кальция. Актуальность данного исследования заключается в оценке новых методов получения сегнетоэлектриков сложного фазового состава, обладающих потенциалом применения в микроэлектронике, фотокатализе и энергетике. В качестве основных методов анализа были применены методы растровой электронной микроскопии и рентгеновской дифракции. Анализ морфологических особенностей позволил установить кинетику изменения не только размеров зерен, но и их геометрии. В ходе проведенных исследований фазовых превращений в зависимости от температуры отжига была установлена следующая зависимость типа TiO_2 – anatase/$CaTi_2O_4$ → TiO_2– anatase /$CaTi_2O_4$/$CaTiO_3$ → $CaTiO_3$/TiO_2 – rutile. При этом при температуре 1000°C происходит формирование устойчивой структуры керамики с перовскитоподобной структурой типа $CaTiO_3$ и высокой степенью структурных упорядочений (более 92%).

Stary O., Суржиков А.П., Малышев А.В., Лысенко Е.Н., Шевелева Е.А.

Ферриттердің пресс ұнтақтарын қалыпқа келтіруші қыздырудың радиациялық және термиялық қақтау кезіндегі тығыздауға әсері.

Радиациялық-термиялық және термиялық қақтау кезінде литий-титан феррит үлгілерінің сызықтық шөгуі зерттелген. Престеу алдында ұнтақтардың бір бөлігі 1273, 1373 және 1473 К температураларда 2 сағат бойы термиялық қыздыруға ұшырады. Ұнтақтарды күйдіргеннен кейін ферриттердің шөгу кинетикасының өзгеруі ақауларды күйдіру есебінен ұнтақтардың термиялық қозуы туралы классикалық ойларға сәйкес келетіні анықталды. Мұндай ақаулар тегістеу кезінде ұнтақ дәндерінде пайда болды. Алынған мәліметтерді талдау ұнтақты ферритінің қақтаудың радиациялық және термиялық белсендірудің ең ықтимал моделін ұсынуға мүмкіндік берді. Тепе-теңсіз ақаулардың релаксациясының радиациялық тежеу моделі алынған.

Stary O., Суржиков А.П., Малышев А.В., Лысенко Е.Н., Шевелева Е.А.

Влияние нормализующего нагрева пресс-порошков ферритов на уплотнение при радиационно-термическом спекании.

Исследована линейная усадка образцов литий-титанового феррита при радиационно-термическом и термическом спекании. Перед прессованием часть порошков подвергалась термическому нагреву в течение 2 часов при температурах 1273, 1373 и 1473 К. Установлено, что изменение кинетики усадки ферритов после отжига порошков согласуется с классическими представлениями о термическом девозбуждении порошков за счет отжига дефектов. Такие дефекты образовывались в зернах порошка при шлифовании. Анализ полученных данных позволил предложить наиболее вероятную модель радиационно-термической активации спекания порошкового феррита. Получена модель радиационного торможения релаксации неравновесных дефектов.

Юров В.М., Гончаренко В.И., Олешко В.С., Sha Minggong

Көміртекті материалдар бетінің анизотропиясы

Жұмыста жетілген монокристалдардың беттік қабатының моделі қолданылады және көміртегі материалдарының наноөлшемді облысында өтетін физикалық процестердегі беттік энергияның рөлі анықталды. Олардың ішінде гауһар, графит, карбин және фуллерендер зерттелген. Кубтық симметриялы алмастың беттік қабатының қалыңдығы 8,2 нм құрайды және нанокұрылым болып табылады. Синтезделген наноалмаздың орташа өлшемі ~ 8 нм реттілікке ие. (100), (110) және (111) алмас жазықтарына есептеген σ_{hkl}

мәні эксперименттпен және басқа есептеулермен жақсы үйлеседі. *a* осі бойындағы графиттің беттік қабатының қалыңдығы $R(I)_a$ = 8.0 нм-ге тең, сонымен қатар наноқұрылым болып табылады. Бірақ *c* осі бойында қабаттың қалыңдығы шамамен 1,5 нм құрайды, ал моноқабаттар саны тек 2-ге тең. Бұл *c* осінде графитті графенге айналдырып, моноқабат құруға болады. Графиттің *a* және *c* жазықтықтары бойынша есептеген σ_{hkl} мәні сәйкесінше 25957 және 5515 мДж/м^2 құрайды. Карбиндер sp -будандастырылған көміртек атомдарынан тұратын полимерлі полииинді немесе кумулен тізбегі болып табылады. Егер карбиннің беттік қабатының қалыңдығы *c* осі бойымен бір өлшемді тізбекке созылған деп есептесек, онда α-карбин үшін бұл тізбектің ұзындығы 200 нм-ге дейін құрайды. Фуллерендердің беттік қабатының қалыңдығы таза металдардың беттік қабатының қалыңдығынан едәуір асып түседі. C_{84} және C_{96} фуллерендердің беттік қабатының қалыңдығы Глейтер бойынша наноқұрылымдарға тән 100 нм-ден асады. Фуллерендердің σ_{hkl} беттік энергиясы көміртегі атомдарының саны $C_{36} \rightarrow C_{96}$ артқан сайын жоғарылайды. Ол (111) → (100) → (110) қатарларында да өзгереді.

Юров В.М., Гончаренко В.И., Олешко В.С., Sha Minggong

Анизотропия поверхности углеродных материалов

В работе использована модель поверхностного слоя совершенных монокристаллов и выяснена роль поверхностной энергии в физических процессах, протекающих в области наноразмеров углеродных материалов. Из них исследованы алмаз, графит, карбин и фуллерены. Толщина поверхностного слоя алмаза кубической симметрии составляет 8,2 нм и представляет собой наноструктуру. Средний размер синтезированного наноалмаза имеет порядок ~ 8 нм. Вычисленное нами значение σ_{hkl} по плоскостям алмаза (100), (110) и (111) неплохо согласуется с экспериментом и другими расчетами. Толщина поверхностного слоя графита по оси *a* равно $R(I)_a$ = 8,0 нм и также представляет наноструктуру. А вот по оси *c* мы имеем толщину слоя около 1,5 нм и количество монослоев всего 2. По этой оси *c* графит можно создать монослой, превратив его в графен. Вычисленное нами значение σ_{hkl} по плоскостям *a* и *c* графита равны 25957 и 5515 мДж/м^2, соответственно. Карбины представляют полимерную полииновую или кумуленовую цепочку, состоящую из атомов углерода в sp-гибридизации. Если представить, что толщина поверхностного слоя карбина растянута в одномерную цепочку вдоль оси *c*, то длина этой цепочки составить до 200 нм для α-карбина. Толщина поверхностного слоя фуллеренов значительно превышает толщину поверхностного слоя чистых металлов. Толщина поверхностного слоя фуллеренов у C_{84} и C_{96} превышает 100 нм по Глейтеру, характерную для наноструктур. Поверхностная энергия фуллеренов σ_{hkl} возрастает с ростом числа атомов углерода $C_{36} \rightarrow C_{96}$. Она также изменяется в ряду (111) → (100) → (110).

Тілебаев Қ.Б., Құрманбаева Г.А.

Ультра дисперсті ұнтақ негізіндегі политетрафторэтиленді модификациялау

Бұл жұмыста политрафрафторэтиленнің (327 °С) балқу температурасынан жоғары температураға дейін қыздырылған ультра жұқа ұнтақта құрылымның пайда болуына термиялық және механикалық әсерлердің әсерін зерттеу нәтижелері келтірілген. Ультра жұқа ұнтақ айналмалы пышақ диірменінде политетрафторэтиленнің өнеркәсіптік үлгісін механикалық ұнтақтау арқылы алынды. Ультра ұнтақты микроскопиялық зерттеу ұнтақ бөлшектерінің көлемі 5 мкм болатын квазисфералық бөлшектер екенін көрсетті. Ультра жұқа ұнтақ бөлшектеріне термиялық (агломерациялық, баяу және тез сөндіру) және механикалық (жоғары қысымды құру) әсерлердің нәтижелері Leica DM 6000 автоматтандырылған цифрлық микроскопы, рентгендік дифракция және Викерс әдістерімен анықталды. Супромолекулалық құрылымның пайда болуы әсер етуші күшке (қысымға) және температураға байланысты екендігі анықталды. Модификацияланған үлгінің қаттылығын өлшеу оның өнеркәсіптік үлгінің қаттылығына қатысты қаттылығы 4 бірлікке жоғарылағанын көрсетті.

Тлебаев К.Б., Курманбаева Г.А.

Модификация политетрафтороэтилена на основе ультрадисперсного порошка

В данной работе представлены результаты исследования влияния термического и механического воздействий на формирование структуры в ультрадисперсном порошке нагретого до температуры выше температуры плавления политетрафторэтилена (327°С). Ультрадисперсный порошок был получен механическим измельчением промышленного образца политетрафторэтилена в роторно-ножевой мельнице. Исследования ультра порошка с помощью просвечивающего микроскопа показали, что частицы порошка представляют собой квазисферические частицы размером 5 мкм. Термические (спекание, медленная и быстрая закалка) и механическое (создание высокого давления) эффекты на частицы ультрадисперсного порошка были определены методами автоматизированного цифрового микроскопа Leica DM 6000, рентгеновской дифракции и Виккерса. Было обнаружено, что образование супрамолекулярной структуры зависят от приложенного усилия (давления) и температуры. Измерение твердости модифицированного образца показало, что его твердость по отношению к твердости промышленного образца увеличилась на 4 единицы.

Рахадилов Б.К., Сагдолдина Ж.Б., Байжан Д.Р., Журерова Л.Г., Ескермесов Д.К., Калитова, А.А., Смайылова М.

Детонациялық бүрку әдісімен титан төсемінде гидроксиапатитті жабындарды алу

Мақалада детонациялық бүрку кезінде титан субстратында гидроксиапатитті жабынды қалыптастыру процесін зерттеу нәтижелері қарастырылады. Раман спектроскопиясы және рентгендік құрылымдық талдау әдістерімен бүрку ұнтақтары және бүрку нәтижесінен алынған гидроксиапатит жабындары зерттелді. Детонациялық бүрку әдісімен алынған жабында α-$Ca_3(PO_4)_2$ фазалары пайда болатындығы, бірақ сонымен бірге гидроксиапатит фазасы жабынның құрамында сақталатындығы анықталған. Раман спектрінде алынған нәтижелер гидроксиапатит жабындардың негізгі фазасы екенін көрсетеді. Бүріккіш жабындардың морфологиясы сканерлеуші электронды микроскопия арқылы сипатталды, ал жабындардың элементтік құрамын талдау энергия дисперсиялық спектрометр детекторының көмегімен алынды. Энергия дисперсиялық спектрометриялық талдау нәтижесінде алынған жабындардың элементтік құрамы бастапқы ұнтақтың элементтік құрамына ұқсас екенін көрсетті, бұл жабындардың қызмет ету мерзімін сақтау үшін өте маңызды.

Рахадилов Б.К., Сагдолдина Ж.Б., Байжан Д.Р., Журерова Л.Г., Ескермесов Д.К., Калитова, А.А., Смайылова М.

Получение гидроксиапатитовых покрытий на титановой подложке методом детонационного напыления

В статье рассматривается результаты исследования процесса формирования гидроксиапатитового покрытия на титановой подложке при детонационном напылении. Методами Рамановской спектроскопии и рентгеноструктурного анализа исследованы порошки для напыления и полученные покрытия из гидроксиапатита. Определено, что для покрытия из чистого гидроксиапатита, полученного методом детонационного напыления, характерным являться появление фаз α-трикальцийфосфата, но при этом в составе покрытия сохраняется фаза гидроксиапатита. Результаты, полученные на рамановском спектре указывает на то, что гидроксиапатит является основной фазой в покрытиях. Морфология напыленных покрытий была охарактеризована с помощью сканирующей электронной микроскопии, а анализ элементного состава покрытий был получен с помощью детектора энергодисперсионного спектрометра. Энергодисперсионный спектрометрический анализ показал, что элементный состав полученных покрытий аналогичен элементному составу исходного порошка, что очень важно для сохранения срока службы покрытий.

Алпысова Г.К., Лисицын В.М., Карипбаев Ж.Т., Голковский М.Г.

Радиация ағыны өрісінде синтезделген церий қосылған итрий алюминий гранат керамикасының люминесценциясы

Жұмыста керамикалық үлгілердің люминесцентті қасиеттерінің сәулелендіру кезіндегі тигельдегі орналасуына тәуелділігін зерттеу нәтижелері берілген. Синтез үшін химиялық таза сортты Al_2O_3, Y_2O_3, Gd_2O_3 және Ce_2O_3 тотықтарының қоспаларынан үлгі дайындалды. Зарядтағы оксидтердің қатынасы стехиометриялық қатынасқа сәйкес келді. Оксид ұнтақтарының бөлшектерінің мөлшері шамамен 1 мкм немесе одан аз болды. Синтез РҒФ СБ Ядролық физика институтында (Новосибирск қ.) электрондар үдеткішінде жүргізілді. Люминесцентті қасиеттер 450 нм монохроматикалық сәулелену арқылы SOLAR шығарған СМ 2203 спектрофлориметрінде өлшенді. Үлгілердің екі түрі зерттелді, олар массалық тығыздығы мен итрий оксидінің тарихымен ерекшеленді.

Алпысова Г.К., Лисицын В.М., Карипбаев Ж.Т., Голковский М.Г.

Люминесценция керамики иттрий-алюминиевого граната, активированного церием синтезированном в поле потока радиации

В работе приведены результаты исследований зависимости люминесцентных свойств образцов керамики от их положения в тигле при облучении. Для синтеза готовилась шихта из смеси порошков окислов оксида алюминия, оксида иттрия. Соотношение окислов в шихте соответствовало стехиометрическому. Частицы порошков окислов имели размеры около 1мкм и меньше. Синтез осуществлялся на ускорителе электронов Института ядерной физики СО РАН (г. Новосибирск). Люминесцентные свойства были измерены на спектрофлуориметре СМ 2203 производства «СОЛАР» при возбуждении монохроматическим излучением на 450 нм. Исследованы двавида образцов, отличающиеся величиной насыпной плотности и предысторией оксида иттрия.

Супрун Т.Т.
Жазық беттегі призмалық элементтердің жылу берілуін бағалауға жергілікті тәсіл
Жазық бетте орналасқан призмалық жылу алмасу элементтері көптеген техникалық қолданыстарға тән. Жұмыстың мақсаты жылу-массо-ұқсастық және термо-анемометрия әдістерін пайдалана отырып, жұмыс ортасының сипаттық аймақтарында жылуфизикалық параметрлерді жергілікті бақылау негізінде жұмыс беттердің жылу берілуін бағалауға жергілікті тәсілді әзірлеу болып табылады. Жергілікті тәсіл орап ағып өтетін элементтің шекаралық қабатындағы ағым түрлерін дәлірек анықтауға және сол арқылы жеке призмалық элементтердің және бүкіл құрылымның температуралық күйін дәл анықтауға мүмкіндік береді. Призманың әр бетінің жергілікті жылу берілуін есептеу үшін геометриялық және режимдік параметрлерге байланысты ұқсастық теңдеулері ұсынылған.

Супрун Т.Т.
Локальный подход к оценке теплопередачи призматических элементов на плоской поверхности
Призматические теплообменные элементы, расположенные на плоской поверхности, характерны для многих технических приложений. Целью работы является разработка локального подхода к оценке теплоотдачи рабочих поверхностей на основе локального контроля теплофизических параметров в характерных зонах рабочей среды с использованием методов тепло-массо-аналогии и термо-анемометрии. Локальный подход позволяет более точно диагностировать типы течения в пограничном слое обтекаемого элемента и тем самым более точно определять температурное состояние отдельных призматических элементов и всей конструкции в целом. Для расчета локальной теплоотдачи каждой грани призмы в отдельности и средне-поверхностного теплообмена в зависимости от геометрических и режимных параметров предложены уравнения подобия.

Танашева Н.К., Сакипова С.Е., Миньков Л.Л., Бахтыбекова А.Р., Шуюшбаева Н.Н., Бурков М.А.
Дефлекторы бар цилиндрлік қалақшаның аэродинамикалық сипаттамаларын зерттеу
Мақалада жаңартылатын энергия көздерін пайдаланудың кейбір аспектілері, атап айтқанда, шағын жел энергиясының мәселесі талқыланады. Әлемде және Қазақстанда жел энергиясының даму қарқынына қысқаша талдау ұсынылған. Зерттеу желдің төмен жылдамдығында электр энергиясын өндіруге арналған Magnus эффектісіне негізделген жел электр стансасының қалақшаның оңтайландыру жолдарын табуға арналған. Қосымша іске қосу механизмдерін пайдаланбай, қалақшаның айналуын тәуелсіз іске қосуды қамтамасыз ету үшін турбо-дефлекторы бар цилиндрлік қалақша жасалынды. Сынақ эксперименттері Т-І-М жел туннелінде әр түрлі ағын жағдайында жүргізілген. Аэродинамикалық күштердің әр түрлі шабуыл бұрыштарындағы ауа ағынының жылдамдығына тәуелділігі анықталды.

Танашева Н.К., Сакипова С.Е., Миньков Л.Л., Бахтыбекова А.Р., Шуюшбаева Н.Н., Бурков М.А.
Исследование аэродинамических характеристик цилиндрической лопасти с дефлектором
В статье рассматриваются некоторые аспекты использования возобновляемых источников энергии, в частности, проблемы малой ветроэнергетики. Приведен краткий анализ темпов развития ветроэнергетики в мире и в Казахстане. Исследование посвящено поиску способов оптимизации лопасти ветроэнергетической установки на основе эффекта Магнуса, предназначенной для выработки электрической энергии при малых скоростях ветра. Разработана цилиндрическая лопасть с турбо-дефлектором на торце для обеспечения самостоятельного запуска вращения лопасти без использования дополнительных пусковых механизмов. Проведены тестовые эксперименты на аэродинамической трубе Т-І-М при различных условиях обтекания. Определены зависимости аэродинамических сил от скорости воздушного потока при различных углах атаки.

Темірбекова М.Н., Wójcik W.
Қатты тұрмыстық қалдықтардың органикалық компоненттерін өңдеуге негізделген энергетикалық отын
Мақалада қоршаған ортаның экологиясын сақтау тұжырымдамасымен әртүрлі тәсілдерді қолдануды көздейтін қатты қалдықтардың органикалық фракциясын өңдеудің тиімді технологиялары қарастырылады. Биомассаны жай жинап, жағуға болмайды, авторлар оны қайта өңдеудің тиімді әдісін қолдануды ұсынады, бұл одан отын алуға мүмкіндік береді. Энергия үшін биомассаны әртүрлі технологиялық процестерді, мысалы, ашыту арқылы биогазды немесе сұйық биоотынды өндіру үшін пайдалануға болады. Олар, өз кезегінде, отын элементтерін жағу немесе жасау арқылы электр мен жылуға айналуы немесе автомобильдерге отын ретінде пайдаланылуы мүмкін. Бұл мақаланың мақсаты - тұрмыстық қатты қалдықтардың органикалық фракциясын алдын-ала өңдеудің балама әдістерін қолдану, этанолды алкоголь ашытқысымен және анаэробты ашыту болып табылады. Қатты тұрмыстық қалдықтардың органикалық фракциясының 1.5 кг-нан құрамында алкоголь бар сұйықтық алуға болатындығы көрсетілген, онда этил спиртінің пайызы 97.5% құрайды. Осылайша, органикалық қатты тұрмыстық қалдықтар қазіргі заманғы энергетикада тиімді отын көзі бола алады.

Темирбекова М.Н., Wójcik W.

Энергетическое топливо на основе переработки органических компонентов твердых бытовых отходов

В статье рассматривается эффективные технологии обработки органической фракции твердых отходов, предполагающие использование различных подходов с концепцией сохранения экологии окружающей среды. Биомассу нельзя просто собирать и сжигать, авторы предлагают использовать эффективный способ ее переработки, который позволит получить из нее топливо. Для получения энергии биомасса может быть использована для производства биогаза или жидкого биотоплива с использованием различных технологических процессов, например, путем ферментации. Они, в свою очередь, могут быть преобразованы в электричество и тепло путем сжигания или создания топливных элементов или использоваться в качестве топлива для автомобилей. Цель этой статьи - использовать альтернативные методы для предварительной обработки органической фракции твердых бытовых отходов ферментацию этанола спиртовыми дрожжами и анаэробное сбраживание. Показано, что из 1.5 кг органической фракции твердых бытовых отходов можно получить спиртосодержащую жидкость, в которой процентное содержание этилового спирта составляет 97.5%. Таким образом, органические твердые бытовые отходы могут быть перспективным источником топлива в современной энергетике.

Бедыч Т.В., Шаяхметов А.Б., Омаров М.С., Исинтаев Т.И.

Жеделдетілген бөлмені жылыту жүйесі

Өндірісте және күнделікті өмірде әртүрлі жылыту жүйелері қолданылады. Жылыту жүйесінің қуатты және сарқылмайтын көздерінің бірі - Күн. Күн энергиясын пайдалану орталықтандырылған жылу және электр мен жабдықтау жүйесінен ажыратылған объектілер: шағын ауылдар, фермерлік қожалықтар, шалғайдағы жайылымдар, жылжымалы үйлер үшін маңызды болып табылады. Күн панельдерінің негізінде жасалған күннен жылыту электр жылытқышты орнату арқылы жүзеге асады. Қазіргі уақытта тұтынушылардың назары электр өткізгішті жылу шығаратын карбонды материалға (карбон) бұрыла бастады. Зерттеудің мақсаты фермерлердің жылжымалы тұрғын үйлерін жылытуға арналған жылытқыш ретінде күн радиациясы мен көміртекті жылу шығаратын икемді материал түріндегі баламалы энергия көзін қолдануды зерттеу болды. Зерттеуді жүргізу үшін фермердің жылжымалы үйіне күн станциясы мен көміртекті жылу шығаратын икемді материал мен жылытқыш орнатылды. Зерттеулер көрсеткендей, ұсынылған жүйе тиімді және басқа жүйелермен салыстырғанда, мысалы, күнколлекторларымен, жүйенің бір қатар артықшылықтары бар екен.

Бедыч Т.В., Шаяхметов А.Б., Омаров М.С., Исинтаев Т.И.

Система обогрева мобильного помещения

На производстве и в быту применяются различные обогревающие системы. Одним из мощных и неиссякаемых источников для обогревающей системы является Солнце. Применение солнечной энергии имеет большое значение для объектов, оторванных от систем централизованного тепло- и энергоснабжения: небольших деревень и аулов, фермерских формирований, отгонного животноводства, мобильных домиков. Отопление от солнца, созданное на базе солнечных батарей, осуществляется путём установки электрического нагревателя. В настоящее время все большее внимание потребителей обращается к электропроводящему тепловыделяющему карбоновому материалу (карбон). Целью текущего исследования было изучение использования альтернативного источника энергии в виде солнечного излучения и карбонового тепловыделяющего гибкого материала в качестве обогревателя для обогрева мобильных жилых помещений фермеров. Для проведения исследований на мобильный домик фермера были установлены солнечная станция и обогреватель с карбоновым тепловыделяющим гибким материалом. Проведенные исследования показали, что предлагаемая система работоспособна и по сравнения с другими системами, например с солнечными коллекторами, система имеет ряд преимуществ.

Бекмулдин М.К., Скаков М.К., Бакланов В.В., Градобоев А.В., Акаев А.С.

Жеңіл сулы ядролық реактордың балқымасының реактор асты қайнау ағынына ие ыстыққа төзімді композитті жабын

Мақала балқыманың реактор асты тұзақтарының қолданыстағы нұсқаларын, сонымен бірге бұл тұзақтардың конструкциялары мен кемшіліктерін талдауға арналған. Қайнау қабатына ие ыстыққа төзімді композициялық жабыны бар балқыманың меншікті реактор асты тұзағының вариация ұсынылды. Қайнау қабаты бар ыстыққа төзімді композициялық жабынға эксперименттік зерттеулер жүргізуге арналған қондырғының сипаттамасы келтірілген. Қайнау қабатына ие балқыманың реактор асты тұзағының вариациясын термиялық есептеу нәтижелері келтірілген. Жылулық есептеу көрсеткендей, балқыманың орташа температурасының жоғарылауы фазалық ауысудың өтуі үшін кориумнен металға жылу бөліну есебінен қайнау қабатына ие реактор асты тұзақ моделінде азырақ қарқынмен жүреді.

Бекмулдин М.К., Скаков М.К., Бакланов В.В., Градобоев А.В., Акаев А.С.

Жаростойкое композитное покрытие с кипящим слоем подреакторной ловушки расплава легководного ядерного реактора

Статья посвящена анализу существующих вариантов подреакторных ловушек расплава, конструкций и недостатков данных ловушек. Предложена вариация собственной подреакторной ловушки расплава с жаростойким композитным покрытием с кипящим слоем. Приведено описание установки для проведения экспериментальных исследований жаростойкого композитного покрытия с кипящим слоем. Приведены результаты теплового расчета вариации подреакторной ловушки расплава с кипящим слоем. Тепловой расчет показал, что увеличение средней температуры расплава проходит менее интенсивно в модели подреакторной ловушки с кипящим слоем, за счет теплоотвода от кориума к металлу на совершение фазового перехода.

Сатыбалдин А.Ж., Жакипбаев Б.Е., Түсіпхан А., Байкенов М.И., Халикова З.С., Алпысова Г.К.

Атасу-Алашанькоу станциясының мұнай қоймаларында пайда болған мұнай түбіндегі шөгінділерге жоғары вольтты разряд параметрлерінің әсері

Барлық өндірілетін мұнайдың үштен он пайызына дейінгі бөлігі кейіннен қайта өңдеу үшін пайдаланыла алмайды. Мұнайды мұнай құятын кемелермен тасымалдау және оны резервуарларда сақтау кезінде олардың түбінде үлес салмағы мұнай мен судың тығыздығынан жоғары көбіне парафин қатарындағы минералды және ең ауыр көмірсутектердің бөлшектерінен тұратын мұнай шөгінділері тұнады. Резервуарларды сенімді пайдалану үшін оларды жиналған тұнбадан мезгіл-мезгілімен тазалап отыру керек. Зерттеудің жаңалығы кәсіпшілік жағдайларда мұнайдың түптік шөгінділерін кәдеге жаратудың қалдықсыз технологиясы шеңберінде электргидравликалық эффектімен әсер ету болып табылады. Атасу-Алашанькоу станциясының мұнай қоймаларында мұнайдың түптік шөгінділерінің ыдырауын қамтамасыз ететін электргидравликалық әсердің оңтайлы шарттары айқындалды.

Сатыбалдин А.Ж., Жакипбаев Б.Е., Тусипхан А., Байкенов М.И., Халикова З.С., Алпысова Г.К.

Влияние параметров высоковольтного разряда на нефтяные донные отложения, образующиеся на нефтехранилищах станции Атасу-Алашанькоу

От трех до десяти процентов от всей добываемой нефти, не может быть использовано для последующей переработки. При транспортировке нефти нефтеналивными судами и ее хранении в резервуарах на дне осаждаются нефтяные отложения, состоящие из частиц минералов и наиболее тяжелых углеводородов парафинового ряда, удельный вес которых больше плотности нефти и воды. Для надежной эксплуатации резервуаров их необходимо периодически очищать от накопившегося осадка. Новизной исследования является использование электрогидравлического эффекта для переработки нефтяных донных отложений в рамках безотходной технологии их утилизации в промысловых условиях. Определены оптимальные условия электрогидравлического воздействия, обеспечивающие разрушение донных отложений нефти в нефтехранилищах станции Атасу-Алашанькоу.

Абильмажинов Е.Т., Акимжанов А.Ж., Шаяхметов Е.Я., Анибаев С.М., Нургалиев Н.Н, Шакерхан К.О., Сайлауов Д.М.

Қазақстанда биогаз саласын дамыту және биогаз қондырғыларын енгізу келешегі

Мақалада шетел және Қазақстан биогаз технологияларына шолу, биогаз индустриясындағы шет елдердің тәжірибесі, ауыл шаруашылығының органикалық қалдықтарын, тамақ өндірісін, қайта өңдеу кәсіпорындарын экологиялық және тиімді қайта өңдеу үшін Қазақстан Республикасында биогаз қондырғыларын дамыту және енгізу келешегіне шолу жүргізілген. Қазақстанның (әсіресе Солтүстік, Шығыс және Орталық Қазақстанның) күрделі климаттық жағдайларында биогаз қондырғыларын жобалау ерекшелігі бойынша ұсыныстар берілді. Биогаз қондырғысының жұмыс істеп тұрған конструкциясы - перистальтикалық сорғы және шикізатты ұсақтағыш (толтыру көлемі 3,7 м^3) көрсетілген, оны жобалау кезінде өз конструкциясының агрегаттары пайдаланылған. Тәжірибелер барысында бірқатар қондырғылардың, атап айтқанда жаңа дизайндағы перистальтикалық сорғының тиімділігі көрсетілді.

Абильмажинов Е.Т., Акимжанов А.Ж., Шаяхметов Е.Я., Анибаев С.М., Нургалиев Н.Н, Шакерхан К.О., Сайлауов Д.М.

Развитие биогазовой отрасли и перспективы внедрения биогазовых установок в Казахстане

В статье сделан обзор биогазовых технологий за рубежом и в Казахстане, опыт зарубежных стран в биогазовой индустрии, развитие и перспективы внедрения биогазовых установок в Республике Казахстан для экологичной и выгодной переработки органических отходов сельского хозяйства, пищевых производств, перерабатывающих предприятий. Даны рекомендации по специфике проектирования биогазовых установок в сложных климатических условиях Казахстана (особенно севера, востока и центрального Казахстана). Показана действующая конструкция биогазовой установки (объем заполнения 3,7 м^3), при проектировании которой были использованы агрегаты собственной конструкции, это перистальтический насос и

измельчитель сырья. Эффективность ряда агрегатов, в частности перистальтического насоса новой конструкции, была показана в ходе проведенных экспериментов.

Утепов Е.Б., Ахажанов С.Б., Анискин А., Жарасов Ш.Ж.

Жетілу сенсорының пластикалық корпусының пішіні мен құрылымының оның физикалық және механикалық қасиеттеріне әсері

Бұл мақалада жетілу сенсор корпусының пішіні және физикалық құрылымы оның жұмысына қалай әсер ететіні көрсетілген. Екі бөліктен тұратын тікбұрышты және цилиндрлік конфигурациялы пластикалық корпустары су өткізбеу, соққыға төзімділік және жүктемелерге төзімділік қабілетіне тексерілді. Сынақтардан елеулі ақаулары анықталмаған цилиндрлік корпуспен салыстырғанда тікбұрышты корпустың су өткізбеу және соққыға төзімділік қабілеттерінің әлсіздігін көруге болады. Корпустың екі түрі де барлық үш жағынан қысу сынақтары кезінде жақсы нәтиже көрсетті, жүк көтергіштігі 0.6-дан 2.11 кПа-ға дейін, бұл адам салмағының 65.3 және 165.3 кг-ға тең. Алынған нәтижелерге сүйене отырып, зерттеу әмбебап тестілеу және жетілу сенсорларының корпусын бағалау үшін қарапайым жұмыс процесін көрсетеді. Ұсынылған жұмыс процесі шағын электрондық құрылғылардың басқа түрлеріне де қолданыла алады.

Утепов Е.Б., Ахажанов С.Б., Анискин А., Жарасов Ш.Ж.

Влияние формы и структуры пластикового корпуса датчика зрелости на его физико-механические свойства

В данной статье представлено, как форма и физическая структура узлов соединений влияют на эксплуатационные характеристики корпуса датчика зрелости. Пластиковые корпуса прямоугольной и цилиндрической конфигураций, состоящие из двух частей, были последовательно испытаны на водонепроницаемость, ударопрочность и устойчивость к нагрузкам. Испытания показали слабую водонепроницаемость и ударопрочность прямоугольного корпуса по сравнению с цилиндрическим, в котором не было выявлено серьезных дефектов. Оба типа корпусов хорошо показали себя во время испытаний на сжатие со всех трех сторон, продемонстрировав несущую способность от 0.6 до 2.11 кПа, что эквивалентно 65.3 и 165.3 кг массы человека. Основываясь на полученных результатах, исследование демонстрирует простой в использовании рабочий процесс для универсального тестирования и оценки корпуса датчиков зрелости. Предложенный рабочий процесс может быть применим и для других типов малогабаритных электронных устройств.

Козлов Е.А., Трубицын А.А, Фефелов А.А., Грачев Е.Ю.

Атыс типті микротоғысты рентген түтіктері нысандарындағы көлемдік жылу көздерінің моделі

Жұмыста микротоғысты рентген түтіктерінің құраушы анодындағы жылу процестерін модельдеуге сандық-аналитикалық тәсілі дамытылған. Модельдеудің бірінші кезеңінде белгілі аналитикалық жуықтауды қолдана отырып, көлемдік жылу көздерін таралу функциясы құрылады. Екінші кезеңде бұл функция ақырлы элементтер әдісімен Пуассон теңдеуімен стационарлы шекаралық есепті шешуде қолданылады. Ұсынылған әдістемені қолдана отырып, атыс типті W-Be анодына ие түтіктің максималды қуатын барабар бағалау жүргізілген.

Козлов Е.А., Трубицын А.А, Фефелов А.А., Грачев Е.Ю.

Модель объемных источников тепла в мишенях микрофокусных рентгеновских трубок прострельного типа

В работе развит численно-аналитический подход к моделированию тепловых процессов в составном аноде микрофокусных рентгеновских трубок. На первом этапе моделирования с помощью известных аналитических аппроксимаций строится функция распределения объемных источников тепла. На втором этапе эта функция используется при решении стационарной краевой задачи с уравнением Пуассона методом конечных элементов. С помощью предложенной методики проведена адекватная оценка максимальной мощности трубки с W-Be анодом прострельного типа.

Разина О.В., Цыба П.Ю., Суйкимбаева Н.Т.

Түрлендірудің сызықтық инварианты пішінішең беріндегі тахионизациялық космологиялық моделі

Жұмыс тахиондық өріс негізіндегі космологиялық модельдерді зерттеуге арналады. Фридман-Робертсон-Уокердің кеңістік-жазықтық, біртекті және изотропты кеңістік-уақыт үшін Эйнштейн өрісінің теңдеулерінде пішіннің инвариантты түрлендірулерінен алынған симметрияның пішіннің инвариантты болатындығын көрсетті. Пішіннің түрлендірулердің өзгермейтіндігі жалпы жағдайда $\overline{\rho} = n^2\rho$, сызықтық функциясымен анықталады, атап айтқанда n=-1 арқылы зерттейміз. γ баротропты индексінің мәндерінің бүкіл диапазоны үшін космологиялық модельге тахионизация жүргізілді. Масштабты фактордың қуат функциясы үшін тахиондық өрісінің потенциалы мен функциясын алу әдісі көрсетілген. Алынған потенциал ішек теориясында қолданылатын потенциалға тең.

Разина О.В., Цыба П.Ю., Суйкимбаева Н.Т.

Тахионизационная космологическая модель в рамках линейной форм-инвариантности преобразований

Работа посвящена исследованию космологических моделей на основе тахионного поля. Показали, что уравнения поля Эйнштейна для пространственно-плоского, однородного и изотропного пространства-времени Фридмана-Робертсона-Уокера имеют форм-инвариантность симметрии, получаемую форм-инвариантностью преобразований. Форм-инвариантность преобразований задаем в общем случае линейной функцией $\bar{\rho} = n^2\rho$, и в частности исследуем при $n = -1$. Провели тахионизацию космологической модели для всего диапозона значений баротропного индекса γ. Для степенной функции масштабного фактора показали метод получения потенциала и функции тахионного поля. Полученный потенциал эквивалентен потенциалу используемому в теории струн.

INFORMATION ABOUT AUTHORS | **АВТОРЛАР ТУРАЛЫ МӘЛІМЕТТЕР** | **СВЕДЕНИЯ ОБ АВТОРАХ**

Abilmazhinov, Ye. T. - Doctor of techn. sciences, Associate Professor, Shakarim University of Semey, Semey, Kazakhstan

Akaev, A.S. – Head of the department of non-reactor tests of the "Institute of Atomic Energy" Branch NNC RK, Kurchatov, Kazakhstan

Akhazhanov, S.B. – PhD, Associate Professor, E.A. Buketov Karaganda University, Karaganda, Kazakhstan

Akimzhanov, A.Z. - Engineer, Shakarim University of Semey, Semey, Kazakhstan

Alpyssova, G.K. - PhD student, Department of Technical Physics, L.N. Gumilyov Eurasian National University, Nur-Sultan, Kazakhstan; Teacher, E.A.Buketov Karaganda University, Karaganda, Kazakhstan

Anibaev, S.M. - Engineer, Shakarim University of Semey, Semey, Kazakhstan

Aniskin, A. – Candidate of technical sciences, Assistant Professor, University North, Varaždin, Croatia

Baizhan, D.R. – Master, Engineer, Research center “Surface Engineering and Tribology”, Sarsen Amanzholov East Kazakhstan University, Ust-Kamenogorsk, Kazakhstan

Bakhtybekova, A.R. - PhD student, E.A. Buketov Karaganda University, Karaganda, Kazakhstan

Baklanov, V.V. – PhD, First Deputy Director of the "Institute of Atomic Energy" Branch NNC RK, Kurchatov, Kazakhstan

Baykenov, M. – Doctor of Chem. sciences, Professor, E.A. Buketov Karaganda University, Karaganda, Kazakhstan

Bedych, T.V. - Candidate of techn. sciences, Head of the Department of Energy and Mechanical Engineering, Kostanay Engineering and Economic University named after M. Dulatov, Kostanay, Kazakhstan

Bekmuldin, M.K. – PhD student, Semey University named after Shakarim, Head of the Laboratory of Experimental Thermophysics group, "Institute of Atomic Energy" Branch NNC RK, Kurchatov, Kazakhstan

Burkov, M.A - master student, E.A. Buketov Karaganda University, Karaganda, Kazakhstan

Fefelov, A.A. – Candidate of techn. sciences, Docent, Ryazan State Radio Engineering University named after V.F. Utkin, Ryazan, Russia

Golkovski, M.G. – Candidate of of phys.-math. Sciences, Budker Institute of Nuclear Physics of the Siberian Branch of the RAS, Novosibirsk, Russia

Goncharenko, V.I. - Doctor of techn.sciences, Professor, Director of the Military Institute, Moscow Aviation Institute (National Research University), Moscow, Russia

Grachev, E.Yu. - Candidate of techn. sciences, Docent, Ryazan State Radio Engineering University named after V.F. Utkin, Ryazan, Russia

Gradoboyev, A.V. – Doctor of techn. sciences, Professor, Department of Control and Diagnostics, National Research Tomsk Polytechnic University, Tomsk, Russia

Isintayev, T.I - Candidate of techn.sciences, Associate Professor, Kostanay Regional University named after A. Baitursynov, Kostanay, Kazakhstan

Kalitova, A. A. – PhD, Senior Researcher, Institute for Composite Materials, Ust-Kamenogorsk, Kazakhstan

Karipbayev, Zh.T. - PhD, Senior Lecturer, L.N. Gumilyov Eurasian National University, Nur-Sultan, Kazakhstan

Khalikova, Z. - Candidate of techn. sciences, Associate Professor, E.A. Buketov Karaganda University, Karaganda, Kazakhstan

Kozlov, E.A. – postgraduate student, Ryazan State Radio Engineering University named after V.F. Utkin, Ryazan, Russia

Kozlovskiy, A.L. - PhD, Associate Professor, Head of the Laboratory of Solid State Physics, Astana branch of the Institute of Nuclear Physics of the Ministry of Energy of the Republic of Kazakhstan, Nur-Sultan, Kazakhstan

Kurmanbayeva, G.A. – PhD student, Abai Kazakh National Pedagogical University, Almaty, Kazakhstan

Lisitsyn, V.M. – Doctor of phys.-math. sciences, Professor, National Research Tomsk Polytechnic University, Tomsk, Russia

Lysenko, E.N. - Doctor of techn. sciences, Professor, Head of the Research Laboratory, National Research Tomsk Polytechnic University, Tomsk, Russia

Malyshev, A.V. – Candidate of phys.-math. sciences, Senior Researcher, National Research Tomsk Polytechnic University, Tomsk, Russia

Minkov, L.L. – Doctor of phys.-math.sciences, Professor, National Research Tomsk State University, Tomsk, Russia

Nurgaliyev, N.N. - PhD, Acting Associate Professor, Shakarim University of Semey, Semey, Kazakhstan

Oleshko, V.S. - Candidate of techn.sciences, Professor of the Department, Moscow Aviation Institute (National Research University), Moscow, Russia

Omarov, M.S. - Candidate of techn.sciences, Associate Professor, Kostanay Engineering and Economic University named after M. Dulatov, Kostanay, Kazakhstan

About «Eurasian Physical Technical Journal»

ISSN 1811-1165 (Print); ISSN 2413-2179 (Online)
Abbreviated key title: Eurasian phys. tech. j.

Eurasian Physical Technical Journal (Eurasian phys. tech. j.) is a peer-reviewed open access international scientific journal publishing original research results on actual problems of Technical Physics and other related fields. Since 2004 «Eurasian phys. tech. j.» is published in English. E.A. Buketov Karaganda University is the main organizer and financial sponsor of Eurasian phys. tech. j. The international editorial board consists of leading physicists from 8 countries.

Since 2008, "Eurasian Physics and Technology Journal" has been included in the list of publications recommended by the Ministry of Education and Science of the Republic of Kazakhstan for publishing the main results of candidate and doctoral dissertations in physical and mathematical sciences. This status is confirmed in accordance with Science Committee Order No. 52 dated January 28, 2021.

Re-registration Certificate No.KZ50VPY00027647 of the «Eurasian phys. tech. j.» issued October 6, 2020 by Information Committee of the Ministry of Information and Public Development of the Republic of Kazakhstan. Since 2021 Eurasian phys. tech. j. will be published quarterly.

Since May 2019 «Eurasian phys. tech.j.» has been indexed in the Scopus database on four scientific areas: Energy, Engineering, Materials Science, Physics and Astronomy. Eurasian Physics and Technology Journal's CiteScoreTracker 2020 is 0.5 with a maximum percentile of 23% in Energy. According to update on 4th September 2021 CiteScoreTracker 2021 is 0.7.

Publication Ethics and Malpractice Statement

Submission of an article to the Eurasian phys. tech. j. implies that the paper described has not been published previously, that it is not under consideration for publication elsewhere, that its publication is approved by all authors and tacitly or explicitly by the responsible authorities where the paper was carried out, and that, if accepted, it will not be published elsewhere in the same form, in English or in any other language, including electronically without the written consent of the copyright holder. In particular, translations into English of papers already published in another language are not accepted.

For information on Ethics in publishing and Ethical guidelines for journal publication see http://www.elsevier.com/publishingethics and http://www.elsevier.com/journal-authors/ethics.

The Eurasian phys. tech. j. follows the Code of Conduct of the Committee on Publication Ethics (COPE), and follows the COPE Flowcharts for Resolving Cases of Suspected Misconduct (http://publicationethics.org/files/u2/New_Code.pdf).

To verify originality, your article may be checked by the originality detection service Cross Check http://www.elsevier.com/editors/plagdetect.

Authors are responsible for the content of their publications. No other forms of scientific misconduct are allowed, such as plagiarism, falsification, fraudu-lent data, incorrect interpretation of other works, incorrect citations, etc. Authors are obliged to participate in peer review process and be ready to provide corrections, clarifications, retractions and apologies when needed. All authors of a paper should have significantly contributed to the research.

Reviewers should provide objective judgments and should point out relevant published works which are not yet cited. Reviewed articles should be treated confidentially. The reviewers will be chosen in such a way that there is no conflict of interests with respect to the research, the authors and/or the research funders.

Editors have complete responsibility and authority to reject or accept a paper, and they will only accept a paper when reasonably certain. They will preserve anonymity of reviewers and promote publication of corrections, clarifications, retractions and apologies when needed.

The acceptance of a paper automatically implies the copyright transfer to the Eurasian phys. tech. j.

All submitted papers will the sent for reviewing to leading experts in the given area.

The Editorial Board of the Eurasian phys. tech. j. will monitor and safeguard publishing ethics.
The editors reserve the right to accept or reject manuscripts.

GUIDELINES FOR AUTHORS

Research articles are accepted for exclusive publication in the «**Eurasian phys. tech. j.»** in English. The manuscripts must contain original results of investigation in the following scientific areas:

ENERGY;

ENGINEERING;

MATERIALS SCIENCE;

PHYSICS AND ASTRONOMY.

The publications of manuscripts should be recommended by official a Cover letter of the organization (University) in which the work was performed.

The author who submitted an article for publication will be considered as a corresponding author.

A scientific article should contain the results of original scientific research previously unpublished and not intended for publication in other publications. Scientific articles submitted for publication in scientific journals should comprise at least 70% of the original text.

The structure of the article includes the following sections:

Title: includes a separate line on the left the **UDC** index, information about the authors (surname and initials, name of institution, city, country, e-mail of a corresponding author, title of the article.

Abstract should consist of at least 5-6 sentences, not exceeding 200 words without formula, references, abbreviations. An abstract is a short and powerful summary that describes the focus of a research paper. It could contain the information about why the research study was done, background, what the methodology was and something about the findings of the author(s).

Keywords: at least 3-10 basic terms or short phrases used in the article.

The text should be divided on structural parts: **Introduction, Theoretical part, Methods and materials or Experimental technique, Results and Discussion, Conclusions**.

Conclusions: formulating main results; a comparison of the results with the existing data on this topic; assessment of scientific novelty and practical value of the results**.**

Acknowledgments may be shown at the end of the article text, before References**.**

References: a bibliographic list is compiled according to the requirements:

- Books, abstracts, patents: Surname and initials of the authors (it is enough to indicate the first three or one surnames, et al), *Title of the book* in italics, publish house or city, year and total number of pages.

- Journals, collections of papers, conference proceedings - Surname and initials of the authors (the first three are enough), the title of the article, the *Title of the journal* in italics (you can use the abbreviated title), city and / or country, year, volume, issue number, pages of the "begining and end" (pp. … - … .).

- Internet links also must to indicated the authors, the title and URL

Title, Abstract and Keywords are given in English, Qazaq, and Russian.

The volume of the article, including bibliography, should not exceed 6-10 pages including tables, figures (no more than 6-8) and references (no more than 30-35) of text typed on a computer (Microsoft Word editor. A review paper must not be more than 15-20 pages (including no more than 10 figures).

Fields of the manuscript should be: left, upper, lower - 30 mm, right - 15 mm; font - Times New Roman, size - 11 pt; line spacing - single; alignment - in width; indent - 0.8 cm.

All abbreviations and acronyms, with the exception of obviously well-known, should be deciphered at first use in the text.

All references must be numbered in the text (for example, [1], [2-4]) and listed in numerical order.

Equations in your paper have to be written using the Microsoft Equation Editor or the MathType.

Tables must be inserted into the text.

Figures should be prepared in a digital form suitable for direct reproduction. Figures shall be submitted on the separate sheets or can be included into the text.

The following files must be submitted via e-mail:

- Article text (*.doc);
- Figures (fig1.jpg, fig2.pcx, …);
- Figure captions (*.doc).

The file should be contained data about all authors, organizations, postal code, postal address, telephone, fax, E-mail, scientific topic of the paper, and Cover letter.

It is possible to use **rar** or **zip** compressors and to transmit the files as an attachment.

Title page (specimen)

UDC

TITLE

Smith J.H., Zeinidenov A.K. Cooper H.J.*

E.A. Buketov Karaganda University, Karaganda, Kazakhstan, email@for_correspondence.kz

Abstract: 5-6 sentences

Keywords: no less 3, but no more 10.

Introduction

Article text. Article text. Article text. Article text. Article text. Article text. Article text. Article text. Article text. Article text Article text. Article text. Article text. Article text. Article text Article text. Article text. Article text. Article text. Article text Article text. Article text. Article text. Article text. Article text Article text. Article text. Article text. Article text. Article text……

References Format (specimen)

1 Conrad H., Muhlbauer A., Thomas R. *Elektrothermische Verfahrenstechnik*. Vulkan-Verlag, Essen Publ. House, 2008, 240 p.

2 Nahar J., Wahedra M. Elastic scattering of positrons and electrons by argon. *Physical Rewiew A,* 2016, Vol. 35, No. 5, pp. 2051 – 2064.

3 Rivoalen H., et al. Electrotubular heat exchanger in chemical industry. *Proceeding of the 12th Intern. Congress on Electricity Applications.* Birmingham, 2017, pp. 29 – 39.

4 Muravleva O. Resource saving prospects based on accuracy theory. *Proceeding of the Intern. Conf. on Computer as a Tool.* 2007*,* pp. 1845-1850, doi: 10.1109/EURCON.2007.4400413.

5 Bochkarev V.P. *Development of physical and chemical principles for assessing the effect of surface energy on the properties of materials and processes for microelectronic technology*. Doctor Diss. of the Techn. Science degree, Moscow, 2020. - 299 p. [in Russian]

6 Zhanabaev Z.Zh., Ibraimov M.K., Sagidolda E. Electrical properties of fractal nanofilms of porous silicon. *Eurasian phys. tech. j.* 2013, Vol. 10, No. 1(25), pp. 3 – 6.

7 X-ray Oxford-Instruments Microfocus Tubes. Available at: www.oxford-instruments.com/products/x-ray-tubes-and-integrated-sources/microfocus-x-ray-systems (Jan13, 2020).

The authors should represent References according to the requirements of international journals on physics, but should to consult preliminarily for standard abbrevi-ations of journal's names.

For more information on references guidelines for journal publication you see Harvard reference system: http://www.emeraldgrouppublishing.com/authors/guides/write/harvard.htm?part=2